AICHI INSTITUTE OF TECHNOLOGY

DOCTORAL THESIS

A Study on Signal Processing Algorithms for Multi-Channel Imaging Radar

Author:
Kei SUWA

Supervisor:
Dr. Ayano NAITO

A thesis submitted in fulfillment of the requirements
for the degree of Doctor of Philosophy

in the

Graduate School of Business Administration and Computer Science

September 7, 2025

AICHI INSTITUTE OF TECHNOLOGY

Abstract

Faculty of Information Science
Graduate School of Business Administration and Computer Science

Doctor of Philosophy

A Study on Signal Processing Algorithms for Multi-Channel Imaging Radar

by Kei SUWA

The growing uncertainty in global affairs, the increasing severity of natural disasters, and the widespread impact of pandemics have exacerbated social anxiety. In this context, remote sensing technology has become an essential tool for comprehensive societal monitoring. Among these technologies, Synthetic Aperture Radar (SAR) and Inverse Synthetic Aperture Radar (ISAR) stand out for their ability to provide high-resolution, continuous surveillance regardless of time or weather conditions. This study seeks to enhance image radar technology by developing signal processing algorithms that introduce innovative system concepts through multi-channel and distributed processing. A particular focus is placed on automated transportation and logistics systems, where precise detection and measurement of objectssuch as satellites, aircraft, ships, and vehiclesare critical for assessing shape, position, and movement. This research explores three key aspects of multi-channel processing: (1) polarization-based processing for detailed observation of target shape and characteristics using polarimetric SAR, (2) time-based processing for detecting moving targets and estimating their velocities through SAR-GMTI, leveraging the concept of small SAR satellite formation flight, and (3) spatial processing for simultaneously estimating target motion and three-dimensional shape via distributed ISAR. For polarimetric SAR, advanced signal processing techniques were developed to enhance resolution using polarization data, enabling high-precision image reconstruction while minimizing data volume. Notably, the findings confirm that reducing bandwidth by half does not substantially degrade image quality due to compensatory ground-based processing, making this approach highly effective for mitigating data constraints in satellite applications. In SAR-GMTI, a deterministic algorithm was formulated to improve the accuracy of detecting and estimating the velocity of slow-moving targets. Airborne SAR flight experiments validated the capability to estimate the velocity of targets moving at approximately 5 m/s with an error margin of 0.1 m/s, demonstrating the feasibility of high-precision moving target surveillance. Furthermore, simulations of a formation flight involving three small satellites revealed that optimizing baseline lengths enables the reliable detection of slow-moving targets within a ś1 m/s range. For distributed ISAR, an algorithm was designed to estimate the three-dimensional shape of targets. ISAR typically captures a sequence of images over time, generating projections from various perspectives. This study leveraged this principle to develop a motion estimation algorithm, achieving a position estimation error of less than 1 meter in theoretical analysis. The findings of this research contribute to the advancement of high-precision remote monitoring systems and provide a foundation for future technological innovations in the field.

Acknowledgements

Over the past 25 years since joining Mitsubishi Electric's research institute, I have had the privilege of engaging in a deeply rewarding research journey —one that has ultimately led to the completion of this thesis. Throughout this time, I have been fortunate to learn from distinguished professors, dedicated mentors, supportive colleagues, and insightful peers I encountered at academic conferences. Their invaluable guidance and encouragement have profoundly shaped this work. I extend my heartfelt gratitude to everyone who has contributed to this achievement.

First and foremost, I am profoundly grateful to Professor Ayano Naito, Professor Katsuhiko Kaji and Professor Nobuhiro Ito for their invaluable mentorship, despite their demanding schedules. Beyond offering insightful feedback on my thesis, they instilled in me the importance of pursuing research with enthusiasm and creative freedom. I also owe a deep debt of gratitude to Professor Tadanori Mizuno, whose perspective —"a doctoral degree is a collective achievement"— rekindled my motivation at a time when I had lost sight of its significance. His wisdom and encouragement were instrumental in shaping this dissertation, and without his guidance, its completion would not have been possible. Additionally, I sincerely thank Dr. Haruko Kawahigashi for her unwavering support in countless ways. She consistently motivated me, urging me forward whenever I found myself struggling. No words can truly capture my profound appreciation for her dedication and encouragement.

I am deeply indebted to the late Professor Mitsutoshi Hatori, Professor Kiyoharu Aizawa, Professor Haruto Hirosawa, Professor Akira Hirose and Professor Seisuke Fukuda of The University of Tokyo, who guided me during my undergraduate and master's studies. Their mentorship laid the foundation for my path in research.

At Mitsubishi Electric's Information Technology R&D Center, I had the honor of collaborating with many remarkable supervisors and colleagues, far too numerous to name individually. Among them, Professor Tetsuo Kirimoto, Dr. Masafumi Iwamoto and Dr. Kazuhiko Yamamoto provided comprehensive guidance from the earliest days of my career —not only in technical matters but also in shaping my professional approach as a researcher. During my early years, I refined my skills alongside Mr. Hideki Hasegawa, Mr. Hiroshi Sakamaki, Mr. Katsuya Kusaba, Dr. Takeshi Amishima, Mr. Satoshi Kageme, Dr. Masayoshi Tsuchida and Dr. Tetsuya Kawase. The experiences shared with these colleagues played a pivotal role in my development. I am also deeply grateful to senior colleagues and mentors who supported me throughout my career: Dr. Seiji Mano, Dr. Shusou Wadaka, Dr. Moriyasu Miyazaki, Dr. Hiroaki Miyashita, Mr. Hiroshi Aruga, Professor Yoshio Kosuge, Mr. Toshiyuki Hirai, Dr. Isamu Chiba, Dr. Hiroyuki Miyata, Dr. Atsushi Okamura, Dr. Hirohisa Tasaki, Dr. Toshio Wakayama, Mr. Teruyuki Hara, Dr. Hiroshi Kameda, Dr. Hisakazu Maniwa, Mr. Ryuhei Takahashi, Mr. Masashi Shiraishi, Mr. Yoshitsugu Sawa and Dr. Motofumi Arii. Although they specialized in different fields, Dr. Toru Oka, Mr. Mikio Takabayashi, Mr. Hideto Aikawa, Mr. Kenji Kawakami and Mr. Yuzuru Saito acted as mentors in my corporate life, and their insights had a profoundly positive impact on my research endeavors.

Beyond my mentors, I had the privilege of learning from exceptional junior colleagues who provided fresh perspectives and inspiration. Among them, Mr. Shohei Nakamura and Mr. Takehiro Hoshino were not just collaborators but also trusted peers, with whom I shared deep conversations about the challenges of life as a researcher and engineer. I also continue to be inspired by Mr. Noboru Oishi, Dr. Yuki Takabayashi, Mr. Tadashi Oshima, Dr. Toshihiro Ito and Mr. Takayuki Kitamura.

Furthermore, I wish to express my gratitude to the members of Mitsubishi Electric Research Laboratories (MERL), whose engaging discussions on cutting-edge signal processing

technologies have provided invaluable inspiration and intellectual stimulation. In particular, I deeply appreciate the friendship and insightful exchanges shared with Dr. Petros T. Boufounos, Dr. Philip V. Orlik and Dr. Anthony Vetro.

At Mitsubishi Electric, our research themes have always stemmed from challenges posed by manufacturing sites. I deeply appreciate Mr. Yoshihisa Hara, Mr. Masao Tsuji, Dr. Yu Okada, Mr. Chikafusa Nonaka, Mr. Akihito Imamura, Dr. Rei Ito, Mr. Seiichi Shimura, Mr. Ryoji Maekawa and Dr. Tomoya Matsuda for providing invaluable technical challenges and research opportunities. A special note of gratitude goes to Mr. Yoshihisa Hara, who granted me the extraordinary opportunity to serve as a visiting researcher at the Massachusetts Institute of Technology (MIT).

Having had the privilege of studying under Professor Jin Au Kong at the MIT is an invaluable treasure in my life. Professor Kong treated everyone with unwavering kindness, including myself, fostering an environment of encouragement and intellectual curiosity. His words —"Theoreticians spend half their research time figuring out where this minus sign came from or where this factor of two originated."— constantly encouraged me and reminded me of the importance of rigorous inquiry. His wisdom and steadfast support were a continual source of inspiration throughout my career. Moreover, the friendships I formed with Dr. Tomasz M. Grzegorczyk, Dr. Bae-Ian Wu, Dr. Dongxing Wang and the other members of the laboratory greatly enriched my research experience at MIT.

Through academic conferences, I had the honor of receiving guidance and insightful discussions with Professor Yoshio Yamaguchi, Professor Kazuo Ouchi, Professor Masanobu Shimada, Professor Hiroyoshi Yamada, Professor Motoyuki Sato and Dr. Takeo Tadono, among many others. I am truly grateful for the valuable exchanges and knowledge shared.

Finally, I extend my deepest love and gratitude to my wife, Naho, my daughter, Yuika and my son, Rikuta. Their unwavering support enabled me to pursue and complete this research. I also wish to express my heartfelt appreciation to my parents, my in-laws, my brother, my sister and my entire family. Without their encouragement, none of this would have been possible.

Contents

List of Figures

List of Tables

This thesis is dedicated to the memory of Professor Jin Au Kong, whose unwavering pursuit of academic excellence remained a profound source of inspiration throughout my studies.

Chapter 1

Introduction

1.1 Motivation

This study aims to contribute to the realization of a society where safety and security are firmly ensured. As the 21st century nears its quarter-century mark, humanity continues to navigate daily life amid growing uncertainty and turmoil. From the September 2001 terrorist attacks to the escalating geopolitical tensions exemplified by Russia's invasion of Ukraine in 2022, the devastation of natural disasters such as the Great East Japan Earthquake in 2011 and the increasing frequency of extreme weather events, along with the global outbreak of COVID-19 in 2019, the challenges confronting modern society are unprecedented. At the same time, rapid advancements in information and communication technologies, coupled with the rise of artificial intelligence and demographic shifts —such as declining birth rates and aging populations— are driving the transformation of social systems toward greater informatization, automation, and AI integration. Humanity stands at the threshold of an uncharted era of coexistence with robots and AI. While these innovations hold immense promise for the future, they also introduce a subtle yet undeniable sense of apprehension. This research is fundamentally guided by the question: "What measures are necessary to mitigate these uncertainties and create a society where safety and security are truly ensured?" Understanding and addressing this challenge is central to this study.

In today's increasingly interconnected world, where informatization, automation, and AI-driven advancements continue to evolve on a global scale, ensuring a safe and secure society demands a broad perspective capable of monitoring current conditions and emerging trends worldwide. Remote sensing, the central focus of this study, is a technology that provides such a perspective. Remote sensing encompasses a range of technologies used to observe objects from a distance. These include satellite- and aircraft-mounted sensors that monitor the Earth, as well as ground-based sensors designed to observe distant atmospheric and space environments[1], [2]. By continuously assessing vast areas, remote sensing plays a critical role in safeguarding society from natural disasters and accidents while also mitigating threats posed by human-made hazards. It enables early detection of changes and rapid identification of anomalies as they arise. Recognizing the significance of these technologies, the government convened the Conference on Science and Technology Policy for Building a Safe and Secure Society from 2003 to 2004[3]. This initiative aimed to comprehensively identify the technological advancements necessary for achieving a secure society. The conference's report underscored the importance of remote sensing as a foundational technology, specifically highlighting its role in "measurement and sensing technologies for rapid anomaly detection" —one of the key areas warranting focused attention. Building upon these insights, this study further explores the contributions of remote sensing in enhancing societal safety and security.

This study explores advancements in remote sensing technology, with a particular focus on imaging radar techniques. Remote sensing sensors can be broadly classified into optical and radio wave sensors. Radar, a primary example of a radio wave sensor, is capable of monitoring vast areas, often spanning hundreds of kilometers. As an active sensor, radar enables

continuous observation regardless of day or night. Additionally, by selecting appropriate wavelengths, radar signals can penetrate clouds and rain, ensuring that observations remain unaffected by weather conditions. These attributes make radar an invaluable tool for wide-area surveillance and continuous monitoring, both of which are essential for maintaining safety and security. However, radar faces resolution limitations, making high-detail observation of targets challenging. Imaging radar addresses this issue by employing advanced signal processing algorithms to enhance resolution, enabling the acquisition of high-definition images of monitored objects. For natural disaster monitoring, key observation targets include oceans, sea ice, rivers, forests, and crustal movements, necessitating a spatial resolution in the range of several meters. By the 1990s, the technology behind synthetic aperture radar (SAR) —a form of satellite-mounted imaging radar— had evolved to achieve meter-scale resolution[4], [5]. As a result, from the 1990s to the 2010s, nations worldwide launched SAR satellites dedicated to Earth observation. Japan has remained committed to the continuous development and deployment of such satellites. Notable examples include Germany's TerraSAR-X (launched in 2007)[6], Canada's Radarsat-2 (launched in 2007)[7], and Japan's ALOS-2 "Daichi-2" (launched in 2014)[8]. During this period, research into SAR applications for environmental monitoring, including disaster assessment, gained significant momentum[9], [10]. Conversely, when monitoring accidents and human-made threats, primary observation targets include aircraft, ships, and vehicleswith artificial satellites now added to the list. Detecting, identifying, and tracking these moving objects requires high spatial resolution, typically around 10 cm, and high temporal resolution (observation frequency) of several minutes or less, depending on target velocity. Historically, the movement of such objects was viewed as a threat primarily in military contexts. However, with the advancement of autonomous driving technology and the demographic shift toward aging populations and declining birth rates, reliance on automated transportation and logistics systems will continue to grow. To ensure the proper functioning of these systems, continuous monitoring and rapid anomaly detection will be crucial, driving a growing demand for imaging radar. Despite its importance, research in this domain remains less developed compared to its applications in environmental monitoring. Thus, this study aims to contribute to the development of imaging radar technologies specifically designed for detecting, identifying, and precisely measuring the shape, position, and movement of satellites, aircraft, ships, and vehicles.

1.2 Research Scope

Imaging radar technology, the focus of this study, enables the observation of target images and is broadly categorized into two types: Synthetic Aperture Radar (SAR) and Inverse Synthetic Aperture Radar (ISAR). SAR captures detailed surface images using radar mounted on satellites or aircraft, making it a fundamental tool for Earth observation. ISAR, by contrast, is designed to generate radar images of distant moving targets. Typically integrated into ground-based or airborne radar systems, ISAR plays a crucial role in target identification, helping to distinguish objects such as aircraft and artificial satellites.

The foundational concept of synthetic aperture radar (SAR) is credited to Carl A. Wiley of Goodyear Aircraft Corporation, who first introduced the idea in an internal company report in 1951 before filing a patent in 1954. However, due to its classification by the U.S. military, the patent remained unpublished until 1965. Wiley initially termed his idea Doppler Beam Sharpening (DBS) but later clarified the distinction between DBS and SAR in his memoirs, explaining[11]: "I had the luck to conceive of the basic idea, which I called Doppler Beam Sharpening (DBS), rather than Synthetic Aperture Radar (SAR). Like all signal processing, there is a dual theory. One is a frequency domain explanationthis is Doppler Beam Sharpening. If one prefers, one can analyze the system in the time domain insteadthis is SAR.

The equipment remains the same —just the explanation changes." This statement succinctly captures the core principles of SAR technology and explains why Wiley is recognized as its inventor, despite initially using a different term. During the 1950s and 1960s, SAR was primarily developed for military reconnaissance, with the first satellite-mounted SAR system launched in 1964 aboard Quill, an experimental satellite operated by the National Reconnaissance Office (NRO) [12], [13]. However, its existence remained classified until 2007. SAR technology made its public debut in 1978, when the SEASAT Earth observation satellite became the first officially acknowledged SAR system[14], [15]. In the 1980s, SAR development was largely driven by the United States, with key missions including SIR-A (1982) and SIR-B (1984)[16], [17] —both flown on the Space Shuttle— and the Magellan Venus exploration satellite (1989)[18]. By the 1990s, SAR advancements became more internationally collaborative, with Europe's ERS-1 (1990)[19], [20] and ERS-2 (1995)[21], Japan's JERS-1 (1992)[22], [23], and the U.S.-Germany joint project SIR-C/X-SAR (1994)[24], [25], followed by Canada's Radarsat (1995)[26]. The 2000s saw a decline in U.S. leadership in SAR development while other nations accelerated technological advancements, particularly through the integration of phased-array antennas, which significantly improved imaging performance. Landmark missions from this era include Germany's TerraSAR-X series[6], Italy's Cosmo-SkyMed series[27], Canada's Radarsat-2[7], and Japan's ALOS series[8]. By 2010, satellite-mounted SAR technology had reached a major milestone. Since 2018, the SAR industry has undergone a radical shift, driven by the emergence of small satellite constellations led by start-up companies[28]–[30]. This has significantly reshaped the landscape of SAR market players. Looking ahead, satellite SAR observation frequency is expected to undergo a dramatic improvement, transitioning from daily observations to hourly monitoring, further enhancing its capabilities.

The origins of Inverse Synthetic Aperture Radar (ISAR) date back to the 1950s, with its roots in radar astronomy[31]. To enhance the resolution of radar used for mapping the surfaces of the Moon and planets in the solar system, researchers leveraged Doppler frequency shifts caused by planetary rotation, enabling them to generate radar images. The first successful observations were conducted at the Millstone Hill Observatory in the United States, capturing radar images of the Moon, Venus, and Mercury. Although the term ISAR was not yet in use, the techniques applied were fundamentally the same as those of ISAR. By the late 1960s, radar systems were being developed specifically for satellite surveillance. Notable examples include the Lincoln C-band Observables Radar (ALCOR), designed by the Advanced Research Projects Agency (ARPA)[32], and the Long Range Imaging Radar (LRIR) developed by Lincoln Laboratory[33]. During the late 1980s, ISAR applications expanded beyond astronomical observation into maritime imaging using airborne radar and aircraft imaging via ground-based surveillance radar. Unlike celestial bodies or satellites, these targets exhibited nonlinear motion, necessitating advancements in motion compensation techniques. Around this period, time-frequency analysis methods evolved, allowing ISAR to capture moving targets as dynamic images[34]–[36]. In recent years, the increase in space debris within satellite orbits and the growing geopolitical competition in space have intensified the demand for space surveillance technologies. Consequently, ISAR-based imaging of artificial satellites has once again gained substantial attention[37], [38].

Between the 1980s and 2010s, imaging radar technology was primarily driven by the pursuit of higher resolution. However, since the late 2010s, advancements in hardware performance and miniaturization have introduced new trends, particularly in multi-channel systems, compact designs, and distributed architectures. This study seeks to develop an innovative imaging radar system concept that harnesses multi-channel and distributed radar technologies to detect and precisely measure the shape, position, and movement of objects such as satellites, aircraft, ships, and vehicles. To accomplish this, the research focuses on the development of signal processing algorithms for multi-channel imaging radar.

The first research theme explores Polarimetric Synthetic Aperture Radar (PolSAR), which leverages multi-channel polarization to accurately measure a target's shape and reflective properties. PolSAR transmits and receives two orthogonal polarizations, allowing for the observation of polarization-dependent scattering characteristics. This approach enhances target analysis and visibility by overlaying images from different polarization channels to create pseudo-color representations. However, PolSAR generates four times the data volume of conventional single-polarization SAR, leading to operational constraints, particularly for satellite-based systems. To mitigate this challenge, a signal processing algorithm was developed to lower resolution during observation, reducing data volume, while subsequently enhancing resolution during ground-based processing [39]–[44].

The second theme focuses on SAR-Ground Moving Target Indication (SAR-GMTI), a technique for detecting moving targets on land and sea surfaces while estimating their velocity using multiple antenna apertures aligned along the direction of motion. Satellite-based SAR systems hold significant promise for monitoring traffic patterns, disaster-stricken areas, and security-related activities. However, detecting slow-moving targets (10 km/h) requires widening the antenna aperture spacing to several tens of meters, making it challenging for a single satellite to provide effective SAR-GMTI functionality. To overcome this limitation, a signal processing algorithm was designed to facilitate a formation flight system of small SAR satellites, enabling high-precision detection, position estimation, and velocity measurement [45]–[48].

The third theme investigates three-dimensional shape estimation using an Inverse Synthetic Aperture Radar (ISAR) system with distributed antenna apertures. Traditionally, ISAR captures two-dimensional radar images, but improving target identification necessitates three-dimensional shape observation, which has yet to be practically implemented. ISAR continuously observes a single target over several seconds, producing a sequence of images from varying projection angles. If the orientation of these projection planes can be determined, a 3D shape reconstruction becomes feasible. However, because projection angles are dependent on target motion, motion and shape must be estimated simultaneously. To achieve this, a multistatic system —characterized by its use of three distributed receiving channels— was developed to capture three sets of ISAR images, enabling the joint estimation of a targets three-dimensional shape and movement [49]–[51].

This research establishes signal processing algorithms for multi-channel imaging radar with the overarching goal of advancing system concepts that utilize multi-channel and distributed radar architectures. To ensure feasibility, the study systematically formulates signal processing algorithms for the three themes and defines the relationships between system parameters and performance metrics, enabling reliable scalability assessments.

1.3 Structure of the Thesis

This dissertation is structured into six chapters. Chapter 1 serves as the introduction, broadly presenting the motivation behind this research. It discusses the role of remote sensing in fostering a safe and secure society, provides a historical overview of imaging radar technology, and identifies the challenges that must be addressed.

Chapter 2 outlines the fundamental concepts essential to this dissertation, covering the principles of radar technology and imaging radar, along with an overview of multi-channel imaging radar, establishing the technical foundation for the study.

Chapter 3 introduces a signal processing algorithm designed to enhance the resolution of polarimetric SAR. It includes validation through computer simulations and experiments using real SAR images, accompanied by performance evaluations conducted via simulations. The evaluation begins by redefining polarimetric SAR resolution based on a novel resolution

concept introduced in [52], followed by an analysis of its theoretical limits. The evaluation then examines how closely the proposed method approaches these limits. To the author's knowledge, no prior research has extensively explored the theoretical boundaries of polarimetric SAR resolution, making this study a significant contribution.

Chapter 4 presents a signal processing algorithm for SAR-GMTI (Ground Moving Target Indication), aimed at detecting, locating, and estimating the velocity of moving targets on land and sea surfaces. It summarizes experimental validation using airborne SAR systems, along with theoretical performance analysis of the proposed method. Additionally, this chapter explores satellite deployment strategies optimized for a formation flight system of small SAR satellites.

Chapter 5 introduces a signal processing algorithm for simultaneously estimating the three-dimensional shape and motion of a target using an ISAR system with distributed antenna apertures. It presents principle validation through computer simulations, as well as theoretical analyses crucial for system design optimization. Since the proposed system does not currently exist and would require large-scale experimental setups, real-data evaluations were impractical. Instead, assessments were conducted using electromagnetic scattering simulations and 3D aircraft models, allowing for evaluations under conditions that closely resemble real-world data.

Finally, Chapter 6 provides a comprehensive summary of the findings presented throughout the dissertation and draws conclusions.

Chapter 2

Background

2.1 Radar principles and characteristics

2.1.1 Basic principles

Radar (RAdio Detection And Ranging) is a sensor which detects an object in a distance by transmitting electromagnetic pulse and receiving the echo reflected back from it[53]–[55]. Radar measures the distance r to the object by observing the propagation time τ as shown in Fig 2.1(a). An object of interest is commonly called "target" in the context of radar technology, so we use the term "target" hereafter. Since the electromagnetic pulse propagates in the speed of light c, the relation between the distance r and the propagation time τ satisfies the following equation:

$$\tau = \frac{2r}{c} \quad \Leftrightarrow \quad r = \frac{c\tau}{2}. \tag{2.1}$$

Once the radar measures the propagation time τ, then the distance r can be determined by (2.1). Fig 2.1(b) illustrates the radar signal associated with one transmit pulse. The echo reflected back from the target appears as a power peak at the propagation time τ which corresponds to the range r. Note that the horizontal time axis, which we call delay time axis, can immediately be translated to the range axis by (2.1).

Early version of the radar, which was mostly developed in the early 20th century, literally was a sensor for "detection and ranging". Then in the middle of the 20th century, pulse-Doppler radar, which measures the radial velocity as well as the range of the target, was developed. The pulse-Doppler radar measures the radial velocity v_r of the target by observing the Doppler frequency f_d as shown in Fig 2.2(a). Doppler frequency refers to the frequency

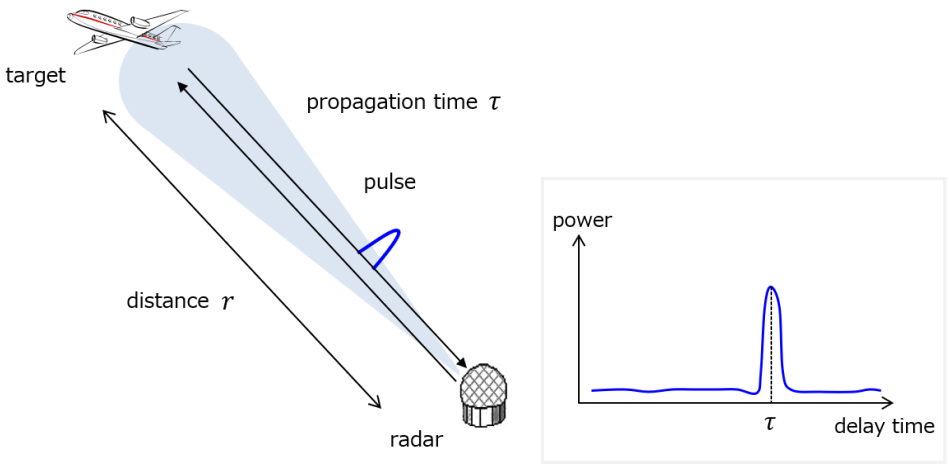

(a) observation geometry (b) signal

FIGURE 2.1: Basic concept of Radar

shift caused by Doppler effect, and the relation between the radial velocity v_r and the Doppler frequency f_d satisfies the following equation:

$$f_d = -\frac{2v_r}{\lambda} \quad \Leftrightarrow \quad v_r = -\frac{f_d \lambda}{2}, \tag{2.2}$$

where λ is the wavelength of the carrier frequency of the transmitted electromagnetic pulse. Once the pulse-Doppler radar measures the Doppler frequency f_d, then the radial velocity v_r can be determined by (2.2). Note that the pulse-Doppler radar measures the radial velocity and the cross range, or azimuth, component of the velocity can not be measured.

Fig 2.2(b) illustrates the pulse-Doppler radar signal. The pulse-Doppler radar employs multiple pulse echos to observe the Doppler frequency. The radar sends out the pulses consecutively, and at each pulse, the radar receives the echo reflected back from the target. Then the received signal is stored in a 2D matrix as shown in this figure. The signal along the delay time axis represents the received signal corresponding to each pulse. At each pulse, echo reflected back from the target appears as a power peak at the propagation time τ. The signals corresponding to the pulses are arranged in order along the time axis according to pulse transmission timing. Strictly speaking, the propagation time τ slightly changes pulse by pulse as the target moves; therefore, the peak position moves accordingly. But in practice, the observation time is short enough, so that the change in τ during one set of observation is negligible compared to the resolution of the system. (The issues on resolution will be discussed later in this section.) While the position of the power peak can be treated as if it stays the same during observation, the signal phase change can not be ignored. The phase ϕ of the echo reflected back from the target at range r is represented as:

$$\phi = -\frac{4\pi r}{\lambda}. \tag{2.3}$$

Therefore, the rate of change of the phase $\dot{\phi}$ can be derived as:

$$\dot{\phi} = -\frac{4\pi \dot{r}}{\lambda} = -\frac{4\pi v_r}{\lambda}. \tag{2.4}$$

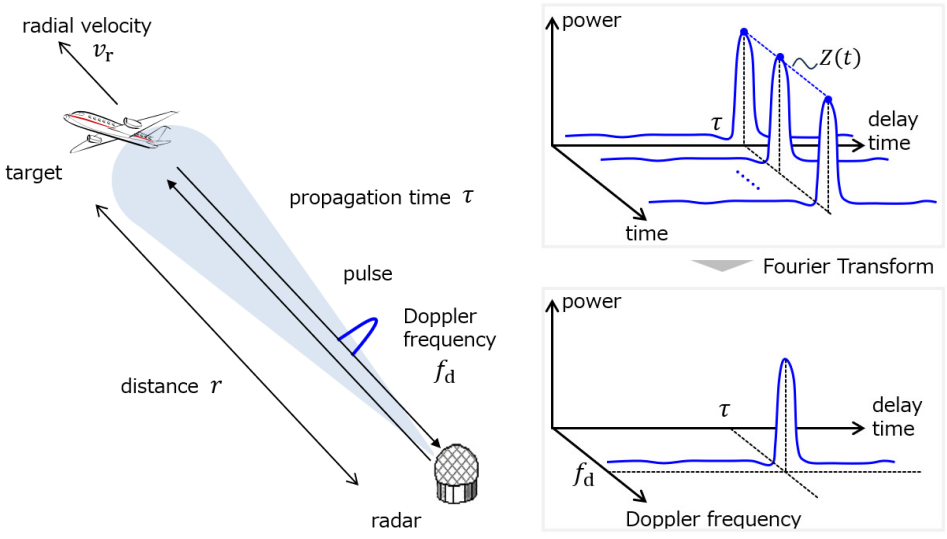

(a) observation geometry (b) signal

FIGURE 2.2: Basic concept of Pulse Doppler Radar

Note that the radial velocity v_r is $\dot{r}$ by definition. Then the complex envelope of the signal at the peak position, i.e., $Z(t)$ in Fig 2.1(b), can be modeled as:

$$Z(t) = A\exp\left\{\dot{\phi}t\right\} = A\exp\left\{-\frac{4\pi v_\mathrm{r}}{\lambda}t\right\} = A\exp\left\{2\pi f_\mathrm{d}t\right\}, \tag{2.5}$$

where t is the time that represents the pulse transmission timing. Observing the equation (2.5), one can see that if we apply Fourier Transform to the received signal in the time t direction, we will get a peak at the Doppler frequency f_d as shown in the bottom of Fig 2.1(b), which is called range-Doppler domain signal. The pulse-Doppler radar detects the signal in the range-Doppler domain, and measures the range and the radial velocity of the target from the signal peak position.

2.1.2 Resolution of radar

The performance of the radar is measured by several factors. Given that radar sensors are designed to detect distant targets, their maximum detection range naturally emerges as the most critical specification. Another important performance index is resolution. Radar resolution is the ability of a radar to separate the echos from different targets, if there exist multiple targets close to each other. The echos from these targets may merge into one, making the radar unable to perceive how many targets there are. But in many cases, it is very important to know the number to get a clear grasp of the situation. In this section, we further discuss the resolution of the radar as an introduction to imaging radar technology, since imaging radar primarily is the technology to enhance the resolution of the radar. The maximum detection range and other performance indices are not discussed in this section, although they are equally important as resolution. Readers are encouraged to read a basic textbook on radar technology such as [55].

As stated before, the definition of radar resolution is simple: the ability of a radar to separate the echos from different targets. However, if you try to take a deep dive on how to quantify the resolution, you immediately notice that it is almost impossible to derive metrics that perfectly reflect this definition. Because if the echo can be resolved by the radar heavily depends on the characteristics of the targets, such as the size, reflectivity and so on [56]. Therefore, the engineers usually employ "the Rayleigh criterion for the diffraction limit" to

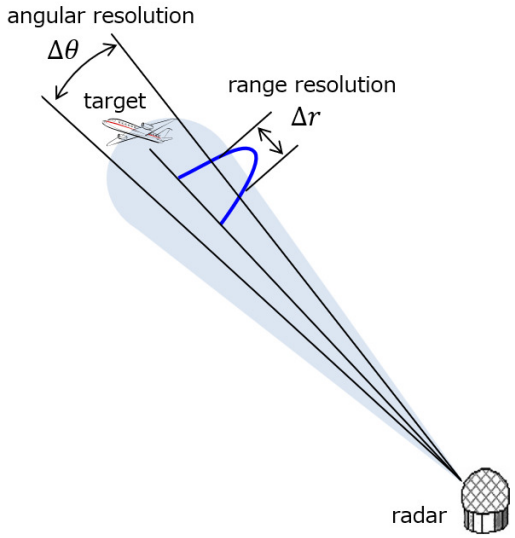

FIGURE 2.3: The resolution of the radar

express the resolution of radar systems. The number is independent of the characteristics of the targets, and it can be derived directly from the radar system parameters. It is a nominal number that gives rough idea of how well the radar system will be able to resolve the echos from the targets close to each other.

The resolution of radar is defined in two directions: range direction and angular direction, as shown in Fig. 2.3. The range resolution Δr describes the resolution capability over the distance. The Rayleigh criterion for the diffraction-limited range resolution is defined by the bandwidth B of the transmitted pulse as follows:

$$\Delta r = \frac{c}{2B}. \tag{2.6}$$

The angular resolution $\Delta\theta$ describes the resolution capability over the angular direction. The Rayleigh criterion for the diffraction-limited angular resolution is defined by the antenna aperture size L as follows:

$$\Delta\theta = \frac{\lambda}{L}. \tag{2.7}$$

For the pulse-Doppler radar, the resolution in the Doppler frequency domain is another important metric. The Rayleigh criterion for the diffraction-limited resolution can also be derived in the Doppler domain, and it is defined by the observation time T as follows:

$$\Delta f_{\mathrm{d}} = \frac{1}{T}. \tag{2.8}$$

Note that once the Doppler frequency resolution is identified, the radial velocity resolution Δv_{r} can immediately be derived from (2.2) as:

$$\Delta v_{\mathrm{r}} = \frac{\Delta f_{\mathrm{d}}\lambda}{2} = \frac{\lambda}{2T}. \tag{2.9}$$

Fig. 2.4 (a), (b) and (c) summarizes the relationship in (2.6), (2.7) and (2.8), respectively. As one can see from these figures, the finite bandwidth, the finite antenna aperture and the finite observation time define the range, angular and Doppler frequency resolution, respectively in the same manner. To get a rough idea of the actual values of the radar resolution, let us consider a sample radar system whose system parameters are listed in Table 2.1. For this radar system, the range resolution Δr is 10m, the angular resolution $\Delta\theta$ is 0.01 rad, the Doppler frequency resolution f_{d} is 200Hz the radial velocity resolution Δv_{r} is 3m/s. Note that these numbers do not guarantee that the radar can always resolve the echos from the targets, if the distance between the targets or the velocity difference of the targets are larger than these numbers.

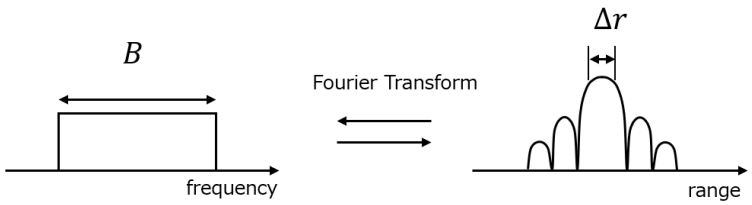

(a) signal bandwidth and range resolution

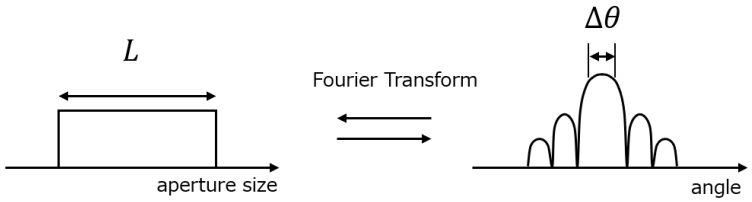

(b) antenna aperture size and azimuth resolution

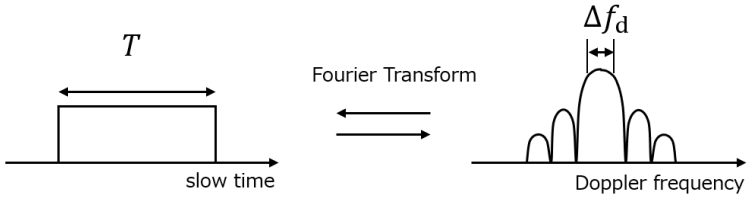

(c) observation time and Doppler resolution

FIGURE 2.4: The resolution of the radar

TABLE 2.1: A sample radar parameters

parameter		value
antenna aperture length	L	3m
wavelength of the carrier frequency	λ	3cm
bandwidth	B	15MHz
observatron time	T	5msec

2.2 Imaging radar principles and characteristics

2.2.1 Imaging radar systems

Imaging radar is an application of pulse-Doppler radar which observes high-resolution two-dimensional images of targets. There are two types of imaging radar: Synthetic Aperture Radar (SAR) and Inverse Synthetic Aperture Radar (ISAR). The concept of imaging radar emerged soon after pulse-Doppler radar was invented. SAR was invented by Carl A. Wiley as early as 1951, while the concept of ISAR was formulated a little bit later in the 1950s. Both SAR and ISAR technologies were developed at an accelerated pace from the 1980s with the development of digital signal processing technology and digital computers.

Fig. 2.5(a) illustrates the SAR observation geometry and an example of SAR image. SAR observes landscape image with pulse-Doppler radar system mounted on aircraft or satellite and points sideways. As the platform moves along its flight path or orbit, the radar sends pulses to the planet's surface sequentially and receives the reflected signal. After some signal processing, it obtains the image of a strip of surface along the flight path. Applications of SAR include environmental monitoring, earth-resource mapping, monitoring of marine and coastal environments, surveillance and so forth. Fig. 2.5(b) illustrates the ISAR observation geometry and examples of ISAR image. ISAR observes images of moving objects such as aircraft in flight, ships at sea, satellites in orbit, asteroids and so forth. Typically, ISAR is implemented as a function of multifunction radar (MFR) which performs many functions such as surveillance, tracking and target recognition. The radar could either be stationary or mounted on moving platforms. Essentially, it is the relative motion of the target to the radar which is exploited to observe the target image.

The advantage of the imaging radar over optical sensor is its all-weather and day-night imaging capability. Since radar is an active sensor which transmits microwave to observe the target, it does not require daylight for observation. In addition, imaging radar can provide the target image regardless of weather, since microwave penetrates through clouds. Therefore, imaging radar provides an ideal means for continuous monitoring of airspace, sea area and land area.

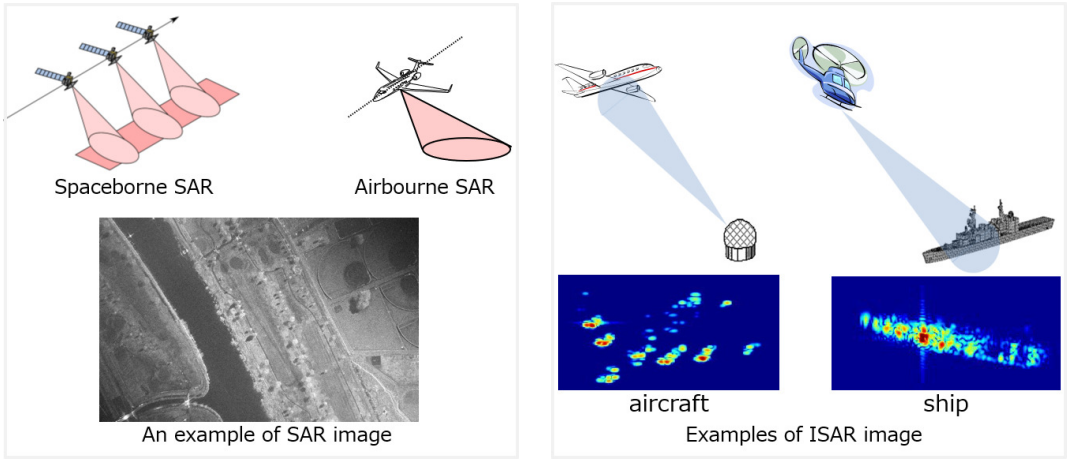

(a) SAR (b) ISAR

FIGURE 2.5: Types of imaging radar

2.2.2 Synthetic aperture radar

Synthetic aperture radar (SAR) is a type of imaging radar system, which observes high-resolution images of landscape. Fig. 2.6 illustrates the SAR observation geometry. A radar system is mounted on a platform such as satellite or aircraft. The radar transmits pulses to the side of the platform and towards the planet surface, then it receives the echo reflected back from the surface. As the platform moves along the orbit or flight path, the radar repeatedly transmits pulses and records the reflected signals. The SAR image, observed in this manner, can represent the image projected onto the plane spanned by the vectors notated as range and azimuth in Fig. 2.6. The range direction refers to the direction of the beam center, or radar line of sight, and the azimuth direction refers to the direction parallel to the orbit, or along track direction. The received signal looks like an image when the spatial resolution, defined by range resolution Δr and azimuth resolution Δa , is sufficiently high.

The range resolution Δr is the same as that of normal radar, and it is defined by the bandwidth B as follows:

$$\Delta r = \frac{c}{2B}. \tag{2.10}$$

To be precise, the range resolution Δr is defined along the radar line of sight on the image projection plane, and since the image plane is slanted, Δr is often referred to as "slant range resolution." SAR systems typically use very wide bandwidth to obtain high resolution image. For example, Capella-SAR, one of the latest modern spaceborne SAR systems, employs 600MHz to achieve the slant range resolution of 25cm.

The azimuth resolution Δa is determined by the angular resolution $\Delta\theta$ of the radar. The azimuth resolution corresponds to the width of the beam footprint at the surface; therefore, if the distance between the radar and the surface is r, the azimuth resolution would be defined by $\Delta\theta$ as follows:

$$\Delta a = R\Delta\theta = \frac{\lambda R}{L}, \tag{2.11}$$

where the last equation is derived from (2.7). However, the azimuth resolution predicted by (2.11) is, in fact, far from satisfactory. For example, if we assume that the antenna aperture

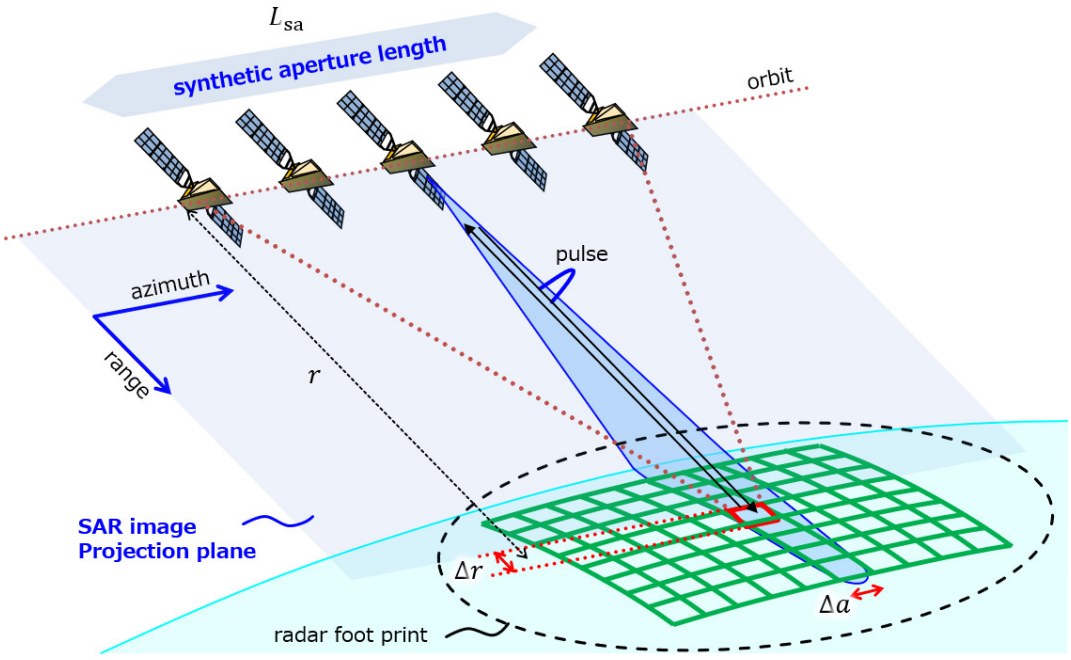

FIGURE 2.6: Observation geometry of Synthetic Aperture Radar

length L is 3m, the wavelength of the carrier frequency λ is 3cm and the distance between the radar and the surface r is 500km, then the azimuth resolution Δa becomes 5,000m, which is too large for the signal to look like an image. To obtain a reasonable azimuth resolution, e.g. a few meters or less, the antenna aperture length is required to be several kilometers, which is unrealistic.

SAR solves this problem by utilizing the motion of the platform to virtually "synthesize" a long antenna. As stated before, the radar repeatedly transmits pulses and records the reflected echo while the platform moves along the orbit. Then the SAR system add up the received signals that are transmitted and received while the platform travels the distance of synthetic aperture length L_{sa} shown in Fig. 2.6 to virtually obtain a much narrower beam width θ_{sa}. Then high azimuth resolution Δa can be achieved as follows:

$$\Delta a = R\Delta\theta_{\mathrm{sa}} = \frac{\lambda R}{2L_{\mathrm{sa}}}. \tag{2.12}$$

For example, if λ is 3cm, r is 500km and the synthetic aperture length L_{sa} is 5,000m, then the azimuth resolution Δa is 1.5m.

SAR achieves the azimuth resolution in (2.12) as long as the targets in the scene are stationary during data acquisition. What happens to the moving target signal will be thoroughly studied in Chapter 4.

Fig. 2.7 illustrates the principle of SAR image formation processing. In this figure, two point targets are assumed to exist in the observed scene as shown in Fig. 2.7(a). As shown in Fig. 2.7(b), the echo from the two point targets form the curved trace in the received signal. This is because the distance to the point target varies as the radar moves by the point target; at first, the platform gets closer to the point target, and when the platform passes by looking sideways at the point target, the distance becomes minimum, then the point target gets farther away as the platform goes on.

In fact, the changes in the distance and phase of the reflected signal from a point target can be calculated from the observation geometry in advance. Based on this prior knowledge, a reference signal is generated. Then, SAR image formation processing is to calculate the correlation between the observed signal and the reference signal. In other words, SAR image essentially is a 2D correlation function between the observed signal and the reference signal. Since performing this correlation processing in the time domain requires an enormous amount of computation, various methods have been proposed to perform high-speed correlation processing in the frequency domain. The most commonly used algorithms include range

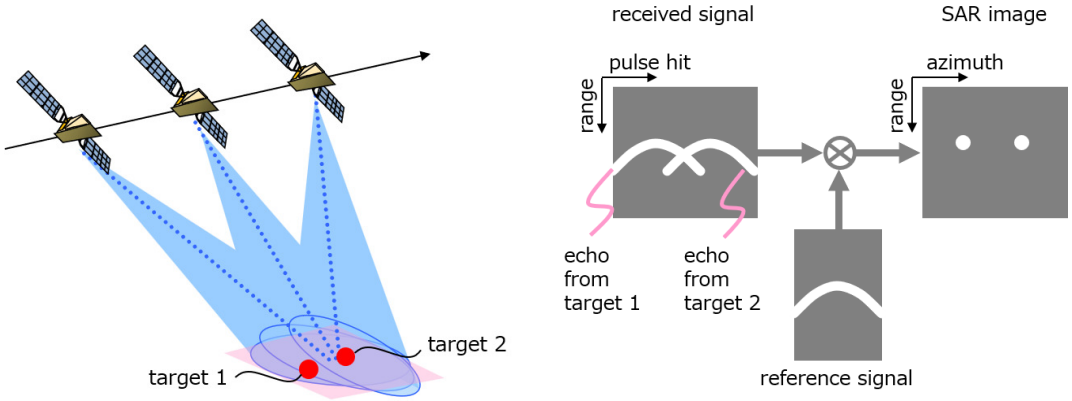

(a) point targets (b) image formation process

FIGURE 2.7: The principle of SAR image formation

doppler algorithm (RDA), chirp scaling algorithm(CSA) and ω-k algorithm (OKA). The details of these SAR image formation algorithms lie outside the scope of this thesis, and we refer the interested readers to [5] and the references therein for a detailed review.

2.2.3 Inverse synthetic aperture radar

Inverse synthetic aperture radar (ISAR) is another type of imaging radar used to observe two-dimensional image of a moving target in a distance, such as a ship, an aircraft, a satellite and so forth [54]. While SAR images are generated by the motion of the sensor platform with respect to the target, ISAR images are generated by target rotation relative to the radar.

In the ISAR observation, the radar tracks the target of interest and repeatedly transmits pulses to the target. Fig. 2.8(a) illustrates the ISAR observation geometry. The operation is basically the same as the pulse-Doppler radar. In fact, the ISAR equipment is nothing but a pulse-Doppler radar. In order to observe an image of the target, ISAR utilizes wide bandwidth signal to obtain high range resolution. The rage resolution of ISAR is also given by:

$$\Delta r = \frac{c}{2B}. \tag{2.13}$$

Typically, an ISAR system employs bandwidth of 150MHz or more to obtain the range resolution higher than 1m. As a result, the target echo signal is "resolved" in range direction as shown in Fig. 2.8(a). Fig. 2.8(b) illustrates the ISAR signal. It is just like the pulse-Doppler radar signal shown in Fig. 2.2(b). The difference is that the propagation time τ_n of the n-th pulse can not be regarded as constant. It is because the range resolution is high and the small change in the distance is observable, in the first place. In addition, the observation time is relatively long in order to obtain high Doppler resolution. The translational motion is compensated as the first step of the ISAR signal processing, and the range profiles are aligned as shown in the bottom part of Fig. 2.8(b).

After the translational motion is compensated, the rotational motion component remains in the signal. Fig. 2.9 illustrates this effect. The red arrows represent the radar line of sight. Paying attention to these red arrows in Fig. 2.9(a), we can see that as a target moves along its path, the target aspect angle changes. Removing the translational motion, the remaining component is rotational motion relative to the radar line of sight as shown in Fig. 2.9(b).

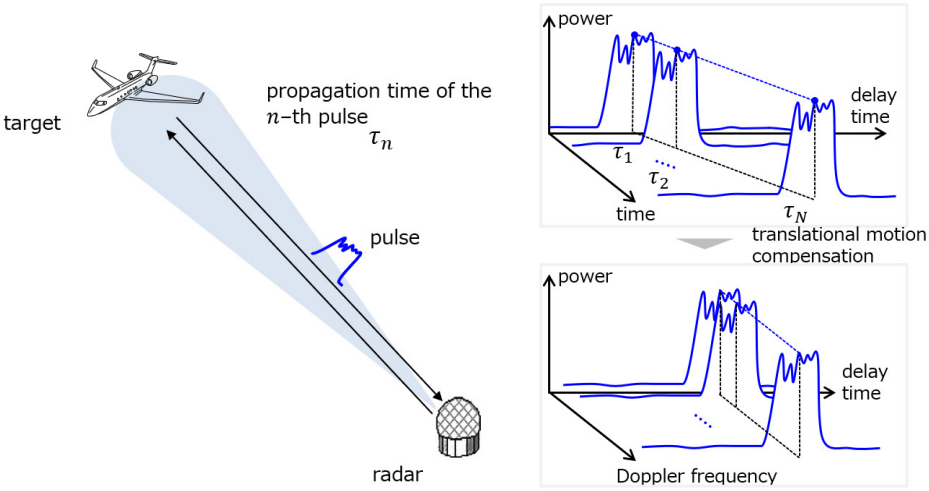

(a) observation geometry (b) signal

FIGURE 2.8: ISAR observation geometry and signal

Fig. 2.10(a) and (b) illustrate the relationship between the target rotational motion and the ISAR image plane. In both figures, the target consists of four point targets a, b, c and d, which are located on x-y plane, and the radar line of sight is along y-axis. In Fig. 2.10(a), the target rotates clockwise around z-axis, and in Fig. 2.10(b) the same target rotates clockwise around x-axis. In Fig. 2.10(a), as the target rotates, the point target "a" moves closer to the radar, so the echo signal from "a" has a positive Doppler frequency. On the other hand, "c" moves away from the radar, and the echo signal from "c" has a negative Doppler frequency. The point targets "b" and "d" move across the radar line of sight so the echo signal from them have zero Doppler frequency. Therefore, if we project this signal onto range-Doppler domain, it will look like the bottom of Fig. 2.10(a). In Fig. 2.10(b), as the target rotates, the point targets "a" and "c" stay at the same position, and the point targets "b" and "d" move across the radar line of sight. Therefore,the echo signal from four targets have zero Doppler frequency. Then the image will look like the bottom of Fig. 2.10(b).

From these examples, we observe that ISAR image plane is defined by the radar line of sight and the direction of rotation of the target. To be precise, let us define the radar line of sight vector $\hat{r}$, and the instantaneous angular velocity vector $\hat{\omega}$. Then the ISAR image plane is spanned by radar line of sight vector $\hat{r}$ and the vector cross product of $\hat{r}$ and $\hat{\omega}$, i.e., $\hat{r} \times \hat{\omega}$. [54]. In the case of Fig. 2.10(a), radar line of sight vector $\hat{r}$ is $[0,1,0]$ and the instantaneous angular velocity vector $\hat{\omega}$ is $[0,0,-1]$. Then the cross product of $\hat{r}$ and $\hat{\omega}$ is $\hat{r} \times \hat{\omega} = [1,0,0]$. Hence, the image plane is defined by $[0,1,0]$ and $[1,0,0]$, which is x-y plane. In the case of Fig. 2.10(b), the instantaneous angular velocity vector is $\hat{\omega} = [-1,0,0]$. Then the cross product is $\hat{r} \times \hat{\omega} = [0,0,1]$. Hence, the image plane becomes y-z plane.

The Doppler resolution is the same as pulse-Doppler radar:

$$\Delta f_{\mathrm{d}} = \frac{1}{T}. \tag{2.14}$$

The achieved resolution in the cross-range dimension is:

$$\Delta a = \frac{\lambda}{2\Delta\theta}. \tag{2.15}$$

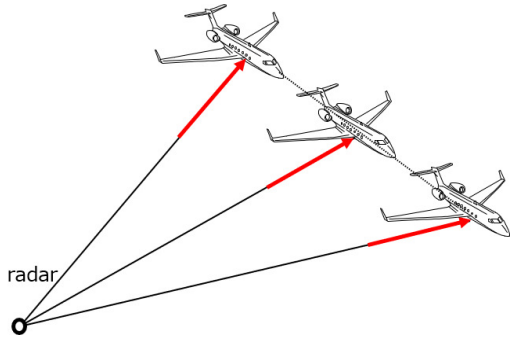

(a) translational motion + rotational motion

(b) rotational motion

FIGURE 2.9: ISAR observation geometry

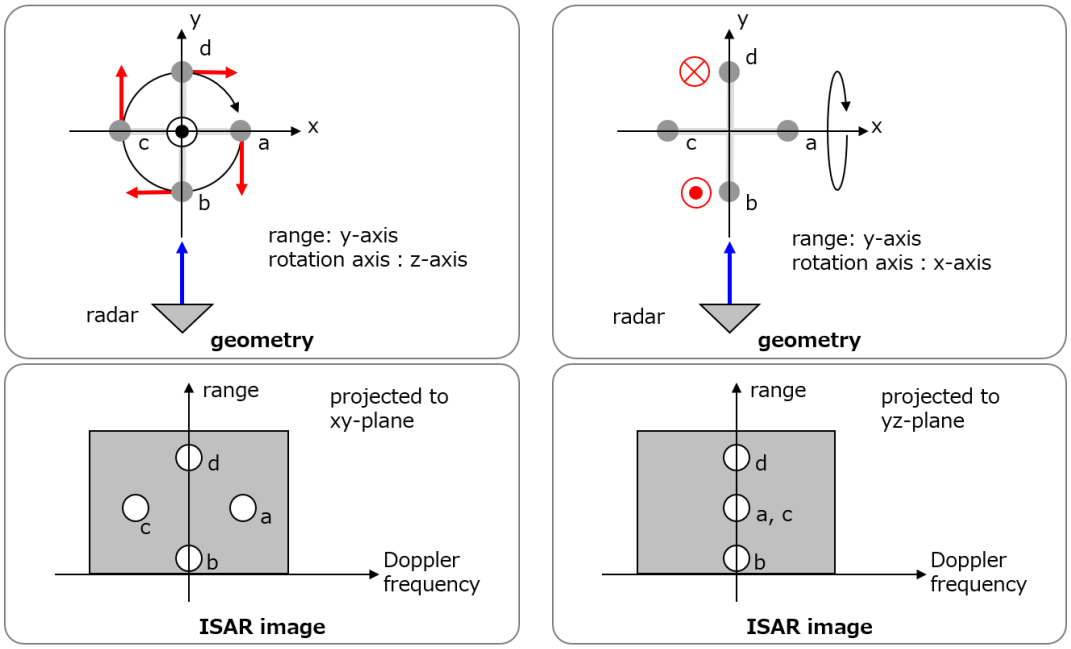

(a) rotation axis : z (b) rotation axis : x

FIGURE 2.10: Target rotational motion and ISAR image plane

where λ is the center wavelength and $\Delta\theta$ is the angle that the target is viewed during the observation time. The value of $\Delta\theta$ is typically no more than a few degrees in ISAR imaging. For example, if the observation time T is 0.5sec, the Doppler resolution is 2Hz. If the instantaneous angular velocity of the target rotational motion during the observation is 2 deg/sec, then $\Delta\theta = 2 \times 0.5 = 1$deg. With the center wavelength $\lambda = 3$cm, the cross-range resolution Δa is 0.85m. In reality, cross-range resolution can not be designed in advance, because this value is determined by the target motion. An ISAR image is a range-Doppler image and physical dimension in the cross-range direction can not be measured by an ISAR image. This issue will be thoroughly discussed in Chapter5.

2.3 Multi-channel Imaging Radar

2.3.1 The technological trend and the scope of this study

The term "multi-channel imaging radar" refers to an imaging radar system with multiple transmit and receive channels. Modern radar systems as well as imaging radar systems operate with multiple transmit and receive channels to enhance the system performance.

Fig 2.11 shows the technological trend of the multi-channel imaging radar systems. Although multi-channel SAR systems have been studied since 1980s and some experimental systems were developed in 1980s and 1990s, it was not until the beginning of the 21st century that they were put into practical use. ALOS-2, which was launched in 2014, is one of the early operating earth observation satellites with spaceborne multi-channel SAR systems. It employs dual receive channels to achieve higher resolution with wider swath width and additional two receive channels to achieve polarimetry capability. ALOS-4, launched in 2024, is equipped with 12 receive channels to realize DBF (Digital Beam Forming) capability to drastically expand the swath width. This trend has caused the increase in the size and weight of satellites; in fact, ALOS-4 is 1.5 times heavier than ALOS-2. The next generation of spaceborne SAR systems, on the other hand, are expected to consist of multiple small satellites, instead of pursuing even larger system. The satellites will be made to operate together and expand the functionality of spaceborne SAR systems with distributed sensing capability. MFR and surveillance radar systems with ISAR capability follow the same trend. The latest operating system such as SPY-6 radar employs many receive channels to achieve DBF capability. Since the system has become very large, there is a growing trend toward distributed system. Japanese space surveillance radar developed in 2024 is an example of such a system. However, ISAR capability with distributed radar is yet to be realized.

The applications of multi-channel SAR system include high-resolution wide-swath imaging, polarimetry and moving target observation. While target motion and three dimensional shape estimation is the main application of multi-channel ISAR system. This study focuses on signal processing algorithms for polarimetric SAR, SAR moving target observation and

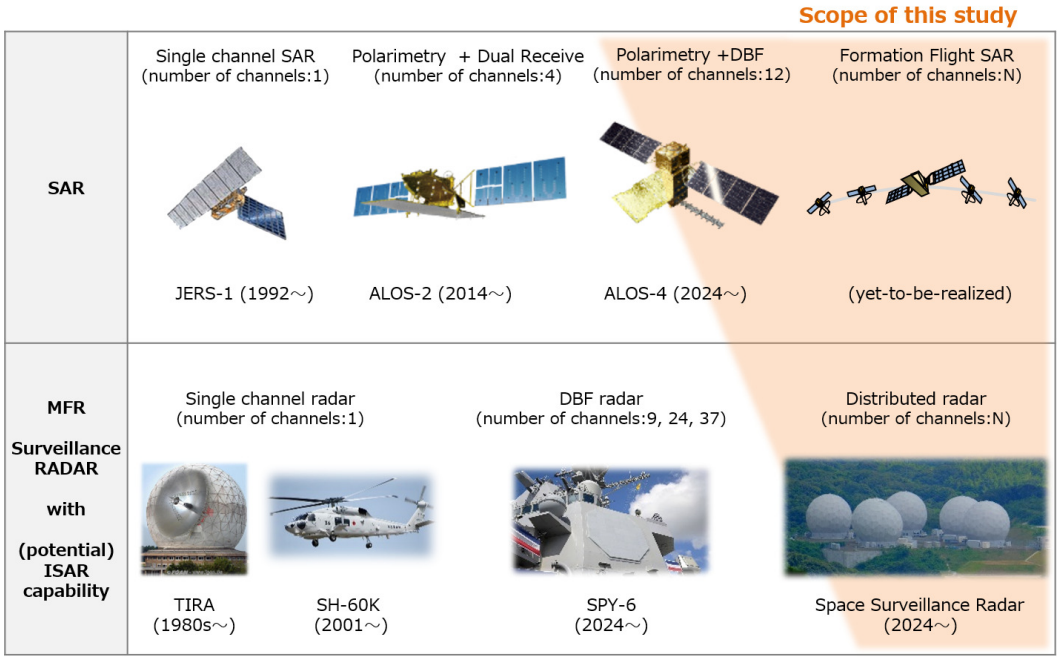

FIGURE 2.11: Multi-channel SAR and Multi-channel Radar

ISAR target motion and three dimensional shape estimation. The high-resolution wide-swath SAR imaging technology using the multi-channel has been widely studied, since the most important performance indicators of a SAR system are resolution and the swath width. This topic is outside the scope of this study, and we refer the interested readers to [57]–[64].

2.3.2 Polarimetric SAR

Advances in polarimetric SAR technology have shown the effect of polarization information on various applications such as target detection, identification, land cover classification, and so forth [65]–[71]. Under the far-field assumption, the polarization property of a target is described by a 2×2 scattering matrix. A polarimetric radar measures the scattering matrices of targets by transmitting and receiving two orthogonal polarizations. In most cases, horizontal(H) and vertical(V) polarizations are employed, and four sets of target response

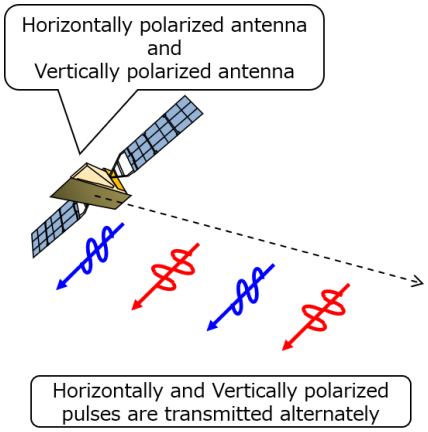

FIGURE 2.12: The pulse transmission sequence of a polarimetric SAR

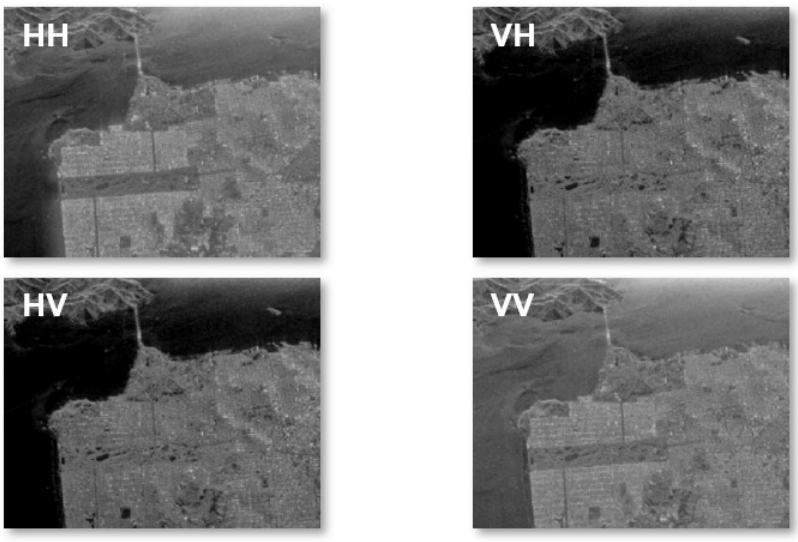

FIGURE 2.13: An example of polarimetric SAR images
(DATA collection: NASA/JPL AIRSAR (San Francisco Bay area)
Frequency: L-band (1.225GHz), Resolution :10m(range) /3m(azimuth))

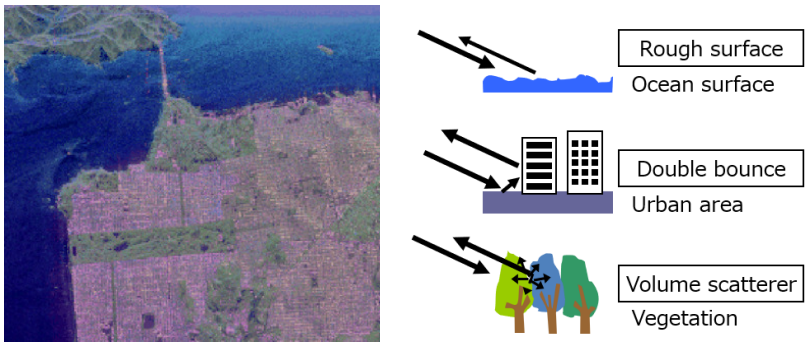

(a) false color image (b) scattering mechanism

FIGURE 2.14: An example of false color polarimetric SAR image

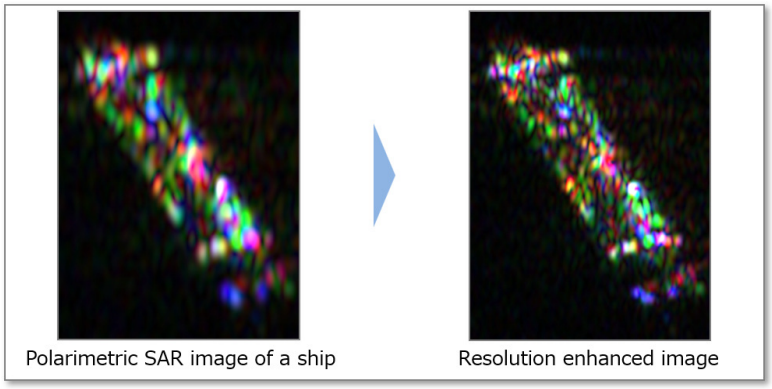

FIGURE 2.15: Resolution enhancement method for Polarimetric SAR

signals, denoted HH, HV, VH and VV channels, are observed[1]. Fig. 2.12 shows the principle of polarimetry. The four scattering matrix elements are measured by first transmitting a pulse through the H antenna and subsequently receiving signals simultaneously on both H and V antennas. The next transmission utilizes the V antenna for transmitting, again followed by simultaneous receiving on both antennas[65]. An example of polarimetric SAR image is shown in Fig. 2.13. The polarimetric SAR image consists of four images corresponding to the four elements of scattering matrix, i.e., HH, HV, VH and VV channels. The scattering matrix carries information about the structure of the target; typical scattering mechanisms that are observed by polarization are rough surface scattering caused by bare soil or water, double bounce caused by buildings and volume scattering caused by the leaves and branches in a forest canopy. (see Fig. 2.14(b)). Fig. 2.14(a) is a false color representation of the polarimetric SAR image, where rough surface, double bounce and volume scattering components are represented in blue, red and green, respectively. Fig. 2.14(a) clearly shows that the polarimetric SAR is very effective in discriminating the scattering mechanisms of the Earth's surface in detail. However, the data volume becomes four times that of single-polarization SAR, which is problematic for spaceborne SAR systems, because downlink bandwidth cannot keep up with the accumulating data volume. To get around this problem, we have developed a signal processing algorithm to enhance the spatial resolution of polarimetric SAR images. The data volume to be downlinked can be reduced by lowering the resolution during observation and then the resolution is recovered on the ground, if we apply the proposed method to the observed low resolution polarimetric SAR image. Fig.2.15 shows a sample result of the

[1] In this thesis, "HV channel" represents the target response signal when horizontal polarization is transmitted and vertical polarization is received.

proposed algorithm, and it will be thoroughly discussed in chapter 3.

2.3.3 SAR moving target observation

SAR is designed and exceptionally effective at imaging stationary scenes, because its processing relies on coherently integrating echoes over time to synthesize a large aperture. When targets move, the assumption of stationary reflectors breaks down. The coherent integration designed for a static scene is disrupted by the varying Doppler shifts and phase errors introduced by the target's motion. As a result, moving targets often appear defocused or displaced in the SAR image. The signal from a moving target may be smeared or substantially weaker compared to the returns from stationary objects, making them difficult to identify without additional processing

SAR-GMTI (Synthetic Aperture Radar - Ground Moving Target Indication) has been studied to overcome these limitations. Fig. 2.16 shows the basic idea of SAR-GMTI. As shown in Fig. 2.16 (a), SAR-GMTI is a multi-channel SAR system, which employs two or more antenna apertures configured along the flight path direction, i.e., the along-track direction. Fig. 2.16 (b) shows an example of the observed SAR images obtained by an airborne SAR-GMTI system. Top two SAR images are observed by antenna 1 and 2 respectively. They are basically the same images. The difference is the time of observation. As one can see in Fig. 2.16 (a), the interval Δt between antenna 1 traversing a specific point and antenna 2 following suit is given by:

$$\Delta t = \frac{d}{V_r}, \tag{2.16}$$

where d is the distance between the two antennas (referred to as "baseline"), and V_r is the platform velocity. The two SAR images can be regarded as having been captured from the same location, separated by a Δt-second interval. The signals from the stationary targets, of course, do not change during the interval, but the signals from moving targets change. Typically, the interval Δt is so small that the signal peak position shift is negligible compared to the range resolution. On the other hand, the signal phase is different. The phase difference $\Delta\phi$ of the target with velocity V_{tgt} is:

$$\Delta\phi = -\frac{4\pi V_t g t \Delta t}{\lambda}. \tag{2.17}$$

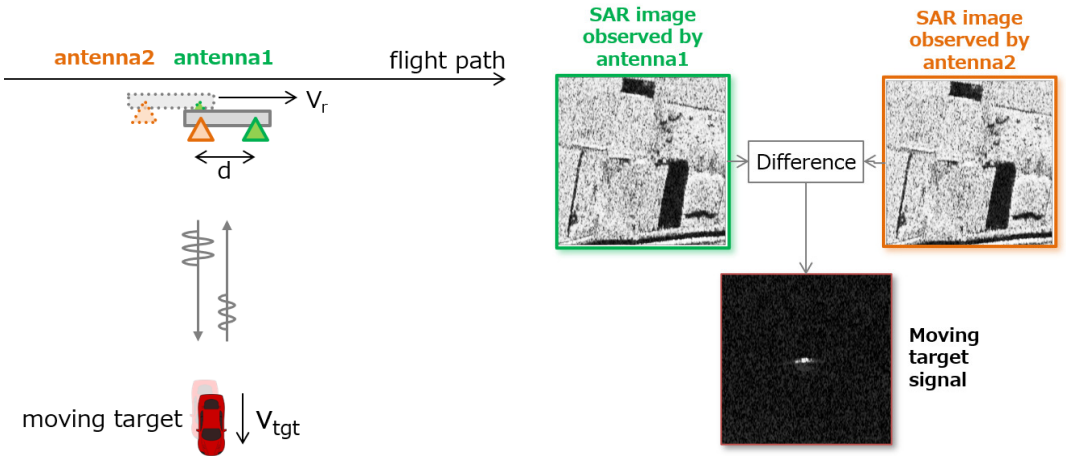

(a) observation geometry (b) SAR-GMTI image

FIGURE 2.16: The principle of SAR-GMTI

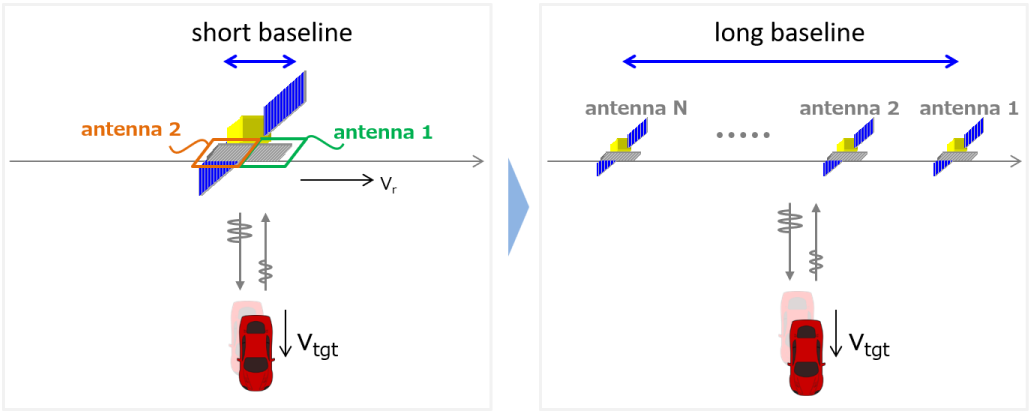

FIGURE 2.17: SAR-GMTI system based on a formation of small satellites

As a consequence, if one calculate the difference between the two images, signals from stationary targets are eliminated and only signal from moving target remains as shown in Fig. 2.16 (b).

When the concept of SAR-GMTI is applied to spaceborne system, it suffers from low performance for detecting slowly moving targets, due to the relatively short baseline for the very high velocity of the satellite. For example, the achievable baseline is on the order of $d = 5$m for a spaceborne system, while typical platform velocity is about $V_r = 7{,}300$ m/s. In that case, the time interval between the two image acquisitions is $\Delta t = 0.68$ ms. A vehicle traveling at 10 km/h (2.7m/s) moves only 1.9mm during that interval. So if the wavelength is $\lambda = 3$cm, the phase difference would be $\Delta phi = 0.25\pi$rad. To resolve this problem, the baseline needs to be expanded to several tens of meters. Recent advances in small satellite technology have made it possible to realize such a system based on formations of small satellites as shown in Fig. 2.17. We have developed a signal processing algorithm that enables the detection, position estimation, and velocity estimation of moving targets, assuming a small satellite formation flight system, and it will be thoroughly discussed in chapter 4.

2.3.4 ISAR target motion and three dimensional shape estimation

ISAR is a technique for observing two dimensional (2D) images of targets from radar reception signals, and it is used as a target identification function in high-resolution radars. In order to enhance the target identification ability, there is a strong desire for three dimensional (3D) shape observation to improve target identification performance.

But before we dive into the 3D shape estimation problem, we need to address the Doppler scaling problem. As shown in Fig. 2.9, ISAR images are organized in the range-Doppler domain, where one axis represents the range and the other represents the Doppler frequency. The Doppler frequency axis reflects the motion-induced frequency shifts. In order to determine the target dimension, the Doppler frequency axis need to be scaled and transformed into the cross-range dimension. However, this mapping is not straightforward due to the dependence of the Doppler frequency on the target's motion geometry, leading to what is known as the Doppler scaling problem. Essentially, it requires some additional source of information to estimate the target motion geometry.

The problem of target motion estimation for ISAR imaging has been addressed in some literatures in contexts of optimum imaging time selection, estimation of cross-range scaling, and so on [72]–[75]. Pastina et al. and Munoz-Ferreras et al. have proposed algorithms for the rotational motion estimation of ship targets [72]–[74]. These algorithms put almost no impact on the hardware requirement, but the application is limited to ship targets, i.e., some

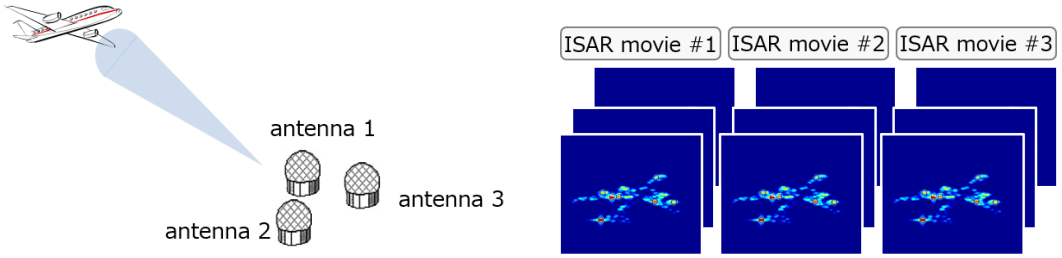

(a) observation geometry (b) ISAR movies

FIGURE 2.18: The principle of multi-channel ISAR

a priori knowledge of the basic shape of ships, such that there usually are a deck and a mast, is exploited. On the other hand, a generic approach for the motion estimation is proposed by Stuff et al. [75]. This method is based on a range tracking of the scattering centers and no assumption is made on the target shape other than that it contains some prominent scattering centers. However, it requires a system with very high range resolution for accurate range tracking.

The multichannel ISAR system as shown in Fig. 2.18(a) is another solution to the target motion estimation. In addition, we have discovered that multichannel ISAR system not only enables to measure the target motion, but it simultaneously enables to estimate the target's three dimensional (3D) shape.

ISAR typically observes the same target continuously for several seconds and generates multiple consecutive ISAR images just like a movie. Fig. 2.18(b) shows the ISAR movie observed by the multichannel ISAR system. Note that the obtained ISAR movie is a collection of multiple images with different projection planes. Once the target motion is estimated, those projection planes are determined, and hence 3D shape can be estimated from those set of ISAR images. We have developed a signal processing algorithm that measures three sets of ISAR movies using a multichannel system composed of three receiving systems, and estimates the 3D shape and motion of the target simultaneously based on that information. It will be thoroughly discussed in chapter 5.

Chapter 3

Resolution Enhancement Method For Polarimetric SAR

3.1 Introduction

Polarization information has been widely utilized in applications such as target detection, identification, and land cover classification ([65]–[68]). In particular, advancements in PolSAR (Polarimetric Synthetic Aperture Radar) technology have demonstrated its impact across various domains [69]–[71]. Under the far-field assumption, a target's polarization properties are represented by a 2×2 scattering matrix. Polarimetric radar systems measure these matrices by transmitting and receiving two orthogonal polarizations, typically horizontal (H) and vertical (V). Consequently, four sets of target response signalsHH, HV, VH, and VV channelsare observed[1].

However, polarization information in SAR is often obtained at the cost of azimuth resolution due to system constraints such as bandwidth constraints in data downlink transmission[76]. For example, Fig. 3.1 presents TerraSAR-X High Resolution SpotLight (HS) images of an airport terminal, with (a) and (b) depicting HH images from the dual and single polarization modes, respectively. Fig. 3.2 shows magnified images of aircraft from Fig. 3.1, where (a) and (b) correspond to HH and VV images in dual polarization mode, (c) presents a composite of HH (red) and VV (blue), and (d) displays a single-polarization HH image. Comparing (a)(c) with (d), the aircraft's shape appears clearer in the single-polarization image. Additionally, while strong target-ground interactions at the tailplane are visible in single-polarization mode, they are less discernible in dual-polarization mode due to resolution limitations. This is regrettable, as polarimetry offers valuable insights into interpreting the target-ground interaction scattering mechanism, as highlighted in [77].

This chapter introduces a super-resolution algorithm tailored for polarimetric SAR, based on bandwidth extrapolation (BWE) [78]–[80]. The proposed polarimetric bandwidth extrapolation (PBWE) [41], [42] leverages full polarization information to enhance resolution beyond conventional BWE methods while preserving scatterers' polarization properties. Additionally, this chapter extends PBWE to a two-dimensional (2D-PBWE) approach, utilizing a 2D polarimetric linear prediction model to expand spatial frequency bandwidth in both range and azimuth directions simultaneously.

This chapter is organized as follows. Section 3.2 summarizes the proposed polarimetric bandwidth extrapolation (PBWE) and two dimensional PBWE (2D-PBWE) method. Section 3.3 presents a numerical example showing the performance of 2D-PBWE, and sample results obtained with real polarimetric SAR images. Section 3.4 provides the theoretical performance analysis of PBWE. Finally, Section 3.5 provides the conclusion.

[1] "HV channel" represents the target response signal when horizontal polarization is transmitted and vertical polarization is received.

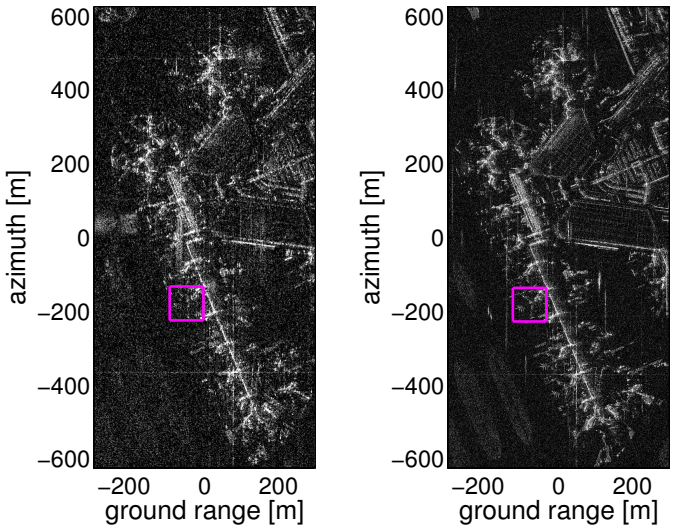

(a) Dual polarization (b) Single polarization

FIGURE 3.1: TerraSAR-X High Resolution SpotLight (HS) images of an airport terminal (©Infoterra GmbH, Distribution [PASCO]). (a) HH/VV dual polarization (only HH image is shown); azimuth resolution 2.2m; ground range resolution 1.4m. (b) HH single polarization; azimuth resolution 1.1m; ground range resolution 0.7m.

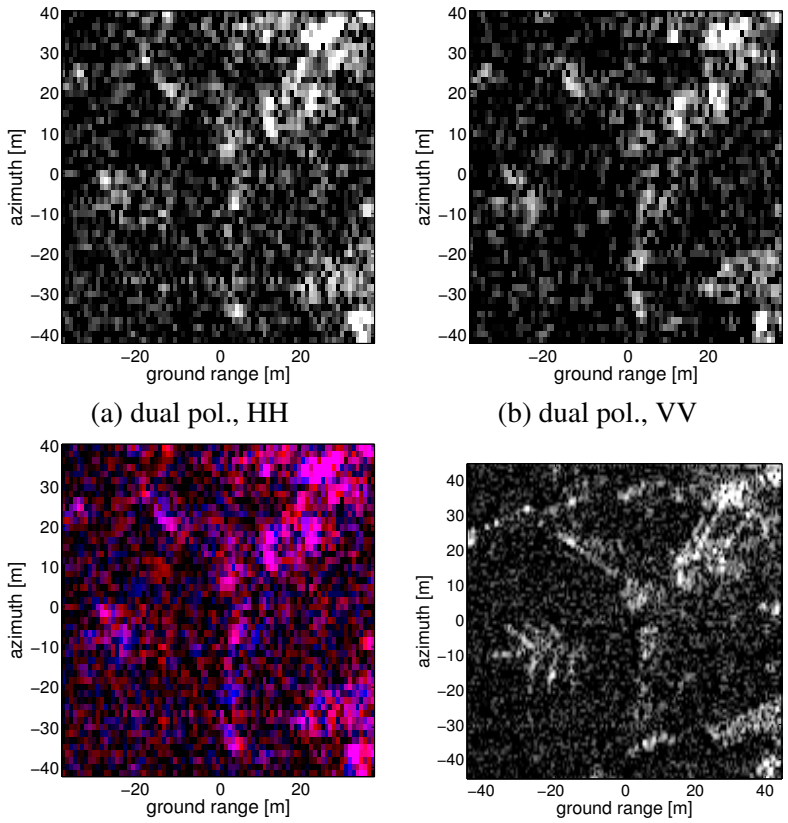

(a) dual pol., HH (b) dual pol., VV

(c) dual pol., HH/VV (d) single pol., HH

FIGURE 3.2: Magnified TerraSAR-X image of aircrafts indicated in Fig. 3.1 (©Infoterra GmbH, Distribution [PASCO]). (a) and (b) are HH and VV image of the dual polarization mode, (c) is a color composite image of HH and VV, where HH and VV are assigned to red and blue, respectively. (d) is HH image of the single polarization mode.

3.2 Algorithm

3.2.1 Polarimetric Bandwidth Extrapolation

Under the far-field assumption, the polarization property of a target is described by a 2×2 scattering matrix[65]. A polarimetric radar measures the scattering matrices of targets by transmitting and receiving two orthogonal polarizations. In most cases, horizontal and vertical polarizations are employed, and four sets of target response signals, denoted HH, HV, VH and VV channels, are observed[2]. Under most conditions, the VH signal is equivalent to the HV signal; thus it is omitted from here on.

At high frequency, a radar target can be considered as a mixture of a finite number of point scatterers with, in general, different polarization properties. First, we consider the one dimensional (range direction only) case. Then, the measured response signal X_p ($p = 1,2,3$ representing the HH, HV and VV channels respectively) from a target at M sampled frequency points f_m ($m = 1,2,\cdots,M$) can be expressed in vector form as follows:

$$\begin{bmatrix} X_1(m) \\ X_2(m) \\ X_3(m) \end{bmatrix} = \sum_{q=1}^{Q} \begin{bmatrix} s_{1,q} \\ s_{2,q} \\ s_{3,q} \end{bmatrix} \exp\left\{-j\frac{4\pi f_m r_q}{c}\right\} \tag{3.1}$$

where Q is the number of point scatterers, $s_{p,q}$ is the complex scattering coefficient of the p-th polarimetric channel associated with the q-th scatterer located down range at r_q, and c is the speed of light. In the model, the scattering matrices are assumed to be constant over the band of incident radar frequencies. The response signal of each polarization channel is Fourier transformed to obtain a range profile, in which the locations and the complex amplitudes of the peaks correspond to the locations and complex scattering coefficients of the point scatterers. The range resolution is given by $c/2B$, where B is the transmitted bandwidth.

The polarimetric linear prediction model assumes that the linear combination of an equispaced set of signal samples $X_j(m-L), X_j(m-L+1), \cdots, X_j(m-1)$, (j=1,2,3) of the three polarization channels will predict the next sample of $X_p(m)$. Then, using vector notation

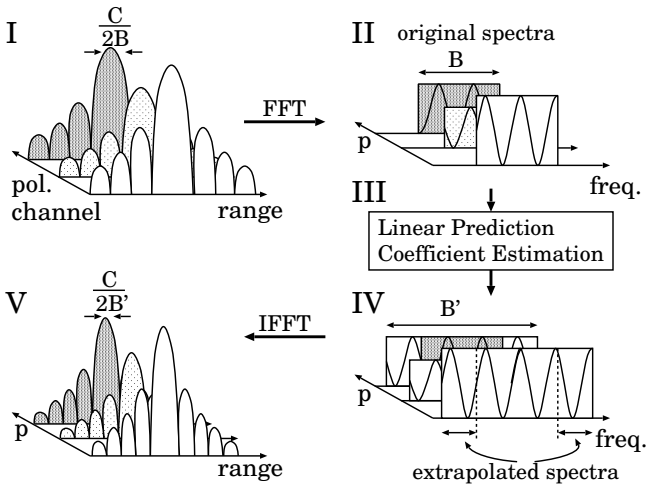

FIGURE 3.3: The illustration of the Polarimetric Bandwidth Extrapolation (PBWE) process.

[2]In this thesis, "HV channel" represents the target response signal when horizontal polarization is transmitted and vertical polarization is received.

$X_m = [X_1(m)\ X_2(m)\ X_3(m)]^T$, the model is given by

$$\hat{X}_m = \Gamma_{\rm f}^{L\,T} Y_{m-1}^L, \qquad \hat{X}_{m-L} = \Gamma_{\rm b}^{L\,T} Y_m^L \qquad (m = L+1, L+2, \cdots, M), \tag{3.2}$$

where,

$$\Gamma_{\rm f}^L = \left[C_{\rm f}^{L,1} \ \cdots \ C_{\rm f}^{L,L} \right]^T \tag{3.3}$$

$$\Gamma_{\rm b}^L = \left[C_{\rm b}^{L,L} \ \cdots \ C_{\rm b}^{L,1} \right]^T \tag{3.4}$$

$$Y_m^L = \left[X_m^T \ \cdots \ X_{m-L+1}^T \right]^T \tag{3.5}$$

$$C_{\rm f}^{L,l} = \begin{bmatrix} c_{{\rm f},l}^{11} & c_{{\rm f},l}^{12} & c_{{\rm f},l}^{13} \\ c_{{\rm f},l}^{21} & c_{{\rm f},l}^{22} & c_{{\rm f},l}^{23} \\ c_{{\rm f},l}^{31} & c_{{\rm f},l}^{32} & c_{{\rm f},l}^{33} \end{bmatrix} \tag{3.6}$$

$$C_{\rm b}^{L,l} = \begin{bmatrix} c_{{\rm b},l}^{11} & c_{{\rm b},l}^{12} & c_{{\rm b},l}^{13} \\ c_{{\rm b},l}^{21} & c_{{\rm b},l}^{22} & c_{{\rm b},l}^{23} \\ c_{{\rm b},l}^{31} & c_{{\rm b},l}^{32} & c_{{\rm b},l}^{33} \end{bmatrix}. \tag{3.7}$$

L is the order of the polarimetric linear prediction model, and T represents the transpose of the matrix. $c_{{\rm f},l}^{ij}$ and $c_{{\rm b},l}^{ij}$ are the l-th coefficients of the forward and backward models, respectively, associated with the j-th channel to predict the next sample of the i-th channel.

Fig. 3.3 illustrates the processing steps of PBWE. The original response signals of each polarization channel (**I**) are Fourier processed individually to obtain the spectra (**II**). Then the polarimetric linear prediction coefficients are estimated from the spectral data (**III**). The estimated coefficients are used to extrapolate the spectral data of each polarization channel (**IV**). The expanded spectra are then inverse Fourier processed to obtain the improved resolution response (**V**).

Fig. 3.4 illustrates the extrapolation procedure for the $L = 3$ case. HV channel is not shown in the figure to avoid complexity. First, the $(M+1)$-th signal value of each polarimetric channel is extrapolated by $X_{M+1} = \Gamma_{\rm f}^{3\,T} Y_M$. Then, the $(M+2)$-th signal values of each polarimetric channel are extrapolated by $X_{M+2} = \Gamma_{\rm f}^{3\,T} Y_{M+1}$. Repeating the procedure, the spectra can be expanded to any arbitrary length.

Polarimetric linear prediction coefficients can be estimated from a set of measurement data by selecting coefficients to minimize the error between the predicted signal values and the measured values. Let the prediction error be

$$f_m^L = X_m - \Gamma_{\rm f}^{L\,T} Y_{m-1}^L \tag{3.8}$$

$$b_{m-L}^L = X_{m-L} - \Gamma_{\rm b}^{L\,T} Y_m^L \qquad (m = L+1, L+2, \cdots, M), \tag{3.9}$$

where f_m^L and b_{m-L}^L are the forward and backward prediction errors, respectively. Then the mean power of the prediction error is given by

$$\varepsilon^L = {\rm E}\left\{ \|f_m^L\|^2 + \|b_{m-L}^L\|^2 \right\}. \tag{3.10}$$

It can be shown that the following normal equations must hold to minimize the prediction error ε^L.

$$R_L \Gamma_{\rm f}^L = U_L, \qquad R_L \Gamma_{\rm b}^L = V_L \tag{3.11}$$

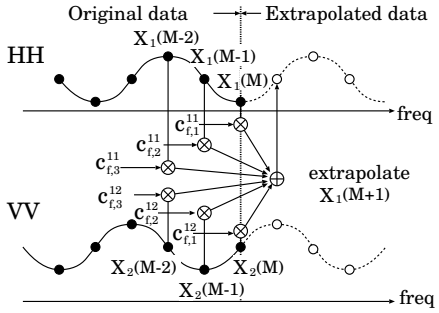

(a)Extrapolate HH channel spectrum

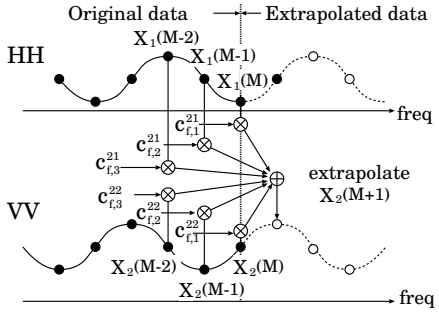

(b)Extrapolate VV channel spectrum

FIGURE 3.4: The illustration of the extrapolation process in the forward direction.

where,

$$R_L = E\left\{Y_{m-1}^{L*} Y_{m-1}^{L\,T}\right\} = E\left\{Y_m^{L*} Y_m^{L\,T}\right\} \tag{3.12}$$

$$= \begin{bmatrix} r_0 & r_1 & \cdots & r_{L-1} \\ r_1^\dagger & \ddots & \ddots & \vdots \\ \vdots & \ddots & \ddots & r_1 \\ r_{L-1}^\dagger & \cdots & r_1^\dagger & r_0 \end{bmatrix}$$

$$r_l = E\left\{X_m^* {X_{m-l}}^T\right\} \equiv \begin{bmatrix} r_l^{11} & r_l^{12} & r_l^{13} \\ r_l^{21} & r_l^{22} & r_l^{23} \\ r_l^{31} & r_l^{32} & r_l^{33} \end{bmatrix} \tag{3.13}$$

$$U_L = E\left\{Y_{m-1}^{L*} {X_m}^T\right\} = [r_1^* \ \cdots \ r_L^*]^T \tag{3.14}$$

$$V_L = E\left\{Y_m^{L*} {X_{m-L}}^T\right\} = [r_L^T \ \cdots \ r_1^T]^T . \tag{3.15}$$

$(* :$ complex conjugate, $T :$ transpose, $\dagger :$ adjoint$)$

Therefore, by solving Eq.(3.11), the polarimetric linear prediction coefficients $\Gamma_{\rm f}^L$ and $\Gamma_{\rm b}^L$ are determined as follows:

$$\Gamma_{\rm f}^L = R_L^{-1}\, U_L, \qquad \Gamma_{\rm b}^L = R_L^{-1}\, V_L\,. \tag{3.16}$$

Note that we need the *a priori* knowledge of the model order L, or L needs to be estimated prior to the procedure.

The multichannel version of the Burg's algorithm is based on the multichannel version of the Levinson recursion. First, Eq.(3.11) is divided into four submatrices as

$$\begin{bmatrix} R_{L-1} & V_{L-1} \\ V_{L-1}^{\dagger} & r_0 \end{bmatrix} \begin{bmatrix} \Gamma_{\mathrm{f}0}^{L} \\ C_{\mathrm{f}}^{L,L^T} \end{bmatrix} = \begin{bmatrix} U_{L-1} \\ r_L^{\dagger} \end{bmatrix} \tag{3.17}$$

$$\begin{bmatrix} r_0 & U_{L-1}^{\dagger} \\ U_{L-1} & R_{L-1} \end{bmatrix} \begin{bmatrix} C_{\mathrm{b}}^{L,L^T} \\ \Gamma_{\mathrm{b}0}^{L} \end{bmatrix} = \begin{bmatrix} r_L \\ V_{L-1} \end{bmatrix} \tag{3.18}$$

where,

$$\Gamma_{\mathrm{f}0}^{L} = \left[C_{\mathrm{f}}^{L,1} \cdots C_{\mathrm{f}}^{L,L-1} \right]^T \tag{3.19}$$

$$\Gamma_{\mathrm{b}0}^{L} = \left[C_{\mathrm{b}}^{L,L-1} \cdots C_{\mathrm{b}}^{L,1} \right]^T. \tag{3.20}$$

Moving $C_{\mathrm{f}}^{L,L}$, $C_{\mathrm{b}}^{L,L}$ to the right hand side of Eqs.(3.17) and (3.18), we obtain

$$\begin{aligned} R_{L-1}\Gamma_{\mathrm{f}0}^{L} &= U_{L-1} - V_{L-1}C_{\mathrm{f}}^{L,L^T} \\ &= R_{L-1}\Gamma_{\mathrm{f}}^{L-1} - R_{L-1}\Gamma_{\mathrm{b}}^{L-1}C_{\mathrm{f}}^{L,L^T} \end{aligned} \tag{3.21}$$

$$\begin{aligned} R_{L-1}\Gamma_{\mathrm{b}0}^{L} &= V_{L-1} - U_{L-1}C_{\mathrm{b}}^{L,L^T} \\ &= R_{L-1}\Gamma_{\mathrm{b}}^{L-1} - R_{L-1}\Gamma_{\mathrm{f}}^{L-1}C_{\mathrm{b}}^{L,L^T}. \end{aligned} \tag{3.22}$$

Then it follows that

$$\Gamma_{\mathrm{f}0}^{L} = \Gamma_{\mathrm{f}}^{L-1} - \Gamma_{\mathrm{b}}^{L-1}C_{\mathrm{f}}^{L,L^T} \tag{3.23}$$

$$\Gamma_{\mathrm{b}0}^{L} = \Gamma_{\mathrm{b}}^{L-1} - \Gamma_{\mathrm{f}}^{L-1}C_{\mathrm{b}}^{L,L^T}. \tag{3.24}$$

This is known as the multichannel version of Levinson's recursion[81]. Substituting Eqs.(3.23) and (3.24) into Eqs.(3.8) and (3.9) yields

$$\begin{aligned} f_m^L &= X_m - \Gamma_{\mathrm{f}}^{L^T} Y_{m-1}^{L} \\ &= X_m - \begin{bmatrix} \Gamma_{\mathrm{f}0}^{L\,T} & C_{\mathrm{f}}^{L,L} \end{bmatrix} \begin{bmatrix} Y_{m-1}^{L-1} \\ X_{m-L} \end{bmatrix} \\ &= X_m - \Gamma_{\mathrm{f}}^{L-1\,T} Y_{m-1}^{L-1} - C_{\mathrm{f}}^{L,L} b_{m-L}^{L-1} \\ &= f_m^{L-1} - C_{\mathrm{f}}^{L,L} b_{m-L}^{L-1} \end{aligned} \tag{3.25}$$

$$b_{m-L}^{L} = b_{m-L}^{L-1} - C_{\mathrm{b}}^{L,L} f_m^{L-1}. \tag{3.26}$$

Equations.(3.25) and (3.26) show the relationship between the prediction errors for models of order $L-1$ and L.

Given the prediction error of order $L-1$, we want to minimize the mean power of the prediction error of order L by adjusting the L-th coefficients of the model $C_{\mathrm{f}}^{L,L}$, $C_{\mathrm{b}}^{L,L}$. We simply solve the normal equation derived from Eqs. (3.25) and (3.26) to get

$$C_{\mathrm{f}}^{L,L} = D_{L-1}{B_{L-1}}^{-1} \tag{3.27}$$

$$C_{\mathrm{b}}^{L,L} = D_{L-1}^{\dagger}{F_{L-1}}^{-1}, \tag{3.28}$$

where,

$$F_{L-1} = \sum_{m=L+1}^{M} f_m^{L-1} f_m^{L-1\,\dagger} \tag{3.29}$$

$$B_{L-1} = \sum_{m=L+1}^{M} b_{m-L}^{L-1} b_{m-L}^{L-1\,\dagger} \tag{3.30}$$

$$D_{L-1} = \sum_{m=L+1}^{M} f_m^{L-1} b_{m-L}^{L-1\,\dagger}. \tag{3.31}$$

The multichannel version of Burg's method is summarized below.

1) Set the forward and backward prediction errors for the $L = 0$-th order model as follows:

$$f_m^0 = X_m\,, \qquad b_{m-1}^0 = X_{m-1} \tag{3.32}$$
$$(m = 2, 3, \cdots, M)$$

2) L increments are by one.

3) Using Eqs. (3.27) and (3.28), L-th coefficients of the L-th order model $C_{\mathrm{f}}^{L,L}$, $C_{\mathrm{b}}^{L,L}$ are determined based on forward and backward prediction errors for the $(L-1)$-th order model f_m^{L-1}, b_{m-L}^{L-1}.

4) Using Eqs. (3.23) and (3.24), $1 \sim (L-1)$-th coefficients of the L-th order model are calculated based on $C_{\mathrm{f}}^{L,L}$, $C_{\mathrm{b}}^{L,L}$ and coefficients of the $(L-1)$-th order model $\Gamma_{\mathrm{f}}^{L-1}$, $\Gamma_{\mathrm{b}}^{L-1}$.

5) Using Eqs. (3.8) and (3.9), prediction errors f_m^L, b_{m-L}^L are calculated.

6) The mean power of the prediction error of the L-th order model ε^L is calculated as

$$\varepsilon^L = \frac{1}{2(M-L)} \sum_{m=L+2}^{M} \left(\|f_m^L\|^2 + \|b_{m-L}^L\|^2 \right) \tag{3.33}$$

If the mean power of the prediction error ε^L is sufficiently small, L is set to the optimum model order for the data and the process outputs the coefficients of the L-th order model, otherwise the process goes back to step 2.

$$\varepsilon^{L-1} - \varepsilon^L < \text{Threshold} \tag{3.34}$$

3.2.2 Two Dimensional Polarimetric Bandwidth Extrapolation

In this section, the algorithm is expanded to the two dimensional case. The two dimensional spatial frequency spectrum can be represented as the sum of two dimensional complex sinusoids as follows:

$$\begin{bmatrix} X_1(m,n) \\ X_2(m,n) \\ X_3(m,n) \end{bmatrix} = \sum_{q=1}^{Q} \begin{bmatrix} s_{1,q} \\ s_{2,q} \\ s_{3,q} \end{bmatrix} e^{-j(m\omega_r^q + n\omega_a^q)} \tag{3.35}$$
$$(m = 1, 2, \cdots, M; n = 1, 2, \cdots, N)$$

where M and N denote the number of data samples in range and azimuth, respectively; ω_r^q and ω_a^q denote the normalized spatial frequencies associated with the position of the q-th target in range and azimuth, respectively.

The two dimensional polarimetric linear prediction model assumes that the linear combination of an equispaced set of $K \times L \times P$ signal samples of the P polarization channels will predict the surrounding samples, where K and L denote the order of the prediction model in

range and azimuth direction, respectively. The two dimensional polarimetric linear prediction model is expressed as follows:

$$
\begin{aligned}
&\underline{\text{region 1}} \\
X_{m+K,n} &= \sum_{k=0}^{k=K-1}\sum_{l=0}^{l=L-1} C_{k,l}^{K,0} X_{m+k,n+l} \\
X_{m+K,n+1} &= \sum_{k=0}^{k=K-1}\sum_{l=0}^{l=L-1} C_{k,l}^{K,1} X_{m+k,n+l} \\
&\vdots \\
X_{m+K,n+L} &= \sum_{k=0}^{k=K-1}\sum_{l=0}^{l=L-1} C_{k,l}^{K,L} X_{m+k,n+l} \qquad (3.36) \\
&\underline{\text{region 2}} \\
X_{m+K-1,n+L} &= \sum_{k=0}^{k=K-1}\sum_{l=0}^{l=L-1} C_{k,l}^{K-1,L} X_{m+k,n+l} \\
&\vdots \\
X_{m-1,n+L} &= \sum_{k=0}^{k=K-1}\sum_{l=0}^{l=L-1} C_{k,l}^{-1,L} X_{m+k,n+l} \qquad (3.37) \\
&\underline{\text{region 3}} \\
X_{m-1,n+L-1} &= \sum_{k=0}^{k=K-1}\sum_{l=0}^{l=L-1} C_{k,l}^{-1,L-1} X_{m+k,n+l} \\
&\vdots \\
X_{m-1,n-1} &= \sum_{k=0}^{k=K-1}\sum_{l=0}^{l=L-1} C_{k,l}^{-1,-1} X_{m+k,n+l} \qquad (3.38) \\
&\underline{\text{region 4}} \\
X_{m,n-1} &= \sum_{k=0}^{k=K-1}\sum_{l=0}^{l=L-1} C_{k,l}^{0,-1} X_{m+k,n+l} \\
&\vdots \\
X_{m+K,n-1} &= \sum_{k=0}^{k=K-1}\sum_{l=0}^{l=L-1} C_{k,l}^{K,-1} X_{m+k,n+l} \qquad (3.39)
\end{aligned}
$$

where $X_{m,n}$ is a P dimensional polarimetric data vector of (m,n)-th sample, and $C_{k,l}^{k',l'}$ is a $P \times P$ linear prediction coefficient matrix. Using matrix notations R_i, Γ_i, U_i, the linear system of equations in Eq.(3.36–3.39) is expressed by

$$R_i \Gamma_i = U_i, \qquad (i = 1,2,3,4) \tag{3.40}$$

where the subscript i denotes the 4 regions shown in Fig. 3.5 (a). R_i and U_i are matrix of data samples and Γ_i are the matrix of the prediction coefficient matrices $C_{k,l}^{k',l'}$. The matrices R_i,

Γ_i, U_i are defined as follows:

$$
\begin{aligned}
R_1 &= \begin{bmatrix} Z_{1,1} & Z_{2,1} & \cdots & Z_{K,1} \\ Z_{2,1} & Z_{3,1} & \cdots & Z_{K+1,1} \\ \vdots & \vdots & \ddots & \vdots \\ Z_{M-K,1} & Z_{M-K+1,1} & \cdots & Z_{M-1,1} \end{bmatrix} \\
R_2 &= \begin{bmatrix} Z_{2,1} & Z_{3,1} & \cdots & Z_{K+1,1} \\ Z_{3,1} & Z_{4,1} & \cdots & Z_{K+2,1} \\ \vdots & \vdots & \ddots & \vdots \\ Z_{M-K+1,1} & Z_{M-K+2,1} & \cdots & Z_{M,1} \end{bmatrix} \\
R_3 &= \begin{bmatrix} Z_{2,2} & Z_{3,2} & \cdots & Z_{K+1,2} \\ Z_{3,2} & Z_{4,2} & \cdots & Z_{K+2,2} \\ \vdots & \vdots & \ddots & \vdots \\ Z_{M-K+1,2} & Z_{M-K+2,2} & \cdots & Z_{M,2} \end{bmatrix} \\
R_4 &= \begin{bmatrix} Z_{1,2} & Z_{2,2} & \cdots & Z_{K,2} \\ Z_{2,2} & Z_{3,2} & \cdots & Z_{K,2} \\ \vdots & \vdots & \ddots & \vdots \\ Z_{M-K,2} & Z_{M-K+1,2} & \cdots & Z_{M-1,2} \end{bmatrix},
\end{aligned} \tag{3.41}
$$

where,

$$
Z_{m,n} = \begin{bmatrix} X^T_{m,n} & X^T_{m,n+1} & \cdots & X^T_{m,n+L-1} \\ X^T_{m,n+1} & X^T_{m,n+2} & \cdots & X^T_{m,n+L} \\ \vdots & \vdots & \ddots & \vdots \\ X^T_{m,n+N-L-1} & X^T_{m,n+N+L} & \cdots & X^T_{m,n+N-2} \end{bmatrix}. \tag{3.42}
$$

$$
\begin{aligned}
\Gamma_1 &= \begin{bmatrix} D^{K,0}_0 & D^{K,0}_1 & \cdots D^{K,0}_{K-1} \end{bmatrix}^T \\
\Gamma_2 &= \begin{bmatrix} E^{K-1,L}_0 & E^{K-1,L}_1 & \cdots E^{K-1,L}_{K-1} \end{bmatrix}^T \\
\Gamma_3 &= \begin{bmatrix} F^{-1,L-1}_0 & F^{-1,L-1}_1 & \cdots F^{-1,L-1}_{K-1} \end{bmatrix}^T \\
\Gamma_4 &= \begin{bmatrix} G^{0,-1}_0 & G^{0,-1}_1 & \cdots G^{0,-1}_{K-1} \end{bmatrix}^T,
\end{aligned} \tag{3.43}
$$

where,

$$
\begin{aligned}
D_k^{\kappa,\lambda} &= \begin{bmatrix} C_{k,0}^{\kappa,\lambda} & C_{k,1}^{\kappa,\lambda} & \cdots & C_{k,L-1}^{\kappa,\lambda} \\ C_{k,0}^{\kappa,\lambda+1} & C_{k,1}^{\kappa,\lambda+1} & \cdots & C_{k,L-1}^{\kappa,\lambda+1} \\ \vdots & \vdots & \ddots & \vdots \\ C_{k,0}^{\kappa,\lambda+L} & C_{k,1}^{\kappa,\lambda+L} & \cdots & C_{k,L-1}^{\kappa,\lambda+L} \end{bmatrix} \\
E_k^{\kappa,\lambda} &= \begin{bmatrix} C_{k,0}^{\kappa,\lambda} & C_{k,1}^{\kappa,\lambda} & \cdots & C_{k,L-1}^{\kappa,\lambda} \\ C_{k,0}^{\kappa-1,\lambda} & C_{k,1}^{\kappa-1,\lambda} & \cdots & C_{k,L-1}^{\kappa-1,\lambda} \\ \vdots & \vdots & \ddots & \vdots \\ C_{k,0}^{\kappa-K,\lambda} & C_{k,1}^{\kappa-K,\lambda} & \cdots & C_{k,L-1}^{\kappa-K,\lambda} \end{bmatrix} \\
F_k^{\kappa,\lambda} &= \begin{bmatrix} C_{k,0}^{\kappa,\lambda} & C_{k,1}^{\kappa,\lambda} & \cdots & C_{k,L-1}^{\kappa,\lambda} \\ C_{k,0}^{\kappa,\lambda-1} & C_{k,1}^{\kappa,\lambda-1} & \cdots & C_{k,L-1}^{\kappa,\lambda-1} \\ \vdots & \vdots & \ddots & \vdots \\ C_{k,0}^{\kappa,\lambda-L} & C_{k,1}^{\kappa,\lambda-L} & \cdots & C_{k,L-1}^{\kappa,\lambda-L} \end{bmatrix} \\
G_k^{\kappa,\lambda} &= \begin{bmatrix} C_{k,0}^{\kappa,\lambda} & C_{k,1}^{\kappa,\lambda} & \cdots & C_{k,L-1}^{\kappa,\lambda} \\ C_{k,0}^{\kappa+1,\lambda} & C_{k,1}^{\kappa+1,\lambda} & \cdots & C_{k,L-1}^{\kappa+1,\lambda} \\ \vdots & \vdots & \ddots & \vdots \\ C_{k,0}^{\kappa+K,\lambda} & C_{k,1}^{\kappa+K,\lambda} & \cdots & C_{k,L-1}^{\kappa+K,\lambda} \end{bmatrix}.
\end{aligned} \tag{3.44}
$$

$$
\begin{aligned}
U_1 &= \begin{bmatrix} \Sigma_{K+1} & \Sigma_{K+2} & \cdots & \Sigma_M \end{bmatrix}^T \\
U_2 &= \begin{bmatrix} \Omega_{K+1} & \Omega_{K+2} & \cdots & \Omega_M \end{bmatrix}^T \\
U_3 &= \begin{bmatrix} \Xi_1 & \Xi_2 & \cdots & \Xi_{M-K} \end{bmatrix}^T \\
U_4 &= \begin{bmatrix} \Psi_1 & \Psi_2 & \cdots & \Psi_{M-K} \end{bmatrix}^T,
\end{aligned} \tag{3.45}
$$

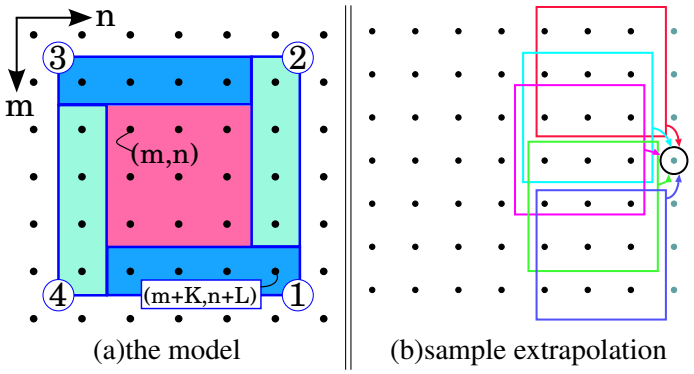

FIGURE 3.5: The two dimensional linear prediction model and the sample extrapolation process. According to the linear prediction model shown in (a), one sample can be predicted from plural sets of different samples as shown in (b).

where,

$$
\begin{aligned}
\Sigma_k &= \begin{bmatrix} X_{k,1} & X_{k,2} & \cdots & X_{k,N-L} \\ X_{k,2} & X_{k,3} & \cdots & X_{k,N-L+1} \\ \vdots & \vdots & & \vdots \\ X_{k,L+1} & X_{k,3} & \cdots & X_{k,N} \end{bmatrix} \\
\Omega_k &= \begin{bmatrix} X_{k,L+1} & X_{k,L+2} & \cdots & X_{k,N} \\ X_{k-1,L+1} & X_{k-1,L+2} & \cdots & X_{k-1,N} \\ \vdots & \vdots & & \vdots \\ X_{k-K,L+1} & X_{k-K,L+2} & \cdots & X_{k-K,N} \end{bmatrix} \\
\Xi_k &= \begin{bmatrix} X_{k,L+1} & X_{k,L+2} & \cdots & X_{k,N} \\ X_{k,L} & X_{k,L+1} & \cdots & X_{k,N-1} \\ \vdots & \vdots & & \vdots \\ X_{k,1} & X_{k,2} & \cdots & X_{k,N-L} \end{bmatrix} \\
\Psi_k &= \begin{bmatrix} X_{k,1} & X_{k,2} & \cdots & X_{k,N-L} \\ X_{k+1,1} & X_{k+1,2} & \cdots & X_{k+1,N-L} \\ \vdots & \vdots & & \vdots \\ X_{k+K,1} & X_{k+K,2} & \cdots & X_{k+K,N-L} \end{bmatrix}
\end{aligned}
\tag{3.46}
$$

The least mean square solution of Eq.(3.40) gives the estimation of the coefficients Γ_i.

$$\Gamma_i = R_i^+ U_i \qquad (i = 1,2,3,4) \tag{3.47}$$

where the superscript $+$ denotes Moore-Penrose pseudo inverse.

The spatial spectrum samples are extrapolated according to the two dimensional polarimetric linear prediction model using the estimated matrix of the coefficients $C_{k,l}^{k',l'}$. Fig. 3.5 (b) shows the extrapolation procedure. The two dimensional linear prediction model predicts all the $K \times L \times P$ samples surrounding the prediction support region. Therefore, the plural number of estimation corresponding to the same sample are obtained as shown in Fig. 3.5 (b). 2D-PBWE uses the mean value of these values as the estimation.

3.3 Experimental Results

3.3.1 Point target simulation

We show a numerical example of three closely located point targets in white noise. The scattering matrices of the three targets used in this example expressed in vector form $[HH\ HV\ VV]$ are given by

$$S_{\mathrm{pl}} = [1\ \ 0\ \ 1], \quad S_{\mathrm{qw}} = [1\ \ 0\ \ j], \quad S_{\mathrm{di}} = [1\ \ 0\ \ -1]\,. \tag{3.48}$$

These three scattering matrices could correspond to, for example, a plate (pl), a quarter wave device (qw), and a dihedral corner reflector (di)[3].

The targets are located to form a regular triangle shape in the range-azimuth plane, and the distance between the targets are set to be half of the Nyquist sample distance [4] T. The signal-to-noise ratio (SNR) is 30dB. Here, the SNR is defined in the frequency domain as the ratio of the power of a single scatterer to the average noise power. The number of the samples of the original data is 16 by 16, and the bandwidth is expanded by a factor of 4 by 2D-PBWE. For comparison, the 1D-PBWE is applied to the same data in both azimuth and range directions.

Fig. 3.6 (a), (b) and (c) show the original image, the bandwidth extrapolated image by applying 1D-PBWE in both azimuth and range directions, and the bandwidth extrapolated image by 2D-PBWE, respectively. As shown in the top right of the Fig. 3.6, the colors in this figure are based on the Pauli basis representation of the scattering matrix given by Eq.(3.49) [82], where blue, red and green represent the magnitude of each component α, β, and γ, respectively.

$$S = \frac{\alpha}{\sqrt{2}}\begin{bmatrix} 1 & 0 \\ 0 & 1 \end{bmatrix} + \frac{\beta}{\sqrt{2}}\begin{bmatrix} 1 & 0 \\ 0 & -1 \end{bmatrix} + \frac{\gamma}{\sqrt{2}}\begin{bmatrix} 0 & 1 \\ 1 & 0 \end{bmatrix} \tag{3.49}$$

Note that this color representation has ambiguity, *i.e.*, different scattering matrix may be represented by the same color, for example, S(in vector form) $= [1\ \ 0\ \ j]$ and $[\sqrt{2}\ \ 0\ \ 0]$ both have components $|\alpha| = |\beta| = 1, |\gamma| = 0$. However, this color representation is handy for this example, since S_{pl}, S_{qw} and S_{di} correspond to different colors (red, purple and blue, respectively). Fig. 3.6(a) shows that the three scatterers are not resolved in the original image as expected. In Fig. 3.6(c), one can see that the positions and the polarization properties of the targets are well restored by 2D-PBWE. On the other hand, Fig. 3.6(b) shows that when 1D-PBWE is applied in both range and azimuth directions, although the three targets are somewhat resolved, the estimated positions and polarization properties of the targets are less accurate, and furthermore, one can observe some undesirable oscillation effect causing spurious peaks or high sidelobes.

[3] In general, the scattering matrix of a target depends on the aspect angle, *e.g.*, the scattering matrix of a dihedral corner reflector takes a form of S_{di} when its symmetry axis is oriented at zero degree (horizontal). Further discussions about this issue can be found in [82].

[4] Nyquist sample distance T in range and azimuth directions are $c/2B$ and $\lambda\rho/2L$, respectively. Where λ is the wavelength, L is the synthetic aperture length, and ρ is slant range.

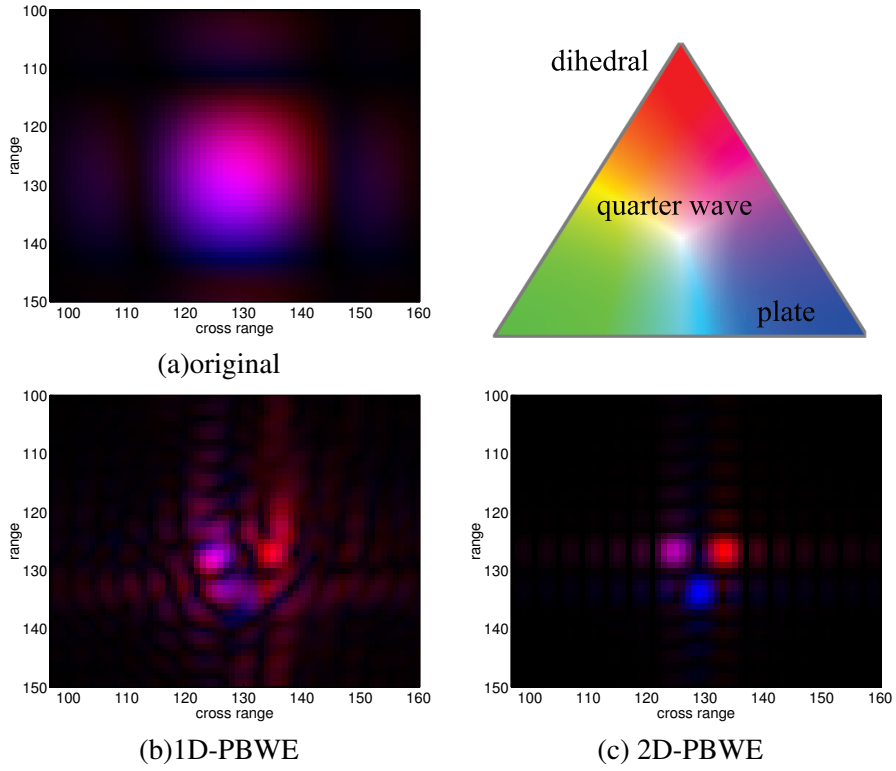

(a)original

(b)1D-PBWE

(c) 2D-PBWE

FIGURE 3.6: Simulated image of three closely located point targets. In (c), one can see the exact positions of dihedral corner reflector, quarter wave and plate counter clockwise from the top right. The number of the samples in the original signal is 16 by 16, the bandwidth is expanded by a factor of 4, linear prediction model order has been set to be $K = L = 4$. Note that the pixel size is 1/16 of the original Nyquist sample distance T. The color is based on the Pauli basis representation of the scattering matrix where blue, red and green represent the magnitude of each component α, β, and γ, respectively (see the text for more detail).

3.3.2 Application to SAR images

Fig. 3.7 shows the output image of the 2D-PBWE method. The bandwidth has been doubled in both range and azimuth direction. In this figure, (a) and (b) show HH and VV images of the PBWE output, (c) shows the color composite of HH and VV, and (d) shows the total power (span) image[5]. One can see that the clarity of the image is improved compared to the original dual polarization image in Fig. 3.1. And we can now observe the target ground interaction of the tailplane in HH image. In addition, we notice that the interaction is weaker in VV image, which provides additional information, e.g., on the electrical properties of the ground etc.

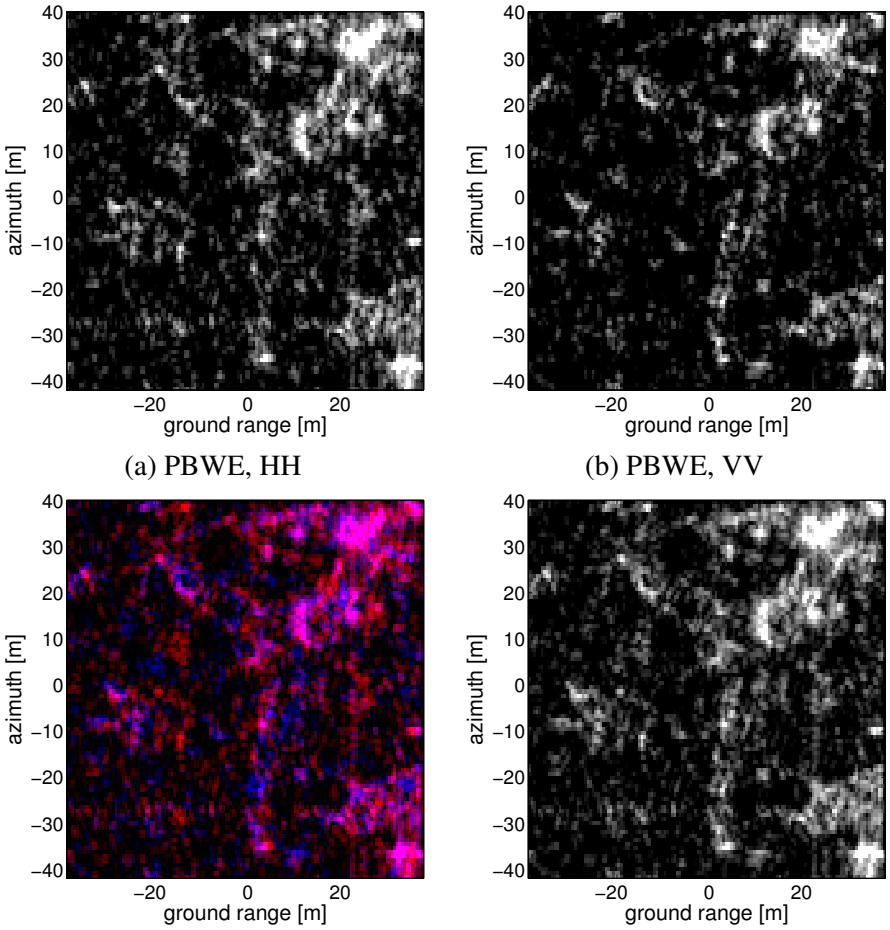

(a) PBWE, HH

(b) PBWE, VV

(c) PBWE, HH/VV

(d) PBWE, total power (span)

FIGURE 3.7: The output image of the 2D-PBWE method. The bandwidth has been doubled in both range and azimuth direction. (a) and (b) are HH and VV image of the output image of the PBWE applied to the TerraSAR-X dual polarization image, (c) is a color composite image of PBWE image, where HH and VV are assigned to red and blue, respectively. (d) is the total power (span) image of the PBWE image.

[5]Total power or span is defined as the sum of the power of the HH and VV images.

Fig. 3.8 presents a real polarimetric SAR image of a ferry on the sea surface, observed using the EMISAR system. Developed at the Technical University of Denmark, EMISAR is a dual-frequency polarimetric SAR system operating at L-band and C-band. The original image has a resolution of 1.5 meters in range and 0.75 meters in azimuth. Fig. 3.8(a) shows the original pseudo-color EMISAR image, which follows the same color scheme as Fig. 3.6., with an image size of 80×160 samples. Fig. 3.8(b) displays a band-limited version, where the bandwidth is reduced to half of the original in both range and azimuth directions. Fig. 3.8(c) and Fig. 3.8(d) show bandwidth-extrapolated images, obtained using 1D-PBWE applied sequentially in range and azimuth and 2D-PBWE, respectively. Similarly, Fig. 3.8(e) presents another band-limited image with bandwidth reduced to one-quarter of the original, while Fig. 3.8(f) and Fig. 3.8(g) display the extrapolated versions using 1D-PBWE and 2D-PBWE, respectively.

In this experiment, the bandwidth is restored to its original state, allowing for a quantitative assessment of the extrapolated images by comparing them to the original using correlation coefficients defined as:

$$\text{correlation coefficient (c.c.)} = \frac{|x_e^* x_i|}{\|x_e\| \|x_i\|}, \tag{3.50}$$

where x_i and x_e are the original image and the bandwidth extrapolated image, and M,N are the number of pixels along range and azimuth direction, respectively.

As shown in Figs. 3.8(c) and (d), when the bandwidth is limited to half, the correlation coefficients of the bandwidth-extrapolated images generated by 1D-PBWE and 2D-PBWE are 0.96 and 0.97, respectively. This result suggests that near-perfect image restoration is achievable even with a reduced bandwidth. Similarly, Figs. 3.8(f) and (g) show that when the bandwidth is further restricted to one-quarter, the correlation coefficients for 1D-PBWE and 2D-PBWE drop to 0.66 and 0.86, respectively, which remains relatively high. Additionally, these findings indicate that the image generated by 2D-PBWE is closer to the original than the one obtained using 1D-PBWE. In fact, while the 1D-PBWE extrapolated image exhibits a more pronounced spiky texture, many of its peaks do not match the original image in terms of position or color.

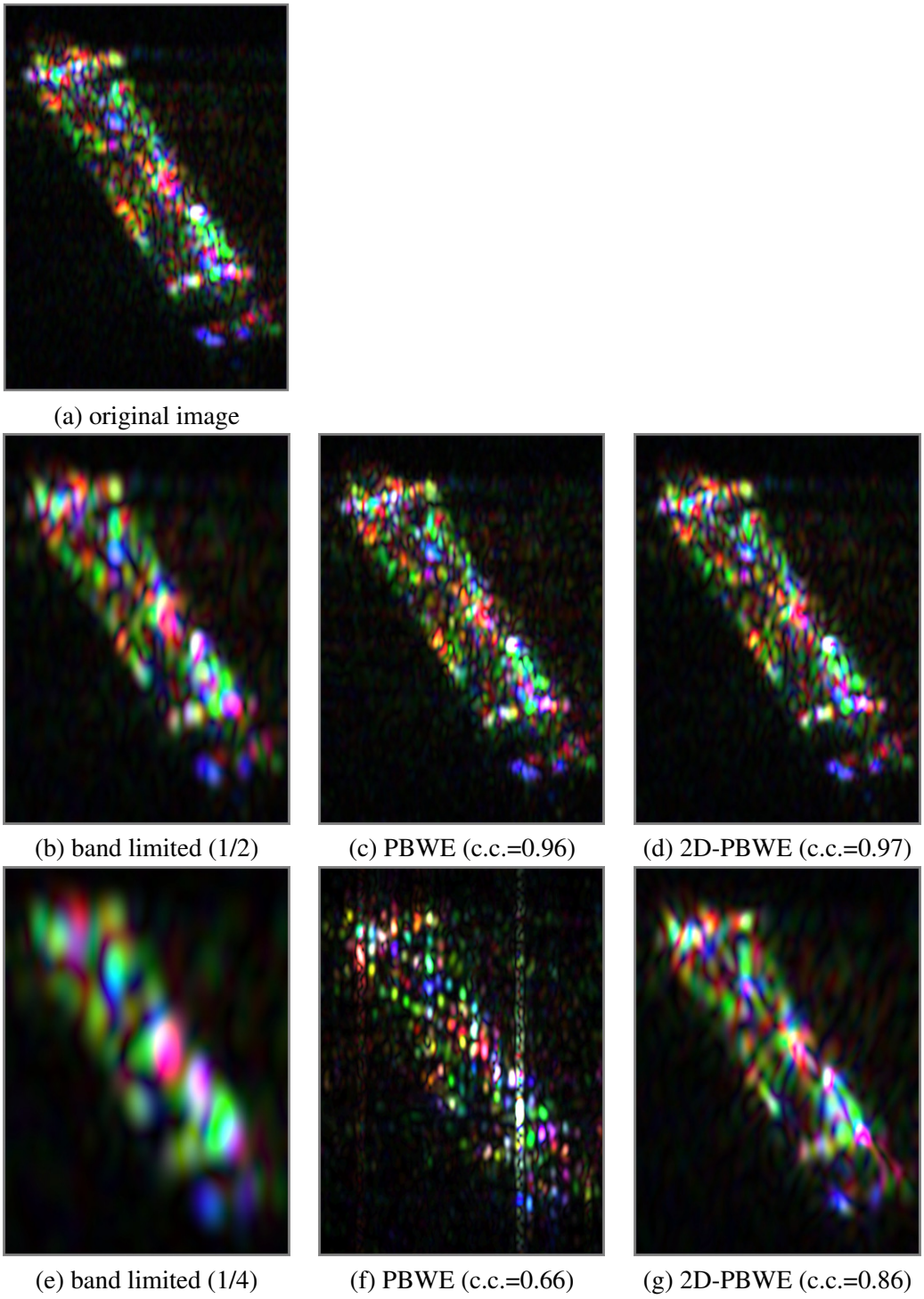

(a) original image

(b) band limited (1/2) (c) PBWE (c.c.=0.96) (d) 2D-PBWE (c.c.=0.97)

(e) band limited (1/4) (f) PBWE (c.c.=0.66) (g) 2D-PBWE (c.c.=0.86)

FIGURE 3.8: Experimental result from the EMISAR polarimetric SAR image of a ferry. The resolution of the original EMISAR image is 1.5m in range and 0.75m in azimuth, the size of the original image is 80×160 samples. The pixel spacing of the images shown in this figure is approximately 0.19m $\times$0.094 m (i.e. the original image is upsampled by a factor of 8). Both rmse and correlation coefficient show the best values for 2D-PBWE. Note that rmse of the band limited image is greater than 1D-PBWE while the correlation coefficient of the band limited image is greater than 1D-PBWE. Also note that rmse of 1D-PBWE and 2D-PBWE images are close but they are visually very different. The EMISAR data is by courtesy of DCRS (Danish Center for Remote Sensing) Electromagnetic Systems at Technical University of Denmark.

3.4 Theoretical Performance Analysis

In this section, theoretical analysis on the resolution of a polarimetric radar is provided. The resolution defined in terms of Rayleigh's criterion is determined by the signal bandwidth[54], and it is clearly independent of polarization information. Our interest is in the performance of parametric spectral estimation (also referred to as super-resolution) techniques applied to the polarimetric radar data. Many attempts have been carried out to evaluate the resolution capability of parametric spectral estimation techniques. A common approach is to utilize the Cramér-Rao bound (CRB), which provides the lower bound for the accuracy of any unbiased estimator. In this approach, usually the CRB for the position estimations of two closely located sources are studied[83]. Recently, a simple metric of the resolution called *statistical resolution limit* (SRL) has been proposed[52] [6]. The SRL is defined as *the source separation that equals its own CRB*. Note that it is defined based on the CRB for the separation, not the positions, of the two targets. We use the SRL to evaluate the resolution of the polarimetric radar.

Along with the resolution, estimation accuracy of the polarization property of the target is studied. And we show that the estimation error of the polarization property can be decreased by processing all the polarization channels together rather than processing channel by channel. This issue is important because we would like to exploit the polarization information in the following image analysis task.

Both CRB for the target separation and the CRB for the polarization estimation error are derived from the full Fisher Information Matrix (FIM) of the target position parameters and complex amplitude parameters. A general expression for the deterministic full FIM of the multichannel signal with non-white Gaussian noise is derived first. The CRBs for the target position parameters and complex amplitude parameters are then obtained from the full FIM. The "complexified" approach is taken, since it simplifies the analysis [52], [85], [86]. The CRBs of the separation and the polarization estimation error are derived from the above mentioned CRB. Especially, an analytic form of the CRB for the separation of two channels case is provided and studied in detail. In addition, the effect of relative signal phase of the two target is throughly studied, since this is the key to understand the effect of polarization on the resolution. Average or limiting performance over the relative signal phase have separately been studied [84], [87]–[94], but each one of them captures one aspect of the phenomenon, respectively. In this section, the average and limiting cases are considered in a unified manner, which enables us to fully understand the effect of relative signal phase. Some numerical examples of the SRL and the CRB for the polarization estimation are shown and discussed. Finally, the performance of the PBWE is evaluated via simulations and compared to the CRBs.

The effect of polarization information on the resolution under stochastic signal model has been investigated in [95]–[97] with applications to diversely polarized antenna arrays. The CRB based on the stochastic signal model is achieved asymptotically with increasing number of snapshots, and tends to give a loose bound when the number of snapshot is small. A quick comparison between the deterministic and the stochastic signal model is also provided.

3.4.1 Signal Model, Full FIM and CRB for the Target Parameters

Signal Model

The polarimetric radar signal can be modeled as a P channel signal, each channel of which having the data size of N. The number of polarization channels P is 4 for a full polarimetric radar and 2 for a dual polarization radar, and so forth. The polarimetric radar signal in the

[6] A similar idea has been proposed separately in [84].

spatial frequency domain can be modeled as follows:

$$\boldsymbol{z} = \boldsymbol{V}(\boldsymbol{\theta})\,\boldsymbol{a} + \boldsymbol{n}. \tag{3.51}$$

In (3.51), $\boldsymbol{z} \in \mathbb{C}^{N\times P}$ is a data matrix, each column of which represent the signal in each channel, $\boldsymbol{a} \in \mathbb{C}^{M\times P}$ is a matrix whose (m,p)-th element corresponds to the complex amplitude of m-th signal in p-th channel, $\boldsymbol{V}(\boldsymbol{\theta}) \in \mathbb{C}^{N\times M}$ is a complex matrix whose columns define the responses of M signals,

$$\boldsymbol{V}(\boldsymbol{\theta}) = [\boldsymbol{v}_1(\boldsymbol{\theta})\ \boldsymbol{v}_2(\boldsymbol{\theta})\ \cdots\ \boldsymbol{v}_M(\boldsymbol{\theta})] \tag{3.52}$$

where $\boldsymbol{v}_m(\boldsymbol{\theta}) \in \mathbb{C}^{N\times 1}$ is a steering vector, and $\boldsymbol{\theta} = [\theta_1, \theta_2, \cdots, \theta_K]^T \in \mathbb{R}^{K\times 1}$ is a vector of real signal parameters, $\boldsymbol{n} \in \mathbb{C}^{N\times P}$ is a complex Gaussian clutter plus noise with covariance matrix

$$\boldsymbol{R} = E\{(\boldsymbol{n}:)(\boldsymbol{n}:)^H\} \qquad \in \mathbb{C}^{NP\times NP} \tag{3.53}$$

where the notation $\boldsymbol{X}$: means the large column vector formed by concatenating all the columns of $\boldsymbol{X}$, *i.e.*, if $\boldsymbol{X}$ is a $N\times P$ matrix, $\boldsymbol{X}$: $\triangleq [x_{11}\cdots x_{N1}\ x_{12}\cdots x_{N2}\cdots\cdots x_{1P}\cdots x_{NP}]^T$. The superscripts T and H denote matrix transpose and conjugate transpose, respectively. Note that the expression of (3.52) is employed for the sake of generality, and each $\boldsymbol{v}_m(\boldsymbol{\theta})$ is not necessarily a function of all the parameters $\theta_1, \cdots, \theta_K$. Also note that the parameter term $(\boldsymbol{\theta})$ is omitted in the following argument. We assume the amplitude matrix $\boldsymbol{a}$ to be unknown and deterministic. We write columns and rows of $\boldsymbol{a}$ as $\boldsymbol{a}_p \in \mathbb{C}^{M\times 1}$ and $\boldsymbol{s}_m \in \mathbb{C}^{1\times P}$, respectively:

$$\boldsymbol{a} = [\boldsymbol{a}_1\ \cdots\ \boldsymbol{a}_P] = [\boldsymbol{s}_1;\ \cdots;\ \boldsymbol{s}_M]\,. \tag{3.54}$$

Here, the semicolon is used as in the MATLAB convention, *i.e.*, the row vectors $\boldsymbol{s}_m$ are concatenated vertically. $\boldsymbol{a}_p$ is just the collection of the complex amplitudes of the M targets in the p-th channel. $\boldsymbol{s}_m$ represents the polarization property of the m-th target by its "direction" in the complex polarization space $\mathbb{C}^{1\times P}$. We call $\boldsymbol{s}_m$ a polarization vector of the m-th target. From (3.51), the likelihood function of the data $\boldsymbol{z}$ is given by

$$f(\boldsymbol{z}: |\boldsymbol{a}, \boldsymbol{\theta}) = \frac{1}{\pi^N |\boldsymbol{R}|} \exp\left[-\{(\boldsymbol{z} - \boldsymbol{V}\boldsymbol{a}):\}^H \boldsymbol{R}^{-1} \{(\boldsymbol{z} - \boldsymbol{V}\boldsymbol{a}):\}\right]. \tag{3.55}$$

and the log likelihood function is (when constant terms are ignored)

$$L(\boldsymbol{z}: |\boldsymbol{a}, \boldsymbol{\theta}) = -\{(\boldsymbol{z} - \boldsymbol{V}\boldsymbol{a}):\}^H \boldsymbol{R}^{-1} \{(\boldsymbol{z} - \boldsymbol{V}\boldsymbol{a}):\}. \tag{3.56}$$

FIM and CRB

Consider an unbiased estimator of some unknown real parameters $\boldsymbol{\Phi} \in \mathbb{R}^{L\times 1}$, then Cramér-Rao inequality gives a lower bound on the covariance of the estimate of $\hat{\boldsymbol{\Phi}}$ by the inverse of the FIM. Namely,

$$\begin{aligned} &\boldsymbol{C}_{\boldsymbol{\Phi}} = E\left\{(\hat{\boldsymbol{\Phi}} - \boldsymbol{\Phi})(\hat{\boldsymbol{\Phi}} - \boldsymbol{\Phi})^T\right\} \geq \boldsymbol{G}_{\boldsymbol{\Phi}}^{-1} \\ &(\Leftrightarrow \boldsymbol{C}_{\boldsymbol{\Phi}} - \boldsymbol{G}_{\boldsymbol{\Phi}}^{-1} \text{ is positive semidefinite}) \end{aligned} \tag{3.57}$$

where $\boldsymbol{C}_{\boldsymbol{\Phi}}$ is the covariance of the estimate $\hat{\boldsymbol{\Phi}}$ and

$$\boldsymbol{G}_{\boldsymbol{\Phi}} = E\left\{(\partial_{\boldsymbol{\Phi}}^T L)(\partial_{\boldsymbol{\Phi}} L)\right\} = -E\left\{\partial_{\boldsymbol{\Phi}}^T \partial_{\boldsymbol{\Phi}} L\right\} \tag{3.58}$$

is the FIM. Assume that the parameter $\boldsymbol{\Phi}$ is partitioned into two sets so that $\boldsymbol{\Phi} = [\boldsymbol{\Phi}_1; \boldsymbol{\Phi}_2]$. Then FIM of (3.58) can be partitioned as follows:

$$\boldsymbol{G}_{(\boldsymbol{\Phi}_1;\boldsymbol{\Phi}_2)} = \begin{bmatrix} \boldsymbol{G}_{\boldsymbol{\Phi}_1\boldsymbol{\Phi}_1} & \boldsymbol{G}_{\boldsymbol{\Phi}_1\boldsymbol{\Phi}_2} \\ \boldsymbol{G}_{\boldsymbol{\Phi}_2\boldsymbol{\Phi}_1} & \boldsymbol{G}_{\boldsymbol{\Phi}_2\boldsymbol{\Phi}_2} \end{bmatrix} \tag{3.59}$$

where, $\boldsymbol{G}_{\boldsymbol{\Phi}_i\boldsymbol{\Phi}_j} = -E\{\partial^T_{\boldsymbol{\Phi}_i}\partial_{\boldsymbol{\Phi}_j}L\}$. From the formula of matrix inversion in block form, the inverse of the FIM is given by the following form

$$\boldsymbol{G}^{-1}_{\boldsymbol{\Phi}} = \begin{bmatrix} \boldsymbol{S}^{-1}_{\boldsymbol{\Phi}_1} & * \\ * & \boldsymbol{S}^{-1}_{\boldsymbol{\Phi}_2} \end{bmatrix} \tag{3.60}$$

where,

$$\boldsymbol{S}_{\boldsymbol{\Phi}_i} = \boldsymbol{G}_{\boldsymbol{\Phi}_i\boldsymbol{\Phi}_i} - \boldsymbol{G}_{\boldsymbol{\Phi}_i\boldsymbol{\Phi}_j}\boldsymbol{G}^{-1}_{\boldsymbol{\Phi}_j\boldsymbol{\Phi}_j}\boldsymbol{G}_{\boldsymbol{\Phi}_j\boldsymbol{\Phi}_i}, \quad i,j \in \{1,2\},\ i \neq j. \tag{3.61}$$

(The off diagonal elements of (3.60) are irrelevant to the subsequent analysis.) Thus, when one of the parameter sets is being estimated, the CRB for that parameter set is given by,

$$\boldsymbol{C}_{\boldsymbol{\Phi}_i} \geq \boldsymbol{S}^{-1}_{\boldsymbol{\Phi}_i} \qquad i \in \{1,2\}. \tag{3.62}$$

The other (undesired) set of parameters is called "nuisance parameters." In fact, it can be seen from (3.61) that the nuisance parameters negatively influence the estimation of the parameters of interest.

To obtain the FIM of $\boldsymbol{a}$ and $\boldsymbol{\theta}$, we follow the approach presented in [52], [86]; namely, we use the complexified approach for the complex amplitude parameter $\boldsymbol{a}$ and the standard real/imaginary approach for the signal parameter $\boldsymbol{\theta}$. First, we rewrite the log likelihood function without a constant term as

$$\begin{aligned} L(\boldsymbol{z}:|\boldsymbol{a},\boldsymbol{\theta}) &= -\sum_{p=1}^{P}\sum_{q=1}^{P}\big(\boldsymbol{z}_p^H\boldsymbol{R}^{\triangledown}_{pq}\boldsymbol{z}_q + \boldsymbol{a}_p^H\boldsymbol{V}^H\boldsymbol{R}^{\triangledown}_{pq}\boldsymbol{V}\boldsymbol{a}_q \\ &\quad -\boldsymbol{a}_p^H\boldsymbol{V}^H\boldsymbol{R}^{\triangledown}_{pq}\boldsymbol{z}_q - \boldsymbol{z}_p^H\boldsymbol{R}^{\triangledown}_{pq}\boldsymbol{V}\boldsymbol{a}_q\big). \end{aligned} \tag{3.63}$$

Then the second derivatives of the log likelihood function are

$$-\partial^T_{\boldsymbol{a}_p}\partial_{\boldsymbol{a}_q}L = 0 \tag{3.64}$$

$$-\partial^T_{\bar{\boldsymbol{a}}_p}\partial_{\boldsymbol{a}_q}L = \boldsymbol{\Xi}_{pq}, \quad -\partial^T_{\boldsymbol{a}_p}\partial_{\bar{\boldsymbol{a}}_q}L = \boldsymbol{\Xi}^T_{qp} \tag{3.65}$$

$$-\partial^T_{\boldsymbol{\theta}}\partial_{\boldsymbol{a}_p}L = \sum_{q=1}^{P}\Big(\boldsymbol{a}_q^H\boldsymbol{\Xi}_{qp[\boldsymbol{\theta}]} - \boldsymbol{z}_q^H\boldsymbol{R}^{\triangledown}_{qp}\boldsymbol{V}_{[\boldsymbol{\theta}]}\Big) \tag{3.66}$$

$$-\partial^T_{\boldsymbol{\theta}}\partial_{\bar{\boldsymbol{a}}_p}L = \sum_{q=1}^{P}\Big(\boldsymbol{a}_q^T\bar{\boldsymbol{\Xi}}_{qp[\boldsymbol{\theta}]} - \boldsymbol{z}_q^T\bar{\boldsymbol{R}}^{\triangledown}_{qp}\bar{\boldsymbol{V}}_{[\boldsymbol{\theta}]}\Big) \tag{3.67}$$

$$\begin{aligned} -\partial^T_{\boldsymbol{\theta}}\partial_{\boldsymbol{\theta}}L &= \sum_{p=1}^{P}\sum_{q=1}^{P}\Big(\boldsymbol{a}_p^H\boldsymbol{\Xi}_{pq[\boldsymbol{\theta}\boldsymbol{\theta}]}\boldsymbol{a}_q - \boldsymbol{a}_p^H\boldsymbol{V}^H_{[\boldsymbol{\theta}\boldsymbol{\theta}]}\boldsymbol{R}^{\triangledown}_{pq}\boldsymbol{z}_q \\ &\quad -\boldsymbol{z}_p^H\boldsymbol{R}^{\triangledown}_{pq}\boldsymbol{V}_{[\boldsymbol{\theta}\boldsymbol{\theta}]}\boldsymbol{a}_q\Big) \end{aligned} \tag{3.68}$$

where,

$$\boldsymbol{\Xi}_{pq} = \boldsymbol{V}^H\boldsymbol{R}^{\triangledown}_{pq}\boldsymbol{V} \tag{3.69}$$

and $\boldsymbol{R}_{pq}^{\triangledown} \in \mathbb{C}^{N\times N}$ is a (p,q)-th block of the inverse of the covariance matrix $\boldsymbol{R}$.

$$\boldsymbol{R}^{-1} = \begin{bmatrix} \boldsymbol{R}_{11}^{\triangledown} & \cdots & \boldsymbol{R}_{1P}^{\triangledown} \\ \vdots & \ddots & \vdots \\ \boldsymbol{R}_{P1}^{\triangledown} & \cdots & \boldsymbol{R}_{PP}^{\triangledown} \end{bmatrix} \tag{3.70}$$

Then it follows that the FIM for parameter vector $[\boldsymbol{\alpha};\boldsymbol{\theta}]$ ($\boldsymbol{\alpha} = [(\boldsymbol{a}:);(\bar{\boldsymbol{a}}:)]$) is given by

$$\boldsymbol{G}_{(\boldsymbol{\alpha};\boldsymbol{\theta})} = \left[\begin{array}{cc:c} 0 & \boldsymbol{\Xi}^T & \boldsymbol{\Lambda}^T \\ \boldsymbol{\Xi} & 0 & \bar{\boldsymbol{\Lambda}}^T \\ \hdashline \boldsymbol{\Lambda} & \bar{\boldsymbol{\Lambda}} & 2\boldsymbol{\Delta} \end{array}\right] \tag{3.71}$$

where,

$$\boldsymbol{\Delta} = \boldsymbol{\Delta}_d + \boldsymbol{\Delta}_c \tag{3.72}$$

$$\boldsymbol{\Delta}_d = \sum_{p=1}^{P} \mathrm{Re}\left\{ \boldsymbol{a}_p^H \boldsymbol{V}_{[\boldsymbol{\theta}]}^H \boldsymbol{R}_{pp}^{\triangledown} \boldsymbol{V}_{[\boldsymbol{\theta}]} \boldsymbol{a}_p \right\} \tag{3.73}$$

$$\begin{aligned} \boldsymbol{\Delta}_c = \sum_{p=1}^{P-1} \sum_{q=p+1}^{P} \mathrm{Re}\Big\{ & \boldsymbol{a}_p^H \boldsymbol{V}_{[\boldsymbol{\theta}]}^H \boldsymbol{R}_{pq}^{\triangledown} \boldsymbol{V}_{[\boldsymbol{\theta}]} \boldsymbol{a}_q \\ & + \boldsymbol{a}_p^H \left[\boldsymbol{V}_{[\boldsymbol{\theta}]}^H \boldsymbol{R}_{qp}^{\triangledown} \boldsymbol{V}_{[\boldsymbol{\theta}]} \right]^H \boldsymbol{a}_q \Big\} \end{aligned} \tag{3.74}$$

$$\boldsymbol{\Lambda} = \sum_{q=1}^{P} [\boldsymbol{\Lambda}_{1q} \;\; \boldsymbol{\Lambda}_{2q} \;\cdots\; \boldsymbol{\Lambda}_{Pq}] \tag{3.75}$$

$$\boldsymbol{\Lambda}_{pq} = \boldsymbol{a}_q^H \boldsymbol{V}_{[\boldsymbol{\theta}]}^H \boldsymbol{R}_{qp}^{\triangledown} \boldsymbol{V} \tag{3.76}$$

$$\boldsymbol{\Xi} = \begin{bmatrix} \boldsymbol{\Xi}_{11} & \cdots & \boldsymbol{\Xi}_{1P} \\ \vdots & \ddots & \vdots \\ \boldsymbol{\Xi}_{P1} & \cdots & \boldsymbol{\Xi}_{PP} \end{bmatrix}. \tag{3.77}$$

The subscripted notation "$[\boldsymbol{\theta}]$" denotes the substitution of the first derivative with respect to θ_k wherever the k-th index of $\boldsymbol{\theta}$ is required (readers are encouraged to see Appendix B of [52]). Using the relations of (3.61) and (3.62), the CRB for $\boldsymbol{\alpha}$ and $\boldsymbol{\theta}$ are obtained from (3.71) as

$$\boldsymbol{C}_{\boldsymbol{\alpha}} \geq \boldsymbol{S}_{\boldsymbol{\alpha}}^{-1} = \begin{bmatrix} \boldsymbol{\Pi} & \boldsymbol{\Omega}^T \\ \boldsymbol{\Omega} & \boldsymbol{\Pi}^H \end{bmatrix}^{-1} \tag{3.78}$$

$$\boldsymbol{C}_{\boldsymbol{\theta}} \geq \boldsymbol{S}_{\boldsymbol{\theta}}^{-1} = \frac{1}{2}[\Delta - \boldsymbol{M}]^{-1} \tag{3.79}$$

where,

$$\boldsymbol{\Omega} = \boldsymbol{\Xi} - \frac{1}{2}\boldsymbol{\Lambda}^H \boldsymbol{\Delta}^{-1} \boldsymbol{\Lambda}\,, \quad \boldsymbol{\Pi} = -\frac{1}{2}\boldsymbol{\Lambda}^T \boldsymbol{\Delta}^{-1} \boldsymbol{\Lambda} \tag{3.80}$$

$$\boldsymbol{M} = \mathrm{Re}\left\{ \boldsymbol{\Lambda} \boldsymbol{\Xi}^{-1} \boldsymbol{\Lambda}^H \right\}. \tag{3.81}$$

(3.78) and (3.79) are the main results of this section, and they are very general expressions. The model (3.51) has a similar structure as in the case of the single channel sensor with P multiple snapshots; therefore, (3.79) reduces to the CRB given in (4.1) of [83], when $\boldsymbol{R} = \boldsymbol{I}$. On the other hand, when $P = 1$, (3.79) surely reduces to the CRB given in (24) of [52].

If the background noise is spatially uncorrelated and uniform but correlated between polarization channels, then the covariance matrix $\boldsymbol{R}$ can be expressed as follows:

$$\boldsymbol{R} = \boldsymbol{R}_p \otimes \boldsymbol{I}, \quad \boldsymbol{R}_p = E\left\{\boldsymbol{n}_{(n,\cdot)}^T \bar{\boldsymbol{n}}_{(n,\cdot)}\right\}, \quad \forall n \in \{1,\cdots,N\} \tag{3.82}$$

where $\boldsymbol{n}_{(n,\cdot)}$ is the n-th row of the noise matrix $\boldsymbol{n}$. This model is suitable when the background is uniform but has some certain polarization properties, *e.g.*, ground clutter *et cetera*. $\boldsymbol{R}_p$ in this case is equivalent to the clutter polarization covariance matrix which frequently appears in the literatures on polarimetric radar signal processing[66], [98].

When the covariance matrix is expressed by (3.82), the CRB for $\boldsymbol{\theta}$ is still expressed by (3.79), but the expressions for $\boldsymbol{\Delta}$,$\boldsymbol{M}$,$\boldsymbol{\Xi}$,$\boldsymbol{\Lambda}$ can be modified as follows (note that $\boldsymbol{R}^{-1} = \boldsymbol{R}_p^{-1} \otimes \boldsymbol{I}$):

$$\boldsymbol{\Delta} = \boldsymbol{\Delta}_d + \boldsymbol{\Delta}_c \tag{3.83}$$

$$\boldsymbol{\Delta}_d = \sum_{p=1}^{P} \mathrm{Re}\left\{r_{pp}^{\triangledown} \boldsymbol{a}_p^H \boldsymbol{V}_{[\boldsymbol{\theta}]}^H \boldsymbol{V}_{[\boldsymbol{\theta}]} \boldsymbol{a}_p\right\} \tag{3.84}$$

$$\begin{aligned}\boldsymbol{\Delta}_c = \sum_{p=1}^{P-1}\sum_{q=p+1}^{P} \mathrm{Re}\Big\{r_{pq}^{\triangledown}\Big(&\boldsymbol{a}_p^H \boldsymbol{V}_{[\boldsymbol{\theta}]}^H \boldsymbol{V}_{[\boldsymbol{\theta}]} \boldsymbol{a}_q \\ &+ \boldsymbol{a}_p^H \left[\boldsymbol{V}_{[\boldsymbol{\theta}]}^H \boldsymbol{V}_{[\boldsymbol{\theta}]}\right]^H \boldsymbol{a}_q\Big)\Big\}\end{aligned} \tag{3.85}$$

$$\boldsymbol{\Lambda} = \sum_{q=1}^{P} [\boldsymbol{\Lambda}_{1q} \ \boldsymbol{\Lambda}_{2q} \ \cdots \ \boldsymbol{\Lambda}_{Pq}] \tag{3.86}$$

$$\boldsymbol{\Lambda}_{pq} = r_{qp}^{\triangledown} \boldsymbol{a}_q^H \boldsymbol{V}_{[\boldsymbol{\theta}]}^H \boldsymbol{V} \tag{3.87}$$

$$\boldsymbol{\Xi} = \boldsymbol{R}_p^{-1} \otimes \boldsymbol{\Xi}_n \tag{3.88}$$

$$\boldsymbol{\Xi}_{\boldsymbol{n}} = \boldsymbol{V}^H \boldsymbol{V} \tag{3.89}$$

$$\boldsymbol{M} = \mathrm{Re}\left\{\sum_{p=1}^{P}\sum_{q=1}^{P} r_{pq}^{\triangledown} \boldsymbol{M}_{pq}\right\} \tag{3.90}$$

$$\boldsymbol{M}_{pq} = \boldsymbol{\Lambda}_p \boldsymbol{\Xi}_n^{-1} \boldsymbol{\Lambda}_q^H \tag{3.91}$$

$$\boldsymbol{\Lambda}_p = \boldsymbol{a}_p^H \boldsymbol{V}_{[\boldsymbol{\theta}]}^H \boldsymbol{V} \tag{3.92}$$

$$\boldsymbol{\Xi} = \boldsymbol{V}^H \boldsymbol{V} \tag{3.93}$$

and $r_{pq}^{\triangledown}$ is the (p,q)-th element of $\boldsymbol{R}_p^{-1}$.

3.4.2 Statistical Resolution Limit and Polarization Estimation Error

Point target model

The radar targets can be considered as a mixture of individual reflection points, also called scatterers. Generally, it was found that the scatterers on targets remain roughly fixed and that their reflection amplitude remain reasonably constant over the observation bandwidth and aspect angle[54]. Based on this observation, a radar target is often regarded as a mixture of a finite number of point targets. Here, the point target is defined as an ideal target whose complex amplitude is uniform over spatial frequencies.

To discuss the resolution of the polarimetric radar, the point target model is employed in the rest of this section. And in the following analysis, we consider the case where two point targets are closely located with each other. The signal model and the definition of SNR (Signal to Noise Ratio) is provided in this subsection.

Note that the point target model is an approximation, and it is insufficient to fully describe the entire backscattering behavior of real targets, as it is extensively studied in [56], [99]. Nevertheless, we employ the point target model for our analysis, because it is reasonably consistent with the data[54], and attempts to describe the diverse nature of the further details of real target by mathematically tractable models seem impractical [56]. The theoretical resolution limit derived based on the point target model would serve as a reasonable and comprehensible standard. The performance of a real data can be measured relative to the standard provided here.

From the definition of the point target, it is represented by a pole on a unit circle, thus the steering matrix is given by

$$\boldsymbol{V} = [\boldsymbol{v}_1(\rho_1) \;\; \boldsymbol{v}_2(\rho_2)] \tag{3.94}$$

where,

$$\boldsymbol{v}_k(\rho_k) = \left[\rho_k^{-\frac{N-1}{2}} \;\; \rho_k^{-\frac{N+1}{2}} \;\; \cdots \;\; \rho_k^{\frac{N-1}{2}}\right]^T \tag{3.95}$$

$$\rho_1 = 1, \qquad \rho_2 = e^{j\Delta\phi}. \tag{3.96}$$

(3.96) indicates that $\Delta\phi$ is the separation of the two targets (in radians). To obtain the CRB for the signal parameter $\boldsymbol{\theta}$, the real/imaginary approach is taken as stated before, and in this case $\boldsymbol{\theta}$ becomes

$$\boldsymbol{\theta} = [x_1 \;\; y_1 \;\; x_2 \;\; y_2]^T \tag{3.97}$$

where, x_k and y_k are the real and imaginary parts of the pole ρ_k, respectively.

Both targets are assumed to have the same magnitude in all the polarization channels, and the complex amplitude is given by

$$\begin{aligned} \boldsymbol{a} &= a\begin{bmatrix} 1 & 1 & \cdots & 1 \\ e^{j\psi_1} & e^{j\psi_2} & \ldots & e^{j\psi_P} \end{bmatrix} \\ &= a\begin{bmatrix} 1 & 1 & \cdots & 1 \\ e^{j\psi} & e^{j(\psi+\chi_2)} & \ldots & e^{j(\psi+\chi_P)} \end{bmatrix} \end{aligned} \tag{3.98}$$

where $\psi = \psi_1$ is the relative phase of the target #2 to the target #1 in the first channel. $\chi_p = \psi_p - \psi_1$ is the relative phase of the p-th channel to the first channel of the target #2. Since, in this example, the magnitudes are all the same, χ_p are the only parameters that define the difference in polarization properties of the targets #1 and #2. ψ is the relative phase between the two targets in the first channel, and it is a function of the radial distance between the two targets as well as of the center frequency of the transmit signal. It is well understood that relative magnitude between the polarization channels also is important to characterize the polarization property of the target. Some discussion on this issue is given in Appendix A.2.

The SNR (Signal to Noise Ratio) is defined in the image domain for each target and for each polarization channel. Under above signal model, the SNR of the p-th channel becomes

$$\text{SNR} = \frac{(Na)^2}{P_n^{(p)}} \tag{3.99}$$

where, $P_n^{(p)}$ is the noise power of the p-th polarization channel. In the following analysis, both targets are assumed to have the same magnitude in all the polarization channels, and further more, the noise power in all the polarization channels are assumed to be the same. Therefore, we need only one SNR value to represent one set of data. For example, for the white Gaussian noise (WGN) with covariance matrix $\boldsymbol{R} = \boldsymbol{I}$, the SNR becomes Na^2.

Definition of the statistical resolution limit

A theoretical measure of the resolution called "Statistical resolution limit (SRL)" is introduced in [52]. It is defined as follows

$$\mathrm{SRL} \triangleq \Delta\phi \quad s.t. \quad \Delta\phi = \{\mathrm{CRB}(\Delta\phi)\}^{1/2}, \Delta\phi > 0 \tag{3.100}$$

where $\mathrm{CRB}(\Delta\phi)$ is the CRB for the source separation estimation. In other words, the statistical resolution is the source separation that equals its own CRB (root squared). In this definition, the sources are regarded to be "resolved" when the standard deviation of the source separation estimation is equal to the true separation.

A mathematically equivalent idea with some generalization is also proposed in [84]. The main difference is that they introduce a user selected parameter γ to adjust the confidence interval as follows.

$$\mathrm{RL} \triangleq \Delta\phi \quad s.t. \quad \Delta\phi = \gamma\{\mathrm{CRB}(\Delta\phi)\}^{1/2}, \Delta\phi > 0. \tag{3.101}$$

This resolution limit becomes identical with the SRL when $\gamma = 1$. As pointed out in [52], in practice, $\gamma = 1$ gives a sufficiently meaningful bound. If the separation is too small, and the parametric spectral estimation methods fail to resolve the two sources, then the two spectral peaks of each signal tend to coalesce into one; namely, the separation is estimated to be zero. In this case, the standard deviation of the separation estimation error is approximately equal to the true separation.

The CRB for the source separation estimation $\Delta\phi$ is derived in the following way[52]. First, we define the difference between the two poles as follows.

$$\boldsymbol{\delta} = [x_1 - x_2 \;\; y_1 - y_2]^T = \boldsymbol{D}\boldsymbol{\theta}, \tag{3.102}$$

where,

$$\boldsymbol{D} = \begin{bmatrix} 1 & -1 & 0 & 0 \\ 0 & 0 & 1 & -1 \end{bmatrix}. \tag{3.103}$$

Noting that $\|\boldsymbol{\delta}\| \approx \Delta\phi$ when $\Delta\phi$ is small, the CRB for the separation is given by

$$\mathrm{CRB}(\Delta\phi) \approx \mathrm{CRB}(\|\boldsymbol{\delta}\|) = \boldsymbol{D}\boldsymbol{S}_{\boldsymbol{\theta}}^{-1}\boldsymbol{D}^T. \tag{3.104}$$

Taking the point target signal model given by (3.94)–(3.98) and assuming the WGN model with covariance $\boldsymbol{R} = \boldsymbol{I}$ for the noise, (3.104) becomes

$$\mathrm{CRB}(\Delta\phi) \approx \left(\frac{N}{2\pi}\right)^2 \cdot \frac{2N}{\mathrm{SNR}} \cdot \frac{Pd_0 + d_1 c_p}{P^2 d_0^2 - d_1^2(c_p^2 + s_p^2)}, \tag{3.105}$$

where,

$$c_p = \sum_{p=1}^{P} \cos(\Delta\phi - \psi_p) \tag{3.106}$$

$$s_p = \sum_{p=1}^{P} \sin(\Delta\phi - \psi_p), \tag{3.107}$$

and

$$d_0 = -s''(0) - \frac{s(0)s'(\Delta\phi)^2}{s(0)^2 - s(\Delta\phi)^2} \tag{3.108}$$

$$d_1 = -s''(\Delta\phi) - \frac{s(\Delta\phi)s'(\Delta\phi)^2}{s(0)^2 - s(\Delta\phi)^2}. \tag{3.109}$$

$s(\Delta\phi)$ is a Dirichlet kernel:

$$s(\Delta\phi) = \sum_{n=-(N-1)/2}^{(N-1)/2} e^{jn\Delta\phi} = \frac{\sin\frac{N}{2}\Delta\phi}{\sin\frac{1}{2}\Delta\phi}. \tag{3.110}$$

The prime and the double prime as in $s'(\Delta\phi)$ and $s''(\Delta\phi)$ represent the first and second derivative, respectively. The derivation of (3.105) from (3.104) is given in Appendix A.

The merit of defining the resolution based on the CRB is that it gives the lower bound for any algorithm, under the condition where the CRB holds (high SNR, unbiased estimators, and no modeling or signal mismatch). Although the CRB has widely been used to assess the resolution, what makes the SRL different from others is that the CRB for the source separation is used to bound resolution, while the majority of works use the CRB for the source accuracies themselves. Technically, this means that the SRL takes the off-diagonal elements of the CRB into account, while the others only treat diagonal elements. As shown later, when the sources are close, the off-diagonal effects are not negligible.

CRB for the target separation estimation for the Single and the Dual Polarization Cases

In order to illustrate the effect of the polarization information on the resolution, the CRB and the SRL for the single and dual polarization, say HH and VV, cases are compared.

The CRB for the single polarization case can be derived by setting the number of polarization channels to one ($P = 1$) in (3.105).

$$\mathrm{CRB}(\Delta\phi|\psi) \approx \left(\frac{N}{2\pi}\right)^2 \cdot \frac{2N}{\mathrm{SNR}} \cdot \frac{d_0 + d_1\cos(\Delta\phi - \psi)}{d_0^2 - d_1^2}, \tag{3.111}$$

(3.111) indicates that the CRB depends on the relative phase ψ. When $\psi = 0$, the result becomes equivalent to (49)–(57) of [52], although the closed form expression is not given there. The CRB for the dual polarization case ($P = 2$) is derived in the same manner:

$$\begin{aligned}\mathrm{CRB}(\Delta\phi|\psi,\chi) &\approx \left(\frac{N}{2\pi}\right)^2 \cdot \frac{N}{\mathrm{SNR}} \\ &\quad \times \frac{d_0 + d_1\cos(\frac{\chi}{2})\cos(\Delta\phi - \frac{\chi}{2} - \psi)}{d_0^2 - d_1^2\cos^2(\chi/2)},\end{aligned} \tag{3.112}$$

where, $\chi = \chi_2$. Note that the CRB now depends not only on ψ but also on χ which is the parameter that defines the difference in polarization properties of the targets #1 and #2. For example, when $\chi = 0$, the polarization vectors of the two targets (normalized by the first channel) are equal and can be expressed as $\boldsymbol{s}_1 = \boldsymbol{s}_2 = [1,\ 1]$. On the other hand, when $\chi = \pi$, the polarization vectors of the two targets are $\boldsymbol{s}_1 = [1,\ 1]$, $\boldsymbol{s}_2 = [1,\ -1]$, and thus they are orthogonal. Note that for HH and VV dual polarization case, $\boldsymbol{s}_1 = [1,\ 1]$ and $\boldsymbol{s}_2 = [1,\ -1]$ represent the polarization properties of odd-bounce and even-bounce targets, respectively[65].

In addition, the CRB for the single polarization case when L pulses are transmitted is derived here for the discussion in the later part of this section; the CRB can be obtained just

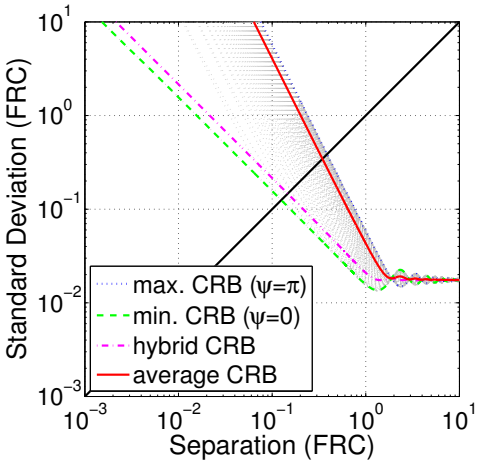

FIGURE 3.9: The CRB for the target separation as a function of target separation. Each dotted gray line shows the CRB of a certain value of ψ. The dotted blue line, dashed green line, dash-dot magenta line, and solid red line show the maximum ($\psi = \pi$), the minimum ($\psi = 0$), the hybrid, and the average CRB, respectively. The solid black line represents "separation = standard deviation." The intersections between the square root of the CRB and the solid black line give the SRL. (SNR=33dB, single channel)

by dividing (3.111) by L.

$$\mathrm{CRB}_L(\Delta\phi|\psi) \approx \left(\frac{N}{2\pi}\right)^2 \cdot \frac{2N}{L\cdot \mathrm{SNR}} \cdot \frac{d_0 + d_1\cos(\Delta\phi - \psi)}{d_0^2 - d_1^2}, \tag{3.113}$$

Here, the targets are assumed to be unchanged between the pulses, and the noise is temporally uncorrelated. (3.113) shows that transmitting L pulses has the effect of improving the SNR by the factor of L.

The CRB for the single polarization case (3.111) and the dual polarization case (3.112) are shown in Fig. 3.9 and Fig. 3.10, respectively. We discuss the effect of polarization on the resolution through investigating the results given in these figures.

Analysis on the effect of relative phase on the CRB for the Single Polarization Case

In Fig. 3.9, the dotted gray lines represent the square root of the CRB for the single polarization case given in (3.111) as functions of separation $\Delta\phi$ in units of FRC (Fourier Resolution Cell[52][7]) Each dotted gray line corresponds to a certain value of ψ, and ψ has been searched from $-\pi$ to π with an interval of $\pi/72$. Other parameters in this figure are $N = 50$ and SNR=33dB. Note that the figure shows square root of the CRB, not the CRB itself, and thus it shows the lower bound of the standard deviation of the estimation error.

From Fig. 3.9, it can be seen that when the separation is smaller than 1 FRC, the CRB rapidly increases as the separation decreases, and the dispersion of the CRB with respect to the relative phase ψ increases due to the increasing influence of the signal interference. On the other hand, when the separation is larger than 1 FRC, the CRB becomes almost constant, and the dispersion of the CRB with respect to ψ becomes very small.

Let's first look at the region where the separation of the two signals is larger than 1 FRC, in order to familiarize the expression in (3.111). Fig. 3.11 shows d_0 and d_1 as functions of

[7] 1FRC corresponds to the Rayleigh resolution for the signals that are windowed by rectangular weighting function[54]. 1 FRC $= 2\pi/N$ [rad].

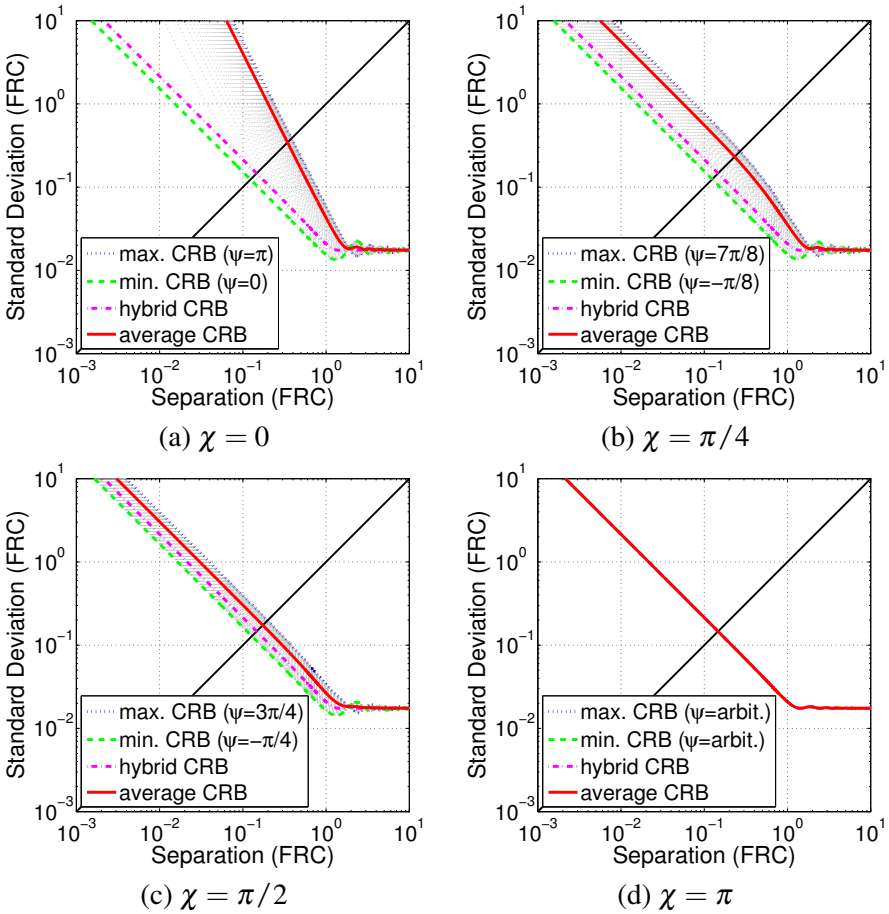

(a) $\chi = 0$ (b) $\chi = \pi/4$

(c) $\chi = \pi/2$ (d) $\chi = \pi$

FIGURE 3.10: The CRB of the target separation as a function of target separation (SNR=30dB, two polarization channels). Note that (a) is exactly the same as Fig. 3.9

target separation $\Delta\phi$ (in units of FRC). From Fig.3.11, it can be seen that when the separation is large (say larger than 3 FRC), the magnitude of d_0 is significantly larger than that of d_1. And from (3.108), $d_0 \to -s''(0)$ when $\Delta\phi \to \pi$, if N is sufficiently large. Therefore, when the two targets are well separated, the expression in (3.111) becomes

$$\mathrm{CRB}(\Delta\phi|\psi) \approx \left(\frac{N}{2\pi}\right)^2 \cdot \frac{2N}{\mathrm{SNR}} \cdot \frac{1}{d_0} \approx \left(\frac{N}{2\pi}\right)^2 \cdot \frac{2N}{\mathrm{SNR}} \cdot \frac{1}{-s''(0)} \,. \tag{3.114}$$

Recall that the well known CRB for the variance of a single signal delay time estimation error $(\hat{\tau} - \tau)$ is given by (see[100, Sec.10.8]).

$$\mathrm{CRB}(\tau) \approx \frac{N_0}{2E_r} \cdot \frac{1}{\beta^2} \tag{3.115}$$

where noise is assumed to be Gaussian and white with two-sided power spectral density $N_0/2$, E_r is the signal energy, β is the rms (root mean square) bandwidth (in rad/s). E_r and β are defined using the power spectrum of the signal $S(f)$ as [101]

$$E_r = \int_{-\infty}^{\infty} S(f)df \,, \quad \beta^2 = \frac{1}{E_r}\int_{-\infty}^{\infty} \omega^2 S(f)df \,, \tag{3.116}$$

and β is related to the signal autocorrelation function $R(\tau)$ by

$$\beta^2 = \frac{-R''(0)}{E_r}. \tag{3.117}$$

Under the current signal model,

$$\frac{N_0}{2E_r} = \frac{1}{\mathrm{SNR}} \,, \quad R(\tau) = s\left(\frac{2\pi}{N}\tau\right) \quad (\tau \text{ is in FRC}) \tag{3.118}$$

and by substituting (3.117) and (3.118) into (3.115), we obtain

$$\mathrm{CRB}(\tau) \approx \left(\frac{N}{2\pi}\right)^2 \cdot \frac{N}{\mathrm{SNR}} \cdot \frac{1}{-s''(0)} \;\; [\mathrm{FRC}^2]. \tag{3.119}$$

Comparing (3.114) with (3.119), we see that the CRB for the separation estimation error is approximately equal to the sum of the CRB for the position estimation error of each target, when the targets are well separated:

$$\mathrm{CRB}(\Delta\phi|\psi) \approx 2 \cdot \mathrm{CRB}(\tau) \tag{3.120}$$

This is because when the two targets are far enough, the interference between the two becomes negligible.

Now, we investigate the region where the separation is smaller than 1 FRC. The solid black line in Fig. 3.9 represents "std $= \Delta\phi$." Namely, from the definition (3.100), the intersections between the square root of the CRB and the solid black line give the SRL. One can see in Fig. 3.9 that since the CRB depends on ψ, the SRL also depends on ψ, and in this case, the SRL ranges from 0.125 to 0.386 FRC.

The fact that the CRB depends on the relative phase ψ is well known[89], [90], [92]. We further look into this issue in more detail. To analyze the influence of ψ on the CRB and the SRL, we employ four representative values; the maximum (or the worst case) CRB [89], the minimum (or the best case) CRB [84], the hybrid (or *a posteriori*) CRB [87], [91]–[93], and the average CRB (also known as Miller-Chang Bound) [88], [93], [94]. The first

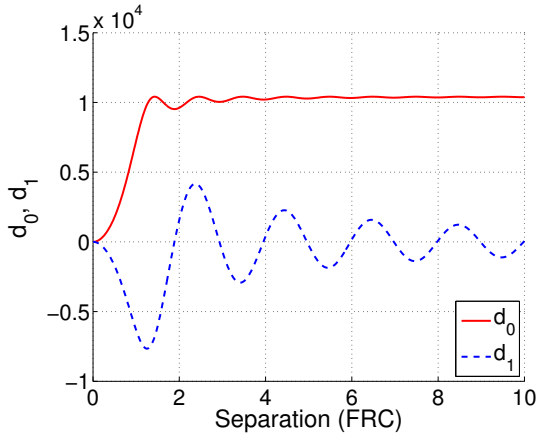

FIGURE 3.11: d_0 and d_1 as a function of target separation ($N = 50$). The magnitude of d_0 and d_1 are comparable when the separation is smaller than 1 FRC. When the separation is large, the magnitude of d_0 is significantly larger than that of d_1.

two are the limiting cases. In Fig. 3.9, the dotted blue line and dashed green line show the maximum CRB and the minimum CRB with respect to ψ for small $\Delta\phi$, respectively. The maximum CRB results at $\psi \approx \pi$, when the two targets interfere destructively. On the other hand, the minimum CRB is achieved at $\psi \approx 0$. It is also clear from (3.111), noting that d_0 and d_1 have opposite signs for small $\Delta\phi$ (see Fig. 3.11), that these limiting cases are given at $\psi \approx \pi$ and $\psi \approx 0$, respectively, when $\Delta\phi$ is small. The hybrid CRB and the average CRB are both "average" type values. In Fig. 3.9, dash-dot magenta line, and solid red line show the hybrid CRB and the average CRB, respectively. The "average" performance is derived by regarding the phase ψ as a random variable. One way to obtain the average bound is to use the following relationship:

$$p(\boldsymbol{z}|\boldsymbol{\theta},a) = \int_{-\infty}^{\infty} p(\boldsymbol{z}|\boldsymbol{\theta},a,\psi)p_{\psi}(\psi)d\psi \tag{3.121}$$

where, $p_{\psi}(\psi)$ is the *a priori* distribution of ψ, which we can assume to be uniformly distributed over $[-\pi,\pi)$. From this relation, the bound of the average covariance matrix (averaged over the phase ψ) is obtained as the inverse of the average FIM (again, averaged over ψ) [87], [91], [92]. The CRB thus obtained is called the hybrid CRB. Note that hybrid CRB is a bound for the estimators which need to be unbiased only over the ensemble. On the other hand, the average CRB is obtained by averaging the CRB (not FIM) over ψ [88]. This is derived by conditioning the estimator to be unbiased for every value of the phase ψ. As an immediate result from the definition, the hybrid CRB is always looser than the average CRB, and one can see this property in Fig. 3.9.

The four CRBs are expressed as follows (see Appendix A.1):

$$\mathrm{CRB}_{\max} = \left(\frac{N}{2\pi}\right)^2 \frac{2N}{\mathrm{SNR}} \cdot \frac{1}{d_0 + d_1} \tag{3.122}$$

$$\mathrm{CRB}_{\min} = \left(\frac{N}{2\pi}\right)^2 \frac{2N}{\mathrm{SNR}} \cdot \frac{1}{d_0 - d_1} \tag{3.123}$$

$$\mathrm{CRB}_{\mathrm{hyb}} = \left(\frac{N}{2\pi}\right)^2 \frac{2N}{\mathrm{SNR}} \cdot \frac{1}{d_0} \tag{3.124}$$

$$\mathrm{CRB}_{\mathrm{ave}} = \left(\frac{N}{2\pi}\right)^2 \frac{2N}{\mathrm{SNR}} \cdot \frac{d_0}{d_0^2 - d_1^2}. \tag{3.125}$$

The SRL corresponding to the four representative CRBs can be obtained, by numerically solving (3.100), to be $\mathrm{SRL}_{\max} = 0.386$, $\mathrm{SRL}_{\min} = 0.125$, $\mathrm{SRL}_{\mathrm{hyb}} = 0.147$, and $\mathrm{SRL}_{\mathrm{ave}} = 0.345$, when SNR is 30dB.

Analysis on the CRB for the Dual Polarization Case

In Fig. 3.10, the dotted gray lines represent the square root of the CRB for the dual polarization case given in (3.112) as functions of separation $\Delta\phi$ in units of FRC. The dotted blue line, dashed green line, dash-dot magenta line, and solid red line show the maximum, the minimum, the hybrid, and the average CRB, respectively. Fig. 3.10 (a), (b), (c), and (d) are for different χ values as indicated in the figure. Other parameters in this figure are $N = 50$ and SNR=30dB. The four CRBs for the dual polarization case conditioned on χ are expressed as follows (also see Appendix A.1):

$$\mathrm{CRB}_{\max|\emptyset} = \left(\frac{N}{2\pi}\right)^2 \cdot \frac{N}{\mathrm{SNR}} \cdot \frac{1}{d_0 + d_1|\cos(\chi/2)|} \tag{3.126}$$

$$\mathrm{CRB}_{\min|\emptyset} = \left(\frac{N}{2\pi}\right)^2 \cdot \frac{N}{\mathrm{SNR}} \cdot \frac{1}{d_0 - d_1|\cos(\chi/2)|} \tag{3.127}$$

$$\mathrm{CRB}_{\mathrm{hyb}|\emptyset} = \left(\frac{N}{2\pi}\right)^2 \cdot \frac{N}{\mathrm{SNR}} \cdot \frac{1}{d_0} \tag{3.128}$$

$$\mathrm{CRB}_{\mathrm{ave}|\emptyset} = \left(\frac{N}{2\pi}\right)^2 \cdot \frac{N}{\mathrm{SNR}} \cdot \frac{d_0}{d_0^2 - d_1^2\cos^2(\chi/2)} \tag{3.129}$$

where, the maximum and the minimum CRB are respectively given by $\psi = \pi - \chi/2$ and $\psi = -\chi/2$. The corresponding SRLs in units of FRC are summarized in Table 3.1 along with the SRLs for the single polarization case. Note that in order to see the contribution of only the polarization property, the SNR has been set to 33dB for the single polarization case and 30dB for the dual polarization case. Since two pulses are transmitted in HH, VV dual polarization case, we assume that two pulses are also transmitted for the single polarization case. Thus, from (3.113), SNR for the single polarization case has been set to 3dB higher.

From the results shown above, first we see that Fig. 3.10 (a) coincides with Fig. 3.9. This is because when $\chi = 0$, the expression (3.125) becomes equivalent to (3.113) with $L = 2$, which means that if the polarization properties of the two targets are the same, polarimetric information does not help and it is the same as sending two pulses by a single polarization radar[8].

[8]This statement is true only when the magnitude of both of the target is the same for all the polarization channels.

TABLE 3.1: The SRL corresponding to the four representative CRBs

χ	$\mathrm{SRL}_{\max}$	$\mathrm{SRL}_{\min}$	$\mathrm{SRL}_{\mathrm{hyb}}$	$\mathrm{SRL}_{\mathrm{ave}}$
Single polarization, SNR=33dB				
–	0.386	0.125	0.147	0.345
Dual polarization, SNR=30dB				
0	0.386	0.125	0.147	0.345
$\pi/4$	0.270	0.125	0.147	0.232
$\pi/2$	0.198	0.128	0.147	0.174
π	0.147	0.147	0.147	0.147

Then comparing Fig. 3.10 (a), (b), (c), and (d), we see that the dispersion of the CRB with respect to the relative phase ψ decreases as χ increases, and in the limiting case of $\chi = \pi$, the CRB is independent of ψ. We can also see that the maximum CRB and the average CRB decrease as χ increases. This suggests that the polarization information contributes to suppression of the signal interference effect. As χ increases, suppression effect increases, and it is most effective when the polarization properties of the two targets are orthogonal to each other. Note that if $\chi = \pi$, when the signals interfere destructively in one polarization channel, then the signals interfere non-destructively in the other polarization channel. The fact that the average CRB decreases as χ increases suggests that the resolution is improved, on average, by the signal interference suppression effect of polarization information. From Table 3.1, the SRL corresponding to the average CRB is lower for the dual polarization case than the single polarization case, except for when $\chi = 0$. The improvement factor is maximum at $\chi = \pi$ and it is about 2.3(=0.345/0.147).

On the other hand, the hybrid CRB is constant over χ. The hybrid CRB would be achieved when the signal phases are fluctuating and multiple 'snapshots' are available. In this case, having two polarization channels is equivalent to double the number of snapshots. But it is not the case for the normal POLSAR observation. In fact, in the later section, the performance of the PBWE is shown to be bounded by the average CRB.

It is interesting to compare the properties observed above with the study on diversely polarized antenna arrays reported in [95]–[97], [102], in which the CRB for the stochastic signal model is derived. For example, Fig. 3 (a) in [95] shows that the CRB for the diversely polarized antenna is independent of the DOA (direction of arrival) separation of two sources. Even when the two sources are located at the same position, the diversely polarized antenna array is capable of separating the two sources on the basis of their polarization difference. Some studies on source correlation are presented in [96], [102]. Note that the stochastic CRB can be achieved asymptotically with increasing number of snapshots and can never be achieved by a single snapshot.

Comparison of the Dual and Single Polarization Cases

We just showed that the maximum improvement factor of the dual polarization over single polarization is about 2.3, and it is obtained when $\chi = \pi$. In order to capture the overall performance, we average (3.129) over χ assuming that χ is uniformly distributed over $[-\pi, \pi)$, which gives

$$\underset{\chi}{E}\left\{\mathrm{CRB}_{\mathrm{ave}|\emptyset}\right\} = \left(\frac{N}{2\pi}\right)^2 \cdot \frac{N}{\mathrm{SNR}} \cdot \frac{1}{\sqrt{d_0^2 - d_1^2}} \,. \tag{3.130}$$

In Fig. 3.12, The dotted magenta line and the dash-dot magenta line show the square root of the average CRB given by (3.112) with $\chi = 0$ and $\chi = \pi$, respectively. The solid red line shows the square root of the overall CRB given by (3.130). These CRBs are again calculated

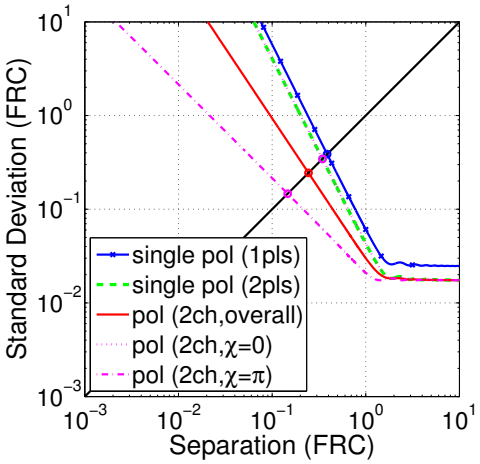

FIGURE 3.12: The average CRB for the estimation error of target separation as a function of target separation (N=50,SNR=30dB). The solid blue line and dashed green line show the average CRB for the single polarization with 1 pulse and 2 pulses, respectively. The dotted magenta line and the dash-dot magenta line show the average CRB for the 2 polarization channels case with $\chi = 0$ and $\chi = \pi$, respectively. The solid red line shows the overall CRB for the 2 polarization channels case. Note that the two polarization channels case with $\chi = 0$ (dotted magenta line) coincides with the single polarization with 2 pulses (dashed green line).

for $N = 50$ and SNR=30dB. It can be seen that the overall CRB for the two polarization channels case is always lower than the CRB for the single polarization case. Also note that the two polarization channels case with $\chi = 0$ (dotted magenta line) coincide with the single polarization with 2 pulses (dashed green line).

The statistical resolution limits of the single polarization channel case and two polarization channels case are solved numerically and are shown in Fig. 3.13 as functions of SNR. The statistical resolution limits of the single polarization with 1 pulse case, for example, is obtained by equating the square root of the right hand side of (3.111) with the target separation $\Delta\phi \times N/2\pi$. The single polarization with 2 pulses, two polarization channels case for some χ, and overall performance of two polarization channels are obtained likewise using (3.113), (3.125), and (3.130), respectively. In Fig. 3.13, the solid blue line and dashed green line show the statistical resolution limit for the single polarization with 1 pulse and 2 pulses, respectively. The dotted magenta line and the dash-dot magenta line show the 2 polarization channels case with $\chi = 0$ and $\chi = \pi$, respectively. The solid red line shows the overall performance of the 2 polarization channels case.

Fig. 3.13 indicates that the statistical resolution limit is linear in the log scale. By simple line fitting, we obtain the following approximation for the statistical resolution limit D.

$$D_{\text{single,1pls}} \approx 1.23 \cdot \text{SNR}^{-1/6} \tag{3.131}$$

$$D_{\text{single,2pls}} \left(= D_{\text{2pol},\chi=0}\right) \approx 1.09 \cdot \text{SNR}^{-1/6} \tag{3.132}$$

$$D_{\text{2pol,overall}} \approx 0.97 \cdot \text{SNR}^{-1/5} \tag{3.133}$$

$$D_{\text{2pol},\chi=\pi} \approx 0.82 \cdot \text{SNR}^{-1/4} \tag{3.134}$$

Note that the statistical resolution limit for single polarization case given by (3.131) differs from that presented in [52] where the CRB with $\psi = 0$ case is employed. The result given here looks largely pessimistic, because it takes the signal interference effect into account. However this representation is useful in order to compare the performance of the single and

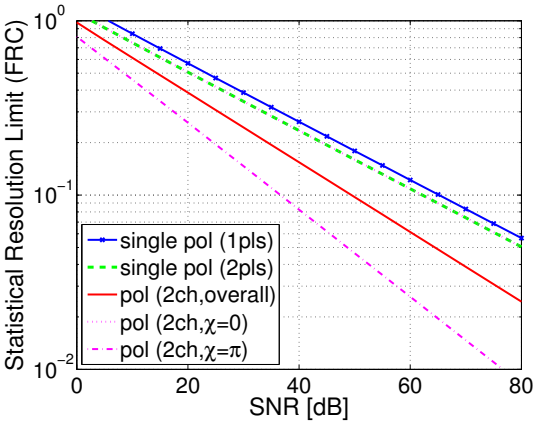

FIGURE 3.13: Comparisons of Statistical Resolution Limits: The solid blue line and dashed green line show the statistical resolution limit for the single polarization with 1 pulse and 2 pulses, respectively. The dotted magenta line and the dash-dot magenta line show the 2 polarization channels case with $\chi = 0$ and $\chi = \pi$, respectively. The solid red line shows the overall performance of the 2 polarization channels case.

the dual polarization cases. Because the polarization information contributes to suppressing the interference effect and improves the performance 'on average' as mentioned before.

Polarimetric, Colored Gaussian Noise case

If the background noise is dominated by homogeneous clutter, *e.g.*, ground clutter, the noise could show some polarization property. In such a case, and for two polarization channels, the noise covariance can be modeled as follows:

$$\boldsymbol{R}_p = \begin{bmatrix} 1 & \rho\sqrt{r}e^{j\chi_r} \\ \rho\sqrt{r}e^{-j\chi_r} & r \end{bmatrix}, \qquad \boldsymbol{R}_n = \boldsymbol{I} \tag{3.135}$$

where, r is the relative power of the 2nd channel and $\rho e^{j\chi_r}$ is the correlation coefficient between the two channels. Then the CRB is given by

$$\sigma_\delta \geq \frac{r(1-\rho)}{a^2} \cdot \frac{(\gamma_1+\gamma_2)d_0 + 2d_1c_{12}}{\gamma_1\gamma_2 d_0^2 - d_1^2(c_{12}^2+s_{12}^2)} \tag{3.136}$$

where,

$$\begin{aligned}
\gamma_1 &= r+1-2\rho\sqrt{r}\cos\chi_r && (3.137)\\
\gamma_2 &= r+1-2\rho\sqrt{r}\cos(\psi_1-\psi_2-\chi_r) && (3.138)\\
c_{12} &= r\cos(\Delta\phi-\psi_1)+\cos(\Delta\phi-\psi_2) \\
&\quad -\rho\sqrt{r}\{\cos(\Delta\phi-\psi_1+\chi_r)+\cos(\Delta\phi-\psi_2-\chi_r)\} && (3.139)\\
s_{12} &= r\sin(\Delta\phi-\psi_1)+\sin(\Delta\phi-\psi_2) \\
&\quad -\rho\sqrt{r}\{\sin(\Delta\phi-\psi_1+\chi_r)+\sin(\Delta\phi-\psi_2-\chi_r)\}. && (3.140)
\end{aligned}$$

Some effects of the noise correlation are shown in Fig. 3.14. In Fig. 3.14, the CRB given by (3.136) is shown as a function of χ. In this example, the target separation is 0.3FRC, SNR=30dB, and relative noise power in the 2nd channel is $r = 1$. Fig. 3.14 (a) and (b) respectively show the CRBs for the phase of correlation coefficients $\chi_r = 0$ and π case for some values of ρ. The correlation coefficient $\rho = 0$ corresponds to the white noise case.

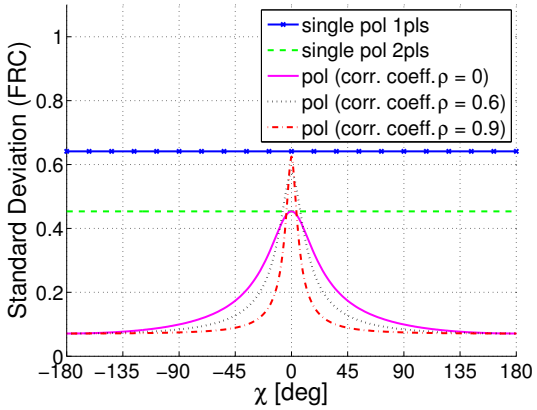

(a) The phase of correlation coefficients $\chi_r = 0$

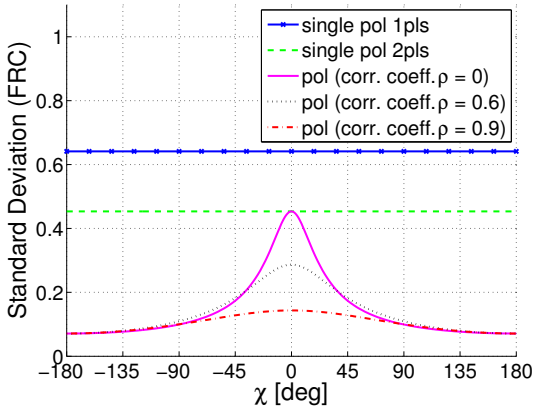

(b) The phase of correlation coefficients $\chi_r = \pi$

FIGURE 3.14: The CRB for the target separation as a function of χ: (SNR=30dB, Separation = 0.3FRC). The relative noise power in the 2nd channel is $r = 1$. The solid blue line and the dashed green line respectively show the average CRB of the single polarization case for 1 pulse and 2 pulses case, the solid red line shows the overall CRB of the 2 polarization channels case obtained by averaging the result of (3.136) over χ, and the dash-dot magenta line shows the average CRB of the 2 polarization channels case given by (3.136).

As Fig. 3.14 (a) shows, when $\chi_r = 0$ and ρ increases, the CRB decreases except when $|\chi|$ is small. The CRB at $\chi = 0$ approaches that of the single polarization with 1 pulse case when ρ increases. In the limiting case of $\rho = 1$ (perfect correlation), the two polarization channels observe exactly the same value, and thus it is essentially equivalent to just observing once with single polarization channel. On the other hand, when $\chi_r = \pi$, Fig. 3.14 (b) shows that the CRB at $\chi = 0$ decreases when ρ increases. This is because, in this case, most of the background noise energy is localized around the $[1 \ \ -1]$ direction in the complex polarization space $\mathbb{C}^{1\times 2}$ when ρ is large, while two signals are both in the $[1 \ \ 1]$ direction. Therefore, the polarization information separates the noise from the targets, resulting in lower CRB.

Polarization vector estimation error

We investigate the accuracy of the estimated polarization property, which is expressed by the polarization vector defined in (3.54). We first derive the CRB for the polarization vectors $\boldsymbol{s}_1$

and $\boldsymbol{s}_2$. For the signal model given in (3.98) with WGN, FIM for $\boldsymbol{\alpha}$ given in (3.78) reduces to

$$\boldsymbol{S}_{\boldsymbol{\alpha}} = \begin{bmatrix} 0 & \boldsymbol{\Omega}^T \\ \boldsymbol{\Omega} & 0 \end{bmatrix} \tag{3.141}$$

where,

$$\boldsymbol{\Omega} = \begin{bmatrix} \boldsymbol{H}+\boldsymbol{F} & \bar{\boldsymbol{G}} \\ \boldsymbol{G} & \boldsymbol{H}+\bar{\boldsymbol{F}} \end{bmatrix} \tag{3.142}$$

$$\boldsymbol{H} = \begin{bmatrix} s(0) & s(\Delta\phi) \\ s(\Delta\phi) & s(0) \end{bmatrix} \tag{3.143}$$

$$\boldsymbol{F} = \begin{bmatrix} f_0 & f_1 e^{-j\frac{\chi}{2}} \\ f_1 e^{j\frac{\chi}{2}} & f_0 \end{bmatrix} \tag{3.144}$$

$$\boldsymbol{G} = \begin{bmatrix} e^{j\chi} & 0 \\ 0 & 1 \end{bmatrix} \boldsymbol{F}, \tag{3.145}$$

and

$$f_0 = \frac{s'(\Delta\phi)^2 s''(0)}{2s''(0)^2 - 2s''(\Delta\phi)^2\cos^2(\chi/2)} \tag{3.146}$$

$$f_1 = \frac{s'(\Delta\phi)^2 s''(\Delta\phi)\cos(\chi/2)}{2s''(0)^2 - 2s''(\Delta\phi)^2\cos^2(\chi/2)}. \tag{3.147}$$

Note that the relative phase ψ disappears in (3.141)-(3.147), i.e., $\boldsymbol{S}_{\boldsymbol{\alpha}}$ is independent of ψ. Since the diagonal elements in (3.141) are zero, the complex FIM [103] for $\boldsymbol{a}$ is $\boldsymbol{S}_{\boldsymbol{a}} = \boldsymbol{\Omega}$ and the CRB for $\boldsymbol{a}$ is obtained as

$$\mathrm{CRB}(\boldsymbol{a}) = \boldsymbol{S}_{\boldsymbol{a}}^{-1} = \boldsymbol{\Omega}^{-1}\,. \tag{3.148}$$

Then the CRB for the polarization vectors $\boldsymbol{s}_1$ and $\boldsymbol{s}_2$ are obtained as follows.

$$\mathrm{CRB}(\boldsymbol{s}_m) = \boldsymbol{D}_m\boldsymbol{\Omega}^{-1}\boldsymbol{D}_m^T \qquad (m=1,2) \tag{3.149}$$

where

$$\boldsymbol{D}_1 = \begin{bmatrix} 1 & 0 & 0 & 0 \\ 0 & 0 & 1 & 0 \end{bmatrix},\ \boldsymbol{D}_2 = \begin{bmatrix} 0 & 1 & 0 & 0 \\ 0 & 0 & 0 & 1 \end{bmatrix} \tag{3.150}$$

In the following analysis, the estimation error of the polarization vectors are decomposed into two components, which are parallel and orthogonal to the polarization vector. The variance of these two components $\sigma^2_{\parallel,m}$, $\sigma^2_{\perp,m}$ are bounded by the following CRBs.

$$\sigma^2_{\parallel,m} \geq \hat{\boldsymbol{s}}_m^H\boldsymbol{D}_m\boldsymbol{\Omega}^{-1}\boldsymbol{D}_m^T\hat{\boldsymbol{s}}_m \tag{3.151}$$

$$\sigma^2_{\perp,m} \geq \mathrm{trace}\left\{\boldsymbol{P}\boldsymbol{D}_m\boldsymbol{\Omega}^{-1}\boldsymbol{D}_m^T\boldsymbol{P}^H\right\} \qquad (m=1,2), \tag{3.152}$$

where

$$\hat{\boldsymbol{s}}_m = \frac{\boldsymbol{s}_m}{\|\boldsymbol{s}_m\|},\ \boldsymbol{P} = \boldsymbol{I} - \hat{\boldsymbol{s}}_m\hat{\boldsymbol{s}}_m^H \tag{3.153}$$

Since the polarization property is represented by the direction of the polarization vector, the orthogonal component of the estimation error expresses the polarization estimation error. On the other hand, the parallel component of the error is only related to the magnitude of the

polarization vector. Therefore, the polarization estimation error is regarded to be small as long as the orthogonal component of the error is small.

Fig. 3.15 shows the polarization vector estimation error normalized by the total power (or span) of the polarization vector $\|\boldsymbol{s}_m\|^2 = 2a^2$, as a function of target separation. Figs. 3.15 (a), (b), (c), and (d) are for different χ values as indicated in the figure. Other parameters in this figure are $N = 50$ and SNR=30dB. The solid blue line and the solid red line show the CRB for the parallel and orthogonal component represented by (3.151) and (3.152), respectively. The results shown in Fig. 3.15 are for target number $m = 1$. Note that the results for $m = 2$ are identical.

As a comparison, the polarization vector estimation error when the two polarization channels are individually processed is shown as dashed lines; the dashed blue line and the dashed red line show the CRB for the parallel and orthogonal component, respectively. When the two polarization channels are individually processed, the variance of the polarization vector estimation error for the m-th target is given by

$$\sigma^2_{\text{single}\parallel,m} \geq \hat{\boldsymbol{s}}_m^H \boldsymbol{D}_m \boldsymbol{\Omega}^{-1}_{\text{single}} \boldsymbol{D}_m^T \hat{\boldsymbol{s}}_m \tag{3.154}$$

$$\sigma^2_{\text{single}\perp,m} \geq \text{trace}\left\{ \boldsymbol{P}\boldsymbol{D}_m \boldsymbol{\Omega}^{-1}_{\text{single}} \boldsymbol{D}_m^T \boldsymbol{P}^H \right\} \qquad (m = 1,2), \tag{3.155}$$

where

$$\boldsymbol{\Omega}_{\text{single}} = \begin{bmatrix} \boldsymbol{H} + \boldsymbol{F}_{\text{single}} & 0 \\ 0 & \boldsymbol{H} + \bar{\boldsymbol{F}}_{\text{single}} \end{bmatrix} \tag{3.156}$$

$$\boldsymbol{F}_{\text{single}} = \frac{s'(\Delta\phi)^2}{s''(0)^2 - s''(\Delta\phi)^2} \begin{bmatrix} s''(0) & s''(\Delta\phi) \\ s''(\Delta\phi) & s''(0) \end{bmatrix} \tag{3.157}$$

When the two polarization channels are individually processed, the distribution of the polarization vector estimation error is isotropic. Therefore, the CRB for parallel and orthogonal components are identical, and in Fig. 3.15, the dashed blue line always coincides with the dashed red line.

From Fig. 3.15 (a)-(d), we see that when the target separation is larger than 1 FRC, the CRB is the same for all cases and almost constant over the separation, and it is given by "$-\text{SNR} - 3$[dB]," i.e., -33dB in this case. Noting that sum of the parallel and the orthogonal components is -30dB, we notice that this result is consistent with the CRB for the amplitude of a single target in a single polarization channel given by "$-$SNR[dB]" [100, Sec.10.8]. When the target separation is sufficiently large, the interference between the two targets is low, so the CRB becomes equivalent to the single target case.

On the other hand, when the separation is below 1 FRC, the estimation error increases as the separation between the targets decreases, due to the increasing influence of the signal interference. The orthogonal component of the CRB for the dual polarization case is significantly lower than that for individually processed case. It is especially low when $\chi = 0$, but it is relatively constant over χ if $\chi \geq \pi/4$. The parallel component of the CRB for the dual polarization case also is lower than that for individually processed case. It depends on χ, e.g., when $\chi = 0$, it coincides with the individually processed case, while when $\chi = \pi$, it almost coincide with orthogonal component of the CRB for the dual polarization case. This result means that when the polarization vectors of the two targets are identical, even when the signal interference is high, only parallel component of the CRB is high and the orthogonal component is kept low. When the polarization vectors of the two targets are orthogonal, the signal interference is minimum, thus both parallel and orthogonal components of the CRB are low.

These results suggest that the super-resolution method based on multi-channel signal

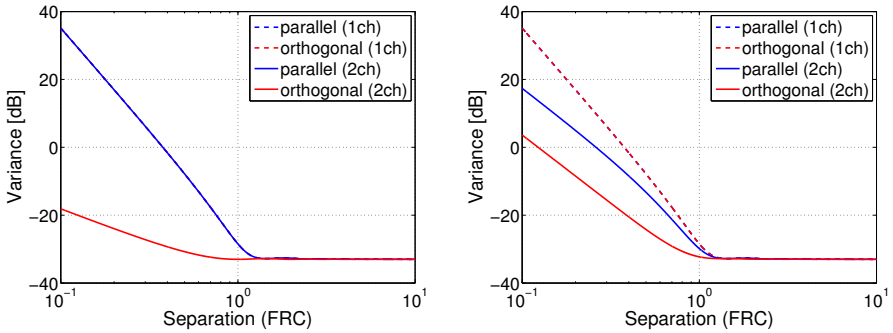

(a) $\chi = 0$ (b) $\chi = \pi/4$

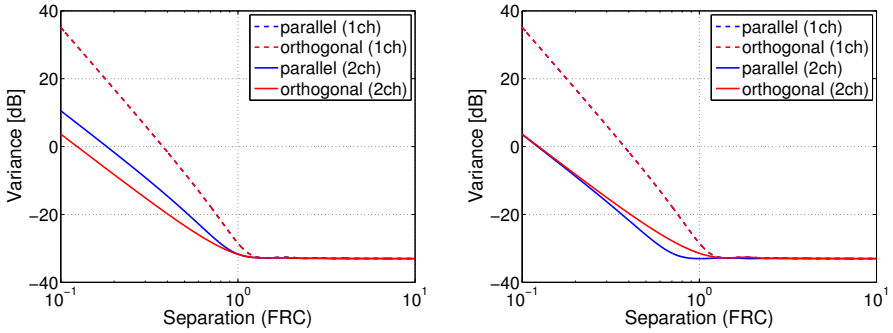

(c) $\chi = \pi/2$ (d) $\chi = \pi$

FIGURE 3.15: The polarization vector estimation error normalized by the total power (or span) of the polarization vector $\|\boldsymbol{s}_m\|^2 = 2a^2$, as a function of target separation. (a), (b), (c), and (d) show the results for $\chi = 0$, $\pi/4$, $\pi/2$ and π, respectively. Other parameters in this figure are $N = 50$ and SNR=30dB. The solid blue line and the solid red line show the CRB for the parallel and orthogonal component. the dashed blue line and the dashed red line show the CRB for the parallel and orthogonal component of the polarization vector estimation error when the two polarization channels are individually processed. Note that the dashed blue line and the dashed red line always coincide with each other.

model such as PBWE has the potential to obtain the better estimation accuracy of the polarization properties of the targets than the methods based on single-channel signal model.

3.4.3 Performance of the PBWE

The performance of the PBWE is evaluated via simulation and compared with the CRBs derived in the previous chapters. The performance of BWE (Bandwidth Extrapolation) algorithm for single channel signal[104] is also evaluated for comparison. In the BWE algorithm, a linear prediction model is fitted to the spatial spectrum of the each polarization channel, and the model is used to extrapolate the bandwidth channel by channel. PBWE utilizes a multi-variate linear prediction model, which we call the polarimetric linear prediction model. The model is fitted to all the polarization channel spectra and the bandwidth of the all the polarization channel is simultaneously extrapolated according to the model [41], [42]. In the simulation, the performance of the two method has been evaluated via Monte Carlo simulation with 1,000 iterations. At each iteration, the relative phase ψ is randomly generated from a uniform distribution over the range of $(-\pi, \pi]$. The data size N is 50 for both cases and the order of the linear prediction filter for BWE and PBWE is set to be 6. Fig. 3.16 and Fig. 3.17 show the rmse (root mean square error) of the target separation estimation, and Fig. 3.18 – Fig. 3.21 show the polarization vector estimation error. In these figures, the performance evaluation results of the BWE and the PBWE are shown along with the CRBs for single and dual polarization cases.

Fig. 3.16 and Fig. 3.17 show the results for SNR=40dB and 30dB, respectively. The sub-figures (a) – (d) of Fig. 3.16 and Fig. 3.17 show the results for $\chi = 0$, $\pi/4$, $\pi/2$ and π, respectively. The dashed green line and the dashed magenta line show the rmse of the target separation estimation by the BWE and the PBWE, respectively. The solid blue line and the solid red line show the square root of the average CRB for the target separation of the single polarization case given by (3.125) and the dual polarization case given by (3.129), respectively. The dotted blue line and the dotted red line show the square root of the hybrid CRB for the dual polarization case given by (A.3) and the single polarization case given by (3.124), respectively.

It can be seen from Fig. 3.16 that the BWE and the PBWE nearly achieve the average CRB for single polarization case and dual polarization case, respectively. Note that the CRB for the dual channel case would not be achieved by applying the BWE individually to each polarization channel; that is, a super resolution algorithm such as the PBWE is required to exploit the polarization information for the resolution enhancement. From the intersection between the dashed green line and the solid black line, the resolution of the BWE is evaluated to be around 0.4∼0.5FRC. Also, from the intersection between the dashed magenta line and the solid black line, the resolution of the PBWE is evaluated to be around 0.4∼0.5FRC for $\chi = 0$, about 0.2FRC for $\chi = \pi/4$ and around 0.1∼0.2FRC for $\chi = \pi/2$ and π.

Note that the target separation estimation error is bounded by the average CRB for both BWE and PBWE. This is reasonable, because in order to accurately extrapolate the spectrum, the target positions, hence the target separation, must be estimated without bias regardless of the relative phase ψ. Since the hybrid CRB is a bound for the estimators that are unbiased only over ensemble of the relative phase ψ, it will not be attained by the BWE nor the PBWE. We would like to point out that the performance of MUSIC and ESPRIT given in [52] also shows the same trend as that of BWE.

From Fig. 3.17, one can see that the target separation estimation error of the BWE is significantly larger than the average CRB for the single polarization case, when SNR=30dB. Likewise, the target separation estimation error of the PBWE is large compared to the average CRB when $\chi = 0$. However, if the polarization properties of the two targets are not identical, PBWE still almost achieves the average CRB.

Fig. 3.18 and Fig. 3.19 respectively show the orthogonal and the parallel components of the polarization vector estimation error for SNR=40dB. Fig. 3.20 and Fig. 3.21 show the same results for SNR=30dB. The sub-figures (a) – (d) of Fig. 3.18 – Fig. 3.21 show

the results for $\chi = 0$, $\pi/4$, $\pi/2$ and π, respectively. The dashed green line and the dashed magenta line show the rmse of the polarization vector estimation by the BWE and the PBWE, respectively. The solid blue line and the solid red line show the square root of the CRB for the polarization vector estimation error for the dual polarization case and the individually processed case.

It can be seen from Fig. 3.18 that the PBWE nearly achieves the average CRB for the orthogonal component of the polarization vector estimation. In Fig. 3.18(a), we see a significant deviation from the CRB when target separation is around 0.3FRC. This indicates that the polarization estimation error of the PBWE could grow large around the SRL; note that from Fig. 3.16 and Table 3.1, we see that the SRL is 0.345FRC when $\chi = 0$. On the other hand, the orthogonal component of the polarization vector estimation error of the BWE is 10 to 20dB larger than the CRB. From Fig. 3.19, the parallel component of the polarization vector estimation error of the BWE and the PBWE are both larger than the CRB by around 10dB. As mentioned before, the parallel component do not affect the estimation accuracy of the polarization property of a target. In addition, the error is below -10dB for well separated targets. From Fig. 3.20 and Fig. 3.21, we can see that the the trend observed in Fig. 3.18 and Fig. 3.19 still holds for SNR=30dB. In Fig. 3.20(b), we see a significant deviation from the CRB when target separation is around 0.4FRC. This is because the resolution limit of the PBWE for $\chi = \pi/4$ and SNR=30dB is around 0.4FRC as we can see from Fig. 3.17. From these results, we can conclude that the polarization estimation accuracy of the PBWE nearly achieves the CRB, and it is higher than that of the BWE. But at the same time, the result does suggest that there is a room for the performance improvement.

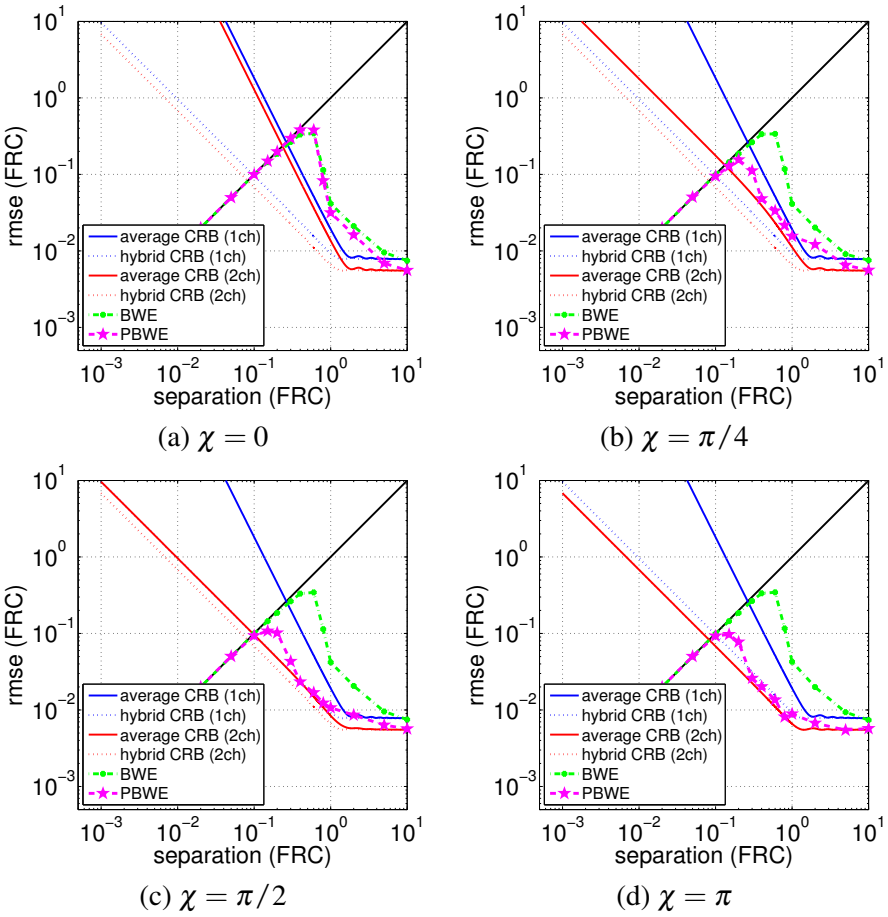

(a) $\chi = 0$ (b) $\chi = \pi/4$

(c) $\chi = \pi/2$ (d) $\chi = \pi$

FIGURE 3.16: The target separation estimation rmse of BWE and PBWE along with the average and the hybrid CRB for the dual and single polarization cases. The solid blue line and the solid red line show the square root of the average CRB for the target separation of the single polarization case and the dual polarization case, respectively. The dotted blue line and the dotted red line show the square root of the hybrid CRB for the dual polarization case and the single polarization case, respectively. The dashed green line and the dashed magenta line show the rmse of the target separation estimation by BWE and PBWE, respectively. ($N = 50$ / SNR=40dB / order of the linear prediction filter for BWE and PBWE = 6)

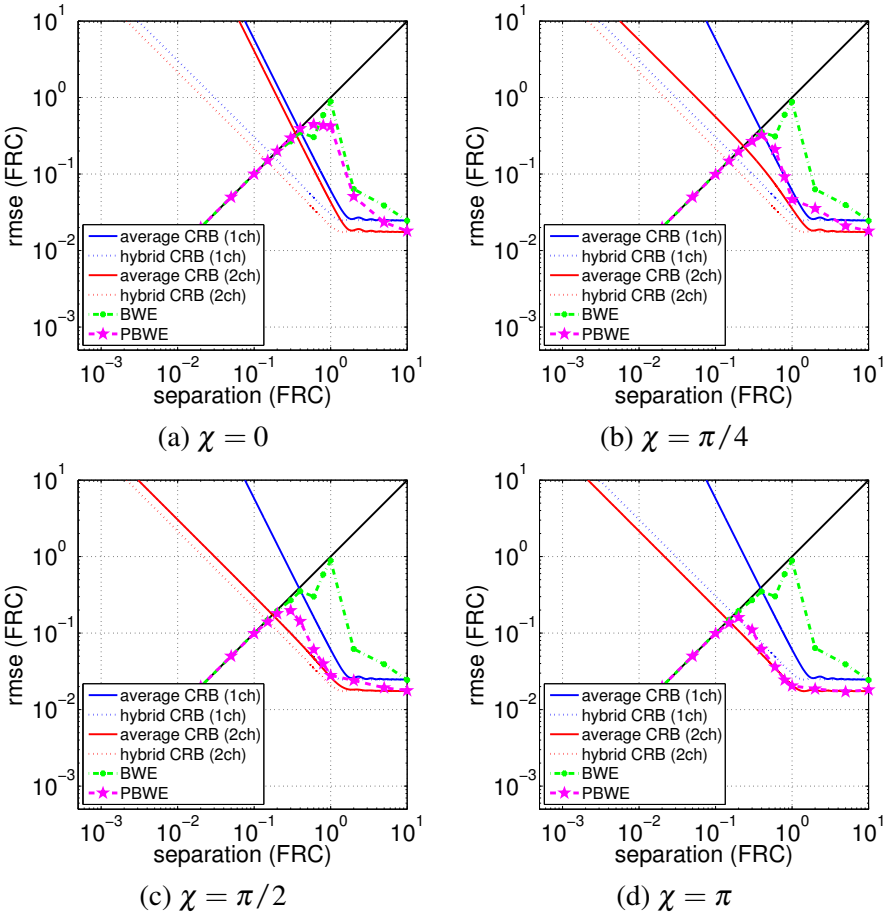

(a) $\chi = 0$ (b) $\chi = \pi/4$

(c) $\chi = \pi/2$ (d) $\chi = \pi$

FIGURE 3.17: The target separation estimation rmse of BWE and PBWE along with the average and the hybrid CRB for the dual and single polarization cases for SNR=30dB. Other parameters are same as Fig. 3.16.

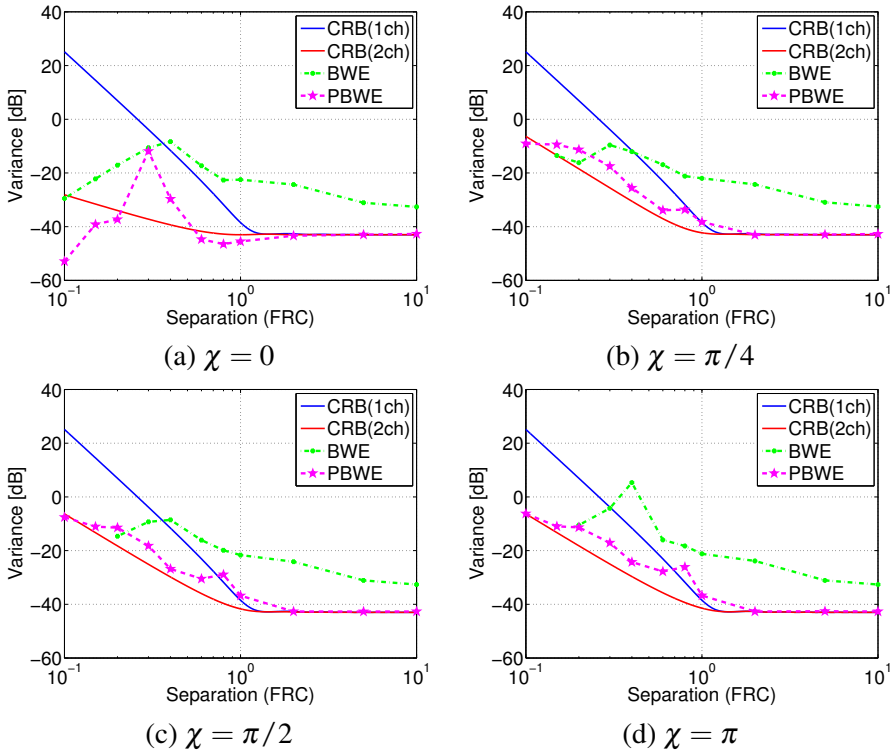

(a) $\chi = 0$ (b) $\chi = \pi/4$

(c) $\chi = \pi/2$ (d) $\chi = \pi$

FIGURE 3.18: The orthogonal components of the polarization vector estimation error for SNR=40dB case. (a) – (d) show the results for $\chi = 0$, $\pi/4$, $\pi/2$ and π, respectively. The solid blue line and the solid red line show the square root of the CRB for the orthogonal component of the polarization vector estimation error for the dual polarization case given by (3.152) and the individually processed case given by (3.155). The dashed green line and the dashed magenta line show the rmse of the polarization vector estimation by the BWE and the PBWE, respectively. ($N = 50$ / SNR=40dB / order of the linear prediction filter for BWE and PBWE = 6)

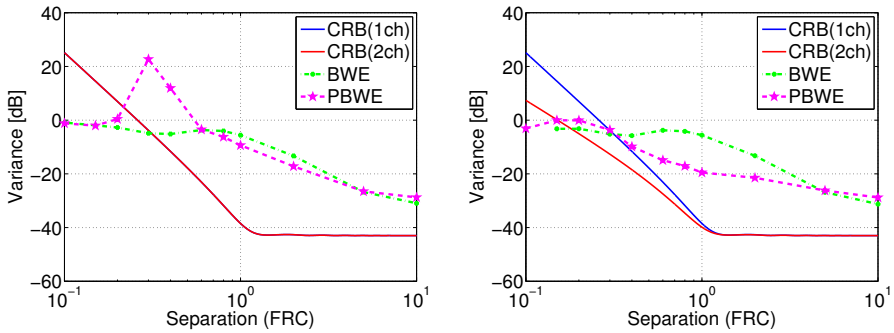

(a) $\chi = 0$ (b) $\chi = \pi/4$

(c) $\chi = \pi/2$ (d) $\chi = \pi$

FIGURE 3.19: The parallel components of the polarization vector estimation error for SNR=40dB case. The solid blue line and the solid red line show the square root of the CRB for the parallel component of the polarization vector estimation error for the dual polarization case given by (3.151) and the individually processed case given by (3.154). In (a), the CRB for single and dual polarization case coincide with each other. ($N = 50$ / SNR=40dB / order of the linear prediction filter for BWE and PBWE = 6)

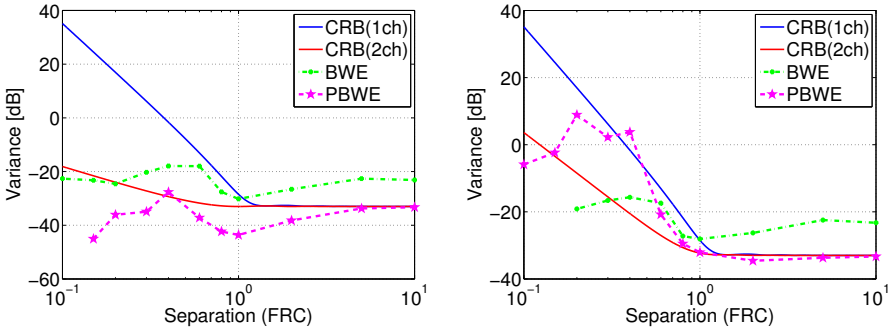

(a) $\chi = 0$ (b) $\chi = \pi/4$

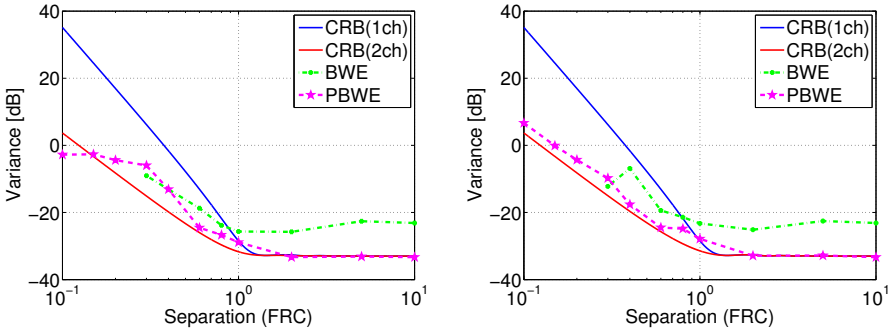

(c) $\chi = \pi/2$ (d) $\chi = \pi$

FIGURE 3.20: The orthogonal components of the polarization vector estimation error for SNR=30dB case. ($N = 50$ / SNR=30dB / order of the linear prediction filter for BWE and PBWE = 6)

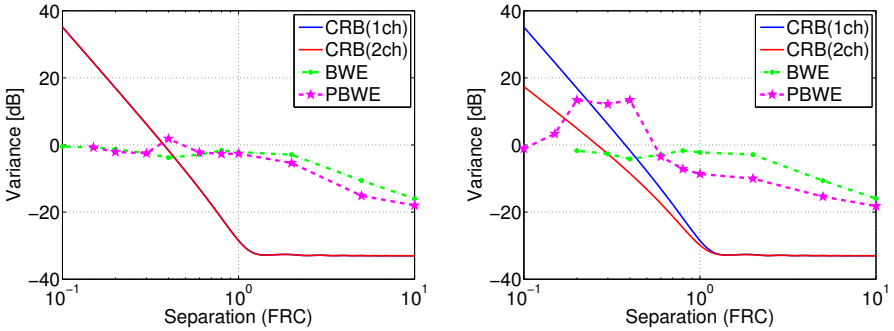

(a) $\chi = 0$ (b) $\chi = \pi/4$

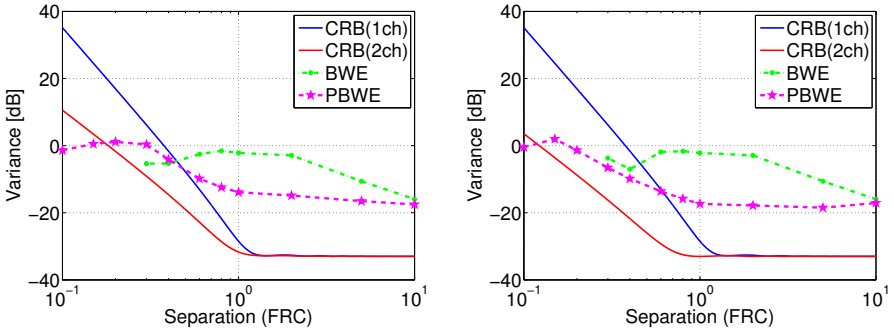

(c) $\chi = \pi/2$ (d) $\chi = \pi$

FIGURE 3.21: The parallel components of the polarization vector estimation error for SNR=30dB case. In (a), the CRB for single and dual polarization case coincide with each other. ($N = 50$ / SNR=30dB / order of the linear prediction filter for BWE and PBWE = 6)

3.5 Conclusion

In this chapter, we introduced a super-resolution algorithm designed for polarimetric SAR, termed Polarimetric Bandwidth Extrapolation (PBWE). Based on bandwidth extrapolation (BWE), which was originally developed for single-polarization SAR, PBWE utilizes full polarization information to enhance resolution while preserving scatterers' polarization properties. We further extended PBWE to a two-dimensional framework (2D-PBWE), enabling simultaneous bandwidth expansion in both range and azimuth directions. To evaluate the effectiveness of 2D-PBWE, we applied it to real PolSAR images with bandwidth restricted to half of its full range. The reconstructed images demonstrated a correlation coefficient of 0.97 with the original, signifying near-perfect restoration of image quality. Given that PolSAR generates four times the data volume of single-polarization SAR, bandwidth constraints in data transmission are a concern. However, our findings show that 2D-PBWE effectively mitigates this issue by reducing bandwidth to half while maintaining near-original resolution through ground processing, significantly alleviating transmission bottlenecks.

Furthermore, we derived and analyzed the Spatial Resolution Limit (SRL) of polarimetric radar, comparing it to that of single-polarization radar. Our results indicate that polarization information plays a critical role in suppressing signal interference effects, leading to a lower SRL for polarimetric radar on average. Specifically, when the polarization properties of two closely located targets are orthogonal, interference is minimized, and the SRL becomes independent of relative phase. At an SNR of 30 dB, dual-polarization radar exhibits up to 2.3 times the resolution improvement over single-polarization radar. Additionally, we derived the Cramér-Rao Bound (CRB) for polarization vector estimation, demonstrating that PBWE substantially improves polarization estimation accuracy beyond conventional methods. Numerical simulations confirmed that PBWE nearly achieves the average CRB for target separation estimation at high SNR (30–40 dB). Moreover, the CRB for dual-channel cases cannot be attained by independently applying BWE to each polarization channel, underscoring the necessity of PBWE for maximizing resolution enhancement.

While PBWE achieves remarkable accuracy in polarization estimation, some discrepancies in target magnitude estimation remain, indicating room for further refinement. The SRL and CRB derived in this study serve as theoretical benchmarks against which real-world performance can be assessed. Future research should explore PBWEs efficacy across diverse target types and further investigate the impact of interference from nearby objects.

Chapter 4

Target Detection and Velocity Estimation Methods for Multi-Channel SAR-GMTI

4.1 Introduction

Recently, SAR-GMTI (Synthetic Aperture Radar -Ground Moving Target Indication) is employed not only by airborne SAR systems, but by spaceborne SAR systems as well, and it is becoming more evident that SAR-GMTI significantly enhances the capability of spaceborne SAR systems to monitor activities in the observed area(e.g. [105]). Meanwhile, the current spaceborne SAR-GMTI systems often suffer from their low performance for detecting slowly moving targets, due to the relatively short baseline for the very high velocity of the satellite. A possible solution for this is to employ multi-channel system with large and preferably non-uniform baselines. In this paper, we propose algorithms for multi-channel SAR-GMTI system to enhance the target detection performance as well as target velocity estimation.

SAR-GMTI algorithms can roughly be categorized into two classes. The first class of algorithms work on the processed SAR image (e.g. [106]), and the second class of algorithms work on the raw data (e.g. [107]–[110]). We propose SAR-GMTI algorithms for multi-channel SAR systems that work on the processed images, which we call Multi-channel DPCA (Displaced Phase Center Antenna), Multi-channel ATI (Along Track Interferometry) and Multi-channel DPCA-ATI[45], [46][1]. Multi-channel DPCA is a deterministic algorithm which suppresses the clutter and azimuth ambiguity at the same time and achieves high target detection performance. The algorithm is constructed based on the observation that the relative phase of the azimuth ambiguity between the multiple receive channels is fully determined by the observation geometry and sensor parameters. Therefore, a notch type filter that suppresses the ambiguity, as well as the clutter, can be prepared solely from the observation geometry and sensor parameter information, and it is feasible because the SAR observation geometry is usually well under control. Most adaptive algorithms such as STAP (Space Time Adaptive Processing) [107], assume that the clutter covariance is uniform around the sample of interest and estimate the clutter covariance from the adjacent samples; however, this approach often suffers from strong azimuth ambiguities which tend to behave as isolated (and somewhat blurred) targets. On the other hand, the proposed Multi-channel DPCA successfully suppresses this type of azimuth ambiguity, since it does not require the uniform clutter covariance assumption. Multi-channel ATI is the set of ATI images of all the pairs of multi-channel SAR, and the target radial velocity is estimated by applying the matched filter bank to Multi-channel ATI output. Multi-channel DPCA-ATI is a combination of Multi-channel

[1]Similar ideas have been proposed [111]–[114], but to the best of authors' knowledge, exact same ideas do not seem to have appeared in the literatures. Recently proposed EDPCA (Extended DPCA) includes refocusing of moving target and is quite different from the proposed Multi-channel DPCA[110].

DPCA and Multi-channel ATI. The clutter suppressed signal is provided by Multi-channel DPCA as the input for the Multi-channel ATI. Both Multi-channel ATI and Multi-channel DPCA-ATI reduce the target radial velocity ambiguity by exploiting the multiple receive channel signals. Multi-channel DPCA-ATI further achieves robust performance to clutter influence by suppressing the clutter and the azimuth ambiguity in advance.

This chapter is organized as follows. In Section 4.2, the geometry and the signal model is provided, and the proposed algorithms are presented in Section 4.3. Section 4.4 presents the effects of the proposed algorithms through airborne Ku-band three-channel SAR experiments. Section 4.5 provides statistical performance analysis of the proposed algorithms to discuss the potential performance on the spaceborne system. A straightforward method for determining the optimal baselines for non-uniformly spaced multi-channel system that minimize the moving target signal loss is also provided in this section.

4.2 Geometry and signal model

We consider a multi-channel SAR-GMTI system with N_a antennas located along the flight direction. Fig. 4.1 illustrates the observation geometry of the system with $N_\mathrm{a} = 3$. The platform moves with constant velocity V_r along x-axis at altitude h above ground. The moving target is assumed to be on the ground, and the slant plane is defined as the plane containing the flight path and the target position at the time when the target is at the beam center. The y-axis is defined as the cross-track direction in the slant plane. The radar pulses are assumed to be transmitted from the first antenna A_1 and received by all the antennas A_q ($q = 1, 2, \cdots, N_\mathrm{a}$), in which case, the location of the phase center of the q-th channel can be approximated by the midpoint P_q of the transmit antenna A_1 and the receive antenna A_q. The distance from the phase center P_p to P_q along x-axis, which we call effective baseline, is denoted by d_{pq}. Note that in this paper, the effective baseline d_{pq} is a signed value with the sign representing the direction along x-axis.

In Fig. 4.1, (x_0, y_0) represents the position of the moving target at $\eta = 0$, where η is the azimuth time (slow time) referenced to the time when the target is at the beam center. The origin O is set at the position of the phase center P_1 at $\eta = 0$. Then the positions of the phase centers P_q ($q = 1, 2, \cdots, N_\mathrm{a}$) at azimuth time η are expressed as

$$(V_r\eta + d_{1q},\ 0), \tag{4.1}$$

where we define that $d_{11} = 0$. The position of the moving target at azimuth time η is expressed as

$$(x_0 + v_{x0}\eta + g_x(\eta),\ y_0 + v_{y0}\eta + g_y(\eta)), \tag{4.2}$$

where, $\bar{v}_0 = [v_{x0}\ v_{y0}]^T$ is the target velocity at $\eta = 0$ and $g_x(\eta)$ and $g_y(\eta)$ are higher order terms and the superscript of T represents the transpose. From (4.1) and (4.2), the distance

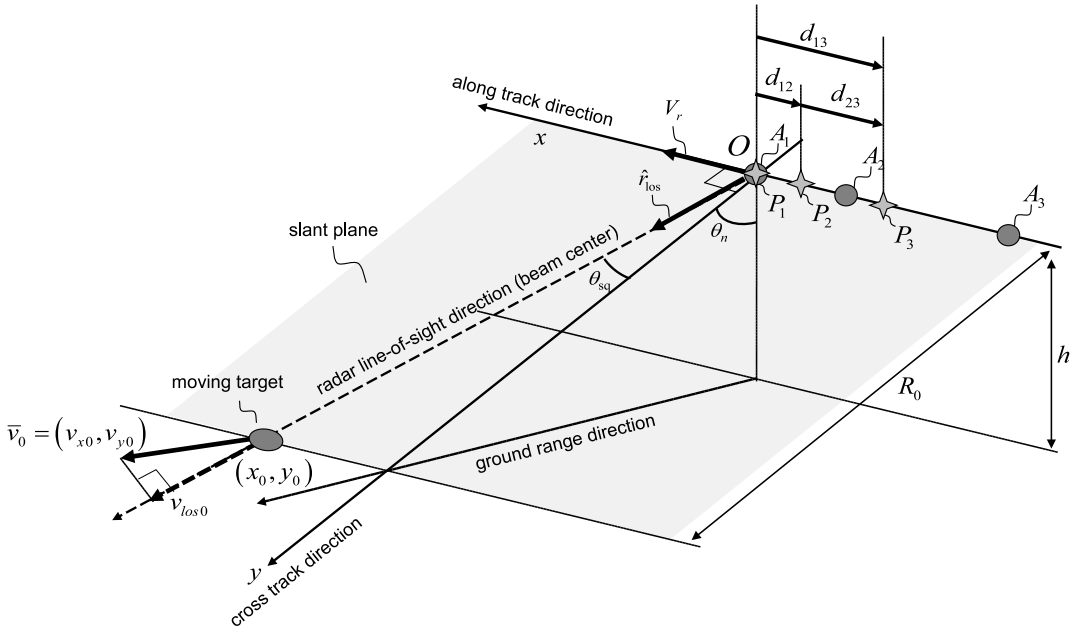

FIGURE 4.1: The observation geometry of the multi-channel SAR system ($Na = 3$).

between the phase center P_q and the moving target at the azimuth time η is given by

$$R_q(\eta) = \sqrt{\begin{array}{c}\{x_0 + v_{x0}\eta + g_x(\eta) - V_r\eta - d_{1q}\}^2 \\ + \{y_0 + v_{y0}\eta + g_y(\eta)\}^2\end{array}}, \quad (q = 1,2,\cdots,N_{\mathrm{a}}). \tag{4.3}$$

In the algorithm proposed in this paper, the SAR images observed by the N_{a} channels are first registered to the first channel (reference channel) and the channel imbalances are compensated. If the phase centers are not exactly aligned on the track, e.g. due to the attitude of the platform, topographic phase correction is required. In most cases, the cross track baseline can be kept relatively small; therefore, the influence of the topographic phase is limited, and it can readily be removed by an algorithm such as the one we previously presented in [115]. The registered and balanced multi-channel SAR images are modeled as follows:

$$\begin{aligned} \boldsymbol{z}_{m,n} &\equiv [z_1(m,n),\cdots z_{N_{\mathrm{a}}}(m,n)]^T \\ &= \boldsymbol{s}_{m,n} + \boldsymbol{u}_{m,n} + \boldsymbol{w}_{m,n}, \end{aligned} \tag{4.4}$$

where, $z_q(m,n)$ is the pixel value at pixel number (m,n) of the SAR image observed by the q-th channel, $\boldsymbol{s}_{m,n}$, $\boldsymbol{u}_{m,n}$, $\boldsymbol{w}_{m,n}$ are N_{a} dimensional vectors which represent the moving target signal, clutter and white Gaussian noise, respectively.

The signal phase of the moving target in the q-th channel of the registered SAR images is

$$\phi_q = \frac{4\pi}{\lambda} R_q(\eta_{1q}) + \phi_{\mathrm{tgt}}, \quad \eta_{1q} = -\frac{d_{1q}}{V_r}, \tag{4.5}$$

where η_{1q} is delay time of the q-th channel to the first channel (also called as the inter-channel travel time[116])[2], ϕ_{tgt} represents the phase shift upon reflection, which is assumed to be constant over the channels. Then the phase difference between the q-th channel and the first channel is given by

$$\begin{aligned} \Delta\phi_{1q} &= \phi_q - \phi_1 \\ &\simeq \left.\frac{d\phi_q}{d\eta_{1q}}\right|_{\eta_{1q}=0} \cdot \eta_{1q} \quad (\eta_{1q} \ll 1) \\ &= \frac{4\pi}{\lambda} v_{\mathrm{los0}} \eta_{1q}, \end{aligned} \tag{4.6}$$

where $v_{\mathrm{los0}} = \bar{v}_0 \cdot \hat{r}_{\mathrm{los}}$ is the target velocity in the radar line-of-sight direction $\hat{r}_{\mathrm{los}}$. In this paper, we call v_{los0} the target radial velocity. Note that the phase difference $\Delta\phi_{1q}$ corresponds to the displacement of the moving target in radar line-of-sight direction between the time of acquisition of the q-th channel and the first channel. Also note that even though the moving target image is, in general, blurred in the SAR image due to the motion[117], the phase difference $\Delta\phi_q$ is independent of the blur as long as the effective baseline is sufficiently small so that $\eta_{1q} \ll 1$. From (4.5) and (4.6), the moving target signal in the q-th channel $s_q(m,n)$ can be modeled as

$$s_q(m,n;v_{\mathrm{los0}}) = Ae^{-j\Delta\phi_{1q}} = Ae^{-j\frac{4\pi}{\lambda}v_{\mathrm{los0}}\eta_{1q}} \tag{4.7}$$

where A is the complex amplitude with phase $\angle A = \phi_1$. The amplitude A can be regarded to be constant over the channels.

[2]Note that the positive delay η_{1q} corresponds to the negative d_{1q} and that $\eta_{11} = 0$ for the first channel.

The clutter is assumed to be perfectly stable over the observation time. Then, if the DPCA condition is satisfied, i.e., no resampling is required upon registration, the clutter including the azimuth ambiguity component is identical over the channels[116], and the clutter can be modeled as $\boldsymbol{u}_{m,n} = c(m,n)\mathbf{1}$, where $\mathbf{1}$ is an N_a dimensional vector whose elements are all 1 and $c(m,n)$ is the clutter amplitude. If the DPCA condition is not satisfied, resampling introduces phase shift to azimuth ambiguity component. The clutter including the azimuth ambiguity component can be modeled as (the derivation is provided in Appendix B)

$$\begin{aligned} \boldsymbol{u}_{m,n} &= \boldsymbol{D}\boldsymbol{c}_{m,n} \\ \boldsymbol{D} &= \begin{bmatrix} 1 & \cdots & 1 & \cdots & 1 \\ e^{-j2\pi K_\mathrm{a} F_\mathrm{a} \eta_{12}} & \cdots & 1 & \cdots & e^{j2\pi K_\mathrm{a} F_\mathrm{a} \eta_{12}} \\ \vdots & \vdots & \vdots & \vdots & \vdots \\ e^{-j2\pi K_\mathrm{a} F_\mathrm{a} \eta_{1N_\mathrm{a}}} & \cdots & 1 & \cdots & e^{j2\pi K_\mathrm{a} F_\mathrm{a} \eta_{1N_\mathrm{a}}} \end{bmatrix} \\ \boldsymbol{c}_{m,n} &= \left[c^{\langle -K_\mathrm{a} \rangle}(m,n), \cdots, c^{\langle 0 \rangle}(m,n), \cdots, c^{\langle K_\mathrm{a} \rangle}(m,n) \right]^T \end{aligned} \tag{4.8}$$

where F_a is the pulse repetition frequency (PRF), K_a is the maximum order of the azimuth ambiguity and $c^{\langle k \rangle}(m,n)$ represents the azimuth ambiguity of k-th order in the first (reference) channel. $\boldsymbol{D}$ is $N_\mathrm{a} \times K$ matrix ($K = 2K_\mathrm{a} + 1$) which represents the signal space for the clutter and the azimuth ambiguity.

4.3 Algorithm

4.3.1 Multi-channel DPCA for clutter suppression

Substituting the clutter model given in (4.8) into (4.4), the signal model of the multi-channel SAR images is expressed by

$$\boldsymbol{z} = \boldsymbol{s} + \boldsymbol{D}\boldsymbol{c} + \boldsymbol{w}. \tag{4.9}$$

If the order of the azimuth ambiguity is sufficiently small to satisfy $K < N_{\mathrm{a}}$, the clutter and the azimuth ambiguity component can be suppressed by the orthogonal projection given by[103]

$$\check{\boldsymbol{z}} = \left\{ \boldsymbol{I} - \boldsymbol{D}\left(\boldsymbol{D}^H\boldsymbol{D}\right)^{-1}\boldsymbol{D}^H \right\}\boldsymbol{z} = \boldsymbol{P}\boldsymbol{z}, \quad \check{\boldsymbol{z}} = \left[\check{z}_1, \cdots, \check{z}_{N_{\mathrm{a}}}\right]^T, \tag{4.10}$$

where $\boldsymbol{I}$ is the $N_{\mathrm{a}} \times N_{\mathrm{a}}$ identity matrix, $\boldsymbol{P}$ is an orthogonal projection matrix, the superscript of H represents the conjugate transpose, and $\check{\boldsymbol{z}}$ is an N_{a}-dimensional signal after clutter suppression. The detection test statistic is given by $\|\check{\boldsymbol{z}}\|^2$, which is the power sum of the clutter suppressed signals $\check{z}_q$ ($q = 1, \cdots, N_{\mathrm{a}}$). In the case of the dual channel system operated under DPCA condition ($N_{\mathrm{a}} = 2$ and $\boldsymbol{D} = \boldsymbol{1}$), the test statistic becomes $\|\check{\boldsymbol{z}}\|^2 = |z_1 - z_2|^2/2$, which is essentially the conventional DPCA power image. Namely, the algorithm can be regarded as a natural extension of the conventional DPCA to the multi-channel system, so we call the algorithm Multi-channel DPCA.

In practice, the major cause of the azimuth ambiguity is the aliased mainlobe clutter as shown in Fig.4.2, where $U_{\mathrm{org}}(f_\eta)$ is the Doppler spectrum of the clutter and f_η represents the Doppler frequency[3]. In this case, the azimuth ambiguity can effectively be suppressed by dividing the Doppler spectrum into half and apply different orthogonal projection matrix for each half, i.e., the orthogonal projection matrices for the lower and the upper half are constructed to suppress the ambiguity of order $k = -1$ and $k = 1$, respectively. For example, in case of a three-channel system, the orthogonal projection matrices for the lower and the

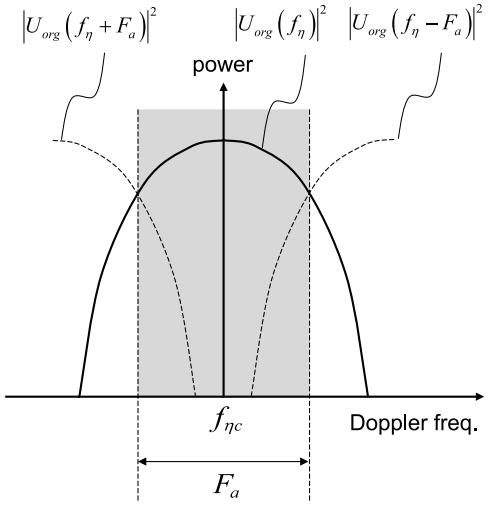

FIGURE 4.2: The Doppler power spectrum.

[3]See Appendix B for more detailed definition of $U_{\mathrm{org}}(f_\eta)$

upper half can be obtained by setting $\boldsymbol{D}$ with $\boldsymbol{D}_-$ and $\boldsymbol{D}_+$, respectively, which are given by

$$\boldsymbol{D}_- = \begin{bmatrix} 1 & 1 \\ 1 & e^{-j2\pi F_{\mathrm{a}}\eta_{12}} \\ 1 & e^{-j2\pi F_{\mathrm{a}}\eta_{13}} \end{bmatrix}, \quad \boldsymbol{D}_+ = \begin{bmatrix} 1 & 1 \\ 1 & e^{j2\pi F_{\mathrm{a}}\eta_{12}} \\ 1 & e^{j2\pi F_{\mathrm{a}}\eta_{13}} \end{bmatrix}. \tag{4.11}$$

After obtaining the clutter suppressed images for both upper and lower band images, they can either be coherently or incoherently combined.

Note that the projection matrix $\boldsymbol{P}$ is determinstic and uniform over the entire image, and it is determined solely by the observation geometry and sensor parameter information. Unlike most adaptive algorithms such as STAP, Multi-channel DPCA does not assume the clutter covariance to be locally uniform; therefore, it successfully suppresses strong azimuth ambiguities which tend to behave as isolated (and somewhat blurred) targets.

4.3.2 Multi-channel ATI, Multi-channel DPCA-ATI

The Multi-channel ATI outputs a $C(N_{\mathrm{a}},2)$ dimensional vector $\boldsymbol{\xi}$ which consists of the ATI images of all the pairs of the multi-channel SAR images, and the ν-th element of which is given by

$$\begin{aligned} [\boldsymbol{\xi}]_\nu &= \sum_{m,n\in\Omega_{N_{\mathrm{L}}}} z_p(m,n) z_q^*(m,n) \,, \\ & p = 1,\cdots,N_{\mathrm{a}}-1 \,, \\ & q = p+1,\cdots,N_{\mathrm{a}} \,, \\ & \nu = q + \sum_{r=0}^{p-1} r\,(N_{\mathrm{a}}-r) \end{aligned} \tag{4.12}$$

where $\Omega_{N_{\mathrm{L}}}$ denotes the group of N_{L} neighboring pixels, i.e., N_{L} is the multilook number. Using the output $\boldsymbol{\xi}$, the target radial velocity v_{los0} is estimated as follows:

$$\begin{aligned} \tilde{v}_{\mathrm{los0}} &= \underset{v_{\mathrm{los0}}}{\operatorname{argmax}} \left\{ P_{\mathrm{mati}}\left(v_{\mathrm{los0}}\right) \right\} \,, \\ P_{\mathrm{mati}}\left(v_{\mathrm{los0}}\right) &= \left| \boldsymbol{h}_{\mathrm{mati}}^H\left(v_{\mathrm{los0}}\right) \boldsymbol{\xi} \right|^2 . \end{aligned} \tag{4.13}$$

In (4.13), $\boldsymbol{h}_{\mathrm{mati}}\left(v_{\mathrm{los0}}\right)$ is a matched filter and the k-th element of which is given by:

$$\begin{aligned} \left[\boldsymbol{h}_{\mathrm{mati}}\left(v_{\mathrm{los0}}\right)\right]_\nu &= s_p\left(v_{\mathrm{los0}}\right) s_q^*\left(v_{\mathrm{los0}}\right) \,, \\ & p = 1,\cdots,N_{\mathrm{a}}-1 \,, \\ & q = p+1,\cdots,N_{\mathrm{a}} \,, \\ & \nu = q + \sum_{r=0}^{p-1} r\,(N_{\mathrm{a}}-r) \end{aligned} \tag{4.14}$$

where $s_q\left(v_{\mathrm{los0}}\right)$ is given in (4.7).

For the Multi-channel DPCA-ATI, the Multi-channel DPCA outputs, instead of the original multi-channel SAR images, are put into the Multi-channel ATI, and the matched filter

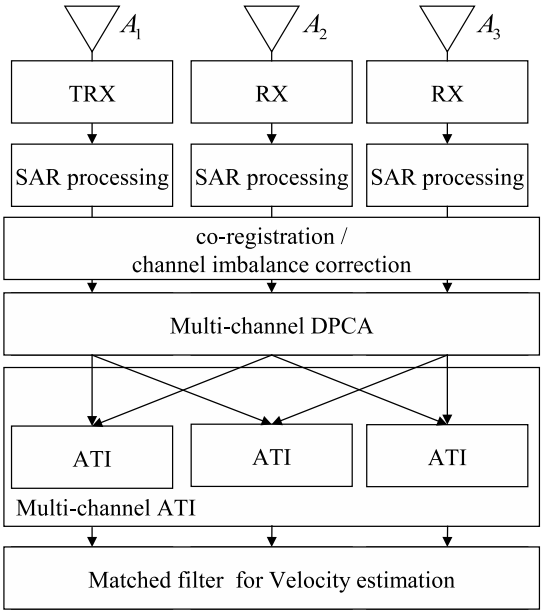

FIGURE 4.3: Multi-channel DPCA-ATI method.

for this case is given by:

$$\begin{aligned}
\left[\boldsymbol{h}_{\text{mdpcaati}}\left(v_{\text{los0}}\right)\right]_v &= \breve{s}_p\left(v_{\text{los0}}\right)\breve{s}_q^*\left(v_{\text{los0}}\right)\ , \qquad (4.15)\\
&\quad p = 1,\cdots,N_{\text{a}}-1\ ,\\
&\quad q = p+1,\cdots,N_{\text{a}}\ ,\\
&\quad k = q+\sum_{r=0}^{p-1} r\left(N_{\text{a}}-r\right)\\
\breve{\boldsymbol{s}}\left(v_{\text{los0}}\right) &= \left\{\boldsymbol{I}-\boldsymbol{D}\left(\boldsymbol{D}^H\boldsymbol{D}\right)^{-1}\boldsymbol{D}^H\right\}\boldsymbol{s}\left(v_{\text{los0}}\right)\ , \qquad (4.16)\\
\breve{\boldsymbol{s}}\left(v_{\text{los0}}\right) &= \left[\breve{s}_1\left(v_{\text{los0}}\right)\cdots\breve{s}_{N_{\text{a}}}\left(v_{\text{los0}}\right)\right]^T \qquad (4.17)
\end{aligned}$$

Fig. 4.3 summarizes the processing steps of the Multi-channel DPCA-ATI method. Similar idea has been presented in [112], where they apply conventional DPCA to the pairs of two images out of the multi-channel image and then apply conventional ATI to the pairs of the DPCA outputs. In their approach, the influence of the clutter can be suppressed by applying DPCA prior to ATI process; however, the azimuth ambiguity components still remain in the DPCA outputs. The Multi-channel DPCA-ATI method suppresses the influence of the azimuth ambiguity as well as clutter.

Once the target radial velocity v_{los0} is estimated, the azimuthal displacement Δx is calculated as[116]

$$\Delta x = -R_0\frac{v_{\text{los0}}}{V_r}, \qquad (4.18)$$

where R_0 is the slant range of the target.

4.3.3 Along track velocity estimation

After a moving target is detected and its radial velocities and the azimuth positions are estimated, the along track velocity is estimated from the azimuth line signal which contains the moving target signal. Fig. 4.4 shows the block diagram of the algorithm. If we let the range

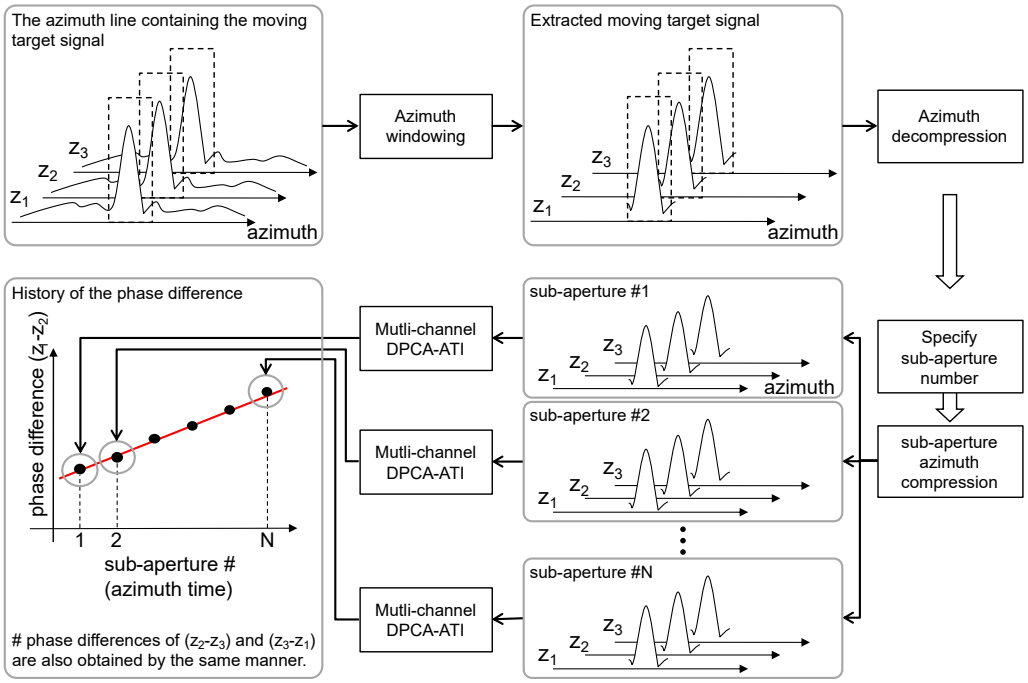

FIGURE 4.4: Along track velocity estimation method.

cell number of the moving target signal be m_t, the azimuth line signal is

$$z_q(m_t,n), \qquad q = 1,,N_a; \quad n = 1,,N. \tag{4.19}$$

First, azimuth window is applied to the azimuth line signal to extract the target signal. Since the moving target signal is blurred in many cases, the window is set sufficiently large to capture most of the signal energy. Then the signal is decompressed by applying the conjugate of the azimuth reference function. The decompressed signal can be expressed as follows:

$$s_q(\eta) = a_q \exp\left\{-j\frac{4\pi}{\lambda}R_q(\eta)\right\}, \quad q = 1,,N_a, \tag{4.20}$$

where η is the parameter that defines the azimuth position of the phase center P_q in slow time domain. The $R_q(\eta)$ is the distance between the phase center P_q at the azimuth position of $V_r\eta$ and the moving target. For the sake of the following development of formula, the signal is expressed as the continuous signal in (4.20), although it is a discrete signal sampled at the rate of PRF (Pulse Repetition Frequency). The moving target range history $R_q(\eta)$is given as follows:

$$R_q(\eta) = \sqrt{(y_0 + v_y 0(\eta + \eta_1 q))^2 + (x_0 + v_x 0(\eta + \eta_1 q) - V_r\eta)^2} \tag{4.21}$$

While the phase difference of the azimuth decompressed signals of the p-th and q-th channel is obtained by

$$\phi_{pq}(\eta) = \angle\{s_p^* \cdot s_q\} = \frac{4\pi}{\lambda}\{R_q(\eta) - R_p(\eta)\} \tag{4.22}$$

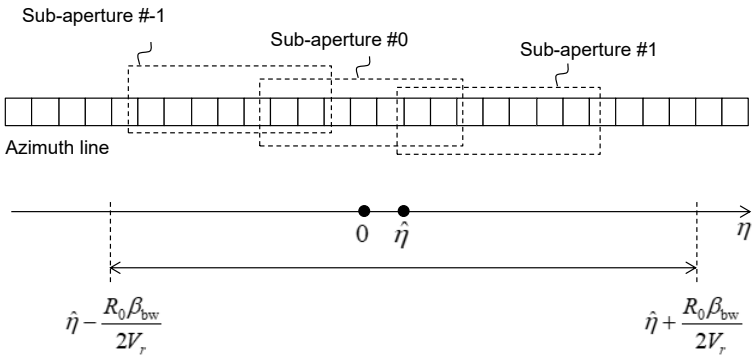

FIGURE 4.5: Sub-aperture setting.

From (4.21) and (4.22), and assuming $|v_{x0}| \ll |V_r|$, the rate of the phase difference at $\eta = 0$ can be expressed as follows:

$$\dot{}_{pq}(0) = \frac{4\pi}{\lambda}\left\{\dot{R}_q(\eta) - \dot{R}_p(\eta)\right\} \tag{4.23}$$

$$\simeq \frac{4\pi}{\lambda}\cdot\frac{\eta_{pq}}{y_0}\left\{v_{x0}\left(v_{x0}-V_r\right)+v_{y0}^2\right\} \tag{4.24}$$

Solving (4.23) for v_{x0}, the target along track velocity is obtained as follows:

$$v_{x0} \simeq \frac{1}{2}\left\{V_r - \sqrt{V_r^2 - 4v_{y0}^2 + \frac{\lambda}{\pi}\cdot\left(\frac{R_p(0)\dot{\phi}_{pq}(0)}{\eta_{pq}}\right)}\right\} \tag{4.25}$$

If the phase difference is evaluated directly from the azimuth line signal as in (4.23), residual clutter and noise could affect the accuracy of the calculated phase difference. In order to improve the SNR and SCR before calculating the phase difference, sub-aperture processing is applied to the azimuth decomposed signal as shown in Fig. 4.5. Then the phase difference is obtained at the peak of the target signal. In addition, DPCA can be applied to each sub-aperture image to further suppress the clutter before obtaining the phase difference as in (4.22). In that case, (4.25) has to be slightly modified so that the phase difference of the DPCA images are utilized to estimate the along track velocity.

4.3.4 Summary of the algorithm

In summary, Fig.4.6 shows the block diagram of the full process. After co-registered and balanced multichannel SAR images are generated, multi-channel DPCA is applied to the images to detect the moving target. For each detected target, the radial velocity is estimated using multichannel DPCA-ATI, and the azimuth position of the moving target is estimated based on the estimated radial velocity. Finally, along track velocity of the moving target is estimated from the azimuth line signal which contains the moving target signal.

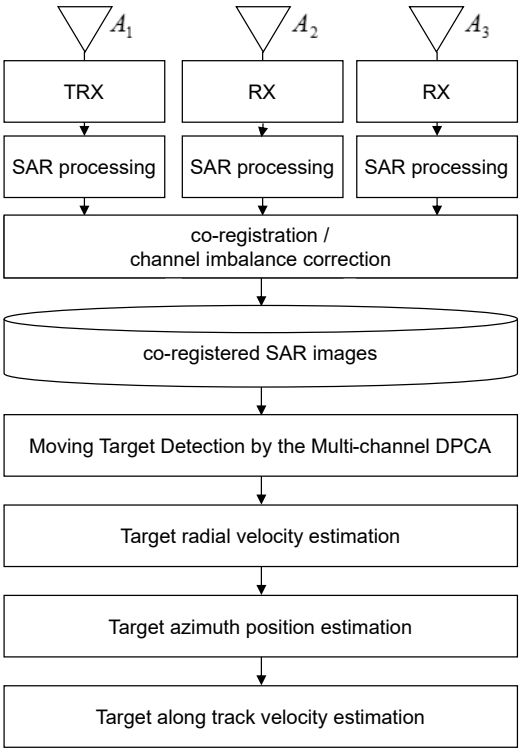

FIGURE 4.6: Full process of the moving target detection and velocity estimation method.

4.4 Experimental results

4.4.1 Experimental setup and parameters

In July 2011, we have conducted a SAR-GMTI experiment using an airborne Ku-band three-channel SAR system shown in Fig. 4.7. Table 4.1 shows the specifications of the system and the acquisition parameters. Three antennas A_1, A_2 and A_3 are connected to receivers, and the rearmost antenna (the antenna A_3 at the far right in Fig. 4.7) is also connected to a transmitter via a circulator. The physical baselines between the apertures are 0.622m, 0.330m and 0.952m corresponding to the effective baselines of $d_{12} = 0.311$m, $d_{23} = 0.165$m and $d_{13} = 0.476$m, respectively. The relatively large baselines enable the detection of slowly moving target, and the non-uniform spacing contributes to the reduction of blind velocities. The PRF has been set rather low ($F_a = 2,500$Hz) to see the influence of the azimuth ambiguity.

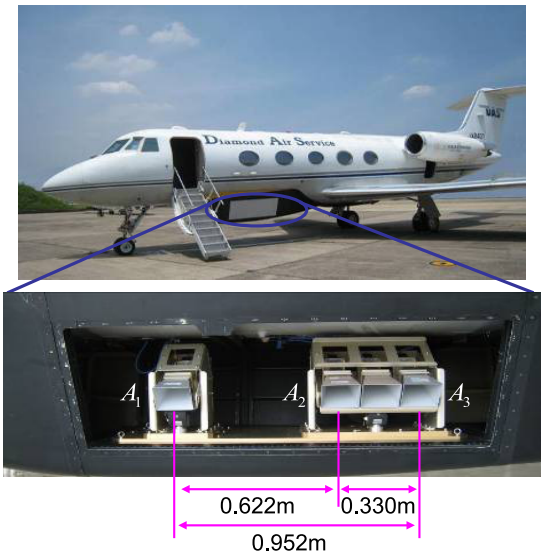

FIGURE 4.7: Airborne Ku-band SAR system. Three antennas are connected to receivers, and the rearmost antenna (the antenna at the far right in the picture) is used for transmitting. The physical baselines between the apertures are 0.622m, 0.330m and 0.952m corresponding to the effective baselines of $d_{12} = 0.311$m, $d_{23} = 0.165$m and $d_{13} = 0.476$m, respectively.

TABLE 4.1: Specifications of the airborne Ku-band SAR system

Parameters	Value
Center frequency	16.45GHz
Transmitted signal bandwidth	250MHz
Peak transmitted power	300W
Pulse Repetition Frequency	2500Hz
Polarization	VV
Platform velocity	98.98 m/s
Effective baseline	0.311, 0.165m, 0.476m
Off-nadir angle	60deg
SAR mode	Strip map
Swath width	$\sim$ 3km
Platform	Gulfstream II

(a) Motorcycle (b) Van

FIGURE 4.8: The vehicles used for the experiment. (a) A motorcycle with two corner reflectors attached on the front and the rear part. (b) A middle-sized van.

In this experiment, two vehicles equipped with GPS data logger, shown in Fig. 4.8, drove along frontage roads running parallel to the street running across the flight direction. Besides the controlled vehicles, several vehicles were found on the street at the time of observation.

4.4.2 The clutter and azimuth ambiguity suppression results of Multi-channel DPCA

Fig. 4.9 shows the co-registered and balanced SAR images of the area containing the controlled vehicles. From Fig. 4.9, one can observe that the three images are visually quite the same. Also note that the azimuth ambiguity is unrecognizable in these images.

Fig. 4.10 shows the Multi-channel DPCA output power images $\|\check{\boldsymbol{z}}\|$ of the corresponding area. Fig. 4.10(a), (b) and (c) show the output images of Multi-channel DPCA with $\boldsymbol{D} = \boldsymbol{1}$ using full, lower half and upper half Doppler bands, respectively. The clutter is well suppressed in these images; however, significant amount of azimuth ambiguity is observed besides the moving target signal. Note that the azimuth ambiguity patterns observed in (b) and (c) are different, and the azimuth ambiguity pattern in (a) is the superposition of the two patterns. Fig. 4.10(d), (e) and (f) show the output images of Multi-channel DPCA with ambiguity suppression. For (e) and (f), $\boldsymbol{D} = \boldsymbol{D}_-$ and $\boldsymbol{D}_+$ in (4.11) are employed, respectively. For (d), $\boldsymbol{D} = \boldsymbol{D}_-$ and $\boldsymbol{D}_+$ are employed for lower and upper Doppler bands, respectively, and the clutter (as well as ambiguity) suppressed Doppler bands are coherently combined to obtain the final image. Comparing (d), (e) and (f) with (a), (b) and (c), respectively, one can observe that the azimuth ambiguity is well suppressed. Quantitative analysis on azimuth ambiguity suppression is given in Fig. 4.11. Let the power images in Fig. 4.10 (a) and (d) be $\|\check{\boldsymbol{z}}\|_1$ and $\|\check{\boldsymbol{z}}\|_2$, respectively, then Fig. 4.11 (a) shows the ratio of the two images, $\|\check{\boldsymbol{z}}\|_1 / \|\check{\boldsymbol{z}}\|_2$. Fig. 4.11 (b) shows the histogram of the ratio. From Fig. 4.11, more than 20dB suppression is observed for very strong azimuth ambiguity.

A magnified small area containing the controlled moving target (the van) signal is shown in Figs. 4.12, 4.13. Comparing Fig. 4.12 and Fig. 4.13, one can see that the background clutter is suppressed on the order of 15–20dB, and the moving target signal at the center of the scene can readily be identified in the Multi-channel DPCA output. In addition, we find that the azimuth ambiguity is more suppressed in Fig. 4.13(d), (e) and (f) than in Fig. 4.13(a), (b) and (c). The ratio of the power images in Fig. 4.13(a) and (d) is shown in Fig. 4.14(a) and (b) in the form of an image and a histogram, respectively. From Fig. 4.14, the azimuth ambiguity surrounding the target signal is suppressed up to on the order of 10dB.

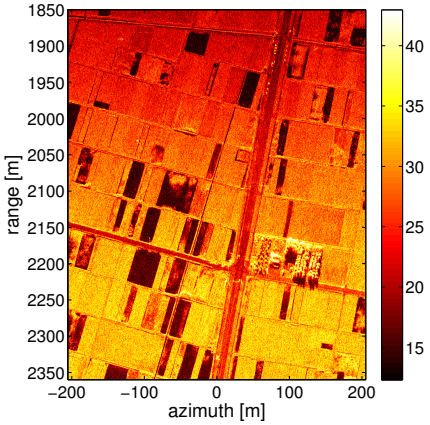

(a) Channel 1 (A_1)

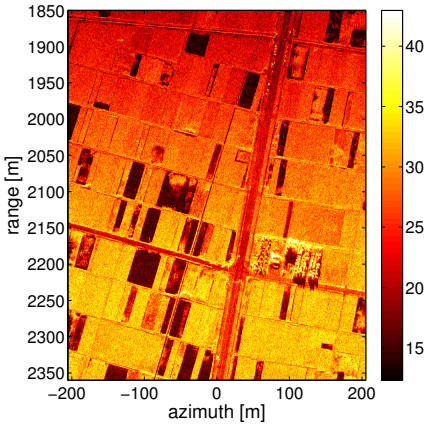

(b) Channel 2 (A_2)

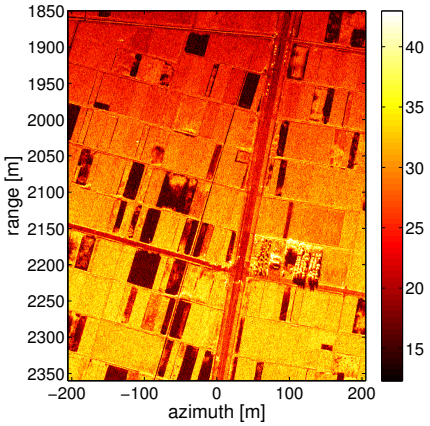

(c) Channel 3 (A_3)

FIGURE 4.9: The co-registered and balanced Multi-channel SAR images. The second channel has been used as the reference channel. The topographic phase has been removed using the algorithm shown in [115]. The unit for the side bars is 'dB.'

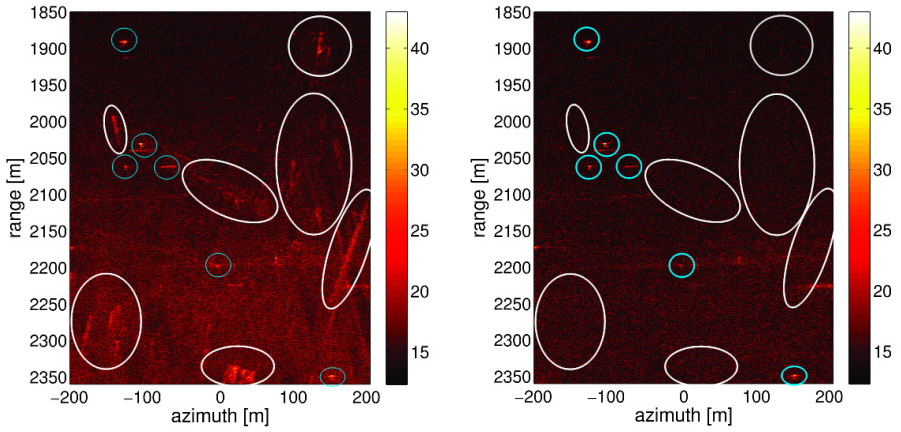

(a) full Doppler band ($\boldsymbol{D} = \mathbf{1}$)

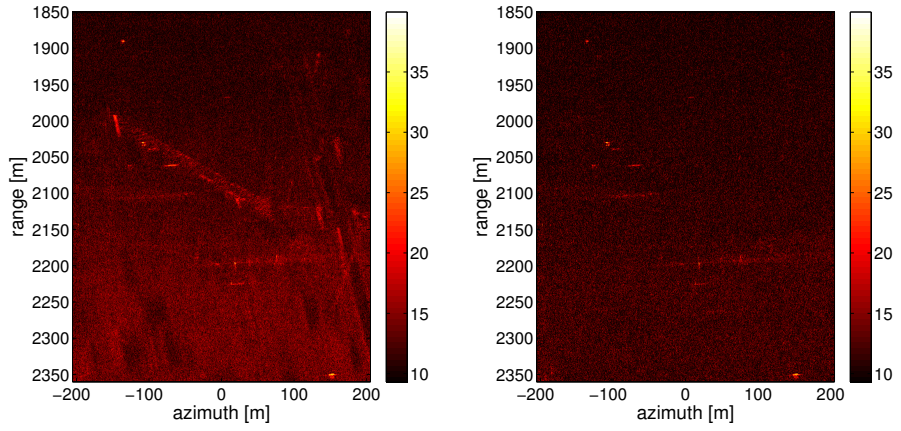

(b) lower half ($\boldsymbol{D} = \mathbf{1}$)

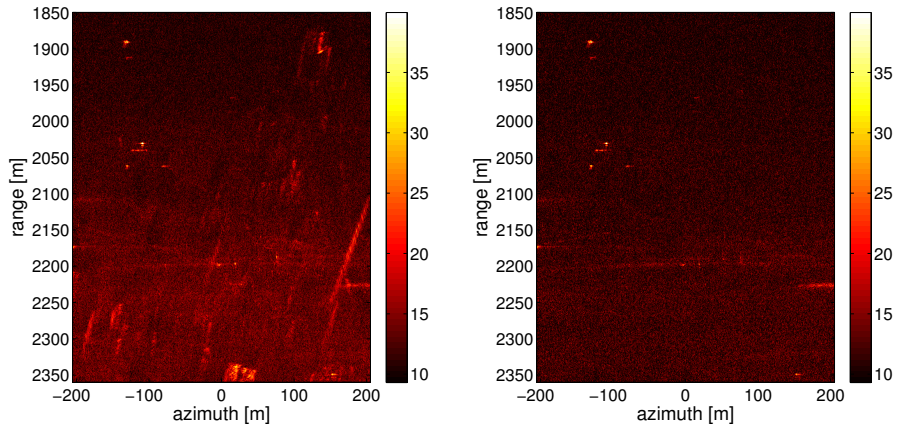

(c) upper half ($\boldsymbol{D} = \mathbf{1}$)

(d) full Doppler band ($\boldsymbol{D} = \boldsymbol{D}_-, \boldsymbol{D}_+$)

(e) lower half ($\boldsymbol{D} = \boldsymbol{D}_-$)

(f) upper half ($\boldsymbol{D} = \boldsymbol{D}_+$)

FIGURE 4.10: The output power image $\|\check{\boldsymbol{z}}\|$ of the Multi-channel DPCA. (a), (b) and (c) show the output images of Multi-channel DPCA with $\boldsymbol{D} = \mathbf{1}$ using full, lower half and upper half Doppler bands, respectively. (d), (e) and (f) show the output images of Multi-channel DPCA with ambiguity suppression. For (e) and (f), $\boldsymbol{D} = \boldsymbol{D}_-$ and $\boldsymbol{D} = \boldsymbol{D}_+$ in (4.11) are employed, respectively. For (d), $\boldsymbol{D} = \boldsymbol{D}_-$ and $\boldsymbol{D} = \boldsymbol{D}_+$ are employed for lower and upper Doppler bands, respectively, and the clutter and ambiguity suppressed Doppler bands are coherently combined to obtain the final image. The unit for the side bars is 'dB.' The dynamic range of (b),(c),(e) and (f) are set 3dB lower from the others, in order to level the brightness of the noise floor. In (a) and (d), white and cyan circles indicate the strong azimuth ambiguities and moving target images, respectively. Comparing (d)-(f) with (a)-(c), we can see that the azimuth ambiguities are successfully suppressed.

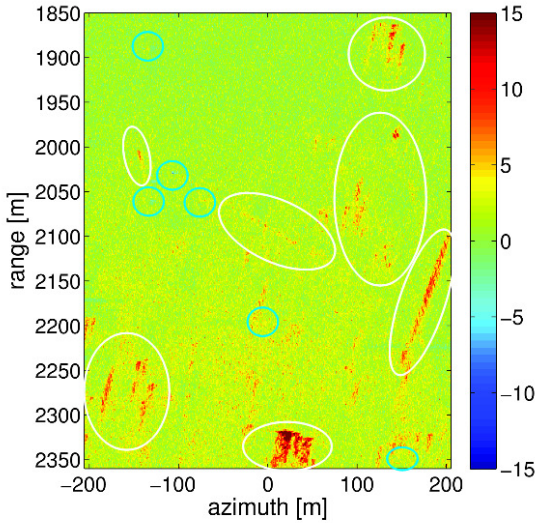

(a) the image of the power ratio $\|\breve{z}\|_1 / \|\breve{z}\|_2$

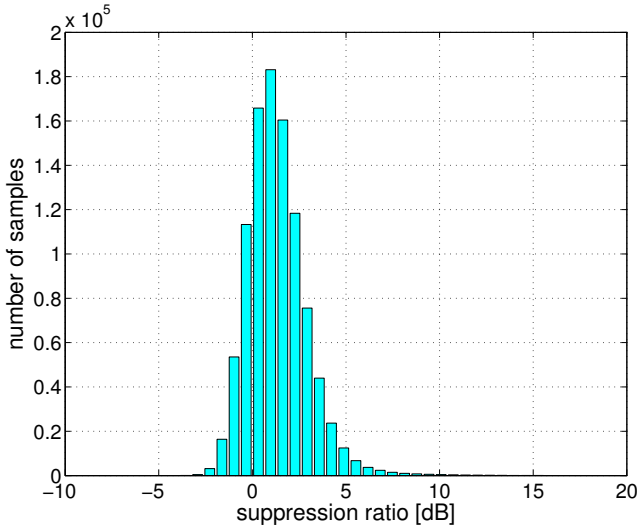

(b) the histogram of the power ratio $\|\breve{z}\|_1 / \|\breve{z}\|_2$

FIGURE 4.11: The ratio of the Multi-channel DPCA output power images shown in Fig. 4.10 (a) ($\|\breve{z}\|_1$) and (d) ($\|\breve{z}\|_2$). The unit for the side bar in (a) is 'dB.'

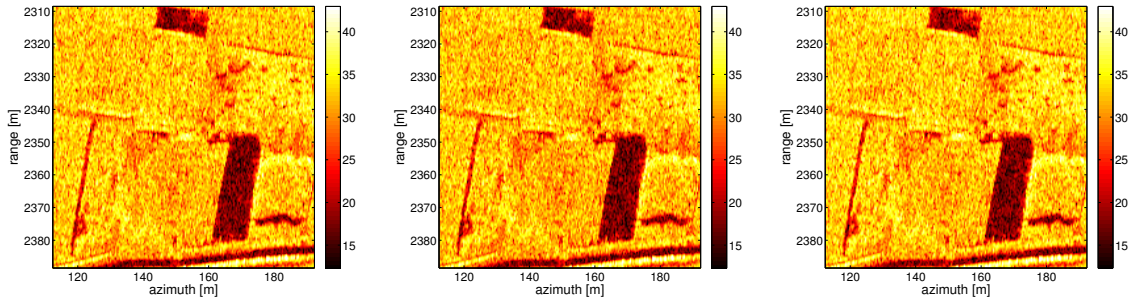

(a) ch.1 (b) ch.2 (c) ch.3

FIGURE 4.12: The co-registered and balanced Multi-channel SAR images (magnified around a moving target signal). The unit for the side bars is 'dB.'

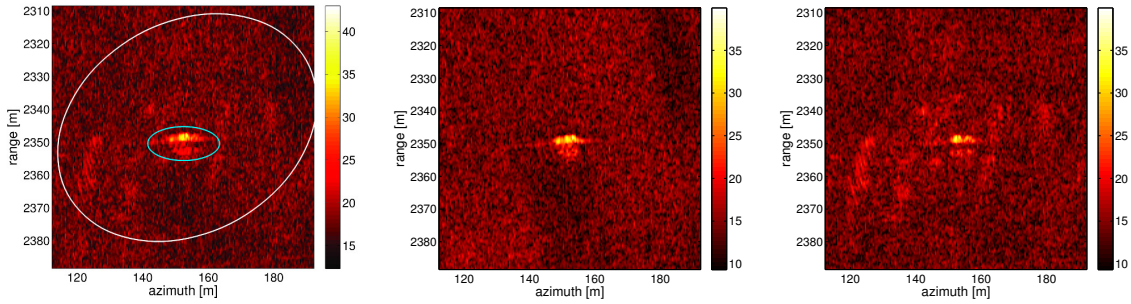

(a) full spectrum ($\boldsymbol{D} = \mathbf{1}$) (b) lower half ($\boldsymbol{D} = \mathbf{1}$) (c) upper half ($\boldsymbol{D} = \mathbf{1}$)

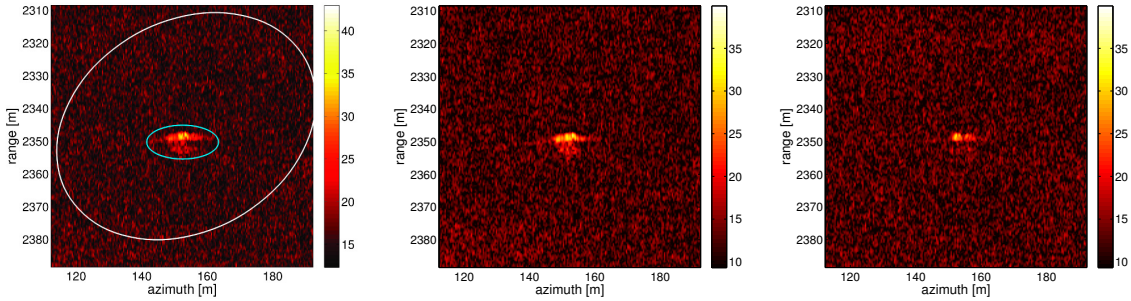

(d) full spectrum ($\boldsymbol{D} = \boldsymbol{D}_-, \boldsymbol{D}_+$) (e) lower half ($\boldsymbol{D} = \boldsymbol{D}_-$) (f) upper half ($\boldsymbol{D} = \boldsymbol{D}_+$)

FIGURE 4.13: The output power image $\|\check{\boldsymbol{z}}\|$ of the Multi-channel DPCA (magnified around a moving target signal). The unit for the side bars is 'dB.' In (a) and (d), the cyan circle indicates the moving target image. In (a), strong azimuth ambiguities are observed in the whte circle.

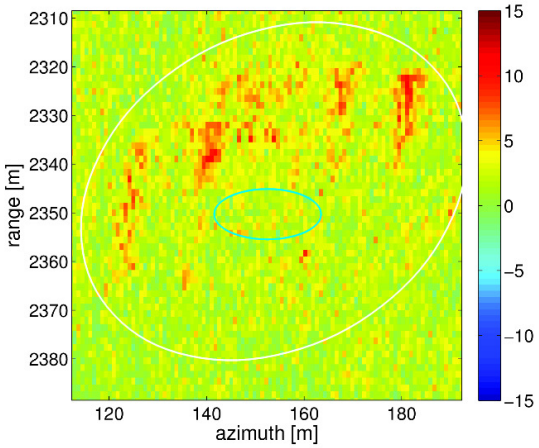

(a) the image of the ratio $\|\check{z}\|_1 / \|\check{z}\|_2$

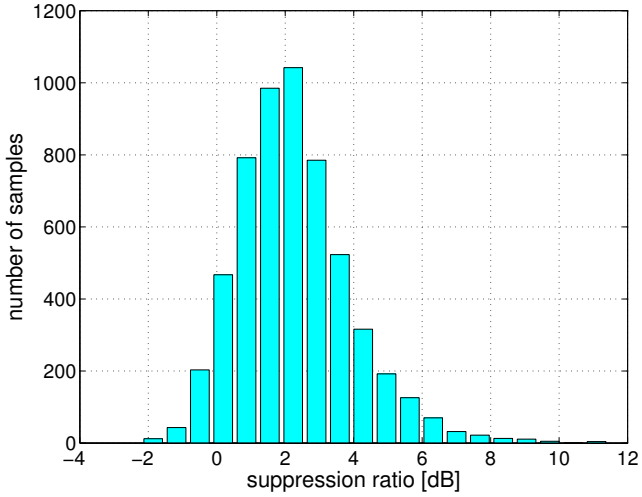

(b) the histogram of the ratio $\|\check{z}\|_1 / \|\check{z}\|_2$

FIGURE 4.14: The ratio of the Multi-channel DPCA output power images shown in Fig. 4.13 (a) ($\|\check{z}\|_1$) and (d) ($\|\check{z}\|_2$). The unit for the side bar in (a) is 'dB.'

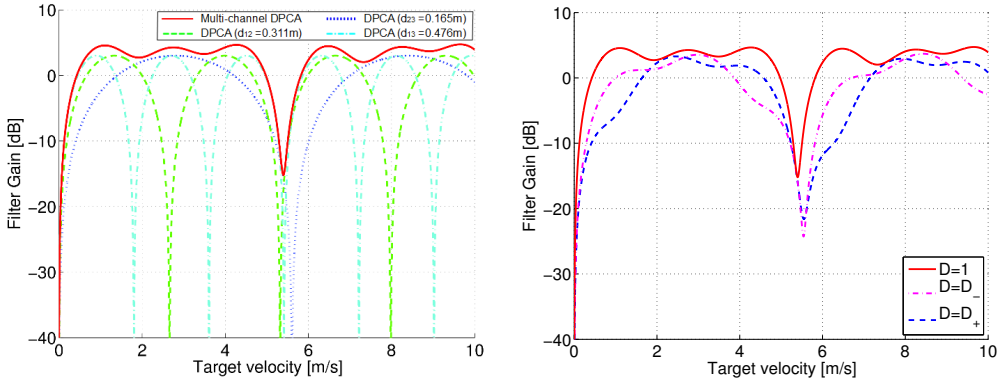

(a) (b)

FIGURE 4.15: The DPCA filter gain, defined as the DPCA output power normalized by the input signal power, as a function of the target radial velocity. (a) The solid red line shows the filter gain of the Multi-channel DPCA with $\boldsymbol{D} = \mathbf{1}$. The dashed green line, dotted blue line and dash-dot cyan line show the filter gain of the conventional two-channel DPCA with effective baseline $d_{12} = 0.311$m, $d_{23} = 0.165$m and $d_{13} = 0.476$m, respectively. (b) The solid red line, dash-dot magenta line and dashed blue line show the filter gain of the Multi-channel DPCA with $\boldsymbol{D} = \mathbf{1}$, $\boldsymbol{D} = \boldsymbol{D}_-$ and $\boldsymbol{D} = \boldsymbol{D}_+$, respectively.

Fig. 4.15 shows the DPCA filter gain, defined as the DPCA output power normalized by the input signal power, as a function of the target radial velocity. In Fig. 4.15 (a), the solid red line shows the filter gain of the Multi-channel DPCA with $\boldsymbol{D} = \mathbf{1}$. The dashed green line, dotted blue line and dash-dot cyan line show the filter gain of the conventional two-channel DPCA with effective baseline $d_{12} = 0.311$m, $d_{23} = 0.165$m and $d_{13} = 0.476$m, respectively. In Fig. 4.15 (b), the solid red line, dash-dot magenta line and dashed blue line show the filter gain of the Multi-channel DPCA with $\boldsymbol{D} = \mathbf{1}$, $\boldsymbol{D} = \boldsymbol{D}_-$ and $\boldsymbol{D} = \boldsymbol{D}_+$, respectively. It can be seen from Fig. 4.15 that the blind velocities are resolved in the Multi-channel DPCA; however, it is observed that the filter gain significantly drops at target radial velocity around 5.5m/s. Fig. 4.15 suggests that optimization of the baselines, which determine the filter gain, is desired to minimize the moving target signal loss. This issue is discussed further in the next section.

4.4.3 The radial velocity estimation results of Multi-channel ATI, Multi-channel DPCA-ATI

Fig. 4.16 (a) and (b) show the results of target radial velocity estimation based on the Multi-channel ATI and Multi-channel DPCA-ATI, respectively. In Fig. 4.16, the power average of the three images is assigned to green and blue, while the Multi-channel DPCA power image $\|\check{\boldsymbol{z}}\|$ is assigned to red. Consequently, the moving target signal appears as orangish in these images. In Fig. 4.16, a circle indicates the position where the target signal is detected. The radial velocity and the corresponding azimuthal displacement has been estimated for these detected targets. The azimuthal displacement has been estimated by (4.18). The square indicates the estimated moving target position after correcting the azimuthal displacement, and the arrow indicates the estimated direction of the target radial velocity. Note that the the arrow is not the target velocity vector; it just indicates if the target is moving toward or away from the radar[4].

[4]It would be possible to estimate along track velocity to achieve velocity vector estimation, e.g., by employing an algorithm proposed in [112], but it is beyond the scope of this paper.

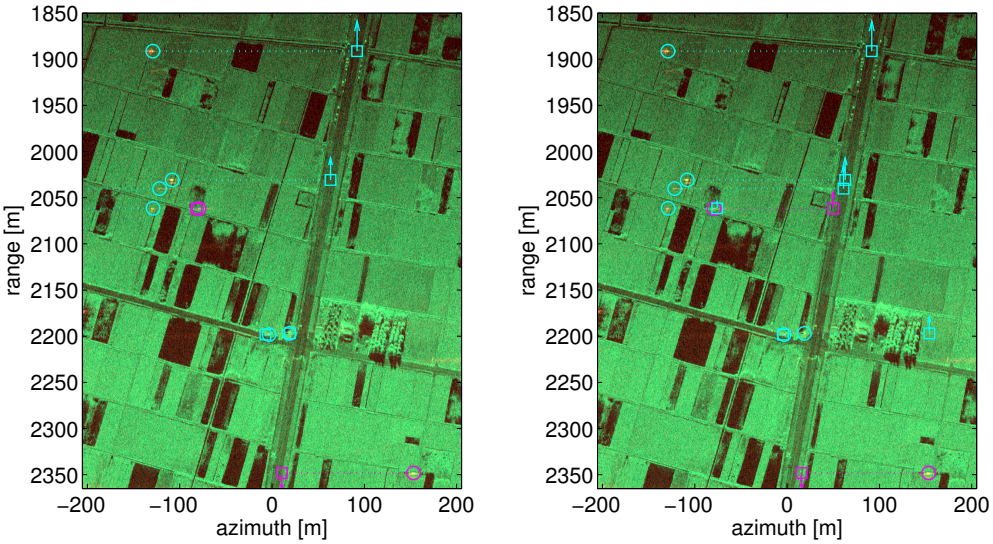

(a) Multi-channel ATI (b) Multi-channel DPCA-ATI

FIGURE 4.16: The results of target radial velocity estimation based on the Multi-channel ATI and Multi-channel DPCA-ATI. The power average of the three images is assigned to green and blue, while the Multi-channel DPCA power image $\|\check{z}\|$ is assigned to red. Consequently, the moving target signal appears as orangish in the images. The circle indicates the position where the target signal is detected. The square indicates the moving target position after correcting the azimuthal displacement, and the arrow indicates the estimated direction of the target radial velocity. The two control vehicles are indicated by magenta and the other detected vehicles are indicated by cyan.

In Fig. 4.16, the two controlled vehicles are indicated by magenta and the other detected vehicles are indicated by cyan. Table 4.2 shows the estimated radial velocity and the azimuth displacement of the two controlled vehicles. The estimation error shown in Table 4.2 has been evaluated from the estimated azimuth position of the target. The magnified images are provided for the two controlled vehicles in Figs.4.17 and 4.18 along with the velocity estimation function $P_{\mathrm{mati}}(v_{\mathrm{los0}})$ and $P_{\mathrm{mdpcaati}}(v_{\mathrm{los0}})$. The radial velocities are estimated from the peak position of the velocity estimation functions indicated by the red circles in Figs.4.17 (c), (d) and Figs.4.18 (c), (d). As it can be seen from Fig. 4.17 (b) and Fig. 4.18 (b), the Multi-channel DPCA-ATI obtains a very accurate estimation, since the estimated azimuth positions of the motorcycle and the van are right on top of the frontage roads where the vehicles were driving [5]. In these cases, the maximum error of the azimuth displacement is evaluated as approximately the lane width (3m), and the corresponding maximum velocity estimation errors have been derived as 0.12m/s and 0.11m/s for the motorcycle and the van, respectively[6]. On the other hand, the estimations obtained by the Multi-channel ATI contain large errors caused by the clutter.

Six non-cooperative targets are detected in Fig. 4.16. Two of them around range 2,200m are false alarms corresponding to a power pole and a sign on the side of the street. Four other targets are likely to be the vehicles driving along the street at the center of the image[7]. It can be seen from Fig. 4.16 (a) that the Multi-channel ATI suffers from significant velocity

[5] Note that cars drive on the left in Japan.

[6] According to the GPS data, the speed of the motorcycle and the van was 22km/h and 23km/h, respectively, which is consistent with the estimated radial velocity of 18.7km/h and 18.0km/h obtained by the Multi-channel DPCA-ATI.

[7] Unfortunately, the video camera set for the groundtruth did not cover the whole street.

TABLE 4.2: The target radial velocity and azimuth displacement estimation error

Algorithm	Target	Radial velocity		Azimuthal displacement	
		estimation	error	estimation	error
Multi-channel ATI	Motorcycle	0.11m/s (0.38km/h)	5.3m/s (19.1km/h)	-2.7m	141m
	Van	5.2m/s (18.7km/h)	0.18m/s (0.65km/h)	-143m	5m
Multi-channel DPCA-ATI	Motorcycle	-5.2m/s (-18.7km/h)	$<$ 0.12m/s (0.43km/h)	129m	$<$ 3m
	Van	5.0m/s (18.0km/h)	$<$ 0.11m/s (0.41km/h)	-138m	$<$ 3m

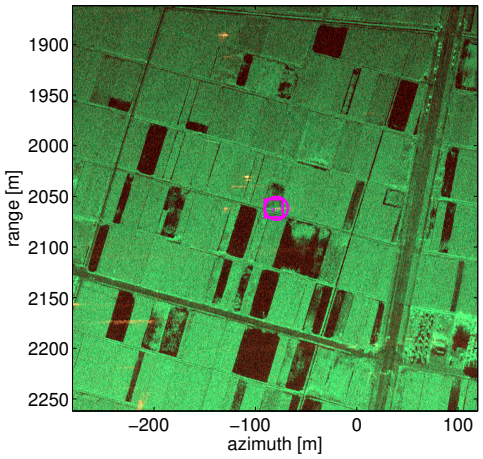

(a) Multi-channel ATI

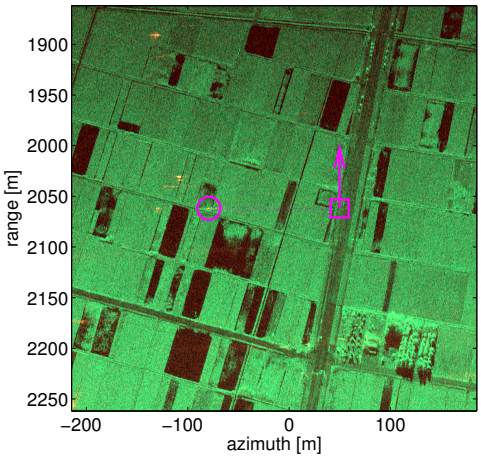

(b) Multi-channel DPCA-ATI

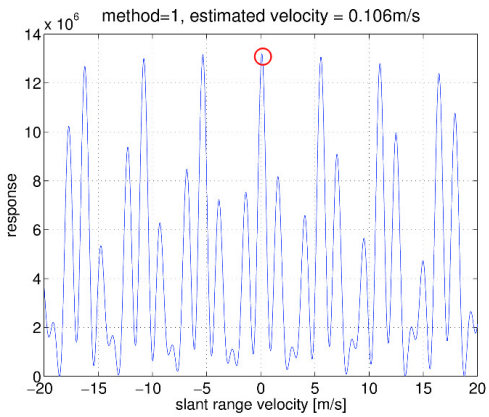

(c) Multi-channel ATI

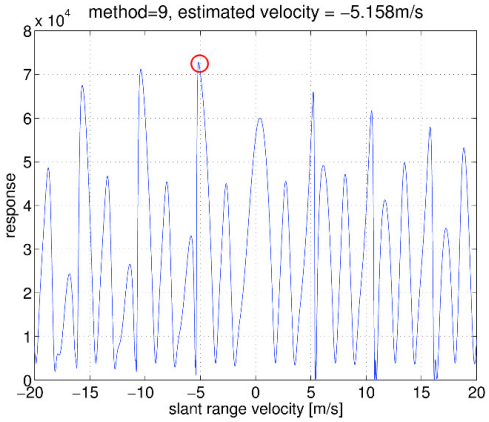

(d) Multi-channel DPCA-ATI

FIGURE 4.17: The radial velocity estimation results of the motorcycle. (a) The magnified Multi-channel ATI image, (b) The magnified Multi-channel DPCA-ATI results (c) The velocity estimation function $P_{\text{mati}}(v_{\text{los0}})$, (d) The velocity estimation function $P_{\text{mdpcaati}}(v_{\text{los0}})$.

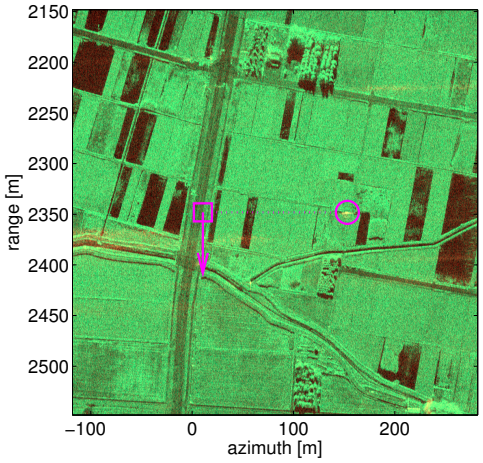

(a) Multi-channel ATI

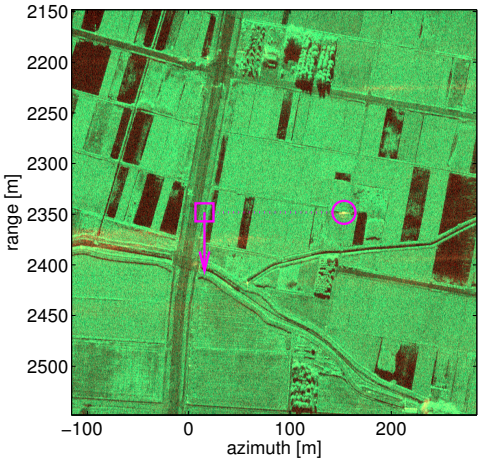

(b) Multi-channel DPCA-ATI

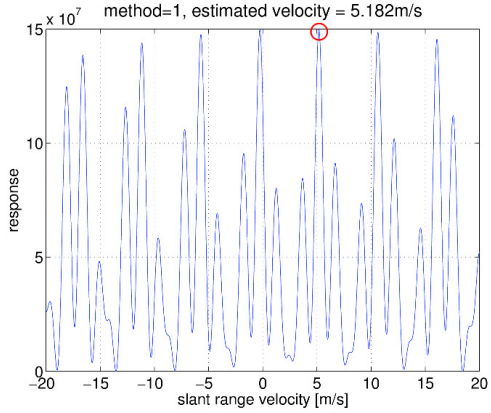

(c) Multi-channel ATI

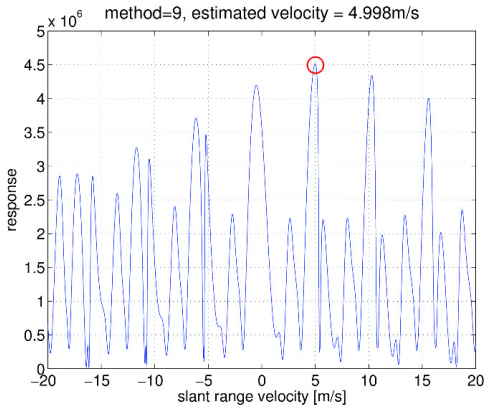

(d) Multi-channel DPCA-ATI

FIGURE 4.18: The radial velocity estimation results of the van. (a) The magnified Multi-channel ATI image, (b) The magnified Multi-channel DPCA-ATI results (c) The velocity estimation function $P_{\text{mati}}(v_{\text{los0}})$, (d) The velocity estimation function $P_{\text{mdpcaati}}(v_{\text{los0}})$.

estimation error for low SCR targets. In Fig. 4.16 (b), only one target is off the street. At the channel imbalance correction stage, the topographic phase has been removed using the algorithm presented in [115]. This could introduce some non-negligible phase error for a target whose phase center height is significantly higher than the surrounding environment. Considering the height of the power pole is about 15m, it is not unlikely that the azimuth position estimation error observed for one of the false alarms in Figs. 4.16 (b) is due to its height.

4.4.4 The along track velocity estimation results

Fig. 4.19 shows the results of target detection and velocity estimation by the proposed algorithm. In Fig. 4.19, the two controlled vehicles are indicated by magenta, and the arrow shows the estimated velocity. Unlike Fig. 4.16, the arrows in this figure do reflect the target velocities —they are estimated velocity vectors. It is obtained from the radial velocity and along track velocity estimated by the full processing shown in Fig. 4.6.

The input SCNR (Signal to Clutter and Noise Ratio) of the motorcycle and the van has been 7.6dB and 10.0dB, respectively. Table 4.3 shows the estimated along track velocity, radial velocity and the azimuth displacement of the vehicles. The estimation error shown in Table 4.3 has been evaluated from the estimated azimuth position of the target. As previously stated, the estimated azimuth positions of the motorcycle and the van are right on top of the frontage roads where the vehicles were driving. Therefore, we can evaluate the maximum error of the azimuth displacement as approximately the lane width (3m), and the corresponding maximum radial velocity estimation errors have been derived as 0.12 m/s and 0.11 m/s for the motorcycle and the van, respectively. Then, in Fig. 4.19, we observe that the arrows are parallel to the frontage roads, which means that the along track velocity also is accurately estimated. Since the estimated velocity vector is parallel to the road, we assume that the maximum along-track velocity error and the radial velocity error are proportional to the estimated values. Based on these observations, the maximum along-track velocity errors have been evaluated as 0.016 m/s for the motorcycle and 0.014 m/s for the van, respectively.

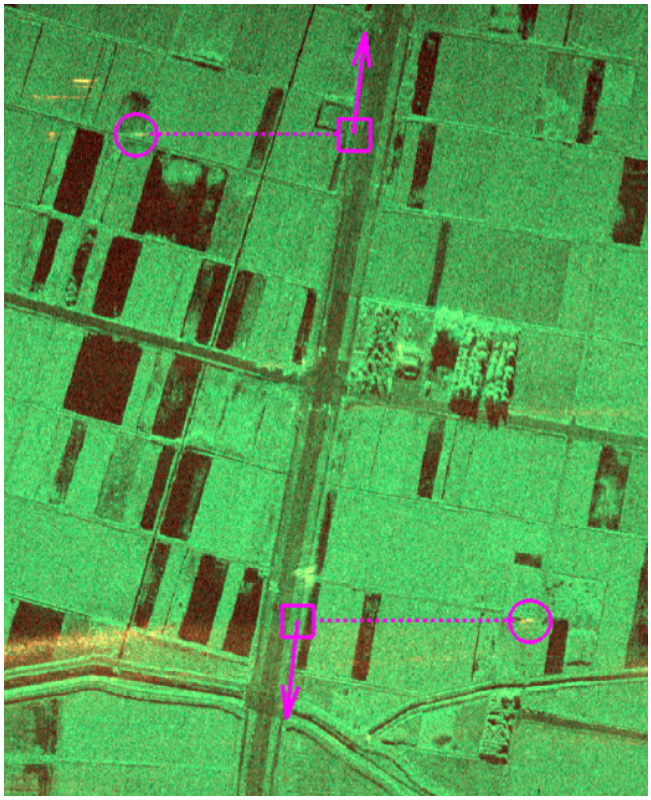

FIGURE 4.19: The along track and radial velocity estimation results of the motorcycle and the van.

TABLE 4.3: The target along track velocity, radial velocity and azimuth displacement estimation error

Target	Along track velocity		Radial velocity		Azimuthal displacement	
	estimation	error	estimation	error	estimation	error
Motorcycle	-0.69 m/s	< 0.016m/s	-5.2m/s	< 0.12m/s	129m	< 3m
Van	0.65 m/s	< 0.014m/s	5.0m/s	< 0.11m/s	-138m	< 3m

4.5 Performance evaluation

In this section, statistical performance of the Multi-channel DPCA, Multi-channel ATI and Multi-channel DPCA-ATI are evaluated to illustrate the expected performance of the proposed algorithms on formation flight spaceborne SAR systems. The detection performance of the Multi-channel DPCA is evaluated analytically, and the target radial velocity estimation performance of Multi-channel ATI and Multi-channel DPCA-ATI are evaluated via numerical simulation.

4.5.1 Optimization of the baselines

As suggested by Fig. 4.15, baselines need to be optimized at first to minimize the moving target signal loss. The optimal baselines can be determined by

$$(d_{12}, d_{13})_{\text{optimal}} \triangleq \underset{d_{12}, d_{13}}{\text{argmax}} \left[\Lambda (d_{12}, d_{13}) \right], \tag{4.26}$$

where $\Lambda (d_{12}, d_{13})$ is the minimum output power of the target whose velocity is between $|v|_{\min}$ and $|v|_{\max}$ and is given by

$$\Lambda (d_{12}, d_{13}) \quad = \quad \min_{v_{\text{los0}}} \{ \| \boldsymbol{P} \boldsymbol{s} (v_{\text{los0}}; d_{12}, d_{13}) \| \}, \tag{4.27}$$

where,

$$|v|_{\min} \leq v_{\text{los0}} \leq |v|_{\max},$$

and

$$\boldsymbol{P} \quad = \quad \boldsymbol{I} - \mathbf{1} \left(\mathbf{1}^H \mathbf{1} \right)^{-1} \mathbf{1}^H.$$

Fig. 4.20 shows the function $\Lambda (d_{12}, d_{13})$ for our airborne Ku-band three-channel SAR system calculated over the predetermined search area of (d_{12}, d_{13}). The search area has been defined to be 0.15 m $\leq d_{12} \leq$ 0.25 m and 0.3 m $\leq d_{13} \leq$ 0.5 m. The minimum and maximun achievable baselines have been determined from the aperture sizes of the antenna and the radome, respectively. In addition, the platform velocity and the target radial velocity range of interest has been assumued to be 100m/s and 1m/s–10m/s, respectively. In Fig. 4.20, the maximum $\Lambda (d_{12}, d_{13})$ has been obtained at $(d_{12}, d_{13}) = (0.168\text{m}, 0.42\text{m})$. Fig.4.21 shows the filter gain obtained by the optimal baselines. Compared with Fig. 4.15 (b), it can be seen that the moving target signal loss can be reduced by optimizing the baselines.

4.5.2 Scenario for the performance evaluation

Table 4.4 shows the parameters of the scenario for the performance evaluation. In this scenario, the baselines are optimized by the method shown in 4.5.1. Fig. 4.22 shows the function $\Lambda (d_{12}, d_{13})$ calculated for the target radial velocity range of 1m/s–40m/s. From Fig.4.23, we can confirm that the moving target signal loss is kept small by employing the optimal baselines.

In addition, the DPCA condition is assumued to be satisfied, so that the clutter signal model reduces to $\boldsymbol{u} = c\mathbf{1}$ as described in Section 4.2. Also the clutter is assumed to be uniform and Gaussian distributed. Under these conditions, the statistical property of the

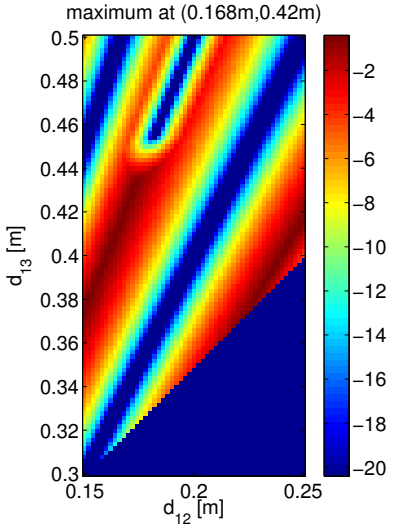

FIGURE 4.20: The function $\Lambda(d_{12}, d_{13})$ calculated over the predetermined search area of (d_{12}, d_{13}). The unit for the sidebar is 'dB.'

clutter plus noise can be described by the covariance matrix $\boldsymbol{R}_{\mathrm{c+n}}$ given by [110]:

$$\begin{aligned} \boldsymbol{R}_{\mathrm{c+n}} &= E\left\{\boldsymbol{u}\boldsymbol{u}^H\right\} + E\left\{\boldsymbol{w}\boldsymbol{w}^H\right\} \\ &= \sigma_{\mathrm{c}}^2 \mathbf{1}\mathbf{1}^T + \sigma_{\mathrm{n}}^2 \boldsymbol{I} \\ &= \sigma^2 \begin{bmatrix} 1 & \rho & \cdots & \rho \\ \rho & 1 & \ddots & \vdots \\ \vdots & \ddots & \ddots & \rho \\ \rho & \cdots & \rho & 1 \end{bmatrix} \\ \sigma^2 &= \sigma_{\mathrm{c}}^2 + \sigma_{\mathrm{n}}^2, \end{aligned} \tag{4.28}$$

where σ^2 is the mean background power, σ_{c}^2 and σ_{n}^2 are the clutter and the noise mean power, respectively, and ρ is the correlation coefficient between two different channels. From the definition, ρ and CNR (Clutter to Noise Ratio) are related as follows:

$$\rho = \frac{\sigma_{\mathrm{c}}^2}{\sigma_{\mathrm{c}}^2 + \sigma_{\mathrm{n}}^2} = \frac{\mathrm{CNR}}{\mathrm{CNR}+1}. \tag{4.29}$$

(4.29) means that the decorrelation of the background signal is fully attributed to the noise in the model. The influence of the azimuth ambiguity, which is the dominant factor for the decorrelation, is excluded from the following performance evaluation[8], because the strong azimuth ambiguities tend to behave as isolated (and somewhat blurred) targets, which are not suited for statistical treatment[9].

[8]Besides the azimuth ambiguity, sources of decorrelation include clutter motion and slight difference of bistatic angles between the receive channels. Even if the decorrelation due to these sources is not negligible, the analysis still gives good idea of the performance if we adjust the noise power σ_{n}^2 to match the correlation coefficient ρ via (4.29).

[9]The authors belive that the influence of the azimuth ambiguity has been well illustrated in the airborne Ku-band three-channel SAR experimets.

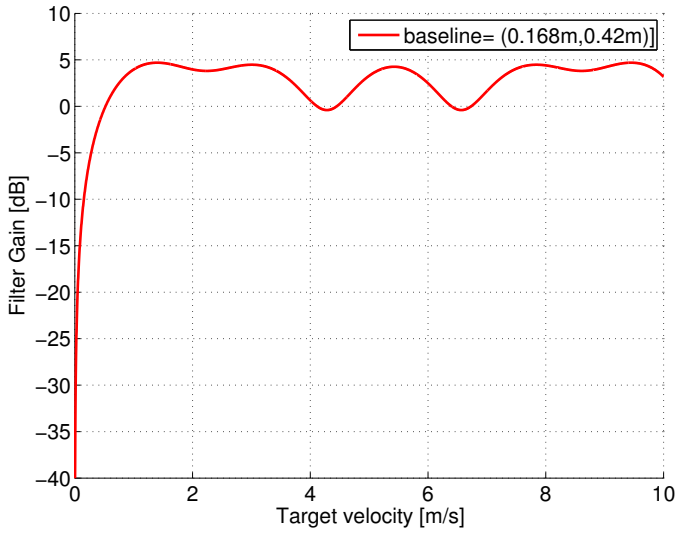

FIGURE 4.21: The filter gain of the Multi-channel DPCA with optimal baselines.

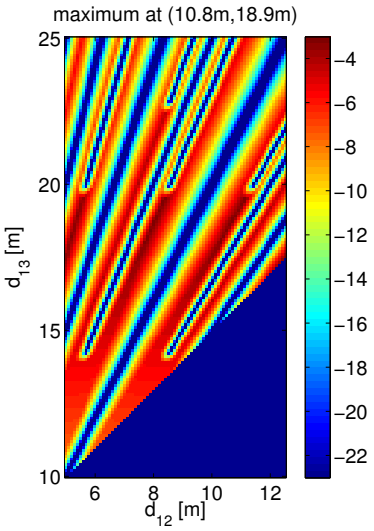

FIGURE 4.22: The function $\Lambda(d_{12},d_{13})$ calculated over the predetermined search area of (d_{12},d_{13}). The unit for the sidebar is 'dB.'

TABLE 4.4: Parameters of a formation flight spaceborne SAR scenario

Parameters	Value
Carrier frequency	9.6GHz
The number of channels	3
Platform velocity	7,300m/s
Target radial velocity detection range	$\|v\|_{\min} = 1$m/s, $\|v\|_{\max} = 40$m/s
Effective baselines search area	$5\text{m} \le d_{12} \le 12.5\text{m}$ $10\text{m} \le d_{13} \le 25\text{m}$
Optimal baselines	$(d_{12},d_{13}) = (10.8\text{m},18.9\text{m})$
Input SCNR / CNR	0dB / 15dB
The number of looks	4
Monte Carlo iteration	100

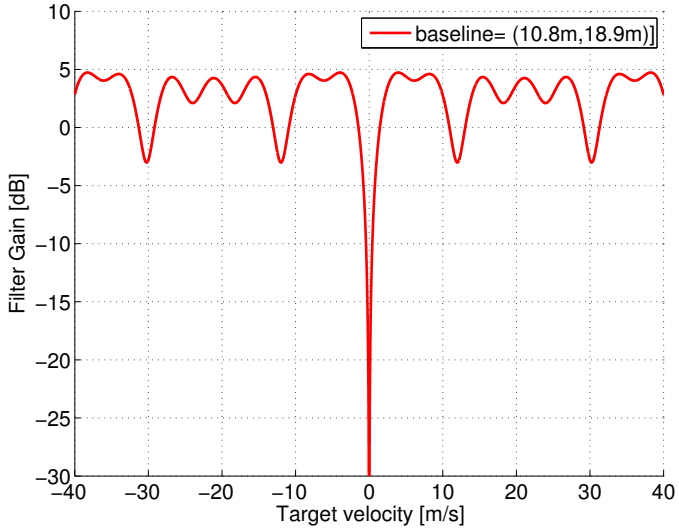

FIGURE 4.23: The filter gain of the Multi-channel DPCA with optimal baselines.

4.5.3 Target detection performance of Multi-channel DPCA

Fig. 4.23 shows the Multi-channel DPCA filter gain as a function of the target radial velocity. One can see that the moving target signal loss is kept up to about 7dB in this case.

In order to roughly estimate the detection performance of the Multi-channel DPCA, we assume simple statistical models for the moving target signal as well as background clutter and noise. As stated in 4.5.2, we exclude the influence of the ambiguity from this analysis, and we employ $\boldsymbol{P} = \boldsymbol{I} - \mathbf{1}\left(\mathbf{1}^H\mathbf{1}\right)^{-1}\mathbf{1}^H$ as the orthogonal projection matrix. In addition, we assume the clutter is fully correlated, in which case the clutter is fully suppressed at the output of Multi-channel DPCA. The residual noise at the output test statistics ζ is a power sum of the $(N_\mathrm{a}-1)$ complex Gaussian distributed random variables. Assuming the multilook processing is performed before thresholding to reduce the false alarm, the N_L-look test statistic is again Gamma distributed, whose shape parameter and the scale parameter are $N_\mathrm{L}(N_\mathrm{a}-1)$ and σ_n^2, respectively. The probability density function (pdf) $f_\mathrm{n}(\zeta)$ and cumulative distribution function (cdf) $F_\mathrm{n}(\zeta)$ of the multilooked test statistic are given by [118], [119]

$$f_\mathrm{n}(\zeta) = \frac{\zeta^{N_\mathrm{L}(N_\mathrm{a}-1)-1}}{\left(\sigma_n^2\right)^{N_\mathrm{L}(N_\mathrm{a}-1)}\Gamma\left\{N_\mathrm{L}(N_\mathrm{a}-1)\right\}}\exp\left(-\frac{\zeta}{\sigma_n^2}\right), \tag{4.30}$$

$$\begin{aligned} F_\mathrm{n}(\zeta) &= \frac{1}{\left(\sigma_n^2\right)^{N_\mathrm{L}(N_\mathrm{a}-1)}\Gamma\left(N_\mathrm{L}(N_\mathrm{a}-1)\right)} \\ &\quad\times\int_0^\zeta \gamma^{N_\mathrm{L}(N_\mathrm{a}-1)-1}\exp\left(-\frac{\zeta}{\sigma_n^2}\right)d\gamma \\ &= 1-\exp\left(-\frac{\zeta}{\sigma_n^2}\right)\sum_{q=0}^{N_\mathrm{L}(N_\mathrm{a}-1)-1}\frac{1}{q!}\left(-\frac{\zeta}{\sigma_n^2}\right)^q. \end{aligned} \tag{4.31}$$

where $\Gamma(\cdot)$ is Gamma function.

We model the observed signal at the pixel that contains the target by the sum of normaly distributed noise and non-fluctuating target signal (Sweling Case 0). Then the test statistic ζ of the pixel that contains the target signal obeys the Noncentral Chi-Squared distribution. After the multilook processing, the pdf and cdf for the N_L-looked target signal are given by

[120]

$$
\begin{aligned}
f_{\mathrm{s}}(\zeta) &= \left\{\frac{\zeta}{N_{\mathrm{L}}(N_{\mathrm{a}}-1)\beta}\right\}^{(N_{\mathrm{L}}(N_{\mathrm{a}}-1)-1)/2} \\
&\quad \times \exp\left[-\{\zeta+(N_{\mathrm{a}}-1)\beta\}\right] \\
&\quad \times I_{N_{\mathrm{L}}(N_{\mathrm{a}}-1)-1}\left[2\sqrt{\zeta N_{\mathrm{L}}(N_{\mathrm{a}}-1)\beta}\right], \qquad (4.32)\\
F_{\mathrm{s}}(\zeta) &= 1-Q_{N_{\mathrm{a}}-1}\left\{\sqrt{2N_{\mathrm{L}}(N_{\mathrm{a}}-1)\beta},\sqrt{2\zeta}\right\}. \qquad (4.33)
\end{aligned}
$$

where, β is the SCNR at the output of Multi-channel DPCA processing and is defined as $\beta = \mathrm{SCNR}_{\mathrm{out}}(v_{\mathrm{los0}})$. $I_\alpha(\zeta)$ and $Q_M(a,b)$ are the first kind modified Bessel function and the Marcum Q-function, respectively, which are given by

$$
\begin{aligned}
I_\alpha(\zeta) &= \sum_{m=0}^{\infty}\frac{1}{m!\Gamma(m+\alpha+1)}\left(\frac{x}{2}\right)^{2m+\alpha}, \qquad (4.34)\\
Q_M(a,b) &= \int_b^\infty x\left(\frac{x}{a}\right)^{M-1} e^{\left(-\frac{x^2+a^2}{2}\right)} I_{M-1}(ax)dx\,. \qquad (4.35)
\end{aligned}
$$

(4.32) and (4.33) assume that the target signal is contained in the N_{L} pixels to be averaged and the target signal power is uniform over these pixels. Obviously, the target signal power is often not unform over a number of pixles in the real world, but (4.32) and (4.33) would give a good approximation, if we define the output SCNR β using the average target signal power within the N_{L} pixels.

Based on the noise and the target statistics shown above, the probability of false alarm P_{fa} and the probability of detection P_{d} are derived as

$$
\begin{aligned}
P_{\mathrm{fa}} &= 1-F_{\mathrm{n}}(T) = \exp\left(-\frac{T}{\sigma_n^2}\right)\sum_{q=0}^{N_{\mathrm{L}}(N_{\mathrm{a}}-1)-1}\frac{1}{q!}\left(-\frac{T}{\sigma_n^2}\right)^q \qquad (4.36)\\
P_{\mathrm{d}} &= 1-F_{\mathrm{s}}(T) = Q_{N_{\mathrm{a}}-1}\left\{\sqrt{2N_{\mathrm{L}}(N_{\mathrm{a}}-1)\beta},\sqrt{2T}\right\}. \qquad (4.37)
\end{aligned}
$$

Fig. 4.24 shows the probability of detection over SCNR β at the output of Multi-channel DPCA, calculated by (4.36) and (4.37). The probability of false alarm has been set to 10^{-8}. According to this analysis, and considering the Multi-channel DPCA filter gain shown in Fig. 4.23, we can evaluate, for example, the required input SCNR to achieve a certain detection performance for various target radial velocity. Fig. 4.25 shows the required input SCNR to achieve $P_{\mathrm{d}} = 0.9$ and $P_{\mathrm{fa}} = 10^{-8}$ by Multi-channel DPCA with the optimal baseline obtained in 4.5.1. The input CNR is assumed to be 15dB. It can be seen from Fig. 4.25 that if the multilook number is 9, the required input SCNR of the moving target with target radial velocity of $\pm$1m/s to be detected is about -5dB.

4.5.4 Target radial velocity estimation performance of Multi-channel ATI and Multi-channel DPCA-ATI

Fig. 4.26 shows the matched filter outputs (noise and clutter free) for targets with various v_{los0}. Fig. 4.26 (a) and (b) show the matched filter outputs of Multi-channel ATI and Multi-channel DPCA-ATI, respectively. Fig. 4.27 (a) and (b) show the radial velocity estimation results of each algorithm with input SCNR=0dB and CNR=15dB. 100 Monte Carlo iteration has been conducted for each true velocity, and each dot in the figure represents the estimated velocity at each iteration. Fig. 4.28 (a) and (b) show the histogram of the target radial velocity

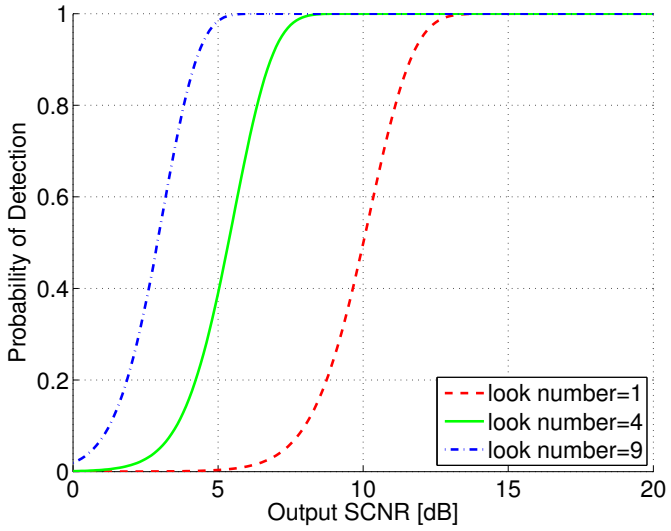

FIGURE 4.24: The probability of detection vs SCNR at the output of Multi-channel DPCA. The probability of false alarm has been set to 10^{-8}. The red dashed line, the green solid line, the blue dashed dotted line represent the probablity of detection for the multilook numbers 1, 4 and 9, respectively.

estimation error. It is observed in Fig. 4.26 that the matched filter output has many local maxima. In Fig. 4.27, one can see that the estimation tends to concentrate around the local maxima. In both cases the peak values of the ambiguous local maxima are smaller than that of the global maximum; therefore, many of the estimation is close to the actual target radial velocity, but under the presence of clutter and noise signal, the estimation tend to jump to the value around local maxima.

From Fig. 4.28, it is clear that the estimation error is reduced for the Multi-channel DPCA-ATI compared with the Multi-channel ATI. In Multi-channel DPCA-ATI, About 35% of the estimation errors are concentrated around $\pm$41m/s, which means that there is velocity ambiguity. Note that if the system has only two channels with the baseline on the order of 10m, then the ambiguous target radial velocity estimates arise every 11m/s [10]. Therefore, we can see that Multi-channel ATI and Multi-channel DPCA-ATI both largely reduce the target radial velocity ambiguity by exploiting the multi-channel signal. The ambiguity of $\pm$41m/s is due to the design of the baselines. Note that the baselines are optimized for detecting the moving targets with absolute radial velocity of 1m/s $\leq |v|_{\text{los0}} \leq$ 40m/s. It can be mitigated by either increasing the number of channels or by setting the baselines to optimized for wider range of the radial velocity allowing the degradation of the detection performance for the low velocity targets.

[10] From (4.6), ambiguous velocity can be derived as $2\pi \cdot \lambda/(4\pi\eta_{12}) \approx 0.031[m/s]/(2 \times 10[m]/7,300[m/s]) \approx$ 11m/s.

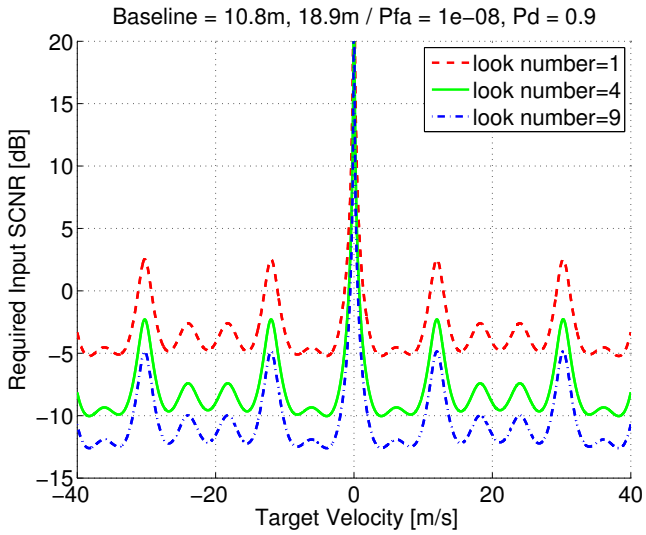

(a)

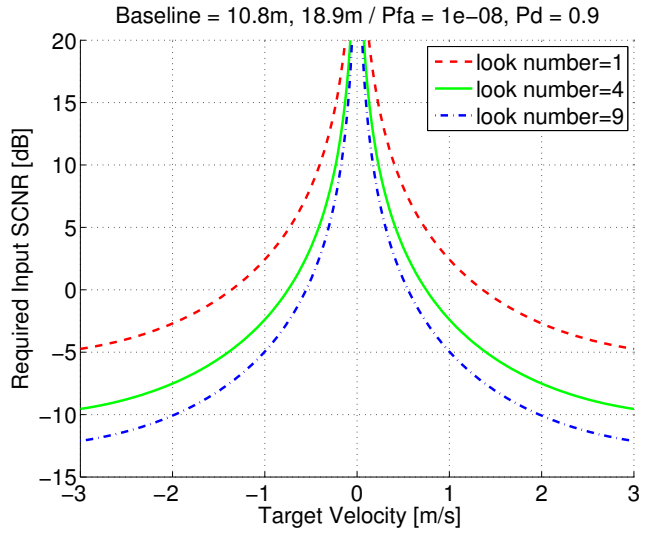

(b)

FIGURE 4.25: Required input SCNR to achieve $P_{\mathrm{d}} = 0.9$ and $P_{\mathrm{fa}} = 10^{-8}$. The input CNR is assumed to be 15dB. The red dashed line, the green solid line, the blue dashed dotted line represent the required SCNR for the multi-look numbers 1, 4 and 9, respectively. (a) and (b) show the detection performance over the target velocity of [-40m/s, 40m/s] and [-3m/s, 3m/s], respectively.

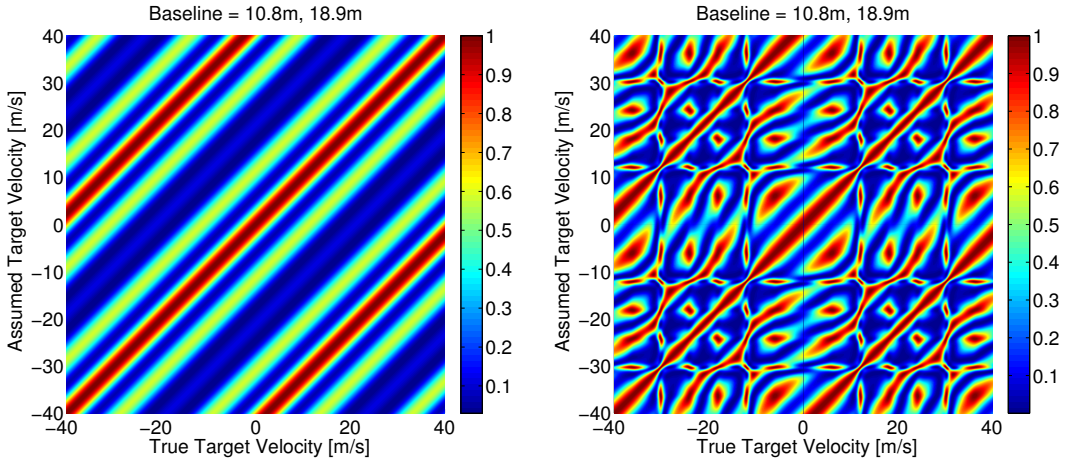

(a) Multi-channel ATI (b) Multi-channel DPCA-ATI

FIGURE 4.26: a
nd (b) Multi-channel DPCA-ATI [$P_{\text{mdpcaati}}(v_{\text{los0}})$].] The velocity estimation functions for (a) Multi-channel ATI [$P_{\text{mati}}(v_{\text{los0}})$] and (b) Multi-channel DPCA-ATI [$P_{\text{mdpcaati}}(v_{\text{los0}})$]. The functions are normalized by its peak value, and the sidebars is unitless.

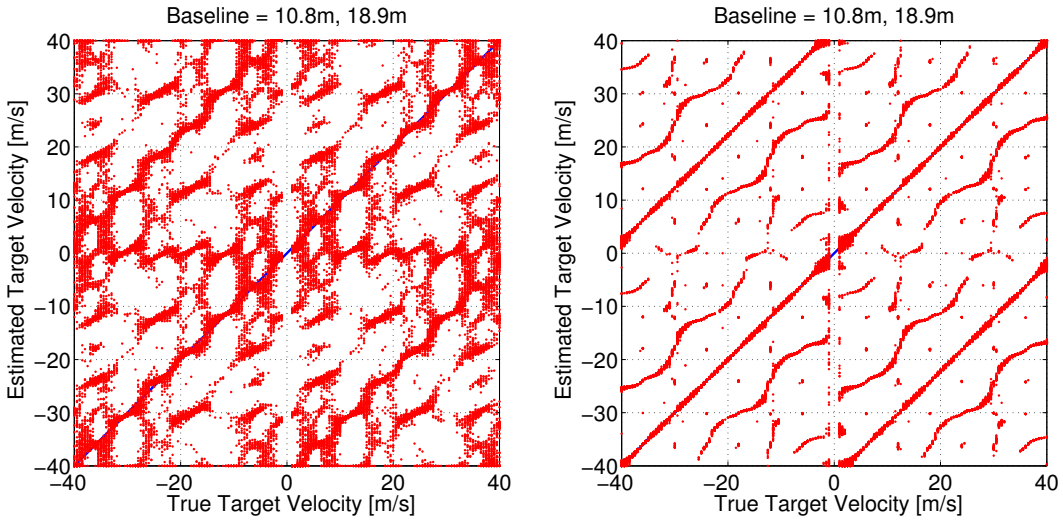

(a) Multi-channel ATI (b) Multi-channel DPCA-ATI

FIGURE 4.27: The estimated radial velocity. The input SCNR=0dB and CNR=15dB. 100 Monte Carlo iteration has been conducted, and each dot in the figure represents the estimated velocity at each iteration.

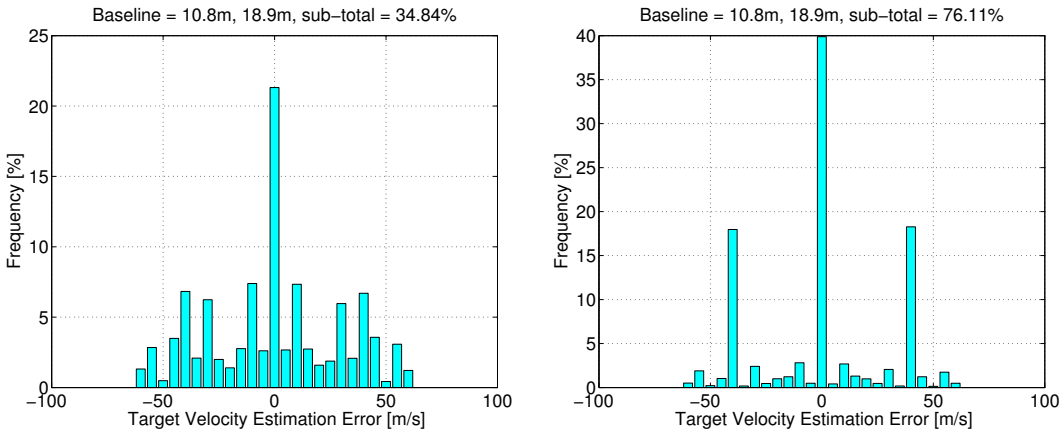

(a) Multi-channel ATI (b) Multi-channel DPCA-ATI

FIGURE 4.28: The histogram of the estimation error of the radial velocity. The input SCNR=0dB and CNR=15dB.

4.6 Conclusion

In this chapter, image based multi-channel SAR-GMTI algorithms, i.e., Multi-channel DPCA, Multi-channel ATI and Multi-channel DPCA-ATI, as well as along track velocity estimation method have been proposed.

Multi-channel DPCA is a deterministic algorithm which suppresses the clutter and azimuth ambiguity at the same time and achieves a high target detection performance. A notch type filter is constructed based on the orthogonal projection principle deterministically from the observation geometry and sensor parameter information, then it is applied to the registered and balanced multi-channel SAR images. Unlike adaptive algorithms such as STAP, the algorithm does not require uniform clutter covariance assumption, since it does not include covariance estimation process. As a consequence, the proposed Multi-channel DPCA successfully suppresses strong azimuth ambiguities, which tend to behave as isolated (and somewhat blurred) targets and deviate from the uniform clutter covariance assumption.

Multi-channel ATI is the set of ATI images of all the pairs of multi-channel SAR, and the target radial velocity is estimated by applying the matched filter bank to Multi-channel ATI output. Multi-channel DPCA-ATI is a combination of Muli-channel DPCA and Multi-channel ATI. The clutter suppressed signal is provided by Muli-channel DPCA as the input for the Multi-channel ATI. Both Multi-channel ATI and Multi-channel DPCA-ATI reduce the target radial velocity ambiguity by exploiting the multiple receive channel signals. The target radial velocity estimation performance of Multi-channel ATI is strongly affected by the clutter, on the other hand, Multi-channel DPCA-ATI is more robust to the clutter since the clutter and the azimuth ambiguity is suppressed in advance.

The proposed along track velocity estimation method works on the co-registered multi-channel SAR images and employ sub-aperture processing to enhance the robustness to the clutter and noise.

It has been observed in the experimental study using the airborne three-channel Ku-band SAR system that strong azimuth ambiguity gets suppressed more than 20dB by the Multi-channel DPCA. It has also been observed that the accuracy of the radial velocity estimation by the Multi-channel DPCA-ATI is on the order of 0.1m/s. Also, it has been shown that the accuracy of the along track velocity estimation of moving target at the range of about 2.5km is on the order of 0.2 m/s.

The statistical performance analysis has been performed under the scenario of three formation flight spaceborne SAR system with effective baselines of 10.8m and 18.9m, in order to provide rough estimates of the expected performance of the proposed algorithms for the spaceborne systems. The Multi-channel DPCA has been shown to detect moving targets with target radial velocity of $\pm$1m/s under input SCNR of -5dB with CNR of 15dB at $P_{\mathrm{d}} = 0.9$ and $P_{\mathrm{fa}} = 10^{-8}$, if the multilook number is 9. The radial velocity estimation performance of the Multi-channel ATI and Multi-channel DPCA-ATI has been evaluated via numerical simulation for SCNR=0dB and CNR=15dB case. It is shown that the estimation error is greatly reduced for the Multi-channel DPCA-ATI compared with the Multi-channel ATI. The radial velocity estimations of the Multi-channel DPCA-ATI concentrate to the true value and the velocity ambiguity which appears every 41m/s. If we compare with a conventional two channel system with the baseline on the order of 10m, which sufferes from the velocity ambiguity of every 11m/s, it can be said that the velocity ambiguity has been reduced by exploiting the multi-channel signals.

Chapter 5

Three-Dimensional Target Geometry And Target Motion Estimation Method Using Multistatic ISAR Movies

5.1 Introduction

Inverse synthetic aperture radar (ISAR) is one of the radar techniques used to observe two-dimensional images of a remotely based target using radio waves[54]. Recently, some algorithms on extracting three-dimensional geometry of the target from ISAR images have been proposed. They can roughly be categorized into three different types.

The first one is 3D ISAR, which is a direct extension of conventional ISAR. 3D ISAR gives the three dimensional distribution of the reflectivity of the target by extending the synthetic aperture to two dimensions. Since the precise knowledge of measurement geometry, including target motion, is required, this method is mainly suitable for the perfectly controlled situation such as turntable experiment [121]–[124].

The second one is interferometric ISAR (InISAR), which employs multiple receivers to generate multiple ISAR images. The locations of the scattering centers are determined by direction of arrival estimation methods [125]–[127]. Advantage of this method is that no knowledge of the target motion is required; however, the accuracy of the estimated geometry largely depends on the baseline between the receivers. In addition, motion compensation is required, in fact, in order to get the two ISAR images derived from corresponding antennas to be registered properly, and a motion compensation algorithm known as 3-D focusing has been proposed[128].

The third one utilizes a sequence of ISAR images, which we call ISAR movie. The authors have proposed an algorithm, which would be categorized into this type [129], [130]. The locations of the scattering centers are determined essentially by the track on the image plane. The three dimensional geometry can be estimated with relatively high accuracy, since the accuracy depends on the range and Doppler resolution of ISAR image; however, the algorithm requires a priori knowledge of the motion of the target. Cooke proposed a method that does not require the motion of the target; however, some constraints had to be put to solve the scaling ambiguity problem [131].

The problem of target motion estimation for ISAR imaging has also been addressed in some literatures in contexts of optimum imaging time selection, estimation of cross-range scaling, and so on [72]–[75]. Pastina et al. and Munoz-Ferreras et al. have proposed algorithms for the rotational motion estimation of ship targets [72]–[74]. These algorithms put almost no impact on the hardware requirement, but the application is limited to ship targets, i.e., some a priori knowledge of the basic shape of ships, such that there usually are a deck

and a mast, is exploited. On the other hand, a generic approach for the motion estimation is proposed by Stuff et al. [75]. This method is based on a range tracking of the scattering centers and no assumption is made on the target shape other than that it contains some prominent scattering centers. However, it requires a system with very high range resolution for accurate range tracking.

In this chapter, a novel method that estimates the relative motion and the three dimensional shape of the target using multistatic ISAR movie is proposed[132]. The proposed method utilizes at least three sets of sequence of ISAR images to estimate the aspect rotation of the target and the positions of point scatters that constitute the target. Unlike interferometric ISAR, the phase differences between the multistatic observations are used to estimate the target motion, rather than to estimate the locations of the scatterers.

The chapter is organized as follows. Section 5.2 gives the description of the observation geometry and signal model of the multistatic ISAR movie. Section 5.3 presents the proposed method, and Section 5.4 presents an example of numerical simulation to show the operation of the proposed method. Section 5.5 presents the performance evaluation. Finally, Section 5.6 provides the conclusion.

5.2 Geometry and signal model

Fig. 5.1 shows the geometry. We assume that the target is rigid and consists of K point scatterers, whose positions are denoted as $\bar{p}_k$ $(k = 1,2,\cdots,K)$. The aspect rotation of the target relative to the radar is assumed to be constant with angular velocity $\bar{\omega}$. If we put the origin O on the axis of the rotation, the velocity $\dot{\bar{p}}_k$ and the acceleration $\ddot{\bar{p}}_k$ of a point scatterer can be expressed as follows.

$$\dot{\bar{p}}_k = \bar{\omega} \times \bar{p}_k \tag{5.1}$$

$$\ddot{\bar{p}}_k = \bar{\omega} \times \dot{\bar{p}}_k = \bar{\omega} \times (\bar{\omega} \times \bar{p}_k) \tag{5.2}$$

In this paper, $\bar{x}$ denotes a vector, $\bar{\bar{A}}$ denotes a matrix, $\hat{x}$ denotes a unit vector and $\dot{x}$ denotes the time derivative of x.

The proposed method requires at least two auxiliary receiver antennas as shown in Fig. 5.1. Here, the antenna 0 transmits pulses and antennas 0, 1 and 2 receive the scattered pulses. Vectors $\bar{d}_1$ and $\bar{d}_2$ represent the baselines from antenna 0 to 1 and 2, respectively, $\hat{r}$ is a unit vector representing the radar line of sight from antenna 0 to the origin, and r_0 is the distance between antenna 0 and the origin. We assume r_0 is sufficiently large compared to the size of the target and baseline length.

$$r_0 \gg \|\bar{d}_1\|,\ \|\bar{d}_2\|,\ \|\bar{p}_k\| \qquad (\forall k, k = 1,2,\cdots,K) \tag{5.3}$$

Using the received signals, we obtain three ISAR movies as shown in Fig. 5.2. The signal from a point scatterer at position $\bar{p}_k$ would appear as a maximum at range r_{kn} and Doppler frequency $f_{\mathrm{d}kn}$ on the n-th frame of the ISAR movie observed by the antenna 0, and the range r_{kn}, Doppler frequency $f_{\mathrm{d}kn}$ satisfy following relationships:

$$r_{kn} = \|\bar{p}_k - \bar{a}_0\| - r_0 \approx \hat{r} \cdot \bar{p}_k \tag{5.4}$$

$$f_{\mathrm{d}kn} = -\frac{2\dot{r}_{kn}}{\lambda} \approx -\frac{2}{\lambda}\hat{r} \cdot \dot{\bar{p}}_k \quad (r_0 \gg \|\bar{p}_k\|) \tag{5.5}$$

where, λ is the wavelength. Note that we define $\bar{p}_k$ as the position of the k-th scatterer at the time when n-th frame is being observed. Also note that due to the condition of Eq. (5.3), r_{kn} and $f_{\mathrm{d}kn}$ observed by antennas 1 and 2 are nearly identical to those observed by antenna 0.

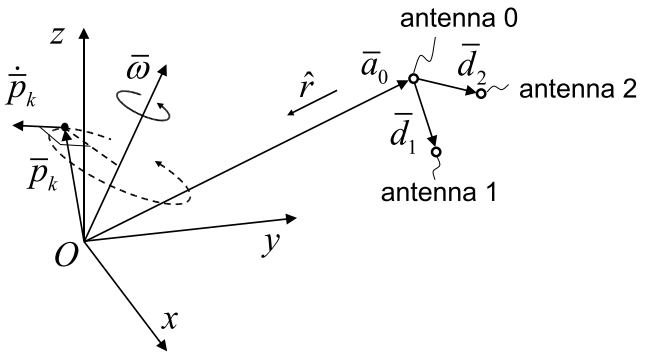

FIGURE 5.1: The observation geometry. The antenna 0 transmits pulses and antennas 0, 1 and 2 receive the scattered pulses. We assume that the target is rigid and consists of K point scatterers, whose positions are denoted as $\bar{p}_k$ $(k = 1,2,\cdots,K)$. The aspect rotation of the target relative to the radar is assumed to be constant with angular velocity $\bar{\omega}$.

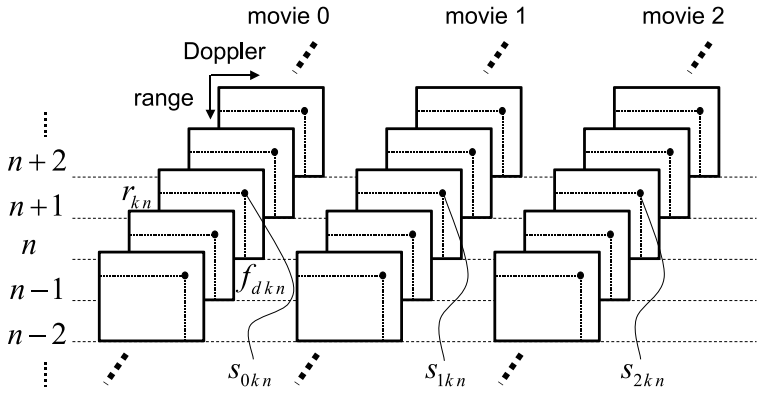

FIGURE 5.2: Three sets of ISAR Movies observed by the three receivers. The movies 0, 1 and 2 represent the ISAR movies obtained from the signals received by antennas 0, 1 and 2, respectively.

In addition, from the complex amplitudes at the maximum in the n-th frame, s_{0kn}, s_{1kn} and s_{2kn} (see Fig. 5.2), we observe the phase differences ϕ_{1kn}, ϕ_{2kn} as follows.

$$\phi_{jkn} = \angle\{s_{jkn}\cdot s_{0kn}^{*}\} \qquad (j=1,2) \tag{5.6}$$

The phase differences ϕ_{jkn} $(j=1,2)$ correspond to the angle of arrival in the direction of each baseline, and they satisfy following relationships.

$$\phi_{jkn} \approx \frac{2\pi}{\lambda}\frac{\bar{p}_k-\bar{a}_0}{\|\bar{p}_k-\bar{a}_0\|}\cdot\bar{d}_j \qquad (r_0 \gg \|\bar{d}_j\|) \tag{5.7}$$

The phase differences ϕ_{jkn} $(j=1,2)$ are time variant due to the aspect rotation of the target, and its rate of change can be expressed as follows.

$$\dot{\phi}_{jkn} = \frac{d\phi_{jkn}}{dt} \approx \frac{2\pi}{\lambda}\bar{d}_j\cdot\left(\bar{\bar{I}}-\hat{r}\hat{r}^T\right)\frac{\dot{\bar{p}}_k}{r_{kn}+r_0} \tag{5.8}$$

The following approximation has been utilized in the derivation of Eq. (5.8).

$$\frac{d}{dt}\frac{\bar{p}_k-\bar{a}_0}{\|\bar{p}_k-\bar{a}_0\|} \approx \left(\bar{\bar{I}}-\hat{r}\hat{r}^T\right)\frac{\dot{\bar{p}}_k}{r_{kn}+r_0} \qquad (r_0 \gg \|\bar{p}_k\|) \tag{5.9}$$

The rate of change of the phase differences $\dot{\phi}_{jkn}$ can be estimated from the phase differences observed in the N frames around n-th frame, ϕ_{jkm} $(m=n-\lfloor N/2\rfloor,\cdots,n+\lceil N/2\rceil-1)$; namely, if we let the frame interval (the inverse of frame rate) of the ISAR movie be t_{fr}, then $\dot{\phi}_{jkn}$ is estimated by least squares method as follows.

$$\dot{\phi}_{jkn} = \frac{\sum_m m\left(\phi_{jkm}-\langle\phi_{jk}\rangle\right)}{\sum_m m^2}\cdot\frac{1}{t_{\mathrm{fr}}} \qquad (j=1,2) \tag{5.10}$$

where, $\langle\phi_{jk}\rangle = \frac{1}{N}\sum_{m=n-\lfloor N/2\rfloor}^{n+\lceil N/2\rceil-1}\phi_{jkm}$. Here, we assume that the phase difference ϕ_{jkn} changes linearly over the N frames, which requires the observation time to be sufficiently short.

Furthermore, the observation of ISAR movie enables us to estimate the rate of change of Doppler frequency $\dot{f}_{\mathrm{d}kn}$ of the scatterers. Using the Doppler frequencies observed in the N frames around n-th frame, $f_{\mathrm{d}km}(m=n-\lfloor N/2\rfloor,\cdots,n+\lceil N/2\rceil-1)$, the rate of change of

Doppler frequency $\dot{f}_{\mathrm{d}kn}$ can be estimated by least squares method as follows.

$$\dot{f}_{\mathrm{d}kn} = \frac{\sum_m m\left(f_{\mathrm{d}km} - \langle f_{\mathrm{d}k}\rangle\right)}{\sum_m m^2} \cdot \frac{1}{t_{\mathrm{fr}}} \tag{5.11}$$

where, $\langle f_{\mathrm{d}k}\rangle = \frac{1}{N}\sum_{m=n-\lfloor N/2\rfloor}^{n+\lceil N/2\rceil-1} f_{\mathrm{d}km}$. Note that the rate of change of Doppler frequency $\dot{f}_{\mathrm{d}kn}$ satisfies the following relationship with the acceleration $\ddot{\vec{p}}_k$.

$$\dot{f}_{\mathrm{d}kn} \quad = \quad -\frac{2\ddot{r}_{kn}}{\lambda} \approx -\frac{2}{\lambda}\hat{r}\cdot\ddot{\vec{p}}_k \tag{5.12}$$

5.3 Algorithm

Based on the signal model shown in section 5.2, we propose an algorithm to estimate the target motion and 3D shape, i.e., the aspect rotation of the target $\bar{\omega}$ and the positions of the scatterers $\bar{p}_k$ $(k = 1,2,\cdots,K)$. The algorithm consists of two steps. In the first step, the velocity and the radial acceleration of each scatterer $\dot{\bar{p}}_k$, $\ddot{r}_k$ are estimated, and in the second step, $\bar{\omega}$ and $\bar{p}_k$ are obtained simultaneously.

Step 1: Estimation of the velocity and the radial acceleration of the scatterers $\dot{\bar{p}}_k$, $\ddot{r}_k$.

From Eqs. (5.5) and (5.8), we have following relationship.

$$\begin{bmatrix} -\frac{\lambda}{2} f_{dkn} \\ \frac{\dot{\phi}_{1kn}(r_{kn}+r_0)}{2\pi} \\ \frac{\dot{\phi}_{2kn}(r_{kn}+r_0)}{2\pi} \end{bmatrix} = \begin{bmatrix} \hat{r}^T \\ \frac{1}{\lambda}\bar{d}_1^T\left(\bar{\bar{I}} - \hat{r}\hat{r}^T\right) \\ \frac{1}{\lambda}\bar{d}_2^T\left(\bar{\bar{I}} - \hat{r}\hat{r}^T\right) \end{bmatrix} \dot{\bar{p}}_k \equiv \bar{\bar{A}}\,\dot{\bar{p}}_k \tag{5.13}$$

where, T denotes transpose of a matrix. Then the velocity of each scatterer can be estimated as follows.

$$\dot{\bar{p}}_k = \bar{\bar{A}}^{-1} \begin{bmatrix} -\frac{\lambda}{2} f_{dkn} \\ \frac{1}{2\pi}\dot{\phi}_{1kn}(r_{kn}+r_0) \\ \frac{1}{2\pi}\dot{\phi}_{2kn}(r_{kn}+r_0) \end{bmatrix} \tag{5.14}$$

Here, $\bar{d}_1$, $\bar{d}_2$ and λ are system parameters, $\hat{r}$ is an arbitrary unit vector; in fact, $\hat{r}$ defines the coordinate, and r_0, r_{kn}, f_{dkn} are observed from ISAR movie of antenna 0, and $\dot{\phi}_{1kn}$, $\dot{\phi}_{2kn}$ are estimated by Eq. (5.10).

The radial acceleration $\ddot{r}_k$ of the scatterers can be estimated according to Eq. (5.12) as follows.

$$\ddot{r}_{kn} = \hat{r}\cdot\ddot{\bar{p}}_k \left(= \hat{r}\cdot\{\bar{\omega}\times(\bar{\omega}\times\bar{p}_k)\}\right) = -\frac{\lambda\,\dot{f}_{dkn}}{2} \tag{5.15}$$

Note that the rate of change of Doppler frequency $\dot{f}_{dkn}$ can be estimated by Eq. (5.11).

Step 2: Estimation of the angular velocity $\bar{\omega}$ and the positions of the scatterers $\bar{p}_k$.

From Eqs. (5.1),(5.2),(5.4) and (5.15), we have following relationship. Note that we already have $\dot{\bar{p}}_k$, $\ddot{r}_k$ from the Step 1.

$$\begin{bmatrix} r_{kn} \\ \dot{\bar{p}}_k \\ \ddot{r}_{kn} \end{bmatrix} = \begin{bmatrix} \hat{r}^T \\ \bar{\bar{\Omega}} \\ \hat{r}^T\bar{\bar{\Omega}}\bar{\bar{\Omega}} \end{bmatrix} \bar{p}_k \equiv \bar{\bar{B}}\bar{p}_k \quad (k = 1,\cdots,K) \tag{5.16}$$

where, $\bar{\bar{\Omega}}\bar{p} = \bar{\omega}\times\bar{p}$ and $\bar{\bar{\Omega}}\bar{\bar{\Omega}}\bar{p} = \bar{\omega}\times(\bar{\omega}\times\bar{p})$. In Eq. (5.16), we have $3+3K$ unknown parameters, $\bar{\omega}$ and $\bar{p}_k(k = 1,\cdots,K)$. On the other hand, noting that the rank of $\bar{\bar{\Omega}}$ is 2, the number of independent equations is $4K$. Therefore, the following condition is required.

$$4K \geq 3+3K \quad \Leftrightarrow \quad K \geq 3 \tag{5.17}$$

Namely, we need at least 3 scatterers on the target. Further conditions are described later in this section.

Eq. (5.16) could be solved numerically by general optimization methods, but noting that $\dot{\bar{p}}_k \perp \bar{\omega}, \forall k$, we have developed a more efficient method. We first estimate only the direction of the axis of the rotation $\hat{\omega}$ by finding a vector orthogonal to all the velocity vectors $\dot{\bar{p}}_k$ and solve for the remaining parameters afterwards. The orthogonal vector can be found by

applying the principal component analysis to $\dot{\bar{p}}_k$ ($k = 1, 2, \cdots, K$). Namely, we first obtain the covariance matrix:

$$\bar{\bar{V}}_n = \frac{1}{K} \sum_{k=1}^{K} \dot{\bar{p}}_k \dot{\bar{p}}_k^T, \tag{5.18}$$

and find the eigenvector $\bar{v}$ corresponding to the minimum eigenvalue. Then $\bar{v}$ would be the optimum estimation of $\hat{\bar{\omega}}$ in the least squares sense. Having the estimate of $\hat{\bar{\omega}}$, Eq. (5.16) can be solved by linear least squares method with an assumption of the magnitude of the angular velocity $\|\bar{\omega}\|$.

$$\bar{p}_k \left(\|\bar{\omega}\| \right) = \left(\bar{\bar{B}}^T \bar{\bar{B}} \right)^{-1} \bar{\bar{B}}^T \begin{bmatrix} r_{kn} \\ \dot{\bar{p}}_k \\ \ddot{r}_{kn} \end{bmatrix} \tag{5.19}$$

where,

$$\bar{\bar{\Omega}} \bar{p} = \bar{\omega} \times \bar{p} = \|\bar{\omega}\| \hat{\bar{\omega}} \times \bar{p} \tag{5.20}$$

Note that the mean square error of the solution is given by:

$$\varepsilon \left(\|\bar{\omega}\| \right) = \left\| \begin{bmatrix} r_{kn} \\ \dot{\bar{p}}_k \\ \ddot{r}_{kn} \end{bmatrix} - \bar{\bar{B}} \bar{p}_k \left(\|\bar{\omega}\| \right) \right\|^2. \tag{5.21}$$

Then, with the search over reasonable range for $\|\bar{\omega}\|$, we can find the final estimation as follows.

$$\bar{p}_k = \bar{p}_k \left(\|\bar{\omega}\|_m \right), \text{ where, } \|\bar{\omega}\|_m = \operatorname{argmin} \left\{ \varepsilon \left(\|\bar{\omega}\| \right) \right\} \tag{5.22}$$

The advantage of this method is that the numerical search is done over just one dimension.

The conditions required on the observation geometry.

In the Step 1, in order for $\bar{\bar{A}}$ to be invertible, the following conditions must hold.

$$\bar{d}_1 \nparallel \bar{d}_2, \quad \hat{r} \neq \alpha \bar{d}_1 + \beta \bar{d}_2 \ (\forall \alpha, \beta \in \mathbb{R}) \tag{5.23}$$

That is, the two baselines are not parallel, and the radar line of sight is not on the plane spanned by the two baselines.

In the Step 2, in order for Eq. (5.16) to have $4K$ independent equations, the following conditions must hold.

$$\hat{r} \cdot \bar{\omega} \neq 0, \qquad \hat{r} \nparallel \bar{\omega} \tag{5.24}$$

That is, the radar line of sight needs to be neither coincide with nor orthogonal to the axis of the target aspect rotation.

5.4 Simulation

In this section, we present one example of numerical simulation to show the behavior of the proposed method. The conditions of the simulation are shown in Table 5.1. The radar line of sight $\hat{r}$ and the baselines $\bar{d}_1$[m], $\bar{d}_2$[m] are set to be as follows.

$$\hat{r} = \begin{bmatrix} 1 \\ 0 \\ 0 \end{bmatrix}, \bar{d}_1 = \begin{bmatrix} 0 \\ 2 \\ 0 \end{bmatrix}, \bar{d}_2 = \begin{bmatrix} 0 \\ 0 \\ 2 \end{bmatrix}, \tag{5.25}$$

From the conditions shown in Table 5.1, observation time per one frame is $T = Ht_{\text{pri}} = 1.28$sec, the total observation time for the 5 frames is $Ht_{\text{pri}} + (N-1)t_{\text{fr}} = 3.84$sec, and the total number of hits is $M = 3.84/t_{\text{pri}} = 384$. The range resolution of the ISAR image is $\Delta r = c/2B = 1.5$m, and the Doppler resolution of the ISAR image is $\Delta f_{\text{d}} = 1/T = 0.78$Hz.

TABLE 5.1: The simulation conditions.

parameter	value
baseline $\|\bar{d}_1\|$	2m
baseline $\|\bar{d}_2\|$	2m
center frequency f_c	33GHz
bandwidth B	100MHz
PRI(t_{pri})	0.01sec
the number of hits per frame H	128
frame interval t_{fr}	0.64sec
the number of frames N	5
the number of scatterers K	6
SNR(before Doppler processing)	40dB
target range r_0	5km
angular velocity $\bar{\omega}$	$[15\ \ 0\ \ 15]^T$ mrad/sec

Fig. 5.3 shows the first and the last frame of the simulated ISAR movie observed by the antenna 0. The signal has been modeled as point scatterers and additive white Gaussian noise (WGN). The magnitude images observed by the antennas 1 and 2 ,not shown here, are almost indistinguishable from that observed by the antenna 0, since the baseline is sufficiently short compared to the target range. From Fig. 5.3, we can see that the relative positions of the point target signal slightly varies with frames. The location of the signal of each point scatterer has been associated from frame to frame by simple nearest neighbor tracking.

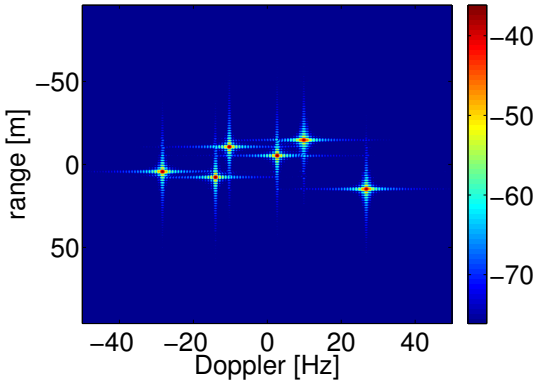

(a) The first frame

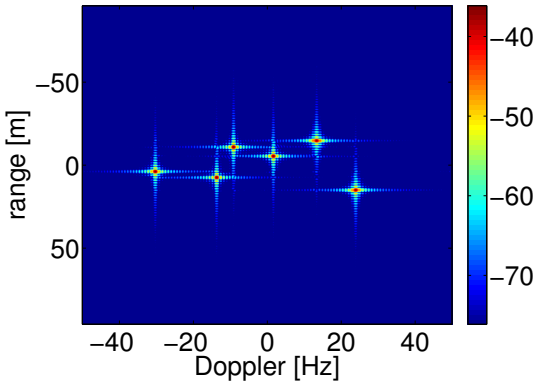

(b) The last (fifth) frame

FIGURE 5.3: The first and the last frame of the simulated ISAR movie observed by the antenna 0. The signal has been modeled as point scatterers and additive white Gaussian noise (WGN). The magnitude images observed by the antennas 1 and 2 ,not shown here, are almost indistinguishable from that observed by the antenna 0, since the baseline is sufficiently short compared to the target range.

Fig. 5.4 shows the result of line fitting to the history of phase differences and the Doppler frequency. In Fig. 5.4, the horizontal axis represents the frame number and the vertical axis represents the phase difference or the Doppler frequency. In Fig. 5.4(a) and (b), the circular plot show the observed phase differences ϕ_{1kn} and the observed Doppler frequency f_{dkn} of each point scatterer, respectively. Here, the color represents each point scatterer. From Fig. 5.4, it can be seen that time dependency of the phase difference or the Doppler frequency are almost linear and that the rate of changes of these values have been well estimated.

Fig. 5.5 shows the estimated positions of the point scatterers along with the given (true) positions. A good agreement is observed in the figure. The estimated angular velocity $\bar{\omega}$ has been $\begin{bmatrix}16.1 & 0.0 & 16.0\end{bmatrix}^T$ mrad/sec.

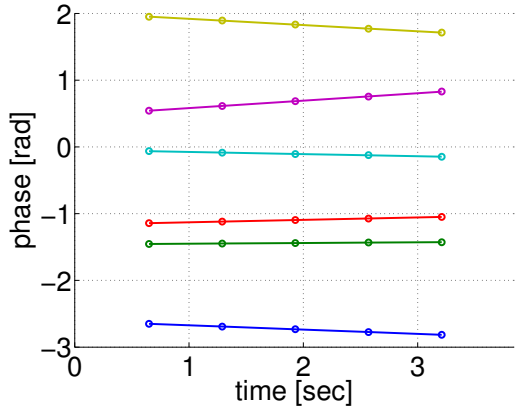

(a) The phase difference ϕ_1

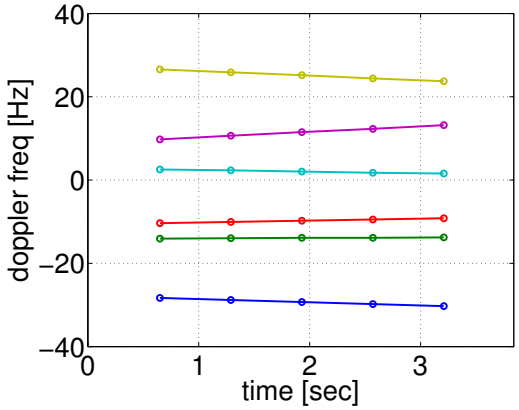

(b) The Doppler frequency f_d

FIGURE 5.4: The estimation result of the rate of change of the phase differences and the Doppler frequency.

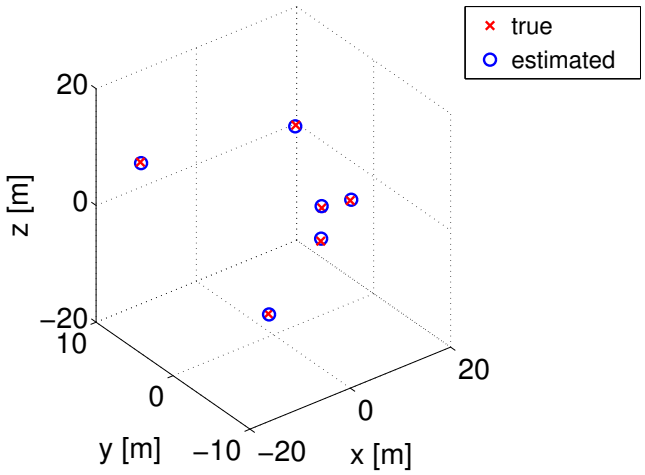

FIGURE 5.5: The estimated positions of the point scatterers along with the given (true) positions. A good agreement is observed in the figure.

5.5 Performance Estimation

The performance estimation of the proposed method is provided in this section. Firstly, the estimation accuracies of the positions of the scatterers and the angular velocity are investigated. The argument here is valid for a target consisting of few prominent scatterers that are sufficiently separated from each other. Secondly, we consider a more realistic scenario with more scatterers on the target and discuss the performance degradation caused by the target scintillation.

5.5.1 The estimation accuracies of the positions of the scatterers and the angular velocity

The estimation accuracies of target velocity $\dot{\bar{p}}_k$ and the radial acceleration $\ddot{r}_k$ estimated in the Step 1 are specified by Cramér-Rao Lower Bound (CRLB). The estimation accuracies of angular velocity $\bar{\omega}$ and the positions of the scatterers $\bar{p}_k$ estimated in the Step 2 are evaluated using numerical simulations.

Since the following analysis is independent of the frame number n, subscript n is omitted hereafter; e.g., $\bar{p}_{kn}$ is expressed as $\bar{p}_k$ and so on.

Step 1 : Expected estimation accuracies of the target velocity $\dot{\bar{p}}_k$ and the radial acceleration $\ddot{r}_k$

First, estimation accuracies of the range and the Doppler frequency r_k and $f_{\mathrm{d}k}$, the rate of change of the phase differences $\dot{\phi}_{1k}$, $\dot{\phi}_{2k}$ and the rate of change of Doppler frequency $\dot{f}_{\mathrm{d}k}$ are evaluated. These are the values directly estimated from the ISAR movie.

In the following discussion, SNR η refers to the signal to noise power ratio after range compression and before Doppler processing. The transmit signal is assumed to have constant spectrum with bandwidth B. The scatterers on the target are assumed to be well separated relative to the range and Doppler resolution of the system.

The CRLB for the target range r_k is given as follows[53].

$$\mathrm{CRLB}\{r_k\} = \left(\frac{c}{2}\right)^2 \cdot \frac{6}{4\pi^2 \eta B^2} \tag{5.26}$$

where, c is the speed of light.

The CRLB for the Doppler frequency $f_{\mathrm{d}k}$ and the rate of change of Doppler frequency $\dot{f}_{\mathrm{d}k}$ is derived. The signal corresponding to the range cell that contains the k-th scatterer can be expressed as follows[1].

$$\begin{aligned} x_{0k}[m] &= s_{0k} \exp\left[-j\left\{2\pi f_{\mathrm{d}k} m t_{\mathrm{pri}} + 2\pi \frac{\dot{f}_{\mathrm{d}k}}{2}(m t_{\mathrm{pri}})^2\right\}\right] \\ &\quad + w_0[m], \quad \left(-\frac{M-1}{2} \le m \le \frac{M-1}{2}\right) \end{aligned} \tag{5.27}$$

where, m is the pulse number, M is the total number of hits to observe the ISAR movie, and $w_0[m]$ is WGN with variance σ^2. Here, we assume that $f_{\mathrm{d}k}$ and $\dot{f}_{\mathrm{d}k}$ are estimated using the ISAR movie observed by the antenna 0; therefore, the complex amplitude of the signal is expressed by s_{0k}.

[1] The derivation of the CRLB is given in Appendix C.1.

According to the signal model given by Eq. (5.27), the CRLB for f_{dk} and $\dot{f}_{dk}$ is obtained as follows.

$$\mathrm{CRLB}\{f_{dk}\} = \frac{6}{4\pi^2 t_{\mathrm{pri}}^2 \eta M(M^2-1)} \tag{5.28}$$

$$\mathrm{CRLB}\left\{\dot{f}_{dk}\right\} = \frac{90}{\pi^2 t_{\mathrm{pri}}^4 \eta M(M^2-1)(M^2-4)} \tag{5.29}$$

Next, the CRLB for the rate of change of phase differences $\dot{\phi}_{1k}$, $\dot{\phi}_{2k}$ is obtained. Here, the signals of antenna 0 and antenna i ($i = 1,2$) are expressed as follows.

$$x_{0k}[m] = s_{0k}\exp\left(-j\phi[m]\right) + w_o[m] \tag{5.30}$$

$$x_{ik}[m] = s_{ik}\exp\left[-j\left\{\phi[m] + \phi_{ik} + \dot{\phi}_{ik} m t_{\mathrm{pri}}\right\}\right] + w_i[m], \quad \left(-\frac{M-1}{2} \le m \le \frac{M-1}{2}\right) \tag{5.31}$$

where, $w_0[n]$, $w_i[n]$ are mutually independent WGN with variance σ^2. According to the signal models given by Eqs. (5.30), (5.31), the CRLB for $\dot{\phi}_{ik}$ ($i = 1,2$) is obtained as follows[2]

$$\mathrm{CRLB}\left\{\dot{\phi}_{ik}\right\} = \frac{12}{t_{\mathrm{pri}}^2 \eta M(M^2-1)} \tag{5.32}$$

Finally, the CRLB for the target velocity $\dot{\bar{p}}_k$ and the radial acceleration $\ddot{r}_k$ is derived. The error sensitivity of $\dot{\bar{p}}_k$ and $\ddot{r}_k$ to the values directly observed from the ISAR movie are derived from Eqs. (5.14),(5.15) as follows.

$$\frac{\partial \dot{\bar{p}}_k}{\partial f_{dk}} = -\frac{\lambda}{2}\bar{\bar{A}}^{-1}\begin{bmatrix}1\\0\\0\end{bmatrix} \tag{5.33}$$

$$\frac{\partial \dot{\bar{p}}_k}{\partial \dot{\phi}_{1k}} = \frac{1}{2\pi}(r_k + r_0)\bar{\bar{A}}^{-1}\begin{bmatrix}0\\1\\0\end{bmatrix} \tag{5.34}$$

$$\frac{\partial \dot{\bar{p}}_k}{\partial \dot{\phi}_{2k}} = \frac{1}{2\pi}(r_k + r_0)\bar{\bar{A}}^{-1}\begin{bmatrix}0\\0\\1\end{bmatrix} \tag{5.35}$$

$$\frac{\partial \dot{\bar{p}}_k}{\partial r_k} = \frac{1}{2\pi}\bar{\bar{A}}^{-1}\begin{bmatrix}0\\\dot{\phi}_{1k}\\\dot{\phi}_{2k}\end{bmatrix} \tag{5.36}$$

$$\frac{\partial \ddot{r}_k}{\partial \dot{f}_{\mathrm{d}}} = -\frac{\lambda}{2} \tag{5.37}$$

$$\frac{\partial \dot{\bar{p}}_k}{\partial \dot{f}_{\mathrm{d}}} = 0, \quad \frac{\partial \ddot{r}_k}{\partial f_{dk}} = \frac{\partial \ddot{r}_k}{\partial \dot{\phi}_{1k}} = \frac{\partial \ddot{r}_k}{\partial \dot{\phi}_{2k}} = \frac{\partial \ddot{r}_k}{\partial r_k} = 0 \tag{5.38}$$

[2]The derivation of the CRLB is given in Appendix C.2.

In the following discussion, we introduce vector form representations of the parameters $\bar{g}_k$ and $\bar{b}_k$, which are defined as follows.

$$\bar{g}_k = \begin{bmatrix} r_k \\ f_{\mathrm{d}k} \\ \dot{\phi}_{1k} \\ \dot{\phi}_{2k} \\ \dot{f}_{\mathrm{d}k} \end{bmatrix}, \quad \bar{b}_k = \begin{bmatrix} r_k \\ \dot{\bar{p}}_k \\ \ddot{r}_k \end{bmatrix}, \quad (k = 1, \cdots, K) \tag{5.39}$$

The vector $\bar{g}_k$ is a collection of the parameters estimated directly from ISAR movie, and the vector $\bar{b}_k$ is a collection of the parameters estimated in the Step 1, i.e., the input to the Step 2, Note that $\bar{b}_k$ includes not only $\dot{\bar{p}}_k$ and $\ddot{r}_k$ but also r_k.

The CRLB for $\bar{b}_k$ can be expressed using the CRLB for $\bar{g}_k$ as follows.

$$\mathrm{CRLB}\left\{\bar{b}_k\right\} = \left(\frac{d\bar{b}_k}{d\bar{g}_k}\right) \mathrm{CRLB}\left\{\bar{g}_k\right\} \left(\frac{d\bar{b}_k}{d\bar{g}_k}\right)^T \tag{5.40}$$

where, $\mathrm{CRLB}\left\{\bar{g}_k\right\}$ is a diagonal matrix whose diagonal elements are the CRLB given by Eqs. (5.26), (5.28), (5.29) and (5.32), and $d\bar{b}_k / d\bar{g}_k$ is the error sensitivity matrix whose elements are given by Eqs. (5.33)–(5.38). The limit of the estimation accuracy of $\bar{b}_k$, i.e., the input to the Step 2, is given by Eq. (5.40).

Some numerical examples are provided below. The system parameters in Table 5.1 are assumed; in addition, the radar line of sight and the two baselines are assumed to be orthogonal with each other for the sake of simplicity.

$$\hat{r} = \begin{bmatrix} 1 \\ 0 \\ 0 \end{bmatrix}, \quad \bar{d}_1 = \begin{bmatrix} 0 \\ d \\ 0 \end{bmatrix}, \quad \bar{d}_2 = \begin{bmatrix} 0 \\ 0 \\ d \end{bmatrix} \tag{5.41}$$

The error sensitivity of $\dot{\bar{p}}_k$ is analyzed using Eqs. (5.33)–(5.36). Substituting Eqs. (5.33)–(5.36) by Eq. (5.41), we obtain the following relations.

$$\begin{aligned} \frac{\partial \dot{\bar{p}}_k}{\partial f_{dk}} &= -\frac{\lambda}{2} \begin{bmatrix} 1 \\ 0 \\ 0 \end{bmatrix} \\ \frac{\partial \dot{\bar{p}}_k}{\partial \dot{\phi}_{1k}} &= \frac{1}{2\pi} \cdot \frac{\lambda (r_k + r_0)}{d} \begin{bmatrix} 0 \\ 1 \\ 0 \end{bmatrix} \\ \frac{\partial \dot{\bar{p}}_k}{\partial \dot{\phi}_{2k}} &= \frac{1}{2\pi} \cdot \frac{\lambda (r_k + r_0)}{d} \begin{bmatrix} 0 \\ 0 \\ 1 \end{bmatrix} \\ \frac{\partial \dot{\bar{p}}_k}{\partial r_k} &= \frac{1}{2\pi} \cdot \frac{\lambda}{d} \begin{bmatrix} 0 \\ \dot{\phi}_{1k} \\ \dot{\phi}_{2k} \end{bmatrix} \end{aligned} \tag{5.42}$$

From Eq. (5.42), one can see that the radial velocity estimation accuracy is determined by the accuracy of the Doppler frequency estimation. The velocity estimation is not very sensitive to the estimation error of the range r_k, because λ / d, $\dot{\phi}_{1k}$ and $\dot{\phi}_{2k}$ are relatively small values, while it would be fairly sensitive to the estimation error of $\dot{\phi}_{1k}$ and $\dot{\phi}_{2k}$, since $r_0 \gg d$.

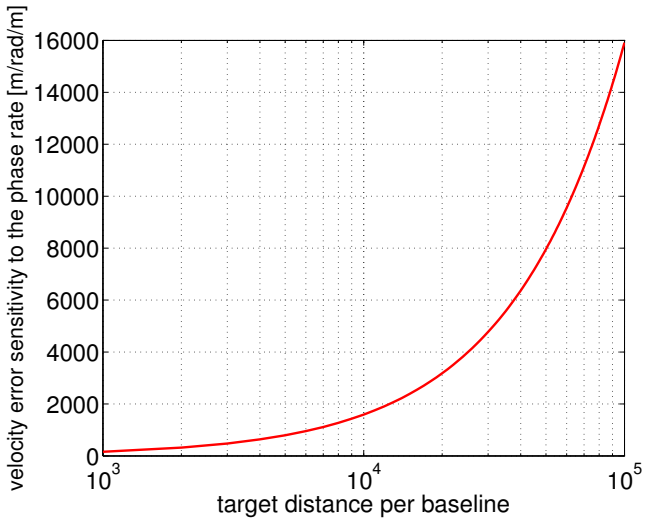

FIGURE 5.6: The sensitivity of the velocity estimation to the estimation error of the rate of phase difference as a function of target distance normalized by the baseline length.

Fig. 5.6 shows the sensitivity of the velocity estimation to the estimation error of the rate of change of the phase difference. The horizontal axis represents the target distance normalized by the baseline and the vertical axis represents the error sensitivity normalized by the wavelength. It can be seen from Fig. 5.6 that the error sensitivity grows rapidly with the target distance relative to the baseline. If the target range and the baseline are 5 km and 2m, respectively, and the wavelength is 9.1mm as in the case of Table 5.1, the error sensitivity would be 3.6 m/rad. This suggests that if the estimation error of the rate of change of the phase difference is 3mrad/sec, then the corresponding velocity estimation error would be 0.01m/sec.

Next, the CRLB expressed by Eqs. (5.26), (5.28), (5.29) and (5.32), are shown in Fig. 5.7. The horizontal axis represents SNR and the vertical axis represents the CRLB. From Fig. 5.7 it is clear that the CRLB for all the parameters become smaller with higher SNR.

Fig. 5.8 (a), (b) shows the evaluated CRLB for $\dot{\tilde{p}}_k$ and $\ddot{r}_k$ as functions of SNR. Fig. 5.8 (c), (d) shows the evaluated CRLB for $\dot{\tilde{p}}_k$ and $\ddot{r}_k$ as functions of incidence angle Φ. The incidence angle Φ is the angle between the target's rotation axis and radar line of sight, as defined in the Fig. 5.9. In Fig. 5.8 (a), (b), the incidence angle Φ is set to be 45°, and in Fig. 5.8 (c), (d), SNR is set to be 25dB. From Fig. 5.8 (a), (b), it can be seen that the CRLB for $\dot{\tilde{p}}_k$ and $\ddot{r}_k$ become smaller with higher SNR, and if SNR=25dB, the square root of the CRLB for $\dot{\tilde{p}}_k$ and $\ddot{r}_k$ are 0.027 m/sec and 2.7×10^{-6} m/sec^2, respectively. In Fig. 5.8 (a), the x and y components of $\dot{\tilde{p}}_k$ coincide with each other, it can be seen in Fig. 5.8 (c) that the CRLB for the x and y components of $\dot{\tilde{p}}_k$ coincides at $\Phi = 45^\circ$. Fig. 5.8 (c) shows that at $\Phi = 0^\circ$, the CRLB for the x and y components of $\dot{\tilde{p}}_k$ are equal. This is because both the x and y components are estimated from the rate of change of the phase differences. Also note that, in this case, the CRLB for the z component of $\dot{\tilde{p}}_k$ is relatively small, because the z component of $\dot{\tilde{p}}_k$ is directly estimated from the Doppler frequency. Fig. 5.8 (d) shows that the CRLB for $\ddot{r}_k$ is independent of Φ, which is trivial.

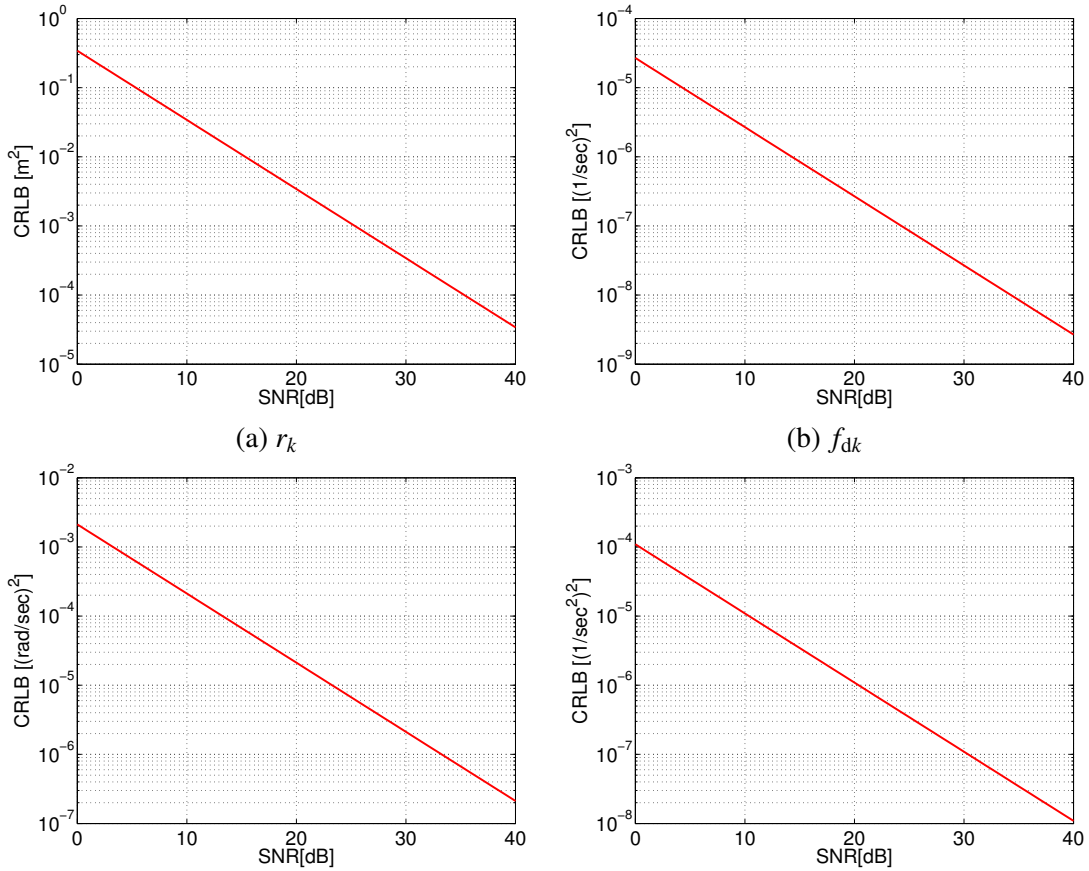

(a) r_k (b) f_{dk}

(c) $\dot{\phi}_{ik}$ $(i = 1,2)$ (d) $\dot{f}_{dk}$

FIGURE 5.7: The CRLB for the parameters directly estimated from the ISAR movies as functions of SNR.

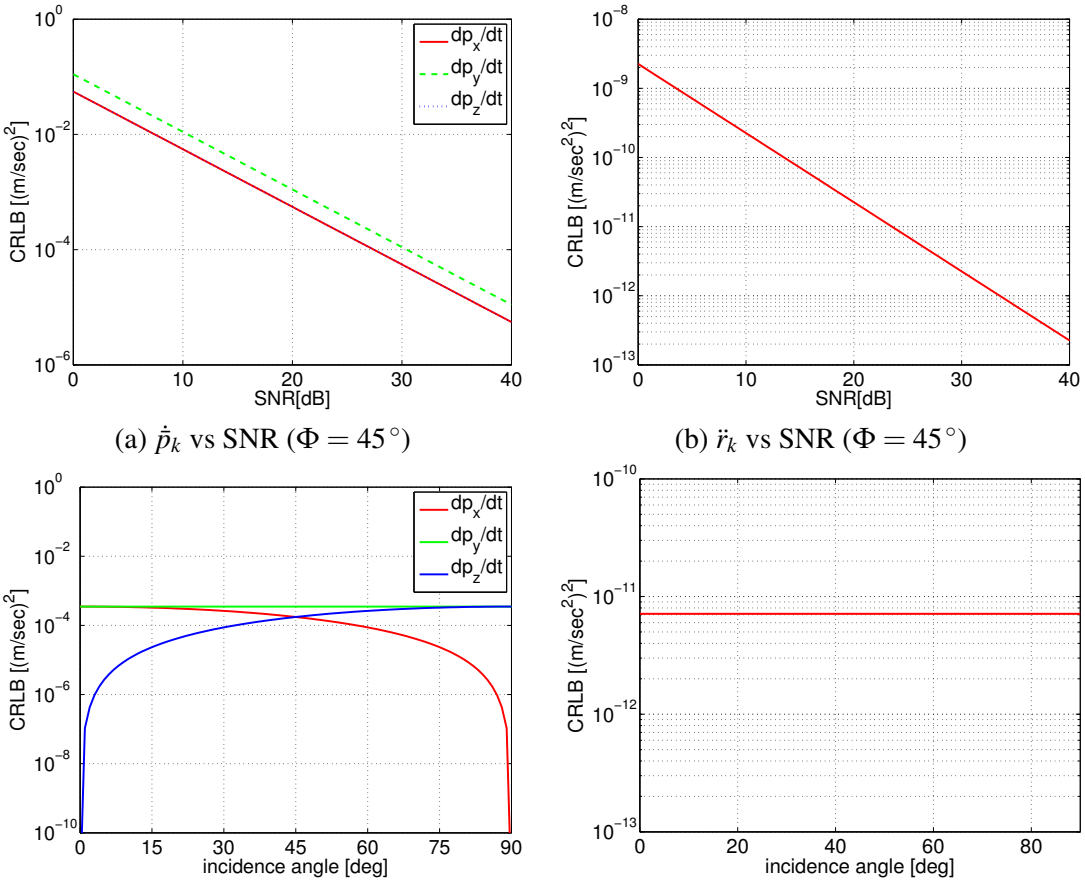

(a) $\dot{\bar{p}}_k$ vs SNR ($\Phi = 45^\circ$)

(b) $\ddot{r}_k$ vs SNR ($\Phi = 45^\circ$)

(c) $\dot{\bar{p}}_k$ vs Φ (SNR=25dB)

(d) $\ddot{r}_k$ vs Φ (SNR=25dB)

FIGURE 5.8: The CRLB for the parameters estimated in the Step 1 as functions of SNR and incidence angle Φ.

Step 2: The estimation accuracies of the scatterer position and angular velocity

The estimation accuracies of the angular velocity $\bar{\omega}$ and the scatterer position $\bar{p}_k$ are evaluated via numerical simulations. In this simulation, the process of the Step 1 is not conducted; instead, the estimation error is added to the input of the Step 2. Namely the input vector $\tilde{b}_k$ is given as follows.

$$\tilde{b}_k = \bar{b}_k + \Delta\bar{b}_k, \tag{5.43}$$

where, $\Delta\bar{b}_k$ is zero mean WGN with covariance matrix given by CRLB$\{\bar{b}_k\}$.

In this simulation, the parameters given in Table 5.1 is employed again. Fig. 5.9 shows the geometry. As shown in Fig. 5.9, the z axis corresponds to the rotation axis, and the angle Φ between the rotation axis and the radar position vector is called incidence angle for convenience' sake. The target consists of six point scatterers distributed uniformly within 20m cube. The positions of the scatterers are redefined each trial. The dominant factors that influences the estimation accuracy of $\bar{\omega}$ and $\bar{p}_k$ are the geometry (especially the incidence angle Φ) and the estimation errors included in the estimates of the Step 1 that are caused by noise. Therefore, the performance is evaluated over the SNR and the incidence angle Φ as parameters.

Fig. 5.10 shows the result of the performance estimation over SNR. The vertical axis shows the standard deviation of the position estimation error [3] and rmse (root mean square error) of the angular velocity estimation. In this case, the incidence angle $\Phi = 45^\circ$ and 10,000 Monte Carlo iterations were performed. In Fig. 5.10, 'total' shows the error, and 'x,y,z' shows the x, y, z component of the error, respectively. From Fig. 5.10 (a), (b), one can see that in order to obtain high accuracy, relatively high SNR is required. If SNR is higher than 30dB, the standard deviation of the position estimation error is smaller than 1m, which is comparable to the range resolution of the system. The rmse of the estimation of the angular velocity is also very small (smaller than 0.002rad/s), if SNR is higher than 30dB. On the other hand, the estimation error of the target position grows rapidly where SNR is lower than

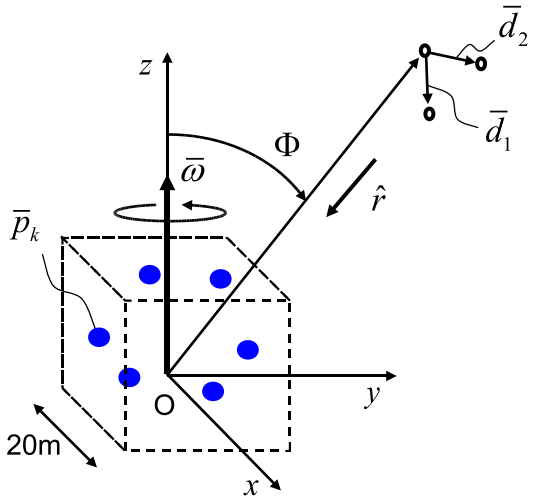

FIGURE 5.9: The geometry used in the simulation. The z axis corresponds to the rotation axis, and the angle Φ between the rotation axis and the radar position vector is called incidence angle for convenience' sake. The target consists of six point scatterers distributed uniformly within 20m cube.

[3]The position estimation error is evaluated by standard deviation, since the bias error does not distort the estimated shape of the target.

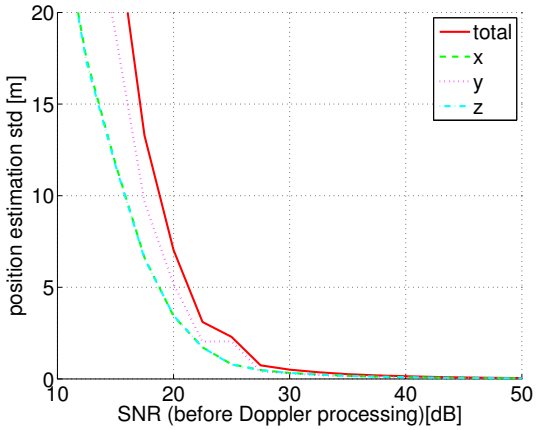

(a) The standard deviation of the position estimation error

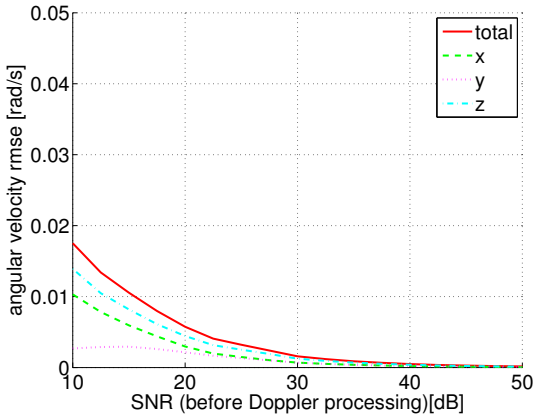

(b) The rmse of the angular velocity estimation

FIGURE 5.10: The estimation error of the target positions and angular velocity as functions of SNR with incidence angle $\Phi = 45^\circ$.

25dB, e.g., the standard deviation of the position estimation error is about 7m when SNR is 20dB.

Fig. 5.11 shows the result of the performance estimation over incidence angle Φ. In this case, SNR is 25dB and 10,000 Monte Carlo iterations were performed. From Fig. 5.11 (a) the position estimation error is fairly small if $\Phi = 5^\circ \sim 50^\circ$; the position estimation error is smaller than approximately 1.5m. On the other hand, the error is large when the incidence angle Φ is near 0° or 90°. This is because the condition given by Eq. (5.24) is violated at $\Phi = 0^\circ, 90^\circ$. Note that the position estimation error is only about 5m at $\Phi = 0$, despite the condition given by Eq. (5.24) is violated. At $\Phi = 0$, Doppler frequency of all the point scatterers are zero; therefore, the estimated positions of the scatterers are essentially all aligned on the radar line of sight. Since all the point scatterers are within the 20m cube, the estimation error does not exceed approximately $10\sqrt{2}$m. As a result, the standard deviation of the position error is 5m at $\Phi = 0^\circ$, Fig. 5.11 (b) shows that the rmse of the angular velocity estimation is almost constant at about 0.002rad/s if the incidence angle is larger than 5° and diverges if the incidence angle is near 0°.

Observing the x, y, z components of the position estimation error shown in Fig. 5.11 (a), (b) gives more insight to the performance of the proposed method. If incidence angle is near 90°, z component of the position estimation error is larger than others. This is because the range r_k, the velocity $\dot{\vec{p}}_k$ and the radial acceleration $\ddot{r}_k$ are all observed in x-y plane in this

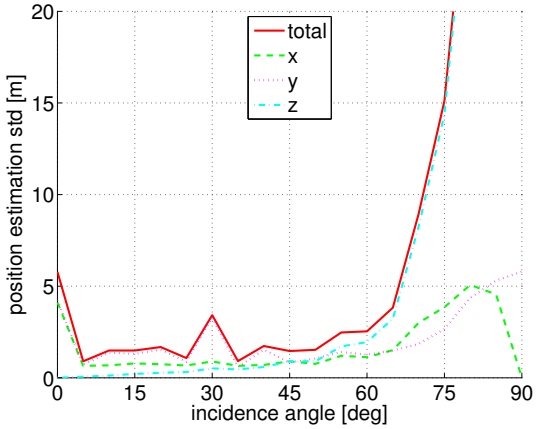

(a) The standard deviation of the position estimation error

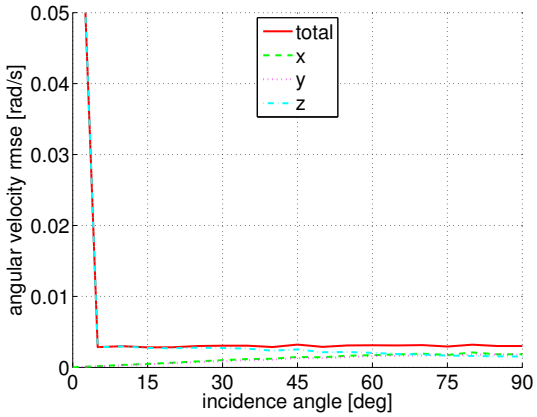

(b) The rmse of the angular velocity estimation

FIGURE 5.11: The estimation error of the target positions and angular velocity as functions of incidence angle Φ with SNR=25dB.

case, and no information about z component is obtained. On the other hand, if the incidence angle is near 0°, the x and y components of the position estimation error are larger, and the z component of the position estimation error is relatively small. This is because z can be directly estimated from the radar range measurement, and no information about the rotational motion of the target can be observed, which causes the x and y components of the position estimation error to be large as well as the z component of angular velocity estimation error.

5.5.2 The performance estimation using an aircraft polygon model

The performance of the proposed method for the case where the target consists of more scatterers is investigated in this section. In this case, target scintillation effect, in other words, the interference between the neighboring scattering centers, may cause some performance degradation. A sample result and a discussion on the effect of the target scintillation on the proposed method is given below. We take an aircraft polygon model, whose shape is shown in Fig. 5.12, and simulate the scattered signal according to the geometrical theory of diffraction (GTD). Table 5.2 shows the simulation conditions. Here, the incidence angle θ and the horizontal aspect angle ψ determine the radar line of sight by $\hat{r} = -[\sin\theta\cos\psi \quad \sin\theta\sin\psi \quad \cos\theta]^T$. No noise has been added, so the main cause of the estimation error is the scintillation effect.

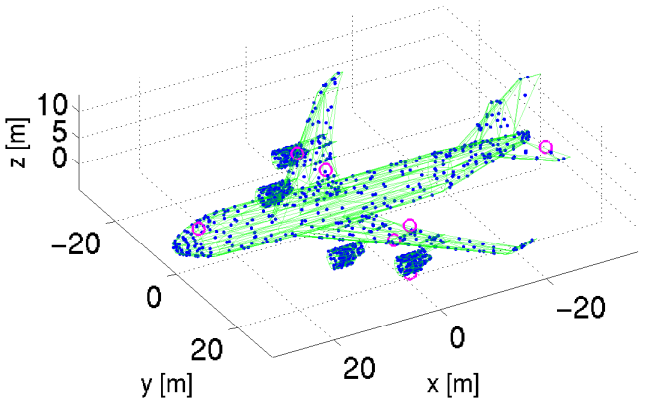

FIGURE 5.12: Aircraft polygon model

TABLE 5.2: The simulation conditions for the aircraft simulation case.

parameter	value
baseline $\|\|\bar{d}_1\|\|$	2m
baseline $\|\|\bar{d}_2\|\|$	2m
center frequency f_c	33GHz
bandwidth B	150MHz
PRI(t_{pri})	5msec
the number of hits per frame H	128
frame interval t_{fr}	32msec
the number of frames N	9
the number of scatterers K	7
SNR(before Doppler processing)	noise free
target range r_0	5km
angular velocity $\bar{\omega}$	$[5 \;\; 0 \;\; -10]^T$ mrad/sec
incidence angle θ	110°
horizontal aspect angle ψ	20°

Figs. 5.13 and 5.14 shows the simulation result. Fig. 5.13(a) shows the first frame of the simulated ISAR movie observed by the antenna 0. Fig. 5.13(b) shows the selected 7 signal peaks. The signals have been manually selected. Due to the scintillation effect, "bright" peak is not always suitable; e.g., the peak at the first engine on the left wing had to be discarded, otherwise, the estimation result was unacceptably distorted. The location of the peaks have been successfully associated from frame to frame by the simple nearest neighbor tracking. In general, scatterers may disappear at some frames; however, in this case, all the prominent scatterers stayed visible during the observation. For a more complex target such as a ship, we would have to employ a more sophisticated tracking algorithm, but it is beyond the scope of this paper.

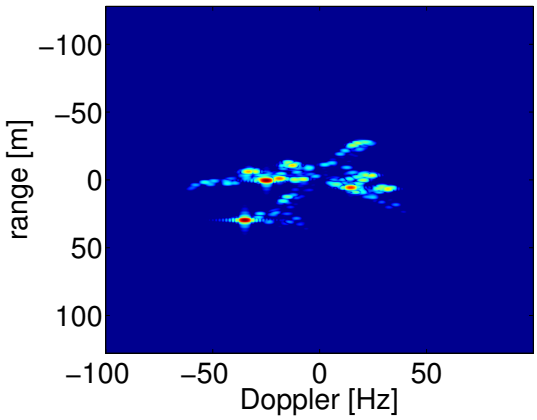

(a) The first frame of the ISAR movie.

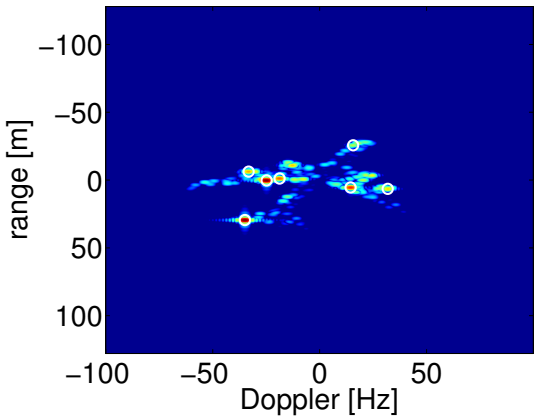

(b) The selected signal peaks.

FIGURE 5.13: The simulation result using an aircraft polygon model and GTD (noise free). (a) The first frame of the simulated ISAR movie observed by the antenna 0. (b) The selected 7 signal peaks. The signals have been manually selected. Due to the scintillation effect, "bright" peak is not always suitable; e.g., the peak at the first engine on the left wing had to be discarded. The simple nearest neighbor tracking have given a satisfactory results for these peaks.

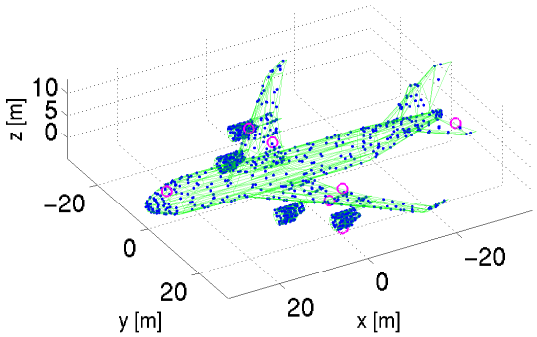

(a) The estimated positions of the selected scattering centers.

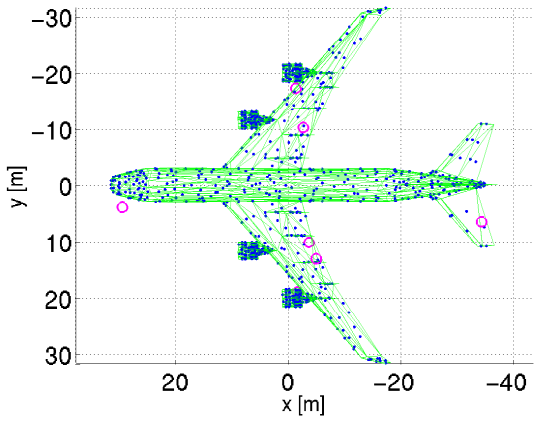

(b) The top view.

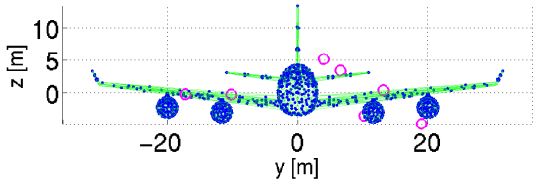

(c) The front view.

FIGURE 5.14: (a)–(c) The estimated positions of the selected scattering centers (magenta circle) along with the shape of the aircraft and the true positions of the centers of the faces of the polygon model (blue dot).

Fig. 5.14(a)–(c) shows the estimated positions of the selected scattering centers (magenta circle) along with the shape of the aircraft and the true positions of the centers of the faces of the polygon model (blue dot). We can see that the estimation result captures the overall rough shape of the aircraft; however, estimation errors of about a few meters are observed, even though no noise has been added. In addition, the estimated angular velocity has been $[4.4 \;\; 0.2 \;\; -10.3]^T$ mrad/sec.

Fig.5.15 shows the result of line fitting to the history of phase differences and the Doppler frequency as in Fig. 5.4. From Fig. 5.15, it can be seen that time dependency of the phase difference or the Doppler frequency is not so linear as in the case of point scatterers. This is due to the interference between the neighboring scattering centers. Therefore, it is desired to select signal peaks whose histories of phase difference and Doppler frequency are as linear as possible. An automatic peak selection method may be developed, in the future, based on this observation.

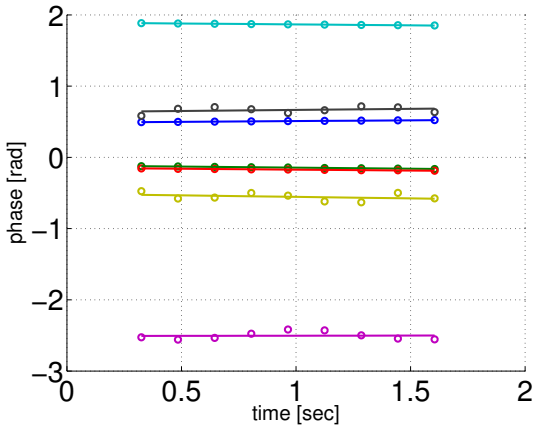

(a) The phase difference ϕ_1

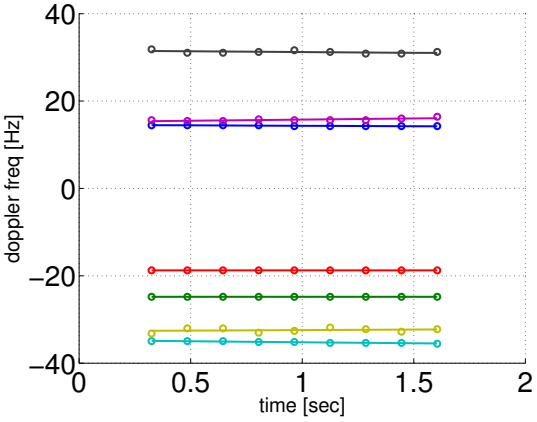

(b) The Doppler frequency f_d

FIGURE 5.15: The estimation result of the rate of change of the phase differences and the Doppler frequency (aircraft case).

5.6 Conclusion

In this chapter, we introduced an algorithm for reconstructing the 3D shape of a target from multistatic ISAR movie sequences. By analyzing three sets of ISAR image sequences, we estimated the target's aspect rotation and the positions of point scatterers composing the object. Unlike Interferometric ISAR, which leverages phase differences to determine scatterer locations, our approach utilizes them to estimate target motion. The algorithm comprises two key steps: first, estimating the velocity and radial acceleration of each scatterer, and second, simultaneously obtaining the angular velocity and scatterer positions.

We provided a detailed performance evaluation of the proposed method. The estimation accuracies of target velocity and radial acceleration in the first step were quantified using the Cramér-Rao Lower Bound (CRLB), while numerical simulations assessed the accuracy of angular velocity and scatterer positions in the second step. Results indicate that, for a system with a center frequency of 33 GHz, a range resolution of 1.5 m, and a baseline length of 2 m, position estimation errors of less than 1 mcomparable to the range resolutioncan be achieved for a target at 5 km with an SNR exceeding 30 dB. This is achieved when five ISAR movie frames, each with an observation time of 1.28 seconds and a frame rate of 0.64 seconds, are processed.

Additionally, a GTD simulation using an aircraft polygon model was conducted to analyze the impact of target scintillation. The study demonstrated that, by carefully selecting scattering centers minimally affected by scintillation, the overall shape of an aircraft can be reconstructed with estimation errors of only a few meters. However, due to the unavoidable nature of target scintillation, an automated method for selecting optimal scattering centers is necessary. Furthermore, for complex targets, signal peaks may disappear in some frames, necessitating a more sophisticated tracking algorithm to ensure the proper association of peaks across frames.

Future research will focus on refining the proposed algorithm, including developing an optimized target selection method and enhancing tracking algorithms. Additionally, extending the method to accommodate time-variant rotation vectors will be explored. Further investigations will also assess performance degradation caused by other error sources, such as clutter and multipath effects.

Chapter 6

Conclusion

This thesis has presented signal processing algorithms for multi-channel imaging radar systems designed to achieve high-precision remote sensing of objects such as satellites, aircraft, ships, and vehicles. By harnessing multi-dimensional signal processing techniques, these algorithms significantly enhance the accuracy of shape, position, and motion estimation. At the core of this research lies the optimal extraction of valuable information from multi-variate signals obtained through multi-channel observations. Imaging radar systems benefit from multi-channel architectures, which broaden the scope of available signal dimensions. These dimensions are primarily categorized into polarization, temporal, and spatial domains. To effectively exploit these aspects, this study introduces advanced methodologies, including resolution enhancement algorithms for Polarimetric SAR (PolSAR), moving target detection and velocity estimation algorithms for SAR-GMTI —specifically designed for formation flight systems of small SAR satellites— and a motion and three-dimensional shape estimation algorithm for distributed ISAR. The key findings and contributions of this research are summarized below.

Resolution enhancement algorithms for Polarimetric SAR

PBWE (Polarimetric Bandwidth Extrapolation) and its two-dimensional extension, 2D-PBWE, have been introduced as super-resolution algorithms for Polarimetric Synthetic Aperture Radar (PolSAR). PBWE builds upon the Bandwidth Extrapolation (BWE) method, originally developed for single-polarization SAR, by incorporating a multivariate linear prediction model that extrapolates bandwidth across all polarization channels simultaneously. By leveraging polarization information, PBWE achieves higher resolution than conventional single-polarization super-resolution techniques. Furthermore, the algorithm not only enhances target separation performance but also improves polarization property estimation accuracy, which is crucial for PolSAR imaging. To assess the effectiveness of the proposed algorithm, 2D-PBWE was applied to real PolSAR images, where the original bandwidth was restricted to half its full range. The reconstructed images were then compared to the original data, demonstrating that the correlation coefficient between the 2D-PBWE-generated image and the original reached 0.97, indicating a near-perfect restoration of image quality. Since PolSAR employs four combinations of transmitted and received polarizations, it inherently generates four times the data volume compared to single-polarization SAR, leading to bandwidth constraints in data downlink transmission. However, the findings show that 2D-PBWE effectively reduces the bandwidth to half, lowering the data volume to one-fourth while still achieving near-original resolution through ground processing, thereby alleviating transmission bottlenecks.

Additionally, this study provides theoretical validation of how polarization information enhances resolution and polarization property estimation accuracy. The results demonstrate that polarization information suppresses interference between closely located signals, thereby

significantly improving the spatial resolution and polarization estimation accuracy of Pol-SAR systems. Numerical simulations comparing PBWE and BWE further reveal that, under high-SNR conditions (3040 dB), PBWE nearly reaches theoretical resolution limits, whereas independent application of BWE to each polarization channel fails to achieve this theoretical bound. These findings confirm the superiority of PBWE, highlighting the critical role of polarization information in resolution enhancement.

Moving target detection and velocity estimation algorithms for SAR-GMTI

Multi-channel DPCA, Multi-channel ATI, and Multi-channel DPCA-ATI have been introduced as signal processing algorithms for detecting moving targets and estimating their velocity in a small SAR satellite formation flight system. These algorithms address three key challenges: - Enhancing detection performance for slow-moving targets - Suppressing azimuth ambiguities - Improving velocity estimation accuracy SAR-GMTI primarily detects moving targets and estimates their velocity by analyzing differences and phase shifts across multiple SAR images captured from the same location at slightly different times. However, as discussed in Chapter 4, simple difference calculations fail to fully eliminate azimuth ambiguities, a phenomenon unique to SAR imaging. In this study, we identified the mechanism behind residual azimuth ambiguities, formulated a signal model, and developed Multi-channel DPCA, a deterministic algorithm that simultaneously suppresses stationary background signals and azimuth ambiguities. Building upon this foundation, we derived two additional algorithms —Multi-channel ATI and Multi-channel DPCA-ATI— which use a lightweight image-domain approach for target detection and velocity estimation.

To validate the proposed method, we conducted flight tests using an airborne SAR system. The observation site was a rice field near the Gifu-Hashima Interchange, where a motorcycle and a van moved at approximately 5 m/s during imaging. The results confirmed that the proposed method successfully detected both vehicles, achieving a velocity estimation error of approximately 0.1 m/s.

Additionally, we investigated optimal satellite spacing for a formation flight system of three small SAR satellites. Assuming a SAR center frequency of 9.6 GHz, we determined the optimal baseline lengths to be 10.8 m and 18.9 m. Under these conditions, performance evaluation of the proposed algorithm demonstrated that, with an input SCNR (Signal-to-Clutter-Noise Ratio) of -5 dB and a CNR (Clutter-to-Noise Ratio) of 15 dB, the system achieved: - Detection probability of Pd = 0.9 - False alarm probability of Pfa = 10^{-8} - Reliable detection of slow-moving targets at velocities of ± 1 m/s These findings suggest that an optimally configured small SAR satellite formation flight can enable a practical SAR-GMTI system, paving the way for large-scale moving target monitoring applications.

A motion and 3D shape estimation algorithm for distributed ISAR

A novel algorithm has been proposed for reconstructing the 3D shape of a target from ISAR motion images acquired by a distributed ISAR system. The algorithm assumes that the target is a rigid body, which can be modeled as an aggregation of multiple point scatterers. Based on this assumption, the method estimates both the target's relative rotational motion and the three-dimensional spatial relationships of its point scatterers using a sequence of at least three ISAR images. In this study, we formulated the algorithm and initially conducted theoretical analysis and numerical simulations for targets represented as point scatterers. The results indicate that, for example, when using a system with a center frequency of 33 GHz, range resolution of 1.5 m, and baseline length of 2 m, under a target distance of 5 km and SNR exceeding 30 dB, analyzing five frames of ISAR motion images with a total observation time of 1.28 seconds and a frame rate of 0.64 seconds achieves a position estimation

error below 1 m, which is comparable to the range resolution. These evaluation conditions assume a helicopter-mounted ISAR system observing ships on the ocean surface, and with an estimation error of approximately 1 m, the method is considered sufficiently accurate for ship shape estimation. However, this evaluation is based on the ideal assumption that the target perfectly conforms to a point scatterer model, which may lead to overestimation of accuracy. To obtain results closer to real ISAR images, we employed a polygon model of the target along with electromagnetic scattering simulations to generate synthetic ISAR motion images. While the overall shape of the target could be reconstructed, unlike the ideal point target case, the influence of signal interference, known as "scintillation," introduced position estimation errors of several meters. Future Challenges for Practical Implementation To advance toward real-world applications, further development is needed, including: - An automatic algorithm to select optimal scattering centers from the signal - An advanced tracking algorithm for accurately associating peak locations across frames Traditional model-based algorithms struggle to overcome these challenges. However, recent advancements in Deep Neural Networks (DNN) open the possibility of integrating data-driven approaches, which may provide a viable solution.

Concluding Remarks

In recent years, increasing global tensions, intensifying natural disasters, and the outbreak of pandemics have contributed to heightened social anxiety. The rapid proliferation of social media has enabled widespread information dissemination, but it has also led to the propagation of unfounded claims and narrowly focused discourse, exacerbating uncertainty and fostering a cycle of amplified fear. While advances in information and communication technology have pushed societal systems toward transformation, humanity has yet to fully acquire the capability to effectively harness these innovations. In the pursuit of a safe and secure society, it has become more critical than ever for human civilization to adopt a global perspective and administer social systems with long-term foresight. Achieving this requires fostering collective abilities to calmly and broadly perceive factual information, engage in constructive discussions based on reality, and derive rational policy directions.

Remote sensing technology plays a crucial role in enabling comprehensive observation of environmental and societal conditions As one of the key tools for objectively grasping large-scale developments, it is expected to gain even greater significance in the future. Among remote sensing techniques, imaging radar technology holds particular promise due to its ability to provide high-resolution, continuous monitoring regardless of time or weather conditions. This study aims to advance imaging radar technology by introducing novel signal processing algorithms that leverage multi-channel architectures and distributed systems. The proposed algorithms facilitate high-precision detection and measurement of shape, position, and motion for objects such as satellites, aircraft, ships, and vehicles, contributing to the realization of advanced remote monitoring systems. The impact of these findings extends beyond national security applications, offering substantial benefits for the constant monitoring of increasingly automated transportation and logistics systems. Ultimately, these technologies are expected to play a vital role in enhancing the reliability and safety of modern societal systems.

As of 2025, research on data-driven approaches utilizing Deep Neural Networks (DNNs) has emerged as a frontier in radar signal processing. However, this study does not adopt a data-driven approach; instead, it focuses on the precise understanding of physical mechanisms and the appropriate modeling of signals. For example, the derivation of the azimuth ambiguity signal model in the proposed Multi-channel DPCA algorithm in Chapter 4 exemplifies the effectiveness of this approach. By accurately understanding the underlying mechanisms, deterministic signal processing has achieved remarkably strong results. Conversely,

the motion and three-dimensional shape estimation algorithm for ISAR proposed in Chapter 5 is based on an overly simplified model that assumes the target consists of point scatterers. While the fundamental concept is valid, its performance falls short when applied to ISAR images simulated to resemble real-world data. Challenges where model-based approaches face inherent limitations —such as this case— can likely be effectively mitigated through the application of DNN.

Moving forward, integrating model-based and data-driven approaches in a complementary manner is expected to lead to the emergence of new system concepts and high-performance algorithms that surpass the capabilities of conventional signal processing frameworks. Nonetheless, when aiming to establish innovative system concepts, an accurate understanding of physical mechanisms remains essential for guiding system design. Therefore, the importance of model-based approaches cannot be understated, and their relevance will persist. This perspective represents one of the key messages of this thesis.

Appendix A

The Derivation of the CRB for the Point Target Signal with WGN model

The CRB for the target separation for the P channels, white noise case ($\boldsymbol{R} = \boldsymbol{I}$) is derived in this appendix. The non-white noise case ($\boldsymbol{R}_p \neq \boldsymbol{I}$) can also be derived in the same manner. With the signal model given in (3.94)–(3.98), we set the parameter vector as follows:

$$\boldsymbol{\theta} = [x_1 \;\; y_1 \;\; x_2 \;\; y_2]^T \tag{A.1}$$

where, x_k and y_k are the real and imaginary part of the pole ρ_k, respectively. Then $\boldsymbol{\Delta}$ defined by (3.83)–(3.85) reduces to

$$\boldsymbol{\Delta} = \sum_{p=1}^{P} |a|^2 \mathrm{Re} \begin{bmatrix} \boldsymbol{A}_p & j\boldsymbol{A}_p \\ j\boldsymbol{A}_p & \boldsymbol{A}_p \end{bmatrix} \tag{A.2}$$

where

$$\begin{aligned} \boldsymbol{A}_p &= \left(\bar{\boldsymbol{a}}_p \boldsymbol{a}_p^T\right) \odot \left(\boldsymbol{V}_{[\boldsymbol{\theta}]}^H \boldsymbol{R}^{-1} \boldsymbol{V}_{[\boldsymbol{\theta}]}\right) \\ &= -\begin{bmatrix} s''(0) & s''(\Delta\phi) e^{-j(\Delta\phi - \psi_p)} \\ s''(\Delta\phi) e^{j(\Delta\phi - \psi_p)} & s''(0) \end{bmatrix} \end{aligned} \tag{A.3}$$

and $\boldsymbol{M}$ defined by (3.90) and (3.91) reduces to

$$\begin{aligned} \boldsymbol{M} &= \mathrm{Re}\left\{ \sum_{p=1}^{P} \boldsymbol{\Lambda}_p \boldsymbol{\Xi}_n^{-1} \boldsymbol{\Lambda}_p^H \right\} \\ &= \sum_{p=1}^{P} |a|^2 \mathrm{Re} \begin{bmatrix} \boldsymbol{E}_p & j\boldsymbol{E}_p \\ j\boldsymbol{E}_p & \boldsymbol{E}_p \end{bmatrix} \end{aligned} \tag{A.4}$$

where,

$$\begin{aligned} \boldsymbol{E}_p &= \frac{|a|^2 s'(\Delta\phi)^2)}{s(0)^2 - s(\Delta\phi)^2)} \\ &\quad \times \begin{bmatrix} s(0) & s(\Delta\phi) e^{-j(\Delta\phi - \psi_p)} \\ s(\Delta\phi) e^{j(\Delta\phi - \psi_p)} & s(0) \end{bmatrix}. \end{aligned} \tag{A.5}$$

Then FIM is obtained as

$$\begin{aligned} S_\theta &= 2(\Delta - M) \\ &= 2|a|^2 \left[\begin{array}{cc:cc} Pd_0 & d_1c_p & 0 & d_1s_p \\ d_1c_p & Pd_0 & -d_1s_p & 0 \\ \hdashline 0 & -d_1s_p & Pd_0 & d_1c_p \\ d_1s_p & 0 & d_1c_p & Pd_0 \end{array}\right]. \end{aligned} \tag{A.6}$$

Therefore the CRB for the parameter θ is

$$\begin{aligned} S_\theta^{-1} &= \frac{1}{2|a|^2} \cdot \frac{1}{P^2d_0^2 - d_1^2(c_p^2+s_p^2)} \\ &\quad \times \left[\begin{array}{cc:cc} Pd_0 & -d_1c_p & 0 & -d_1s_p \\ -d_1c_p & Pd_0 & d_1s_p & 0 \\ \hdashline 0 & d_1s_p & Pd_0 & -d_1c_p \\ -d_1s_p & 0 & -d_1c_p & Pd_0 \end{array}\right]. \end{aligned} \tag{A.7}$$

Then the CRB for the target separation δ is

$$\sigma^2_{\delta|\psi} \geq DS_\theta^{-1}D^T = \frac{2}{|a|^2} \cdot \frac{Pd_0 + d_1c_p}{P^2d_0^2 - d_1^2(c_p^2+s_p^2)} \tag{A.8}$$

and noting that $N|a|^2 = \text{SNR}$, we obtain (3.105).

A.1 Maximum CRB, Minimum CRB, Hybrid CRB and Average CRB for the target separation estimation

In this appendix, the definitions and the derivations of the maximum (or the worst case) CRB [89], the minimum (or the best case) CRB [84], the hybrid (or *a posteriori*) CRB [87], [91]–[93], and the average CRB [88], [93] for the target separation estimation are summarized.

(3.111) is repeated here as (A.1) for convenience (the unit has been changed to radian from FRC).

$$\text{CRB}(\Delta\phi|\psi) \approx \frac{2N}{\text{SNR}} \cdot \frac{d_0 + d_1\cos(\Delta\phi - \psi)}{d_0^2 - d_1^2} \tag{A.1}$$

For $\Delta\phi$ small, the maximum and the minimum CRBs can readily be seen from (A.1), noting that d_0 and d_1 have opposite signs for $\Delta\phi$ small. The maximum CRB is given by $\psi \approx \pi$ and the minimum CRB is given by $\psi \approx 0$.

$$\text{CRB}_{\max} = \max_\psi \{\text{CRB}(\Delta\phi|\psi)\} = \frac{2N}{\text{SNR}} \cdot \frac{1}{d_0 + d_1} \tag{A.2}$$

$$\text{CRB}_{\min} = \min_\psi \{\text{CRB}(\Delta\phi|\psi)\} = \frac{2N}{\text{SNR}} \cdot \frac{1}{d_0 - d_1} \tag{A.3}$$

In contrast to the maximum and the minimum CRBs that give the limiting values, both the hybrid and the average CRBs are "average" type values, and they are given by

$$\begin{aligned} \mathrm{CRB}_{\mathrm{hyb}} &= \mathrm{tr}\left[\boldsymbol{D}\left(\underset{\psi}{E}\{\boldsymbol{S}_{\theta}\}\right)^{-1}\boldsymbol{D}^{T}\right] \\ &= \frac{2N}{\mathrm{SNR}}\cdot\frac{1}{d_0} \end{aligned} \tag{A.4}$$

$$\begin{aligned} \mathrm{CRB}_{\mathrm{ave}} &= \mathrm{tr}\left[\boldsymbol{D}\underset{\psi}{E}\left\{\boldsymbol{S}_{\theta}^{-1}\right\}\boldsymbol{D}^{T}\right] = \underset{\psi}{E}\left\{\Sigma_{\delta|\psi}\right\} \\ &= \frac{2N}{\mathrm{SNR}}\cdot\frac{d_0}{d_0^2-d_1^2}\,, \end{aligned} \tag{A.5}$$

where $\boldsymbol{S}_{\theta}$ is the FIM derived previously assuming ψ is known and fixed. As can be seen in (A.4) and (A.5), the average CRB is just an average of the CRB, while the hybrid CRB is the inverse of the average FIM.

The difference between the hybrid and the average CRBs comes from the different conditioning on the estimators. The hybrid CRB applies to estimators which are unbiased over the ensemble of ψ, while the average CRB requires the estimator to be unbiased for every value of the phase ψ. For both bounds, we first regard ψ as a random variable uniformly distributed over $[-\pi,\pi)$. If the estimator $\hat{\boldsymbol{\theta}}$ is unbiased over the ensemble of ψ; namely,

$$\underset{z,\psi}{E}\left\{\hat{\boldsymbol{\theta}}-\boldsymbol{\theta}\right\} = 0 \tag{A.6}$$

then the following inequality holds[92]:

$$\begin{aligned} \underset{z,\psi}{E}\left\{(\hat{\boldsymbol{\theta}}-\boldsymbol{\theta})(\hat{\boldsymbol{\theta}}-\boldsymbol{\theta})^{T}\right\} &\geq \underset{z,\psi}{E}\left[\partial_{\theta}^{T}\partial_{\theta}\left\{\ln f_{z|\theta,\psi}(\boldsymbol{z}|\boldsymbol{\theta},\psi)\right\}\right]^{-1} \\ &= \underset{\psi}{E}\left[\boldsymbol{S}_{\theta|\psi}+\partial_{\theta}^{T}\partial_{\theta}\left\{\ln f_{\psi}(\psi)\right\}\right]^{-1} \\ &= \underset{\psi}{E}\left\{\boldsymbol{S}_{\theta|\psi}\right\}^{-1} = \mathrm{CRB}_{\mathrm{hyb}}(\boldsymbol{\theta})\,. \end{aligned} \tag{A.7}$$

The last equation follows from the current assumption that $f_{\psi}(\psi)$ is uniform distribution. On the other hand, if we let the estimator $\hat{\boldsymbol{\theta}}$ be unbiased for every value of the phase ψ; namely,

$$\underset{z|\psi}{E}\left\{\hat{\boldsymbol{\theta}}-\boldsymbol{\theta}\right\} = 0, \qquad \forall\psi\in[-\pi,\pi)\,. \tag{A.8}$$

Then the following inequality holds[88]:

$$\begin{aligned} \underset{z,\psi}{E}\left\{(\hat{\boldsymbol{\theta}}-\boldsymbol{\theta})(\hat{\boldsymbol{\theta}}-\boldsymbol{\theta})^{T}\right\} &= \underset{\psi}{E}\left[\underset{z|\psi}{E}\left\{(\hat{\boldsymbol{\theta}}-\boldsymbol{\theta})(\hat{\boldsymbol{\theta}}-\boldsymbol{\theta})^{T}\right\}\right] \\ &= \underset{\psi}{E}\left\{\boldsymbol{C}_{\theta|\psi}\right\} \\ &\geq \underset{\psi}{E}\left\{\boldsymbol{S}_{\theta|\psi}^{-1}\right\} = \mathrm{CRB}_{\mathrm{ave}}(\boldsymbol{\theta})\,. \end{aligned} \tag{A.9}$$

Note that the inequality in (A.9) follows from the condition that the estimate is unbiased for all ψ.

For the dual polarization case, the CRB is a function of ψ and χ. (3.112) is repeated here as (A.10) for convenience.

$$\mathrm{CRB}(\Delta\phi|\psi,\chi) \approx \frac{N}{\mathrm{SNR}} \cdot \frac{d_0 + d_1\cos(\frac{\chi}{2})\cos(\Delta\phi - \frac{\chi}{2} - \psi)}{d_0^2 - d_1^2\cos^2(\chi/2)} \tag{A.10}$$

The four bounds conditioned on χ can readily be obtained from (A.10), and they are given by

$$\mathrm{CRB}_{\max|\emptyset} = \frac{N}{\mathrm{SNR}} \cdot \frac{1}{d_0 + d_1|\cos(\chi/2)|} \tag{A.11}$$

$$\mathrm{CRB}_{\min|\emptyset} = \frac{N}{\mathrm{SNR}} \cdot \frac{1}{d_0 - d_1|\cos(\chi/2)|} \tag{A.12}$$

$$\mathrm{CRB}_{\mathrm{hyb}|\emptyset} = \frac{N}{\mathrm{SNR}} \cdot \frac{1}{d_0} \tag{A.13}$$

$$\mathrm{CRB}_{\mathrm{ave}|\emptyset} = \frac{N}{\mathrm{SNR}} \cdot \frac{d_0}{d_0^2 - d_1^2\cos^2(\chi/2)}\,, \tag{A.14}$$

where, the maximum and the minimum CRB are respectively given by $\psi = \pi - \chi/2$ and $\psi = -\chi/2$.

A.2 Analysis on the effect of the magnitude

In this appendix, the effect of the relative magnitude between the polarization channels is briefly discussed. To illustrate the effect of the magnitude of the targets analytically in a systematic manner, the following target model is employed.

$$\boldsymbol{a} = a\begin{bmatrix} \cos\xi_1 & \sin\xi_1 \\ e^{j\psi}\cos\xi_2 & e^{j\psi}\sin\xi_2 \end{bmatrix} \tag{A.1}$$

where, ξ_1 and ξ_2 determine the relative amplitude between the two polarization channels of the two targets, ψ is the relative phase of the target #2 to the target #1. In this model, the total power in the two channels of the two targets $|a|^2$ are assumed to be identical. By fixing the total power in this manner, the SNR defined in (3.99) is now regarded as the SNR in the total power of the two channels. The target model in (A.1) is theoretical, but it can be related to physically meaningful models. For example, the scattering matrix of a thin cylindrical scatterer (or an elementary dipole) with the orientation angle around radar line of sight ξ (from the horizontal polarization direction) can be expressed as [133], [134]:

$$\boldsymbol{S}_{\mathrm{cyl}} = a\begin{bmatrix} \cos^2\xi & \cos\xi\sin\xi \\ \cos\xi\sin\xi & \sin\xi^2 \end{bmatrix}. \tag{A.2}$$

If we assume that we have a dual polarization system with HH and HV channels, the target signal of a thin cylindrical scatterer can be expressed as $a\cos\xi\cdot[\cos\xi \quad \sin\xi]$, the polarization property of which agrees with the one in (A.1). Thus the target model in (A.1) almost corresponds to the two closely located thin cylindrical scatterers as in Fig.A.1 [1].

[1] In (A.1), the amplitude factor $\cos\xi$ that appears in thin cylinder model is not included. As a result, the model requires the dimension of the thin cylinder to change along with the rotation angle ξ. In addition, when $\xi = \pi/2$, the thin cylinder model no longer explains the model in (A.1) at all.

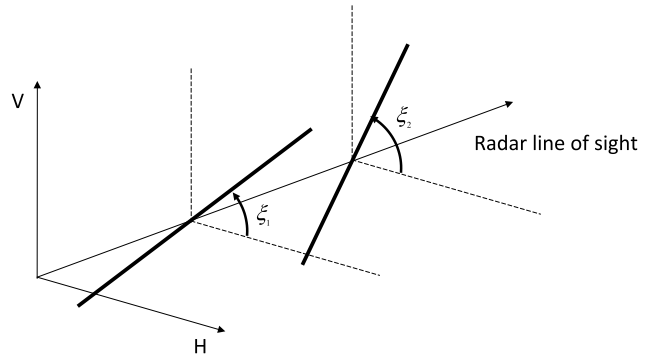

FIGURE A.1: Two closely located thin cylindrical scatterer model

The performance of the PBWE and BWE is evaluated via simulation and compared with the CRBs for the signal model given in (A.1). The simulation conditions are equivalent to those given in section 3.4.3, except that only SNR=40dB case is shown here.

Fig. A.2 show the results for target separation estimation error. The sub-figures (a) – (d) show the results for $\Delta\xi = 0$, $\pi/6$, $\pi/4$ and $\pi/2$, respectively. The dashed green line and the dash-dot yellow line show the rmse of the target separation estimation by the BWE for polarization channels 1 and 2, respectively. And the dashed magenta line show the result of the PBWE. The solid blue line and the cyan line show the square root of the average CRB for the target separation of the single polarization case for polarization channels 1 and 2. And the solid red line show the average CRB for the dual polarization case. The dotted blue line and the cyan line show the square root of the hybrid CRB for the target separation of the single polarization case for polarization channels 1 and 2. And the dotted red line show the hybrid CRB for the dual polarization case.

Following the procedure shown in Appedix A.1, the hybrid CRB and average CRB for the dual polarization case are derived as:

$$\mathrm{CRB}_{\mathrm{hyb}|\Delta_\xi} = \left(\frac{N}{2\pi}\right)^2 \cdot \frac{N}{\mathrm{SNR}} \cdot \frac{1}{d_0} \tag{A.3}$$

$$\mathrm{CRB}_{\mathrm{ave}|\Delta_\xi} = \left(\frac{N}{2\pi}\right)^2 \cdot \frac{N}{\mathrm{SNR}} \cdot \frac{d_0}{d_0^2 - d_1^2\cos^2\Delta\xi} \tag{A.4}$$

where, $\Delta\xi = \xi_1 - \xi_2$. The hybrid CRB and average CRB for the polarization channel 1 are derived as:

$$\mathrm{CRB}_{\mathrm{hyb}|_{\xi,1},\xi_2} = \left(\frac{N}{2\pi}\right)^2 \cdot \frac{N}{\mathrm{SNR}} \cdot \left(\frac{1}{\cos^2\xi_1} + \frac{1}{\cos^2\xi_2}\right)\frac{1}{d_0} \tag{A.5}$$

$$\mathrm{CRB}_{\mathrm{ave}|_{\xi,1},\xi_2} = \left(\frac{N}{2\pi}\right)^2 \cdot \frac{N}{\mathrm{SNR}} \cdot \left(\frac{1}{\cos^2\xi_1} + \frac{1}{\cos^2\xi_2}\right)\frac{d_0}{d_0^2 - d_1^2} \tag{A.6}$$

And for polarization channel 2, $\cos\xi_1$ and $\cos\xi_2$ in (A.5), (A.6) are replaced by $\sin\xi_1$ and $\sin\xi_2$, respectively. Note that in this signal model, the CRBs for the single polarization case depend on polarization channel. In Fig. A.2, ξ_1 is set to be $\pi/6$. Note in (b) and (d), the cyan lines coincide with the blue lines, since in these cases, $\xi_2 = \pi/3$ and $2\pi/3$, and thus $1/\cos^2\xi_1 + 1/\cos^2\xi_2 = 1/\sin^2\xi_1 + 1/\sin^2\xi_2$.

It can be seen from Fig. A.2 that the PBWE nearly achieve the average CRB. On the other hand, the deviation of the results of the BWE from the CRB for the single polarization case is relatively large compared to the results given in Fig. 3.16. From the intersection between

the dashed green line and the solid black line, the resolution of the BWE is evaluated to be around 0.4∼1FRC. Also, from the intersection between the dashed magenta line and the solid black line, the resolution of the PBWE is evaluated to be around 0.4∼0.5FRC for $\Delta\xi = 0$, about 0.3FRC for $\Delta\xi = \pi/6$ and around 0.1∼0.2FRC for $\Delta\xi = \pi/4$ and $\pi/2$.

Fig. A.3 and Fig. A.4 respectively show the orthogonal and the parallel components of the polarization vector estimation error. The sub-figures (a) – (d) of Fig. A.3 show the results for $\Delta\xi = 0$, $\pi/6$, $\pi/4$ and $\pi/2$, respectively. The dashed green line and the dashed magenta line show the rmse of the polarization vector estimation by the BWE and the PBWE, respectively. The solid blue line and the solid red line show the square root of the CRB for the polarization vector estimation error for the dual polarization case and the individually processed case.

The CRB for the polarization vectors $\boldsymbol{s}_1$ and $\boldsymbol{s}_2$ can be calculated according to (3.148),(3.149), where $\boldsymbol{\Omega}$ is replaced by $\boldsymbol{\Omega}_{\mathrm{m}}$.

$$\boldsymbol{\Omega}_{\mathrm{m}} = \begin{bmatrix} \boldsymbol{H}+\boldsymbol{F}_1 & \bar{\boldsymbol{G}}_m \\ \boldsymbol{G}_m & \boldsymbol{H}+\bar{\boldsymbol{F}}_2 \end{bmatrix} \tag{A.7}$$

$$\boldsymbol{H} = \begin{bmatrix} s(0) & s(\Delta\phi) \\ s(\Delta\phi) & s(0) \end{bmatrix} \tag{A.8}$$

$$\boldsymbol{F}_1 = \begin{bmatrix} f_{\mathrm{m0}}\cos^2\xi_2 & f_{\mathrm{m1}}\cos\xi_1\cos\xi_2 \\ f_{\mathrm{m1}}\cos\xi_1\cos\xi_2 & f_{\mathrm{m0}}\cos^2\xi_1 \end{bmatrix} \tag{A.9}$$

$$\boldsymbol{F}_2 = \begin{bmatrix} f_{\mathrm{m0}}\sin^2\xi_2 & f_{\mathrm{m1}}\sin\xi_1\sin\xi_2 \\ f_{\mathrm{m1}}\sin\xi_1\sin\xi_2 & f_{\mathrm{m0}}\sin^2\xi_1 \end{bmatrix} \tag{A.10}$$

$$\boldsymbol{G}_{\mathrm{m}} = \begin{bmatrix} f_{\mathrm{m0}}\cos\xi_2\sin\xi_2 & f_{\mathrm{m1}}\cos\xi_1\sin\xi_2 \\ f_{\mathrm{m1}}\sin\xi_1\cos\xi_2 & f_{\mathrm{m0}}\cos\xi_1\sin\xi_1 \end{bmatrix} \tag{A.11}$$

and

$$f_{\mathrm{m0}} = \frac{s'(\Delta\phi)^2 s''(0)}{2s''(0)^2 - 2s''(\Delta\phi)^2\cos^2\Delta\xi} \tag{A.12}$$

$$f_{\mathrm{m1}} = \frac{s'(\Delta\phi)^2 s''(\Delta\phi)\cos\Delta\xi}{2s''(0)^2 - 2s''(\Delta\phi)^2\cos^2\Delta\xi}. \tag{A.13}$$

The variance of the polarization vector estimation error when the two polarization channels are individually processed is found to be the same as (3.155). Unlike the CRB for target separation, the CRB for the polarization vector estimation error are independent of ξ_1 and ξ_2.

It can be seen from Fig. A.3 that the PBWE nearly achieves the average CRB for the orthogonal component of the polarization vector estimation. On the other hand, the orthogonal component of the polarization vector estimation error of the BWE is 10 to 20dB larger than the CRB. From Fig. A.4, the parallel component of the polarization vector estimation error of the BWE and the PBWE are both larger than the CRB by more than 10dB. These results are mostly consistent with the results in section 3.4.3

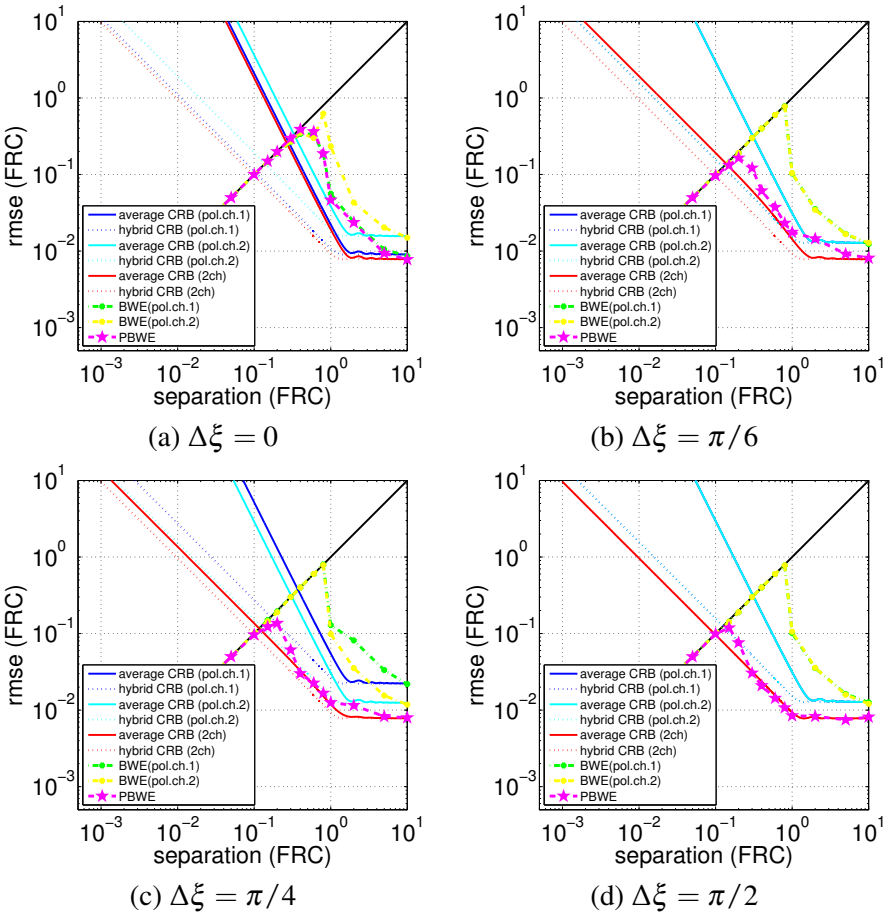

(a) $\Delta\xi = 0$ (b) $\Delta\xi = \pi/6$

(c) $\Delta\xi = \pi/4$ (d) $\Delta\xi = \pi/2$

FIGURE A.2: The target separation estimation rmse of BWE and PBWE along with the average and the hybrid CRB for the signal model given in (A.1). The solid blue line and the cyan line show the square root of the average CRB for the target separation of the single polarization case for polarization channel 1 and 2. And the solid red line show the dual polarization case. The dotted blue line and the cyan line show the square root of the average CRB for the target separation of the single polarization case for polarization channel 1 and 2. And the dotted red line show the dual polarization case. In (b) and (d), the cyan lines corresponds to blue lines. ($N = 50$ / SNR=40dB / $\xi_1 = \pi/6$ / order of the linear prediction filter for BWE and PBWE = 6)

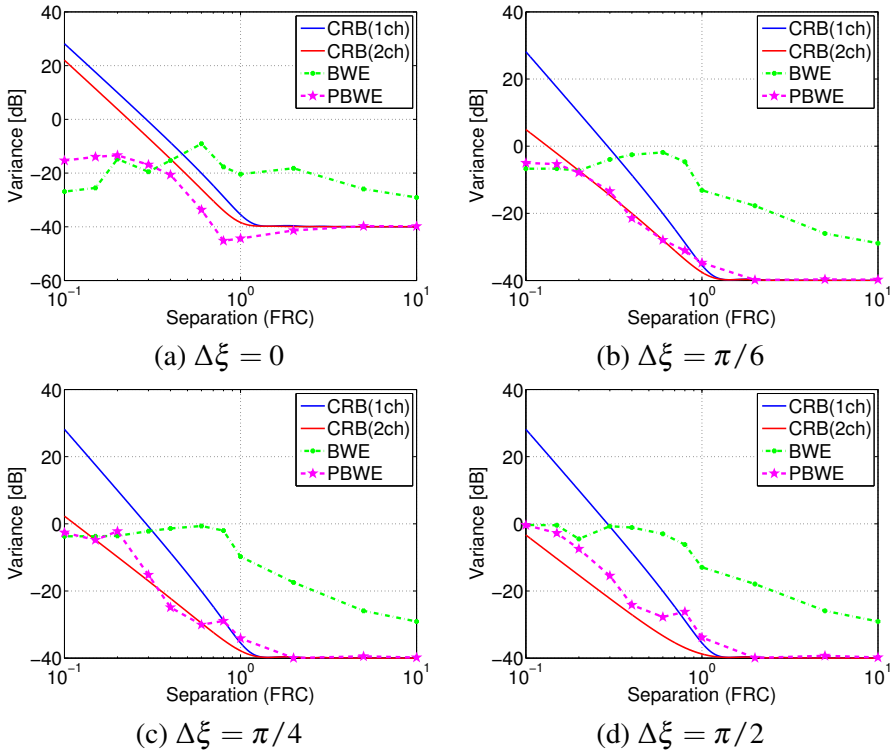

(a) $\Delta\xi = 0$ (b) $\Delta\xi = \pi/6$

(c) $\Delta\xi = \pi/4$ (d) $\Delta\xi = \pi/2$

FIGURE A.3: The orthogonal components of the polarization vector estimation error for the signal model given in (A.1). (a) – (d) show the results for $\Delta\xi = 0$, $\pi/6$, $\pi/4$ and $\pi/2$, respectively. The solid blue line and the solid red line show the square root of the CRB for the orthogonal component of the polarization vector estimation error for the dual polarization case and the individually processed case. The dashed green line and the dashed magenta line show the rmse of the polarization vector estimation by the BWE and the PBWE, respectively. ($N = 50$ / SNR=40dB / $\xi_1 = \pi/6$ / / order of the linear prediction filter for BWE and PBWE = 6)

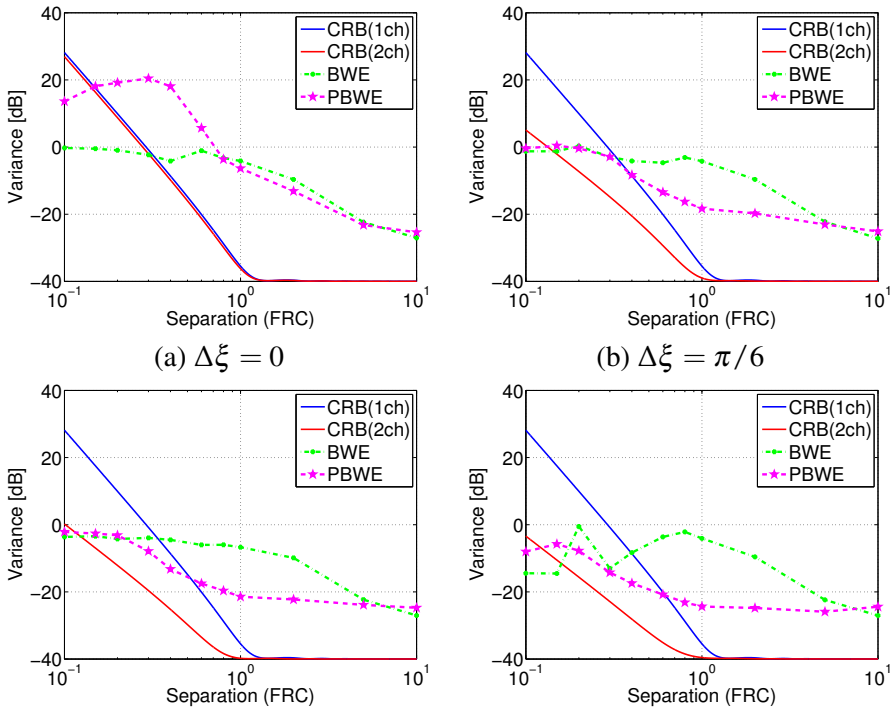

(a) $\Delta\xi = 0$ (b) $\Delta\xi = \pi/6$

(c) $\Delta\xi = \pi/4$ (d) $\Delta\xi = \pi/2$

FIGURE A.4: The parallel components of the polarization vector estimation error for the signal model given in (A.1). The solid blue line and the solid red line show the square root of the CRB for the parallel component of the polarization vector estimation error for the dual polarization case and the individually processed case. In (a), the CRB for single and dual polarization case coincide with each other. ($N = 50$ / SNR=40dB / $\xi_1 = \pi/6$ / / order of the linear prediction filter for BWE and PBWE = 6)

Appendix B

The phase shift introduced by the resampling

Consider the multi-channel signal of one azimuth line before registration $u_{\mathrm{b}q}(n\Delta\eta)$, $(q = 1,\cdots,N_{\mathrm{a}}; n = 1,\cdots,N)$ that contains only static background clutter, where N is the number of the azimuth samples and $\Delta\eta$ [sec] is the azimuth sampling interval given as the reciprocal of the PRF F_{a}, i.e., $\Delta\eta = 1/F_{\mathrm{a}}$. Fourier transform of the first (reference) channel is given by

$$U_{\mathrm{b}1}(f_\eta) = \mathscr{F}\{u_{\mathrm{b}1}(n\Delta\eta)\} = \sum_{k=-K_{\mathrm{a}}}^{K_{\mathrm{a}}} U_{\mathrm{org}}(f_\eta - kF_{\mathrm{a}}), \tag{B.1}$$

where K_{a} is the maximum order of the azimuth ambiguity, and $U_{\mathrm{org}}(f_\eta)$ is the Fourier transform of $u_{\mathrm{b}1}(\eta)$, which is free from the aliasing due to sampling. From the shift property of the Fourier transform, the Fourier transform of the rest of the channels are expressed as follows:

$$\begin{aligned} U_{\mathrm{b}q}(f_\eta) &= \mathscr{F}\left\{u_{\mathrm{b}q}(n\Delta\eta)\right\} \\ &= \sum_{k=-K_{\mathrm{a}}}^{K_{\mathrm{a}}} U_{\mathrm{org}}(f_\eta - kF_{\mathrm{a}})\, e^{-j2\pi(f_\eta - kF_{\mathrm{a}})\eta_{1q}}. \end{aligned} \tag{B.2}$$

The registration process can also be expressed using the shift property of the Fourier transform, and the multi-channel signal of one azimuth line after registration is given by

$$\begin{aligned} u_q(n\Delta\eta) &= \mathscr{F}^{-1}\left\{U_{\mathrm{b}q}(f_\eta)\, e^{j2\pi f_\eta \eta_{1q}}\right\} \\ &= \mathscr{F}^{-1}\left\{\sum_{k=-K_o}^{K_o} U_{\mathrm{org}}(f_\eta - kF_{\mathrm{a}}) \right. \\ &\qquad \left. \times e^{-j2\pi(f_\eta - kF_{\mathrm{a}})\eta_{1q}} e^{j2\pi f_\eta \eta_{1q}}\right\} \\ &= \sum_{k=-K_o}^{K_o} \mathscr{F}^{-1}\left\{U_{\mathrm{org}}(f_\eta - kF_{\mathrm{a}})\right\} e^{j2\pi kF_{\mathrm{a}}\eta_{1q}} \\ &= \sum_{k=-K_o}^{K_o} c^{\langle k\rangle}(n\Delta\eta) e^{j2\pi kF_{\mathrm{a}}\eta_{1q}}, \end{aligned} \tag{B.3}$$

where $c^{\langle k\rangle}(n\Delta\eta)$ represents the azimuth ambiguity of k-th order in the first (reference) channel, which is defined as follows:

$$c^{\langle k\rangle}(n\Delta\eta) = \mathscr{F}^{-1}\left\{U_{\mathrm{org}}(f_\eta - kF_{\mathrm{a}})\right\}. \tag{B.4}$$

From (B.3), the registered clutter $\boldsymbol{u}$ with azimuth ambiguity can be expressed in a vector form as follows:

$$\begin{aligned} \boldsymbol{u} &= \boldsymbol{D}\boldsymbol{c} \qquad\qquad (B.5)\\ \boldsymbol{D} &= \begin{bmatrix} 1 & \cdots & 1 & \cdots & 1 \\ e^{-j2\pi K_{\mathrm{a}} F_{\mathrm{a}} \eta_{12}} & \cdots & 1 & \cdots & e^{j2\pi K_{\mathrm{a}} F_{\mathrm{a}} \eta_{12}} \\ \vdots & \vdots & \vdots & \vdots & \vdots \\ e^{-j2\pi K_{\mathrm{a}} F_{\mathrm{a}} \eta_{1N_{\mathrm{a}}}} & \cdots & 1 & \cdots & e^{j2\pi K_{\mathrm{a}} F_{\mathrm{a}} \eta_{1N_{\mathrm{a}}}} \end{bmatrix} \\ \boldsymbol{c} &= \left[c^{\langle -K_{\mathrm{a}} \rangle}(n\Delta\eta), \cdots, c^{\langle 0 \rangle}(n\Delta\eta), \cdots, c^{\langle K_{\mathrm{a}} \rangle}(n\Delta\eta) \right]^T \end{aligned}$$

Note when the DPCA condition is satisfied, i.e., no resampling is required upon registration, $F_{\mathrm{a}}\eta_{1q}$ becomes integer and (B.5) reduces to

$$\boldsymbol{u} = c\mathbf{1}, \quad \text{where} \quad c = \sum_{k=-K_o}^{K_o} c^{\langle k \rangle}. \qquad (B.6)$$

Appendix C

Derivation of CRLB

C.1 Derivation of CRLB for the Doppler frequency and the rate of change of Doppler frequency

In this appendix, the derivation of CRLB for the Doppler frequency and the rate of change of Doppler frequency is given. For the sake of simplicity, the signal model given in Eq. (5.27) is rewrited as follows.

$$x[m] = a\exp\left[-j\left\{\psi + \omega m\tau + \frac{1}{2}\dot{\omega}(m\tau)^2\right\}\right] + w[m], \qquad -\frac{M-1}{2} \leq m \leq \frac{M-1}{2} \tag{C.1}$$

Here, the variables in Eq. (5.27) are replaced by $s_{0k} = ae^{-j\psi}$, $2\pi f_{\mathrm{d}k} = \omega$, $2\pi \dot{f}_{\mathrm{d}k} = \dot{\omega}$ and $t_{pri} = \tau$, respectively. Since $w[m]$ is assumed to be WGN with variance σ^2, the probability density function of $x[m]$ is given by

$$p(\mathbf{x};\boldsymbol{\xi}) = \frac{1}{\pi^M \sigma^{2M}} \exp\left[-\frac{1}{\sigma^2}(\mathbf{x}-\boldsymbol{\mu}(\boldsymbol{\xi}))^H(\mathbf{x}-\boldsymbol{\mu}(\boldsymbol{\xi}))\right], \tag{C.2}$$

where, the parameter vector $\boldsymbol{\xi}$ is defined as

$$\boldsymbol{\xi} = [a \;\; \psi \;\; \omega \;\; \dot{\omega}]^T, \tag{C.3}$$

and

$$\mathbf{x} = \begin{bmatrix} x\left[-\frac{M-1}{2}\right] \\ \vdots \\ x\left[\frac{M-1}{2}\right] \end{bmatrix}, \qquad \boldsymbol{\mu}(\boldsymbol{\xi}) = \begin{bmatrix} \mu\left[-\frac{M-1}{2}\right] \\ \vdots \\ \mu\left[\frac{M-1}{2}\right] \end{bmatrix}. \tag{C.4}$$

Here, $\mu[m]$ is the mean of $x[m]$, and it is given by

$$\mu[m] = a\exp\left[-j\left\{\psi + \omega m\tau + \frac{1}{2}\dot{\omega}(m\tau)^2\right\}\right]. \tag{C.5}$$

The Fisher Information Matrix (FIM) for the parameter vector $\boldsymbol{\xi}$ is given by [103]

$$[\mathbf{G}(\boldsymbol{\xi})]_{ij} = \frac{2}{\sigma^2}\mathrm{Re}\left[\sum_{-(M-1)/2}^{(M-1)/2} \frac{\partial \mu[m]^H}{\partial \xi_i}\frac{\partial \mu[m]}{\partial \xi_j},\right] \tag{C.6}$$

while the partial derivatives are given as follows.

$$\frac{\partial \mu[m]}{\partial a} = \exp\left[-j\left\{\psi+\omega m\tau+\frac{1}{2}\dot{\omega}(m\tau)^2\right\}\right] \tag{C.7}$$

$$\frac{\partial \mu[m]}{\partial \psi} = -ja\exp\left[-j\left\{\psi+\omega m\tau+\frac{1}{2}\dot{\omega}(m\tau)^2\right\}\right] \tag{C.8}$$

$$\frac{\partial \mu[m]}{\partial \omega} = -jm\tau a\exp\left[-j\left\{\psi+\omega m\tau+\frac{1}{2}\dot{\omega}(m\tau)^2\right\}\right] \tag{C.9}$$

$$\frac{\partial \mu[m]}{\partial \dot{\omega}} = -j\frac{1}{2}(m\tau)^2 a\exp\left[-j\left\{\psi+\omega m\tau+\frac{1}{2}\dot{\omega}(m\tau)^2\right\}\right] \tag{C.10}$$

Substituting Eqs. (C.7)–(C.10) into Eq. (C.6), we obtain the elements of the FIM as follows.

$$[\mathbf{G}(\xi)]_{11} = \frac{2}{\sigma^2}\mathrm{Re}\left[\sum_{-(M-1)/2}^{(M-1)/2} 1\right] = \frac{2M}{\sigma^2} \tag{C.11}$$

$$[\mathbf{G}(\xi)]_{12} = 0 \tag{C.12}$$

$$[\mathbf{G}(\xi)]_{13} = 0 \tag{C.13}$$

$$[\mathbf{G}(\xi)]_{14} = 0 \tag{C.14}$$

$$[\mathbf{G}(\xi)]_{22} = \frac{2a^2}{\sigma^2}\mathrm{Re}\left[\sum_{-(M-1)/2}^{(M-1)/2} 1\right] = \frac{2Ma^2}{\sigma^2} \tag{C.15}$$

$$[\mathbf{G}(\xi)]_{23} = 0 \tag{C.16}$$

$$[\mathbf{G}(\xi)]_{24} = \frac{a^2\tau^2}{\sigma^2}\mathrm{Re}\left[\sum_{-(M-1)/2}^{(M-1)/2} m^2\right] = \frac{a^2\tau^2}{\sigma^2}\cdot\frac{M(M^2-1)}{12} \tag{C.17}$$

$$[\mathbf{G}(\xi)]_{33} = \frac{2a^2\tau^2}{\sigma^2}\mathrm{Re}\left[\sum_{-(M-1)/2}^{(M-1)/2} m^2\right] = \frac{a^2\tau^2}{\sigma^2}\cdot\frac{M(M^2-1)}{6} \tag{C.18}$$

$$[\mathbf{G}(\xi)]_{34} = \frac{a^2\tau^3}{\sigma^2}\mathrm{Re}\left[\sum_{-(M-1)/2}^{(M-1)/2} m^3\right] = 0 \tag{C.19}$$

$$[\mathbf{G}(\xi)]_{44} = \frac{a^2\tau^4}{2\sigma^2}\mathrm{Re}\left[\sum_{-(M-1)/2}^{(M-1)/2} m^4\right] = \frac{a^2\tau^2}{\sigma^2}\cdot\frac{M(M^2-1)(3M^2-7)}{480}, \tag{C.20}$$

which yield the FIM for ξ to be

$$\mathbf{G}(\xi) = \left[\begin{array}{cc|cc} \frac{2M}{\sigma^2} & 0 & 0 & 0 \\ 0 & \frac{2Ma^2}{\sigma^2} & 0 & \frac{a^2\tau^2}{\sigma^2}\cdot\frac{M(M^2-1)}{12} \\ \hline 0 & 0 & \frac{a^2\tau^2}{\sigma^2}\cdot\frac{M(M^2-1)}{6} & 0 \\ 0 & \frac{a^2\tau^2}{\sigma^2}\cdot\frac{M(M^2-1)}{12} & 0 & \frac{a^2\tau^4}{\sigma^2}\cdot\frac{M(M^2-1)(3M^2-7)}{480} \end{array}\right]. \tag{C.21}$$

Then the FIM for ω and $\dot{\omega}$ are obtained as the Schur complement of $\mathbf{G}(\xi)$ as follows.

$$\begin{aligned} \mathbf{G}\left(\left[\begin{array}{c}\omega\\ \dot{\omega}\end{array}\right]\right) &= \frac{a^2}{\sigma^2}\left[\begin{array}{cc} \frac{\tau^2M(M^2-1)}{6} & 0 \\ 0 & \frac{\tau^4M(M^2-1)(3M^2-7)}{480}\end{array}\right] - \frac{a^2}{\sigma^2}\left[\begin{array}{cc} 0 & 0 \\ 0 & \frac{\tau^4M(M^2-1)^2}{288}\end{array}\right] \\ &= \frac{a^2}{\sigma^2}\left[\begin{array}{cc} \frac{\tau^2M(M^2-1)}{6} & 0 \\ 0 & \frac{\tau^4M(M^2-1)(M^2-4)}{360}\end{array}\right] \end{aligned} \tag{C.22}$$

The CRLB for ω and $\dot{\omega}$ can be readily derived by inverting the FIM given by Eq. (C.22). Note that a^2/σ^2 corresponds to the SNR η in Eqs. (5.28), (5.29).

C.2 Derivation of CRLB for the rate of change of phase difference

The signal model given in Eqs. (5.30), (5.31) are rewrited as follows.

$$x_0[m] = a\exp\{-j\psi[m]\} + w_0[m] \tag{C.23}$$
$$x_1[m] = a\exp\left\{-j\left(\psi[m] + \phi + \dot{\phi}m\tau\right)\right\} + w_1[m] \tag{C.24}$$

Here, the variables in Eqs. (5.30), (5.31) are replaced by

$$\begin{aligned} s_{0k}\exp\{-j\psi[m]\} &= s_{ik}\exp\{-j\psi[m]\} = a\exp\{-j\psi[m]\}, \\ \phi_{ik} &= \phi, \\ \dot{\phi}_{ik} &= \dot{\phi}, \end{aligned}$$

respectively. Note that the complex amplitudes are assumed to be identical in the both signal, which is valid if the baseline is sufficiently short compared to the range, and the phase term of the complex amplitude is now included in the phase term $\psi[m]$. Since $w_0[m], w_1[m]$ are assumed to be WGN with variance σ^2, the joint probability density function of $x_0[m]$ and $x_1[m]$ is given by

$$p(\mathbf{x};\boldsymbol{\xi}) = \frac{1}{\pi^M\sigma^{2M}}\exp\left[-\frac{1}{\sigma^2}(\mathbf{x}-\boldsymbol{\mu}(\boldsymbol{\xi}))^H(\mathbf{x}-\boldsymbol{\mu}(\boldsymbol{\xi}))\right], \tag{C.25}$$

where, the parameter vector $\boldsymbol{\xi}$ is defined as

$$\boldsymbol{\xi} = \left[a \;\; \psi\left(-\frac{M-1}{2}\right) \;\; \cdots \;\; \psi\left(\frac{M-1}{2}\right) \;\; \phi \;\; \dot{\phi}\right]^T, \tag{C.26}$$

and

$$\mathbf{x} = \begin{bmatrix} \mathbf{x}_0 \\ \mathbf{x}_1 \end{bmatrix}, \qquad \boldsymbol{\mu}(\boldsymbol{\xi}) = \begin{bmatrix} \boldsymbol{\mu}_0(\boldsymbol{\xi}) \\ \boldsymbol{\mu}_1(\boldsymbol{\xi}) \end{bmatrix},$$
$$\mathbf{x}_p = \begin{bmatrix} x_p\left[-\frac{M-1}{2}\right] \\ \vdots \\ x_p\left[\frac{M-1}{2}\right] \end{bmatrix}, \qquad \boldsymbol{\mu}_p(\boldsymbol{\xi}) = \begin{bmatrix} \mu_p\left[-\frac{M-1}{2}\right] \\ \vdots \\ \mu_p\left[\frac{M-1}{2}\right] \end{bmatrix}, \qquad p = 0,1 \tag{C.27}$$

Here, $\mu_o[m]$, $\mu_1[m]$ are the means of $x_0[m]$, $x_1[m]$, respectively, and they are given by

$$\mu_0[m] = a\exp\{-j\psi[m]\} \tag{C.28}$$
$$\mu_1[m] = a\exp\left\{-j\left(\psi[m] + \phi + \dot{\phi}m\tau\right)\right\}. \tag{C.29}$$

The partial derivatives of $\boldsymbol{\mu}(\boldsymbol{\xi})$ are given as follows.

$$\frac{\partial \mu_0[m]}{\partial a} = \exp\{-j\psi[m]\}, \quad \frac{\partial \mu_1[m]}{\partial a} = \exp\left\{-j[\psi[m]+\phi+\dot{\phi}m\tau]\right\} \tag{C.30}$$

$$\frac{\partial \mu_0[m]}{\partial \psi[m]} = -j\mu_0[m], \quad \frac{\partial \mu_1[m]}{\partial \psi[m]} = -j\mu_1[m] \tag{C.31}$$

$$\frac{\partial \mu_0[m]}{\partial \phi} = 0, \quad \frac{\partial \mu_1[m]}{\partial \phi} = -j\mu_1[m] \tag{C.32}$$

$$\frac{\partial \mu_0[m]}{\partial \dot{\phi}} = 0, \quad \frac{\partial \mu_1[m]}{\partial \dot{\phi}} = -jm\tau\mu_1[m] \tag{C.33}$$

Substituting Eqs. (C.30)–(C.33) into Eq. (C.6), we obtain the elements of the FIM as follows.

$$[\mathbf{G}(\boldsymbol{\xi})]_{11} = \frac{2}{\sigma^2}\mathrm{Re}\left[\sum_{-(M-1)/2}^{(M-1)/2} 1 + \sum_{-(M-1)/2}^{(M-1)/2} 1\right] = \frac{4M}{\sigma^2} \tag{C.34}$$

$$[\mathbf{G}(\boldsymbol{\xi})]_{1\nu} = 0 \qquad (\nu = 2,\cdots,M+1) \tag{C.35}$$

$$[\mathbf{G}(\boldsymbol{\xi})]_{1(M+2)} = 0 \tag{C.36}$$

$$[\mathbf{G}(\boldsymbol{\xi})]_{1(M+3)} = 0 \tag{C.37}$$

$$[\mathbf{G}(\boldsymbol{\xi})]_{\mu\nu} = \frac{2}{\sigma^2}\mathrm{Re}\left[a^2\delta_{\mu,\nu} + a^2\delta_{\mu,\nu}\right] = \frac{4a^2}{\sigma^2}\delta_{\mu,\nu} \qquad (\mu,\nu = 2,\cdots,M+1) \tag{C.38}$$

$$[\mathbf{G}(\boldsymbol{\xi})]_{\mu(M+2)} = \frac{2a^2}{\sigma^2} \qquad (\mu = 2,\cdots,M+1) \tag{C.39}$$

$$[\mathbf{G}(\boldsymbol{\xi})]_{\mu(M+3)} = \frac{2a^2}{\sigma^2}\left(-\frac{M-1}{2}+\mu-2\right)\tau \qquad (\mu = 2,\cdots,M+1) \tag{C.40}$$

$$[\mathbf{G}(\boldsymbol{\xi})]_{(M+2)(M+2)} = \frac{2}{\sigma^2}\mathrm{Re}\left[a^2\sum_{-(M-1)/2}^{(M-1)/2} 1\right] = \frac{2Ma^2}{\sigma^2} \tag{C.41}$$

$$[\mathbf{G}(\boldsymbol{\xi})]_{(M+2)(M+3)} = \frac{2}{\sigma^2}\mathrm{Re}\left[a^2\tau\sum_{-(M-1)/2}^{(M-1)/2} m\right] = 0 \tag{C.42}$$

$$[\mathbf{G}(\boldsymbol{\xi})]_{(M+3)(M+3)} = \frac{2}{\sigma^2}\mathrm{Re}\left[a^2\tau^2\sum_{-(M-1)/2}^{(M-1)/2} m^2\right] = \frac{2a^2\tau^2}{\sigma^2}\cdot\frac{M(M^2-1)}{12} \tag{C.43}$$

which yield the FIM for $\boldsymbol{\xi}$ to be

$$\mathbf{G}(\boldsymbol{\xi}) = \left[\begin{array}{c|c|c|c} \frac{4M}{\sigma^2} & 0 & 0 & 0 \\ \hline 0 & \frac{4a^2}{\sigma^2}\mathbf{I} & \frac{2}{\sigma^2}\mathbf{1} & \frac{2a^2\tau}{\sigma^2}\mathbf{m} \\ \hline 0 & \frac{2}{\sigma^2}\mathbf{1}^T & \frac{2Ma^2}{\sigma^2} & 0 \\ \hline 0 & \frac{2a^2\tau}{\sigma^2}\mathbf{m}^T & 0 & \frac{a^2\tau^2}{\sigma^2}\cdot\frac{M(M^2-1)}{6}, \end{array}\right] \tag{C.44}$$

where $\mathbf{I}$ is an $M\times M$ identity matrix, $\mathbf{1}$ is an M-dimensional column vector whose elements are all one, and $\mathbf{m} = [-(M-1)/2, -(M-3)/2, \cdots, (M-1)/2]^T$. From Eq. (C.44), we can see that the parameter a is independent of other parameters; therefore, the FIM for ϕ and $\dot{\phi}$

are obtained as the Schur complement of the lower right block of the $\mathbf{G}(\boldsymbol{\xi})$ as follows.

$$\begin{aligned}\mathbf{G}\left(\begin{bmatrix}\phi\\ \dot{\phi}\end{bmatrix}\right) &= \begin{bmatrix}\frac{2Ma^2}{\sigma^2} & 0\\ 0 & \frac{a^2\tau^2}{\sigma^2}\frac{M(M^2-1)}{6}\end{bmatrix} - \frac{1}{2a^2}\begin{bmatrix}\mathbf{1}^T\\ a^2\boldsymbol{\tau}\mathbf{m}^T\end{bmatrix}\begin{bmatrix}\mathbf{1} & a^2\boldsymbol{\tau}\mathbf{m}\end{bmatrix}\\ &= \begin{bmatrix}\frac{(2a^4-1)M}{a^2\sigma^2} & 0\\ 0 & \frac{a^2\tau^2}{\sigma^2}\cdot\frac{M(M^2-1)}{12}\end{bmatrix}\end{aligned} \tag{C.45}$$

The CRLB for $\dot{\phi}$ can be readily derived by inverting the FIM given by Eq. (C.45).

Bibliography

[1] R. W. K. Thomas Lillesand, *Remote Sensing and Image Interpretation*. Wiley, 1999.

[2] J. v. Z. Charles Elachi, *Introduction to the Physics And Techniques of Remote Sensing*. Wiley-Interscience, 2006.

[3] "The report on the council on science and technology policy for building a safe and secure society." Accessed: 5 May 2025. (2004), [Online]. Available: https://www.mext.go.jp/a_menu/kagaku/anzen/houkoku/04042302.htm.

[4] R. N. M. John C. Curlander, *Synthetic Aperture Radar: Systems and Signal Processing*. Wiley-Interscience, 1991.

[5] I. G. Cumming and F. H. Wong, *Digital Processing of Synthetic Aperture Radar Data*. Artech House, 2005.

[6] "Tsx (terrasar-x)." Accessed: 5 May 2025. (2023), [Online]. Available: https://www.eoportal.org/satellite-missions/terrasar-x#spacecraft.

[7] "Radarsat-2." Accessed: 5 May 2025. (2024), [Online]. Available: https://www.eoportal.org/satellite-missions/radarsat-2.

[8] "Alos-2 (advanced land observing satellite-2) / daichi-2." Accessed: 5 May 2025. (2024), [Online]. Available: https://www.eoportal.org/satellite-missions/alos-2.

[9] M. Shimada, *Imaging from Spaceborne and Airborne SARs, Calibration, and Applications (SAR Remote Sensing)*. CRC Press, 2018.

[10] K. Ouchi, "Recent trend and advance of synthetic aperture radar with selected topics," *Remote Sensing*, no. 5, pp. 716–807, 2013.

[11] C. A. Wiley, "Synthetic aperture radars," *IEEE Transactions on Aerospace and Electronic Systems*, vol. 21, no. 3, pp. 440–443, 1985.

[12] "A declassified history : Quill." Accessed: 5 May 2025. (2007), [Online]. Available: https://www.nro.gov/About-NRO/history/history-quill/.

[13] R. L. Butterworth, "Quill the first imaging radar satellite," *National Reconnaissance Office document*, 2004.

[14] "Seasat (also called seasat-a or seasat-1)." Accessed: 5 May 2025. (2012), [Online]. Available: https://www.eoportal.org/satellite-missions/seasat.

[15] R. L. Jordan, "The seasat —a synthetic aperture radar system," *IEEE Journal of Oceanic Engineering*, vol. 5, no. 2, pp. 154–164, 1980.

[16] "Sir (shuttle imaging radar)." Accessed: 5 May 2025. (2012), [Online]. Available: https://www.eoportal.org/other-space-activities/sir.

[17] M. S. JoBea Cimino Charles Elachi, "Sir-b-the second shuttle imaging radar experiment," *IEEE Transactions on Geoscience and Remote Sensing*, vol. GE-24, no. 4, pp. 445452, 1986.

[18] W. Johnson, "Magellan imaging radar mission to venus," *Proceedings of the IEEE*, vol. 79, no. 6, pp. 777790, 1991.

[19] "Ers-1 (european remote-sensing satellite-1)." Accessed: 5 May 2025. (2024), [Online]. Available: https://www.eoportal.org/satellite-missions/ers-1.

[20] E. Attema, "The active microwave instrument on-board the ers-1 satellite," *Proceedings of the IEEE*, vol. 79, no. 6, pp. 791–799, 1991.

[21] "Ers-2 (european remote-sensing satellite-2)." Accessed: 5 May 2025. (2024), [Online]. Available: https://www.eoportal.org/satellite-missions/ers-2.

[22] "Jers-1 (japan earth resources satellite)." Accessed: 5 May 2025. (2012), [Online]. Available: https://www.eoportal.org/satellite-missions/jers-1.

[23] M. Shimada, "Jaxa earth observation programs digest," *IEEE Geoscience and Remote Sensing Magazine*, vol. 2, no. 2, pp. 47–52, 2014.

[24] "Sir-c (shuttle imaging radar with payload c)." Accessed: 5 May 2025. (2022), [Online]. Available: https://www.eoportal.org/satellite-missions/sir-c.

[25] R. J. B. H. M. Werner, "The sir-c/x-sar synthetic aperture radar system," *IEEE Transactions on Geoscience and Remote Sensing*, vol. 33, no. 4, pp. 829–839, 1995.

[26] "Radarsat-1." Accessed: 5 May 2025. (2024), [Online]. Available: https://www.eoportal.org/satellite-missions/radarsat-1.

[27] "Cosmo-skymed." Accessed: 5 May 2025. (2023), [Online]. Available: https://www.eoportal.org/satellite-missions/cosmo-skymed.

[28] O. D. L. L. P. L. M. N. Darren Muff Vladimir Ignatenko, "The iceye constellation — some new achievements," *IEEE Radar Conference (RadarConf22)*, 2022.

[29] C. S. M. D. D. E. Davide Castelletti Gordon Farquharson, "Capella space first operational sar satellite," *IEEE International Geoscience and Remote Sensing Symposium (IGARSS)*, 2021.

[30] M. M. D. G. B. H. S. M. K. Krzysztof Orzel Aito Fujita, "Ynspective sar constellation status update: Recent calval activities and the automatic data quality assessment," *IEEE International Geoscience and Remote Sensing Symposium (IGARSS)*, 2023.

[31] R. Vehmas and N. Neuberger, "Inverse synthetic aperture radar imaging: A historical perspective and state-of-the-art survey," *IEEE Access*, vol. 9, pp. 113 917–113 943, 2021.

[32] R. Avent, J. Shelton, and P. Brown, "The alcor c-band imaging radar," *IEEE Antennas and Propagation Magazine*, vol. 38, no. 3, pp. 16–27, 1996.

[33] M. G. Czerwinski and J. M. Usoff, "Development of the haystack ultrawideband satellite imaging radar," *Lincoln Laboratory Journal*, vol. 21, no. 1, pp. 28–44, 2014.

[34] M. Berizzi F.; Diani, "Isar imaging of rolling, pitching and yawing targets," in *Proceedings., CIE International Conference of Radar, 1996.*, 1996, pp. 346–349.

[35] J. H. B. Gibbins D.; Symons, "Ship motion estimation from isar data," in *Proceedings of the Fifth International Symposium on Signal Processing and Its Applications, 1999. ISSPA '99.*, vol. 1, 1999, pp. 333–336.

[36] J. G. R. Hajduch G.; Le Caillec, "Airborne high-resolution isar imaging of ship targets at sea," *IEEE Trans. Aerosp. Electron. Syst.*, vol. 40, no. 1, pp. 378–384, 2004.

[37] Y. Du, Y. Jiang, and W. Zhou, "An accurate two-step isar cross-range scaling method for earth-orbit target," *IEEE Geoscience and Remote Sensing Letters*, vol. 14, no. 11, pp. 1893–1897, 2017.

[38] S. Anger, M. Jirousek, S. Dill, and M. Peichl, "Iosis a high performance experimental imaging radar for space surveillance," in *2019 IEEE Radar Conference (RadarConf)*, 2019, pp. 1–4.

[39] K. Suwa, M. Iwamoto, and T. Kirimoto, "A bandwidth extrapolation technique for improved range resolution of polarimetric radar data," in *Proceedings of the 41st SICE Annual Conference. SICE 2002.*, vol. 5, 2002, 2944–2948 vol.5.

[40] K. Suwa and M. Iwamoto, "A bandwidth extrapolation technique of polarimetric radar data and a recursive method of polarimetric linear prediction coefficient estimation," in *IGARSS 2003. 2003 IEEE International Geoscience and Remote Sensing Symposium. Proceedings (IEEE Cat. No.03CH37477)*, vol. 7, 2003, 4329–4331 vol.7.

[41] K. Suwa and M. Iwamoto, "Bandwidth extrapolation technique for polarimetric radar data," *IEICE Trans. Commun.*, vol. E87-B, no. 2, pp. 326–334, 2004.

[42] K. Suwa and M. Iwamoto, "A two-dimensional bandwidth extrapolation technique for polarimetric synthetic aperture radar images," *IEEE Transactions on Geoscience and Remote Sensing*, vol. 45, no. 1, pp. 45–54, 2007.

[43] K. Suwa, T. Wakayama, and M. Iwamoto, "A study on the resolution limit of polarimetric radar and the performance of polarimetric bandwidth extrapolation technique," in *2011 IEEE International Geoscience and Remote Sensing Symposium*, 2011, pp. 3831–3834.

[44] K. Suwa, M. Iwamoto, and T. Wakayama, "Analysis on the resolution of polarimetric radar and performance evaluation of the polarimetric bandwidth extrapolation method," *IEEE Transactions on Geoscience and Remote Sensing*, vol. 51, no. 7, pp. 4260–4278, 2013.

[45] K. Suwa, K. Yamamoto, M. Tsuchida, *et al.*, "An experimental study on image based multi-channel sar-gmti algorithm," in *Conference Proceedings of 2013 Asia-Pacific Conference on Synthetic Aperture Radar (APSAR)*, 2013, pp. 577–580.

[46] K. Suwa, R. Takahashi, T. Wakayama, S. Nakamura, and M. Iwamoto, "Image based approach for target detection and robust target velocity estimation method for multichannel sar-gmti," in *2013 IEEE International Geoscience and Remote Sensing Symposium - IGARSS*, 2013, pp. 2035–2038.

[47] K. Suwa, K. Yamamoto, M. Tsuchida, S. Nakamura, T. Wakayama, and T. Hara, "Image-based target detection and radial velocity estimation methods for multichannel sar-gmti," *IEEE Transactions on Geoscience and Remote Sensing*, vol. 55, no. 3, pp. 1325–1338, 2017.

[48] K. Suwa and T. Wakayama, "Experimental study on along track target velocity estimation for multiple aperture sar-mti configuration," in *IGARSS 2020 - 2020 IEEE International Geoscience and Remote Sensing Symposium*, 2020, pp. 5–8.

[49] K. Suwa, K. Yamamoto, M. Iwamoto, and T. Kirimoto, "Reconstruction of 3-d target geometry using radar movie," in *7th European Conference on Synthetic Aperture Radar*, 2008, pp. 1–4.

[50] K. Suwa, T. Wakayama, and M. Iwamoto, "Estimation of target motion and 3d target geometry using multistatic isar movies," in *2009 IEEE International Geoscience and Remote Sensing Symposium*, vol. 5, 2009, pp. V–429–V–432.

[51] K. Suwa, T. Wakayama, and M. Iwamoto, "Three-dimensional target geometry and target motion estimation method using multistatic isar movies and its performance," *IEEE Transactions on Geoscience and Remote Sensing*, vol. 49, no. 6, pp. 2361–2373, 2011.

[52] S. T. Smith, "Statistical resolution limits and the complexified Cramer-Rao bound," *IEEE Transactions on Signal Processing*, vol. 53, no. 5, pp. 1597–1609, 2005.

[53] M. Skolnik, *Introduction to Radar Systems, Third Edition*. McGraw Hill, 2001.

[54] D. R. Wehner, *High-Resolution Radar Second Edition*. Artech House, 1995.

[55] G. W. Stimson, *Introduction to Airborne Radar*. Scitech Pub Inc, 1998.

[56] A. Rihaczek and S. J. Hershkowitz, *Radar resolution and complex-Image analysis*. Artech House, 1996.

[57] N. Gebert and G. Krieger, "Azimuth phase center adaptation on transmit for high-resolution wide-swath sar imaging," *IEEE Geoscience and Remote Sensing Letters*, vol. 6, no. 4, pp. 782–786, 2009.

[58] N. Gebert, G. Krieger, and A. Moreira, "Multichannel azimuth processing in scansar and tops mode operation," *IEEE Transactions on Geoscience and Remote Sensing*, vol. 48, no. 7, pp. 2994–3008, 2010.

[59] N. Gebert, F. Queiroz de Almeida, and G. Krieger, "Airborne demonstration of multichannel sar imaging," *IEEE Geoscience and Remote Sensing Letters*, vol. 8, no. 5, pp. 963–967, 2011.

[60] F. Bordoni, M. Younis, and G. Krieger, "Ambiguity suppression by azimuth phase coding in multichannel sar systems," *IEEE Transactions on Geoscience and Remote Sensing*, vol. 50, no. 2, pp. 617–629, 2012.

[61] F. Queiroz de Almeida, M. Younis, G. Krieger, and A. Moreira, "An analytical error model for spaceborne sar multichannel azimuth reconstruction," *IEEE Geoscience and Remote Sensing Letters*, vol. 15, no. 6, pp. 853–857, 2018.

[62] F. Queiroz de Almeida, M. Younis, G. Krieger, and A. Moreira, "Multichannel staggered sar azimuth processing," *IEEE Transactions on Geoscience and Remote Sensing*, vol. 56, no. 5, pp. 2772–2788, 2018.

[63] F. Q. de Almeida, T. Rommel, M. Younis, G. Krieger, and A. Moreira, "Multichannel staggered sar: System concepts with reflector and planar antennas," *IEEE Transactions on Aerospace and Electronic Systems*, vol. 55, no. 2, pp. 877–902, 2019.

[64] A. Barros Cardoso da Silva, S. V. Baumgartner, F. Q. de Almeida, and G. Krieger, "In-flight multichannel calibration for along-track interferometric airborne radar," *IEEE Transactions on Geoscience and Remote Sensing*, vol. 59, no. 4, pp. 3104–3121, 2021.

[65] F. T. Ulaby and C. Elachi, *Radar Polarimetry for Geoscience Applications*. Artech House, 1990.

[66] L. M. Novak, M. C. Burl, and W. W. Irving, "Optimal polarimetric processing for enhanced target detection," *IEEE Transactions on Aerospace and Electronic Systems*, vol. 29, no. 1, pp. 234–244, Jan. 1993.

[67] L. M. Novak, S. D. Halversen, G. Owirka, and M. Hiett, "Effects of polarization and resolution on sar atr," *IEEE Transactions on Aerospace and Electronic Systems*, vol. 33, no. 1, pp. 102–116, Jan. 1997.

[68] J.-S. Lee, M. R. Grunes, E. Pottier, and L. Ferro-Famil, "Unsupervised terrain classification preserving polarimetric scattering characteristics," *IEEE Transactions on Geoscience and Remote Sensing*, vol. 42, no. 4, pp. 722–731, Apr. 2004.

[69] E. Pottier and L. Ferro-Famil, "Advances in sar polarimetry applications exploiting polarimetric spaceborne sensors," in *IEEE Radar Conference*, 2008, pp. 1–6.

[70] Y. Yamaguchi, A. Sato, W.-M. Boerner, R. Sato, and H. Yamada, "Four-component scattering power decomposition with rotation of coherency matrix," *IEEE Transactions on Geoscience and Remote Sensing*, vol. 49, no. 6, pp. 2251 –2258, Jun. 2011.

[71] M. Arii, J. van Zyl, and Y. Kim, "Adaptive model-based decomposition of polarimetric sar covariance matrices," *IEEE Transactions on Geoscience and Remote Sensing*, vol. 49, no. 3, pp. 1104 –1113, Mar. 2011.

[72] D. Pastina, A. Montanari, and A. Aprile, "Motion estimation and optimum time selection for ship isar imaging," in *Proceedings of the 2003 IEEE Radar Conference*, 2003, pp. 7–14.

[73] D. Pastina and C. Spina, "Slope-based frame selection and scaling technique for ship isar imaging," *IET Signal Processing*, vol. 2, no. 3, pp. 265–276, 2008.

[74] J. Munoz-Ferreras and F. Perez-Martinez, "Pitch estimation for noncooperative maritime targets in isar scenarios," *IET Radar, Sonar, Navigation*, vol. 3, no. 5, pp. 521–529, 2009.

[75] M. Stuff, P. Sanchez, and M. Biancalana, "Extraction of three-dimensional motion and geometric invariants from range dependent signals," *Multidimensional Systems and Signal Processing*, vol. 14, no. 1-3, pp. 161–181, 2003.

[76] T. Fritz and M. Eineder, "Terrasar-x ground segment basic product specification document," vol. TX-GS-DD-3302, Oct. 2010.

[77] J.-S. Lee, E. Krogager, T. Ainsworth, and W.-M. Boerner, "Polarimetric analysis of radar signature of a manmade structure," *IEEE Geoscience and Remote Sensing Letters*, vol. 3, no. 4, pp. 555 –559, Oct. 2006.

[78] S. R. DeGraaf, "Sar imaging via modern 2-d spectral estimation methods," *IEEE Trans. Image Proc.*, vol. 7, no. 5, pp. 729–761, May 1998.

[79] S. L. Borison, S. B. Bowling, and K. M. Cuomo, "Super-resolution methods for wideband radar," *The Lincoln Laboratory Journal*, vol. 5, no. 3, pp. 441–461, Mar. 1992.

[80] T. G. Moore, B. W. Zuerndorfer, and E. C. Burt, "Enhanced imagery using spectral-estimation-based techniques," *The Lincoln Laboratory Journal*, vol. 10, no. 2, pp. 171–186, Feb. 1997.

[81] R. A. Wiggins and E. A. Robinson, "Recursive solution to the multichannel filtering problem," *Journal of Geophysical Research*, vol. 70, no. 8, pp. 1885–1891, Apr. 1965.

[82] W. L. Cameron, N. N. Youssef, and L. K. Leung, "Simulated polarimetric signatures of primitive geometrical shapes," *IEEE Transactions on Geoscience and Remote Sensing*, vol. 34, no. 3, pp. 793–803, May 1996.

[83] P. Stoica and A. Nehorai, "Music, maximum likelihood, and Cramer-Rao bound," *IEEE Trans. Acoust., Speech, Signal Process.*, vol. 37, no. 5, pp. 720–741, 1989.

[84] C.-H. J. Ying, A. Sabharwal, and R. L. Moses, "A combined order selection and parameter estimation algorithm for undamped exponentials," *IEEE Transactions on Signal Processing*, vol. 48, no. 3, pp. 693–701, 2000.

[85] A. van den Bos, "A Cramer-Rao lower bound for complex parameters," *IEEE Transactions on Signal Processing*, vol. 42, no. 10, p. 2859, 1994.

[86] S. F. Yau and Y. Bresler, "A compact Cramer-Rao bound expression for parametric estimation of superimposed signals," *IEEE Transactions on Signal Processing*, vol. 40, no. 5, pp. 1226–1230, 1992.

[87] H. Van Trees, *Detection Estimation and Modulation Theory*. John Wiley and Sons, Inc., 1968.

[88] R. W. Miller and C. B. Chang, "A modified Cramer-Rao bound and its applications," *IEEE Transactions on Information Theory*, vol. 24, no. 3, pp. 398–400, 1978.

[89] S. F. Yau and Y. Bresler, "Worst case Cramer-Rao bounds for parametric estimation of superimposed signals with applications," *IEEE Transactions on Signal Processing*, vol. 40, no. 12, pp. 2973–86, 1992.

[90] D. N. Swingler, "Frequency estimation for closely spaced sinsoids: Simple approximations to the Cramer-Rao lower bound," *IEEE Transactions on Signal Processing*, vol. 41, no. 1, pp. 489–494, 1993.

[91] S. Narasimhan and J. L. Krolik, "Fundamental limits on acoustic source range estimation performance in uncertain ocean channels," *Journal of the Acoustical Society of America*, vol. 97, no. 1, pp. 215–226, 1995.

[92] M. Ghogho and A. Swami, "Fast computation of the exact fim for deterministic signals in colored noise," *IEEE Transactions on Signal Processing*, vol. 47, no. 1, pp. 52–61, 1999.

[93] F. Gini and R. Reggiannini, "On the use of Cramer-Rao-like bounds in the presence of random nuisance parameters," *IEEE Transactions on Commnications*, vol. 48, no. 12, pp. 2120–2126, 2000.

[94] Y. Noam and H. Messer, "Notes on the tightness of the hybrid cramer-rao lower bound," *IEEE Transactions on Signal Processing*, vol. 57, no. 6, pp. 2074–2084, 2009.

[95] A. J. Weiss and B. Friedlander, "Performance analysis of diversely polarized antenna arrays," *IEEE Transactions on Signal Processing*, vol. 39, no. 7, pp. 1589–1603, 1991.

[96] A. J. Weiss and B. Friedlander, "Fundamental limitations of diversely polarized antenna arrays," in *IEEE International Conference on Acoustics, Speech, and Signal Processing, 1992. ICASSP-92.*, vol. 4, 1992, pp. 449–452.

[97] B. Friedlander and A. J. Weiss, "The resolution threshold of a direction-finding algorithm for diversely polarized arrays," *IEEE Transactions on Signal Processing*, vol. 42, no. 7, pp. 1719–1727, 1994.

[98] S. R. Cloude and E. Pottier, "A review of target decomposition theorems in radar polarimetry," *IEEE Transactions on Geoscience and Remote Sensing*, vol. 34, no. 34, pp. 498–518, May 1996.

[99] A. Rihaczek and S. Hershkowitz, "Man-made target backscattering behavior: Applicability of conventional radar resolution theory," *IEEE Transactions on Aerospace and Electronic Systems*, vol. 32, no. 2, pp. 809 –824, 1996.

[100] R. N. McDonough and A. D. Whalen, *Detenction of Signals in Noise*. Academic Press, Inc., 1995.

[101] N. Abramson, "Bandwidth and spectra of phase-and-frequency-modulated waves," *IEEE Trans. Commun.*, vol. 11, no. 4, pp. 407–414, 1963.

[102] A. J. Weiss and B. Friedlander, "On the cramér-Rao bound for direction finding of correlated signals," *IEEE Transactions on Signal Processing*, vol. 41, no. 1, pp. 495–499, 1993.

[103] S. M. Kay, *Fundamentals of Statistical Signal Processing*. Prentice-Hall, Inc., 1993.

[104] T. G. Moore, B. W. Zuerndorfer, and E. C. Burt, "Enhanced imagery using spectral-estimation-based techniques," *The Lincoln Laboratory Journal*, vol. 10, no. 2, pp. 171–186, 1997.

[105] S. Suchandt, H. Runge, H. Breit, U. Steinbrecher, A. Kotenkov, and U. Balss, "Automatic extraction of traffic flows using terrasar-x along-track interferometry," *IEEE Transactions on Geoscience and Remote Sensing*, vol. 48, no. 2, pp. 807 –819, 2010.

[106] C. H. Gierull, "Statistical analysis of multilook sar interferograms for cfar detection of ground moving targets," *IEEE Trans. Geosci. Remote Sens.*, vol. 42, no. 4, pp. 691–701, 2004.

[107] J. H. G. Ender, "Space-time processing for multichannel synthetic aperture radar," *ELECTRONICS & COMMUNICATION ENGINEERING JOURNAL*, vol. 11, no. 1, pp. 29–38, 1999.

[108] C. Gierull, "Ground moving target parameter estimation for two-channel sar," *IEE Proceedings - Radar, Sonar and Navigation*, vol. 153, no. 3, pp. 224 –233, 2006, 1648541.

[109] C. H. Gierull, C. H. Gierull, and J. H. G. Ender, "Improved multi-channel gmti via moving target de-chirping and range migration correction," *2008 7th European Conference on Synthetic Aperture Radar (EUSAR)*, pp. 1 –4, 2008.

[110] D. Cerutti-Maori and I. Sikaneta, "A generalization of dpca processing for multichannel sar/gmti radars," *IEEE Transactions on Geoscience and Remote Sensing*, vol. 51, no. 99, pp. 560–572, 2013.

[111] S. Barbarossa and A. Farina, "Space-time-frequency processing of synthetic aperture radar signals," *IEEE Transactions on Aerospace and Electronic Systems*, vol. 30, no. 2, pp. 341 –358, 1994.

[112] S. Baumgartner and G. Krieger, "Acceleration-independent along-track velocity estimation of moving targets," *Radar, Sonar Navigation, IET*, vol. 4, no. 3, pp. 474 –487, 2010.

[113] I. C. Sikaneta, "Eigendecomposition of the multi-channel covariance matrix with applications to sar-gmti," *Signal Processing*, vol. 84, no. 9, pp. 1501–1535, 2004, printed matter only.

[114] I. C. Sikaneta and C. H. Gierull, "Adaptive cfar for space-based multichannel sar-gmti," *IEEE Transactions on Geoscience and Remote Sensing*, vol. PP, no. 99, pp. 1 –10, 2012.

[115] N. Oishi, M. Tsuchida, T. Wakayama, H. Hasegawa, and Y. Okada, "A coherence improvement technique for coherent change detection in sar interferometry"," in *European Radar Conference, 2009. EuRAD 2009.*, 2009, pp. 278 –281.

[116] C. H. Gierull, I. Sikaneta, and D. Cerutti-Maori, "Two-step detector for radarsat-2's experimental gmti mode," *Geoscience and Remote Sensing, IEEE Transactions on*, vol. PP, no. 99, pp. 1 –19, 2012.

[117] J. Sharma, "The influence of target acceleration on dual-channel sar-gmti (synthetic aperture radar ground moving target indication) data," *Master Thesis, University of Calgary, Calgary, Alberta, Canada*, 2004.

[118] C. Oliver and S. Quegan, *Understanding Synthetic Aperture Rada Images*. Artech House, 1998.

[119] W. M. World. "Gamma distribution." Accessed: 5 May 2025. (2025), [Online]. Available: `https://mathworld.wolfram.com/GammaDistribution.html`.

[120] D. Meyer and H. Mayer, *Radar Target Detection, Handbook of Theory and Practice*. Academic Press, 1973.

[121] K. Knaell and G. Cardillo, "Radar tomography for the generation of three-dimensional images," *IEE Proceedings - Radar, Sonar and Navigation*, vol. 142, no. 2, pp. 54 –60, 1995.

[122] J. Mayhan, M. Burrows, K. Cuomo, and J. Piou, "High resolution 3d gsnapshoth isar imaging and feature extraction," *IEEE Transactions on Aerospace and Electronic Systems*, vol. 37, no. 2, pp. 630 –642, 2001.

[123] R. Lord, W. Nel, and M. Abdul Gaffar, "Investigation of 3-d rcs image formation of ships using isar," in *6th European Conference on Synthetic Aperture Radar, EUSAR 2006*, 2006.

[124] T. Kempf, M. Peichl, S. Dill, and H. Suess, "3d tower-turntable isar imaging," in *European Radar Conference, 2007. EuRAD 2007.*, 2007, pp. 114 –117.

[125] V. Wang Genyuan; Xiang-Gen Xia; Chen, "Three-dimensional isar imaging of maneuvering targets using three receivers," *IEEE Transactions on Image Processing*, vol. 10, no. 3, pp. 436–447, 2001.

[126] R. Xu Xiaojian; Narayanan, "Three-dimensional interferometric isar imaging for target scattering diagnosis and modeling," *IEEE Transactions on Image Processing*, vol. 10, no. 7, pp. 1094–1102, 2001.

[127] C. Ma, T. S. Yeo, Q. Zhang, H. S. Tan, and J. Wang, "Three-dimensional isar imaging based on antenna array," *IEEE Transactions on Geoscience and Remote Sensing*, vol. 46, no. 2, pp. 504 –515, 2008.

[128] T. S. Zhang Q; Yeo, "Three-dimensional sar imaging of a ground moving target using the inisar technique," *IEEE TRANSACTIONS ON GEOSCIENCE AND REMOTE SENSING*, vol. 42, no. 9, pp. 1818 –1828, 2004.

[129] M. Iwamoto and T. Kirimoto, "A novel algorithm for reconstructing three-dimensional target shapes using sequential radar images," in *IEEE 2001 International Geoscience and Remote Sensing Symposium, 2001. IGARSS '01.*, vol. 4, 2001, pp. 1607 –1609.

[130] K. Suwa, K. Yamamoto, M. Iwamoto, and T. Kirimoto, "Reconstruction of 3-d target geometry using radar movie," in *EUSAR 2008*, 2008.

[131] T. Cooke, "Ship 3d model estimation from an isar image sequence," in *Proceedings of the International Radar Conference, 2003.*, 2003, pp. 36–41.

[132] K. Suwa, T. Wakayama, and M. Iwamoto, "Estimation of target motion and 3d target geometry using multistatic isar movies," in *IEEE International Geoscience and Remote Sensing Symposium,2009 IGARSS 2009*, vol. 5, 2009, pp. V–429 –V–432.

[133] A. Freeman and S. Durden, "A three-component scattering model for polarimetric sar data," *IEEE Transactions on Geoscience and Remote Sensing*, vol. 36, no. 3, pp. 963 –973, May 1998.

[134] Y. Yamaguchi, T. Moriyama, M. Ishido, and H. Yamada, "Four-component scattering model for polarimetric sar image decomposition," *IEEE Transactions on Geoscience and Remote Sensing*, vol. 43, no. 8, pp. 1699 –1706, Aug. 2005.